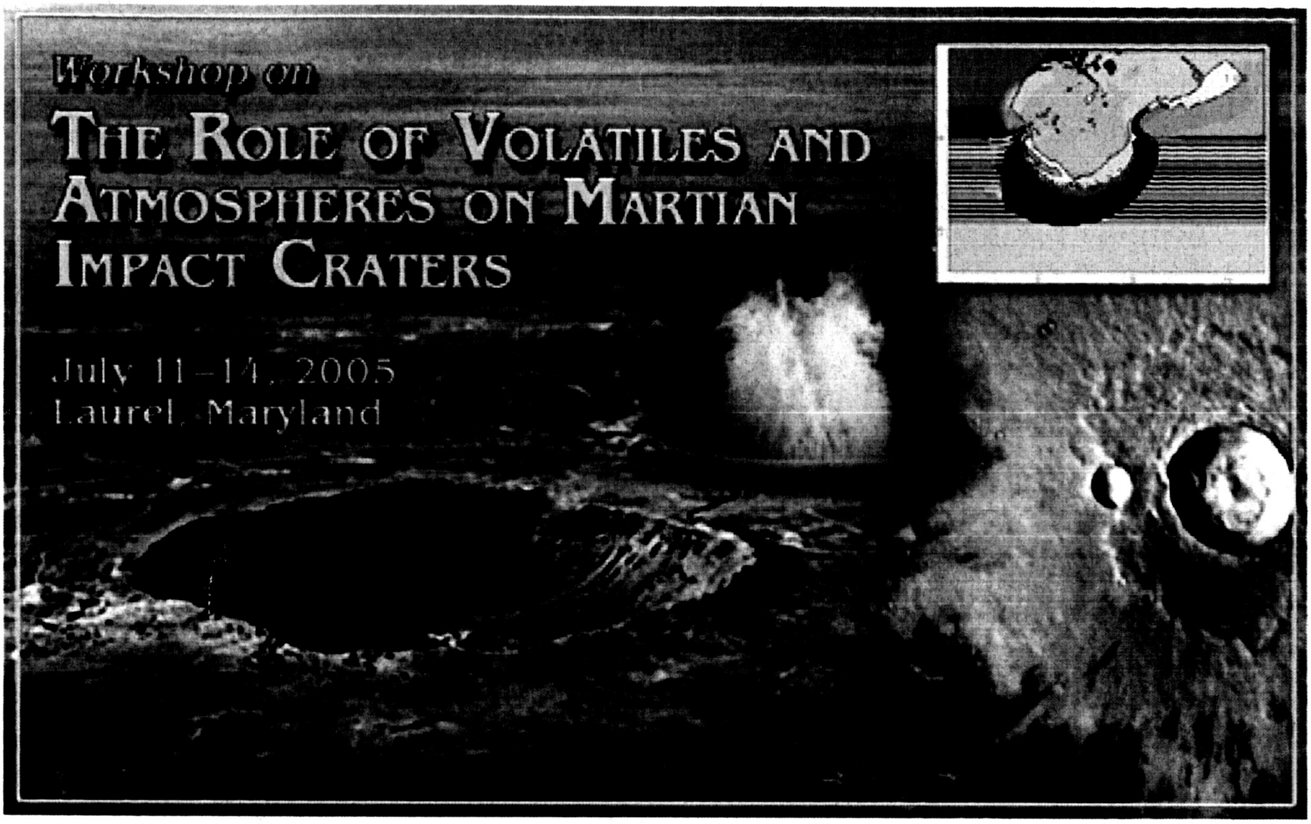

WORKSHOP PROGRAM AND ABSTRACTS

LPI Contribution No. 1273

Workshop on

THE ROLE OF VOLATILES AND ATMOSPHERES ON MARTIAN IMPACT CRATERS

July 11–13, 2005
Laurel, Maryland

Sponsored by

Lunar and Planetary Institute
Mars Crater Consortium
National Aeronautics and Space Administration
Johns Hopkins University Applied Physics Laboratory
Mars Exploration Program Analysis Group

Conveners

Nadine Barlow, *Northern Arizona University*
Olivier Barnouin-Jha, *Johns Hopkins University Applied Physics Laboratory*
Sarah Stewart, *Harvard University*
Joseph Boyce, *University of Hawai'i*
John Grant, *Smithsonian Institution*
Robert Herrick, *University of Alaska, Fairbanks*
Horton Newsom, *University of New Mexico*
Jeffrey Plescia, *Johns Hopkins University Applied Physics Laboratory*
Paul Schenk, *Lunar and Planetary Institute*
Virgil Sharpton, *University of Alaska, Fairbanks*
Livio Tornabene, *University of Tennessee*
Shawn Wright, *Arizona State University*

Lunar and Planetary Institute 3600 Bay Area Boulevard Houston TX 77058-1113

LPI Contribution No. 1273

Compiled in 2005 by
LUNAR AND PLANETARY INSTITUTE

The Institute is operated by the Universities Space Research Association under Agreement No. NCC5-679 issued through the Solar System Exploration Division of the National Aeronautics and Space Administration.

Abstracts in this volume may be cited as

Author A. B. (2005) Title of abstract. In *Workshop on the Role of Volatiles and Atmospheres on Martian Impact Craters,* p. XX. LPI Contribution No. 1273, Lunar and Planetary Institute, Houston.

This volume is distributed by

ORDER DEPARTMENT
Lunar and Planetary Institute
3600 Bay Area Boulevard
Houston TX 77058-1113, USA
Phone: 281-486-2172
Fax: 281-486-2186
E-mail: order@lpi.usra.edu

Mail orders requestors will be invoiced for the cost of shipping and handling.

ISSN No. 0161-5297

Preface

This volume contains abstracts that have been accepted for presentation at the Workshop on the Role of Volatiles and Atmospheres on Martian Impact Craters, July 11–14, 2005, Laurel, Maryland.

Administration and publications support for this meeting were provided by the staff of the Publications and Program Services Department at the Lunar and Planetary Institute.

Contents

Monday, July 11, 2005

WELCOME AND WORKSHOP GOALS
9:00 a.m. Auditorium

9:00 a.m. Nadine Barlow, Sarah Stewart, and Olivier Barnouin-Jha
Overview and Goals

OBSERVATIONS OF MARTIAN IMPACT CRATERS: PART I

Chairs: H. E. Newsom

9:30 a.m. Garvin J. B. * [INVITED]
Impact Craters on Mars: Natural 3D Exploration Probes of Geological Evolution **[#3052]**

9:55 a.m. Barlow N. G. *
The Influence of Volatiles and Atmospheres on Martian Impact Crater Morphologies **[#3032]**

10:15 a.m. Reiss D. * van Gasselt S. Hauber E. Michael G. Jaumann R.
Neukum G. HRSC Co-Investigator Team
Ages and Onset Diameters of Rampart Craters in Equatorial Regions on Mars **[#3012]**

10:35 a.m. Boyce J. M. * Mouginis-Mark P. J.
Martian Craters Viewed by the THEMIS Instrument: Double-layered Ejecta Craters **[#3009]**

10:55 a.m. BREAK

11:10 a.m. Kreslavsky M. A. * Head J. W.
Subkilometer-scale Roughness of Crater Ejecta in the Northern Plains of Mars:
Implications for Climate-related Alteration **[#3040]**

11:30 a.m. Black B. A. * Stewart S. T.
Impact Crater Geometries Provide Evidence for Ice-rich Layers at Low Latitudes on Mars **[#3044]**

11:50 a.m. Herrick R. R. *
Inferences from Oblique Impact Craters About the Role of the Atmosphere and Subsurface Volatiles
in the Impact Cratering Process on Mars **[#3019]**

12:00 p.m. DISCUSSION

12:30 p.m. LUNCH

* *Denotes Speaker*

Monday, July 11, 2005, continued

OBSERVATIONS OF MARTIAN IMPACT CRATERS: PART II
1:45 p.m. Auditorium

Chair: J. M. Boyce

1:45 p.m. Golombek M. * Grant J. A. Crumpler L. S. Haldemann A. F. C.
Athena Science Team [INVITED]
Mars Exploration Rover Field Observations of Impact Craters at Gusev Crater and Meridiani Planum and Implications for Climate Change **[#3016]**

2:15 p.m. Grant J. A. * Golombek M. P. Haldemann A. F. C. Crumpler L. Li R.
Watters W. A. Athena Science Team [INVITED]
Field Studies of Crater Gradation in Gusev Crater and Meridiani Planum Using the Mars Exploration Rovers **[#3004]**

2:45 p.m. Mustard J. F. * [INVITED]
New Insights into Martian Impact Craters from OMEGA Observations

3:15 p.m. DISCUSSION

Monday, July 11, 2005, continued

POSTER SESSION I
3:30 p.m. Lobby

Chair: L. L. Tornabene

Barlow N. G.
A New Model for Pedestal Crater Formation **[#3041]**

Meresse S. Baratoux D. Costard F. Mangold N.
Perched Craters and Episodes of Sublimation on Northern Plains **[#3001]**

Tornabene L. L.
Evidence for the Role of Sub-Surface Volatiles in the Formation of Large Rayed Crater Systems on Mars: Implications for the Ejection of the Martian Meteorites **[#3025]**

Plesko C. S. Asphaug E. Gisler G. R. Gittings M. L.
Verification and Validation of the RAGE Hydrocode in Preparation for Investigation of Impacts into a Volatile-rich Target **[#3022]**

Earl J. Chicarro A. Koeberl C. Marchetti P. G. Milnes M.
Automatic Recognition of Crater-like Structures in Terrestrial and Planetary Images **[#3053]**

Kennedy G. B. Stewart S. T. Senft L. E. Obst A. W. Furlanetto M. R. Payton J. R. Seifter A.
Post-Shock Temperature Measurements of Basalt: Improving the Basalt Equation of State and Modeling of Post-Impact Conditions **[#3051]**

Monday, July 11, 2005, continued

OBSERVATIONS OF MARTIAN IMPACT CRATERS: PART III
4:10 p.m. Auditorium

Chair: J. A. Grant

4:10 p.m. Hartmann W. K. * [TUTORIAL]
Martian Megaregolith Properties: Effects on Launch of SNCs and Secondary Ejecta **[#3043]**

4:45 p.m. DISCUSSION OF OBSERVATIONS, DATABASES, AND MEASUREMENT TECHNIQUES

Tuesday, July 12, 2005

THE ROLE OF THE ATMOSPHERE
9:00 a.m. Auditorium

Chair: S. T. Stewart

9:00 a.m. Schultz P. H. * [INVITED]
Assessing Lithology from Ejecta Emplacement Styles on Mars: The Role of Atmospheric Interactions **[#3049]**

9:25 a.m. Suzuki A. Barnouin-Jha O. S. * Kumagai I. Nagata Y. Kurita K.
Investigating Surface Scouring Processes and Ejecta Deposition by Impact Generated Winds **[#3050]**

9:45 a.m. Wrobel K. E. * Schultz P. H. Crawford D. A.
Effects of an Early-Time Impact Generated Vapor Blast in the Martian Atmosphere: Formation of High-Latitude Pedestal Craters **[#3037]**

10:05 a.m. Sugita S. * [INVITED]
Interaction Between Impact Vapor Clouds and the Early Martian Atmosphere **[#3054]**

10:30 a.m. DISCUSSION and BREAK

INFLUENCE OF TARGET PROPERTIES: ICE
10:55 a.m. Auditorium

Chair: O. S. Barnouin-Jha

10:55 a.m. Ivanov B. A. Artemieva N. A. Pierazzo E. *
Impact Cratering and Material Models: Subsurface Volatiles on Mars **[#3015]**

11:20 a.m. Stewart S. T. * [INVITED]
H_2O Hugoniot and Impact Induced Melting

11:40 a.m. Abramov O. * Kring D. A.
Impact-induced Hydrothermal Activity at Central-Peak and Peak-Ring Craters on Early Mars **[#3028]**

12:00 p.m. DISCUSSION

12:30 p.m. LUNCH

Tuesday, July 12, 2005, continued

CRATER DEFORMATION AND DEGRADATION: ICE
1:45 p.m. Auditorium

Chair: J. B. Plescia

1:45 p.m.	Schulson E. M. * [TUTORIAL] *On the Brittle Failure of Water Ice Ih: A Short Review* **[#3029]**
2:20 p.m.	Turtle E. P. * Pathare A. V. [INVITED] *"Softening" of Martian Impact Craters by Creep of Ice-rich Permafrost* **[#3034]**
2:55 p.m.	Pathare A. V. * Schaller E. L. Murray B. C. *Viscous Relaxation of Secondary Craters Within the Martian South Polar Layered Deposits* **[#3013]**
3:15 p.m.	Soare R. J. * Wan Bun Tseung J. M. *Possible Crater-Floor Thermokarst in Utopia Planitia, Mars* **[#3011]**
3:35 p.m.	Sakimoto S. E. H. * *Martian Polar Craters: Possible Polar Materials Apparent Effects and Post-Impact Modification by Apparent Perrennial Permafrost Mound (Pingo) Formation* **[#3036]**
3:55 p.m.	DISCUSSION and BREAK
4:25 p.m.	DISCUSSION OF OBSERVATIONS AND TESTS RELATED TO THE ROLES OF VOLATILES AND ATMOSPHERES
6:00 p.m.	BANQUET

Wednesday, July 13, 2005

GRANULAR AND EJECTA FLOW DYNAMICS
9:00 a.m. Auditorium

Chair: R. R. Herrick

9:00 a.m.	McSaveney M. J. * Davies T. R. H. [TUTORIAL] *Making a Grain-Bridge Connection Between Two Rocky Planets* **[#3048]**
9:35 a.m.	Campbell C. S. * [TUTORIAL] *Elastic Granular Flows* **[#3003]**
10:10 a.m.	DISCUSSION and BREAK
10:30 a.m.	Mouginis-Mark P. J. * Baloga S. M. *Run-Out Distances of Ejecta Lobes from SLE and MLE Impact Craters on Mars* **[#3010]**
10:50 a.m.	Barnouin-Jha O. S. * *The Runout Efficiency of Fluidized Ejecta on Mars* **[#3005]**
11:10 a.m.	Wada K. * Barnouin-Jha O. S. *Ejecta Flow from 3-D Granular Flow Models* **[#3006]**
11:30 a.m.	DISCUSSION OF EJECTA FLOW DYNAMICS
12:00 p.m.	LUNCH

Wednesday, July 13, 2005, continued

ANALOG STUDIES
1:15 p.m. Auditorium

Chair: V. L. Sharpton

1:15 p.m. Nordyke M. D. * [TUTORIAL]
Nuclear Cratering Experience in the U.S. and Russia **[#3020]**

1:50 p.m. Kenkmann T. * Schönian F. [TUTORIAL]
Impact Craters on Mars and Earth: Implications by Analogy **[#3017]**

2:25 p.m. Ormö J. *
The Influence of Water on the Cratering and Modification of Marine-Target Craters — Some Thoughts Based on Recent Field Studies and Laboratory Experiments **[#3023]**

2:45 p.m. Newsom H. E. * Nelson M. J. Shearer C. K. Dressler B. O.
Hydrothermal Processes and Mobile Element Transport in Martian Impact Craters — Evidence from Terrestrial Analogue Craters **[#3030]**

3:05 p.m. BREAK

3:20 p.m. Pope K. O. *
The Role of the Atmosphere and Target Volatiles in the Emplacement of the Chicxulub Ejecta Blanket and Analogies with Martian Impact Ejecta **[#3027]**

3:40 p.m. Stewart S. T. * Louzada K. L. Maloof A. C. Newsom H. E. Weiss B. P. Wright S. P.
Field Observations of Ground-hugging Ejecta Flow at Lonar Crater, India **[#3045]**

4:00 p.m. Schenk P. *
What Do Craters on Icy Satellites Tell Us About Martian Craters? **[#3033]**

4:20 p.m. DISCUSSION OF MARTIAN CRATER ANALOGS

Wednesday, July 13, 2005, continued

POSTER SESSION II
4:50 p.m. Lobby

Chair: S. P. Wright

Chesapeake Bay Cores

Maloof A. C. Louzada K. L. Stewart S. T. Weiss B. P.
Geology of Lonar Crater, India: An Analog for Martian Impact Craters **[#3046]**

Haldemann A. F. C. Kleindienst M. R. Churcher C. S. Smith J. R. Schwarcz H. P. Osinski G.
Volatiles in the Desert: Subtle Remote-sensing Signatures of the Dakhleh Oasis Catastrophic Event, Western Desert, Egypt **[#3038]**

Horton J. W. Jr. Powars D. S. Gohn G. S. Ormö J.
Chesapeake Bay Impact Structure: Morphology, Crater Fill, and Relevance for Impact Processes on Mars **[#3024]**

King D. T. Jr. Ormö J. Morrow J. R. Petruny L. W. Johnson R. C. Neathery T. L.
The Role of Water in Development of the Late Cretaceous Wetumpka Impact Crater, Coastal Plain of Alabama, USA **[#3035]**

McConnell B. S. Wilt G. L. Gillespie A. Newsom H. E.
Inverted Martian Craters in Lineated Glacial Valleys, Ismenius Lacus Region, Mars **[#3021]**

Barnhart C. J. Tulaczyk S. Asphaug E. Kraal E. R. Moore J.
Crater Lakes on Mars: Development of Quantitative Thermal and Geomorphic Models **[#3018]**

Thursday, July 14, 2005

CRATER DEGRADATION: FLUVIAL PROCESSES
9:00 a.m. Auditorium

Chair: N. G. Barlow

9:00 a.m. Craddock R. A. * [TUTORIAL]
Modified Impact Craters on Mars: Observations, Measurements and Likely Processes **[#3042]**

9:35 a.m. Mest S. C. *
Characteristics of Impact Craters and Interior Deposits: Analysis of the Spatial and Temporal Distribution of Volatiles in the Highlands of Mars **[#3014]**

9:55 a.m. Irwin R. P. III*
Rim Breaching and Ponding in Martian Impact Craters **[#3039]**

10:15 a.m. Berman D. C. * Hartmann W. K. Crown D. A. Baker V. R.
Arcuate Ridges and Gullies in Martian Craters: Dependence on Orientation and Latitude **[#3007]**

10:35 a.m. Kraal E. R. * Moore J. M. Howard A. D. Asphaug E. I.
Distribution and Orientation of Alluvial Fans in Martian Craters **[#3008]**

10:55 a.m. DISCUSSION and BREAK

ATMOSPHERE/CLIMATE EFFECTS
11:10 a.m. Auditorium

Chair: P. Schenk

11:10 a.m. Jakosky B. M. * [TUTORIAL]
Evolution of Martian Atmosphere

11:45 a.m. Colaprete A. * Haberle R. M. Segura T. L. Toon O. B. Zahnle K. [INVITED]
The Effect of Impacts on the Martian Climate **[#3026]**

12:10 p.m. Hamano K. * Abe Y.
Impact Erosion of Atmospheres: Substantial Atmospheric Loss by Horizontal Atmospheric Excavation **[#3031]**

12:30 p.m. Cho J. Y-K. * Stewart S. T.
Dispersion and Mixing of Impact-generated Aerosols in the Martian Middle Atmosphere **[#3047]**

12:50 p.m. LUNCH

Thursday, July 14, 2005, continued

CLOSING DISCUSSION AND FUTURE WORK
1:50 p.m. Auditorium

Chairs: N. G. Barlow
S. T. Stewart
O. S. Barnouin-Jha

1:50 p.m. CLOSING DISCUSSION AND FUTURE WORK

2:30 p.m. OPTIONAL TOUR OF APPLIED PHYSICS LAB

IMPACT-INDUCED HYDROTHERMAL ACTIVITY AT CENTRAL-PEAK AND PEAK-RING CRATERS ON EARLY MARS.

O. Abramov and D. A. Kring, Lunar and Planetary Laboratory, University of Arizona, 1629 E. University Blvd., Tucson, Arizona 85721-0092. (abramovo@LPL.arizona.edu)

Introduction: Impact events locally increase the temperature of a planetary crust, initiating hydrothermal activity if water or ice is present. Impact-induced hydrothermal activity is responsible for mineralogically and morphologically modifying many terrestrial craters [e.g., 1], and has been suggested for Martian craters [2, 3].

While there are probably no active impact-induced hydrothermal systems today, they may have been prevalent at ~3.9 Ga, during an intense period of bombardment lasting 20 to 200 Ma [4, 5]. This cataclysm likely affected Mars, because meteorites from the asteroid belt, as well as the only sample of the ancient Martian crust (meteorite ALH 84001), show effects of impact-induced metamorphism at ~3.9 Ga [6, 7]. Thus, we are focusing on an early Martian environment because it coincides with a sharply higher impact rate, and also because liquid water was likely stable in the subsurface and perhaps on the surface as well.

Goals of this work: One of the goals is to constrain the lifetimes of impact-induced hydrothermal systems on early Mars. Conductive crater cooling models suggest that the lifetimes of hydrothermal systems in craters 20 to 200 km in diameter are ~10^3 to 10^6 years [e.g., 8, 9]. The present work seeks to evaluate the additional effects of heat transport by water and steam.

Another goal is to further understand the mechanics of post-impact hydrothermal circulation, with a focus on locations of near-surface activity. Together with estimates of system lifetimes this allows the prediction of the type, location, and extent of alteration. This in turn can aid in spectroscopic and visual identification of hydrothermal vents and hydrothermally altered minerals at Martian craters.

Finally, we are seeking to understand the biological potential of these systems in terms of their habitable volume, or the rock volume within the temperature range of thermophilic microorganisms that has fluid flow.

Modeling Technique: Hydrothermal activity in early Martian craters 30, 100, and 180 km in diameter was modeled using a modified version of a publicly available program HYDROTHERM [10], a three-dimensional finite difference code developed by the U.S. Geological Survey. For the present work, the program's radial mode is used. HYDROTHERM has been previously applied to hydrothermal systems at Martian craters [11].

HYDROTHERM requires input of topography and temperature distribution, in addition to rock properties, gravity, atmospheric pressure, and the basal heat flux. The surface topography is reconstructed using laser altimetry-derived Martian crater dimensions [12] and morphometry of lunar craters [13]. The temperature distribution underneath Martian craters is obtained from hydrocode simulations [e.g., 14]. Rock properties appropriate for Martian basalts are used, with a density of 2600 kg/m^3, thermal conductivity of 2.5 W/(m K), and heat capacity of 800 J/(kg K). The surface porosity is conservatively estimated at 20% [15] and decreases exponentially with depth, while the permeability has a maximum surface value of 10^{-2} darcies and is a function of depth and temperature. The effect of other permeability values is also evaluated. The early Mars geothermal gradient and atmospheric pressure are estimated to be 13 °C/km [16] and 0.5 bars, respectively.

Results: Our modeling (e.g., Fig. 1) suggests the evolution of a post-impact hydrothermal system on early Mars proceeded as follows. The first step was the gravity-driven rapid draining of the rim and the flooding of the crater cavity by groundwater and any other available water source. The interaction between the incoming water and the hot interior of the crater may have produced large quantities of steam. Eventually, a crater lake should have formed in the basin of the crater, changing the flow of water from a gravity-driven to a hotspot-driven state. Newsom et al. [3] argued that the thermal energy of the impact melt and the central uplift can keep a lake from completely freezing for thousands of years under a thick sheet of ice, even under the current climatic conditions. Our model simulations, plus observations at terrestrial impact sites [e.g., 1, 17], suggest that the most extensive hydrothermal alteration would have occurred in the central peak (for smaller craters) or the peak ring (for larger craters), and the modification zone where fluid flow is facilitated by faults. The region of active hydrothermal circulation extends laterally almost to the crater rim and to a depth of several kilometers. The habitable volume for thermophilic organisms (volume of rock that has water flow and a temperature between 50 and 100 °C) reaches a maximum of ~6000 km^3 in the 180 km crater.

The average lifetimes of impact-induced hydrothermal systems on early Mars are estimated at ~0.065 Ma for the 30-km crater, ~0.29 Ma for the 100-km crater, and ~0.38 Ma for the 180-km crater, and depend strongly on assumed ground permeability (Fig 2).

These long lifetimes are partly explained by the most vigorous circulation taking place near the surface and the hotter parts of the models being impermeable due to the brittle/ductile transition at about 360 °C. Thus, conduction remains the dominant form of heat transport in much of the model, especially for larger craters. Another consideration is vertical heat transport by flowing water, which can increase the temperature of near-surface regions and prolong the lifetime of the system. Finally, convection is less vigorous on Mars due to lower gravity, resulting in less heat removal compared to similar systems on Earth, but this is partly balanced by a higher overall permeability. In general, the combination of relatively long lifetimes and long-lived upwellings suggest that impact-induced hydrothermal systems on early Mars would have resulted in a significant mineralogical alteration of the crust.

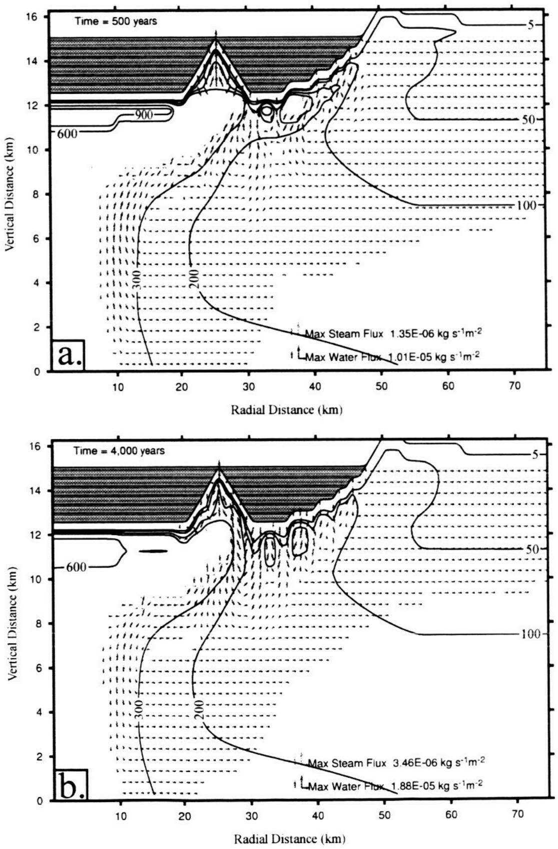

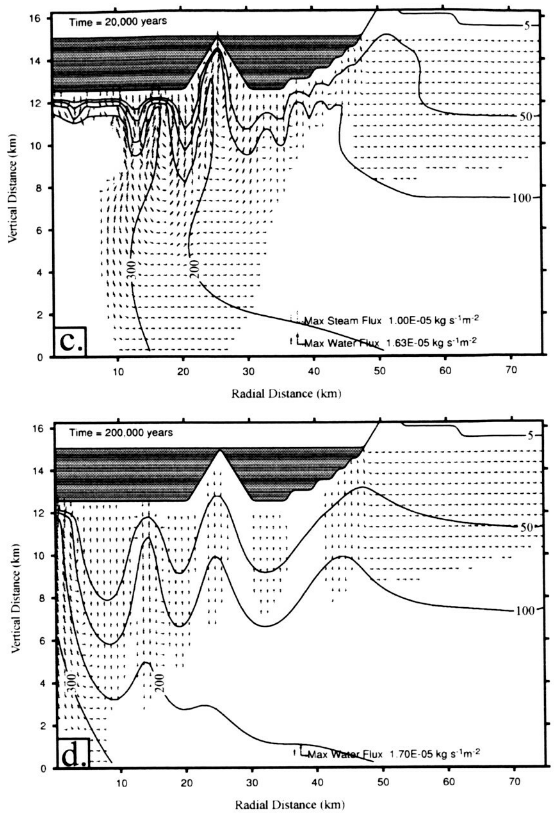

Figure 1. Results of a numerical simulation of the hydrothermal system at a 100-km impact crater on early Mars. Surface permeability is 10^{-2} darcies. Black lines are isotherms, labeled in degrees Celsius, and blue and red arrows represent water and steam flux vectors, respectively. The length of the arrows scales logarithmically with the flux magnitude, and the maximum value of the flux changes with each plot. Panels a to d show the state of the system at 500 years, 4,000 years, 20,000 years, and 200,000 years, respectively.

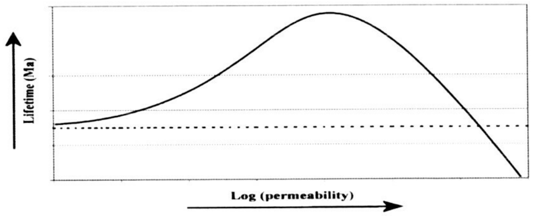

Figure 2. General dependence of system lifetime (defined by near-surface temperatures) on the average permeability of the subsurface. The dashed line indicates the lifetime in the absence of water.

References: [1] Naumov M.V. (2002) In: Plado J. & Pesonen L.J. (eds.) *Impacts in Precambrian Shields*, 117-171, Springer. [2] Newsom, H. E. (1980) *Icarus, 44*, 207-216. [3] Newsom, H. E. et al. (1996) *JGR, 101*, 14951-14956. [4] Tera, F. et al. (1974) *Earth Planet. Sci. Lett., 22*, 1-21. [5] Ryder, G. (2000) *Eos Trans. AGU, 81*(19), Spring Meet. Suppl., abstr. B22B-01. [6] Kring, D. A., and Cohen, B. A. (2002) *JGR, 107*(E2), 4-1 to 4-6. [7] Bogard D. D. (1995) *Meteoritics, 30*, 244-268. [8] Daubar, I. J., and Kring, D. A. (2001) *LPSC XXXII*, Abstract #1727. [9] Turtle, E. P., et al. (2003) *Meteoritics Planet. Sci., 38*(2), 293-303. [10] Hayba, D. O. and Ingebritsen, S. E. (1994) *U.S. Geol. Surv. Water Resour. Invest. Rep., 94-4045*, 85 pp. [11] Rathbun J. A. and Squyres S. W. (2002) *Icarus 157*, 362-372. [12] Garvin, J. B. et al. (2002), *LPSC XXXIII*, Abstract #1255. [13] Melosh, H. J. (1989) *Impact Cratering: A geologic process*, Oxford University Press. [14] Pierazzo et al. (2004) *LPSC XXXV*, Abstract #1352. [15] Clifford, S. M. (1993) *JGR, 98*, 10,973-11,016. [16] Babeyko A. Yu. and Zharkov V. N. (2000) *Phys .Earth Planet. Inter., 117*, 421-435. [17] Osinski, G. R. et al. (2001) *Meteor. and Planet. Sci., 36*, 731-745.

THE INFLUENCE OF VOLATILES AND ATMOSPHERES ON MARTIAN IMPACT CRATER MORPHOLOGIES.

N. G. Barlow, Dept. Physics and Astronomy, Northern Arizona University, Flagstaff, AZ 86011-6010 Nadine.Barlow@nau.edu..

Introduction: Impact craters on Mars display a variety of morphologic features which differ from those seen with craters on dry, atmosphereless bodies like the Moon. These morphologies include layered ("fluidized") ejecta blankets and central pits. The layered ejecta morphologies have been proposed to result from impact into subsurface volatile reservoirs, interactions of the ejecta curtain with the martian atmosphere, or a combination of both processes. Central pits have been proposed to result from impact into volatile-rich targets and/or cometary impacts. Analysis of MGS, Odyssey, and Mars Express data, combined with recent laboratory experiments and numerical modeling, is revealing new insights into the role of volatiles and atmospheres in the formation of these features.

Crater Morphologies: The layered ejecta morphologies were first recognized in Mariner 9 imagery and initial attempts to classify them were conducted through photogeologic analysis of Viking data [c.f. 1]. Many different nomenclature schemes were developed to describe the various ejecta morphologies seen on Mars, often resulting in several distinct classifications for the same feature (see Table 1 in [2]). In 2000, the Mars Crater Consortium proposed standardized nomenclature for these features [2].

Impact craters surrounded by a single layer of ejected material are called single layer ejecta (SLE) craters. If the ejecta blanket terminates in a distal ridge, they are called single layer ejecta rampart (SLER) craters. Those which terminate with a convex profile are called single layer ejecta pancake (SLEP) craters. The ejecta blanket is further characterized by its sinuosity, as defined by the lobateness (Γ) formula [3, 4]:

$$\Gamma = (\text{perimeter})/(4\pi(\text{diameter}))^{1/2}$$

Ejecta blankets with $\Gamma < 1.5$ are classified as circular (e.g., SLEPC) while those with $\Gamma \geq 1.5$ are classified as sinuous (e.g., SLERS).

Similar nomenclature is used to describe the other ejecta morphologies. Craters with two layers of ejecta material are called double layer ejecta (DLE) craters while those with 3 or more partial or complete layers are called multiple layer ejecta (MLE) craters. Radial (lunar-like) ejecta patterns are called single layer ejecta radial (SLERd). Ejecta craters perched above the surrounding terrain are called pedestal craters (Pd). Each of these morphologies are further characterized, as needed, by the R, P, C, and S designations indicated above. Ejecta blankets which are combinations of any of these classes are designated by using the combination of terms: for example, craters which display both secondary craters (radial ejecta) and an SLERS morpholgy are listed as SLERdRS.

Interior morphologies also are associated with many martian impact craters. Many of these are typical interior features seen in craters on other bodies, including central peaks, peak rings, and wall terraces. However, central pits, found both on the crater floors ("floor pits") and atop central peaks ("summit pits") are quite common in martian impact craters. Central pits are rare in lunar impact craters, but floor pits are often seen in craters on icy moons such as Ganymede. Models for central pit formation include impact into volatile-rich target material [5] and cometary impacts [6]. Recent modeling by Pierazzo et al. [7] shows that impact into volatile-rich targets can produce vapor under the central region of the crater floor—the release of this gas might produce central pits.

Distributions: Numerous studies have shown the predominance of SLE craters at all locations across the planet [c.f., 8, and references therein]. Pancake craters (SLEP) are typically more common at higher latitudes while rampart craters (e.g., SLER) typically dominate closer to the equator. Pedestal (Pd) craters tend to be very small craters (< 5-km-diameter) found in fine-grained materials. MLE craters are found largely in the equatorial region, particularly along the highlands-lowlands dichotomy boundary. DLE craters are found at mid-latitudes (35°-60°) in both hemispheres but are most strongly concentrated in the north. Radial ejecta are primarily found around the largest craters, although extremely small craters (typically <3-km-diameter) can also display radial structures.

Crater size appears to be an important factor for many of the ejecta morphologies. The SLE morphology typically is associated with craters between about 3 and 25 km diameter within the equatorial region, but is seen over larger diameter ranges (<1 km to >50 km) at higher latitudes. The DLE morphology is associated with craters in a similar size range (3-30 km) in the regions where this morphology is seen. MLE craters tend to be larger, ranging in size from ~15 km to 60 km. Crater with the radial ejecta are the largest craters (>60 km) while pedestal craters are usually very small.

A Viking-based analysis of central pit craters revealed that pits are found in craters ranging in diameter from ~15 to 65 km, with summit pits occurring in smaller craters than floor pits [9]. That study also found that central pit craters are concentrated along the proposed outer rings of large impact basins on Mars. A new study of central pits, using MGS and Odyssey data, is confirming the range in crater diameters of central pit craters, but is revealing a much larger number of central pits than previously identified [10]. We also are seeing central pits in craters with a large range in preservational state, from very fresh to quite degraded.

Formation of Ejecta Morphologies: Two primary models exist for describing the formation of the layered ejecta morphologies seen on Mars: Impact into and vaporization of subsurface volatiles [11, 12] or interactions of the ejecta curtain with the thin martian atmosphere [13, 14]. Each model explains the gross-scale features associated with layered ejecta morphologies on Mars, but differ on the finer-scale predictions—it will be analysis of these features which will help determine if one model is to be preferred over the other or if a combination of both models is needed. The variation in the diameter of the smallest craters displaying a layered ejecta morphology is consistent with the proposed distribution of subsurface volatiles, and the distributions of some crater morphologies correlate with other indicators of subsurface volatiles. However, the very large run-out distances of the ejecta for the outer layers of DLE and MLE craters is most consistent with the atmospheric model. A review of our current understanding of martian ejecta morphologies and their relationships to the two formation models is provided in [15]. At present, the evidence supports a dominant role of subsurface volatiles in the creation of many of the observed features, with some modifications provided by atmospheric interactions with the ejected debris.

Pedestal (Pd) craters may have a different origin than the other layered ejecta morphologies seen on Mars. Pd craters are those in which both the crater and its ejecta are elevated above the surrounding terrain. The traditional theory for the formation of Pd craters is that they form in fine-grained material which subsequently is deflated by strong winds, leaving the crater and its armored ejecta perched above the surroundings [16]. However, the small sizes of these craters and their locations in fine-grained materials which are also believed to be ice-rich may be more consistent with removal of the surrounding material by ice sublimation. An accompanying abstract (Barlow, this volume) discusses this idea in more detail.

Central pits are perhaps even better indicators of the presence of subsurface volatiles. The regional variations in the distribution of central pit craters supports the model that subsurface volatiles are key to their formation—if central pits form only because of comet impacts, we should see a more random distribution of central pit craters across Mars (plus we should also see such features on bodies like the Moon, where they are absent). The recent numerical modeling by Pierazzo et al. [7] provides a theoretical basis to the influence of subsurface volatiles on the formation of these features. More work remains to be done to understand the conditions favoring summit pit versus floor pit formation and why areas with other indicators of subsurface volatiles do not always show craters with central pits. But the presence of central pits in craters with a variety of preservational ages indicates that subsurface volatiles have been present on Mars for much of the planet's history.

Discussion: Impact craters excavate into the subsurface region where ice and/or liquid water may be present on Mars. In addition, ejecta is tossed upward and can interact with the thin martian atmosphere. Thus both subsurface volatiles and the martian atmosphere likely affect the formation of certain crater morphologies. Based on present analysis, many of the features associated with the layered ejecta morphologies found around fresh martian impact craters are most consistent with the influence of subsurface volatiles, but a few features may indicate the influence of the martian atmosphere. Central pits almost certainly indicate the presence of long-lived subsurface volatile reservoirs. Continued geomorphic, numerical, and laboratory analysis of martian impact craters and their terrestrial analogs will help us better understand how volatiles and atmospheres affect the formation of many impact crater morphologic features.

References: [1] Mouginis-Mark, P. (1979), *JGR, 84*, 8011-8022.. [2] Barlow, N. G. et al. (2000), *JGR, 105*, 26733-26738. [3] Kargel, J. S. (1989), *4th Intern. Conf. Mars*, Tucson, Univ. AZ, 132-133. [4] Barlow, N. G. (1994), *JGR, 99*, 10927-10935. [5] Wood, C. et al. (1978), *PLPSC 9th*, 3691-3709. [6] Croft, S. K. (1983), *PLPSC 14, JGR, 88*, B71-B89. [7] Pierazzo, E. et al. (2004), *LPSC XXXV*, Abstract #1352. [8] Barlow, N. G. and C. B. Perez (2003), *JGR, 108*, 10.1029/2002JE002036. [9] Barlow, N. G. and T. L. Bradley (1990), *Icarus, 87*, 156-179. [10] Hillman, E. and N. G. Barlow (2005), *LPSC XXXVI*, Abstract #1418. [11] Carr, M. H. et al. (1977), *JGR, 82*, 4055-4065. [12] Stewart, S. T. et al. (2001), *LPSC XXXII*, Abstract #2092. [13] Schultz, P. H. (1992), *JGR, 97*, 11623-11662. [14] Barnouin-Jha, O. S. et al. (1999), *JGR, 104*, 27105-27115 and 27117-27131. [15] Barlow, N. G. (2005), *GSA SP 384*, 433-442. [16] Arvidson, R. E. et al. (1976), *Icarus, 27*, 503-516.

A NEW MODEL FOR PEDESTAL CRATER FORMATION.

N. G. Barlow, Dept. Physics and Astronomy, Northern Arizona University, NAU Box 6010, Flagstaff, AZ 86011-6010 Nadine.Barlow@nau.edu.

Introduction: Pedestal craters are unique landforms on Mars where both the crater and ejecta blanket are elevated above the surrounding terrain (Fig. 1). The distributions and characteristics of these craters indicate that they form within a fine-grained layer. Traditionally, eolian deflation of the surrounding material has been the proposed formation mechanism [1]. However, new models of the latitudinal distribution of ice-rich mantles suggest that pedestal craters may result from sublimation of the surrounding ice-rich material.

Pedestal Crater Characteristics and Distributions: Pedestal craters are typically <5 km in diameter and occur in fine-grained deposits which often correlate with the high-H_2O-content regions identified by the Mars Odyssey Gamma Ray Spectrometer (GRS). Although most pedestal craters are found at high latitudes, particularly in the north, we have also identified pedestal craters in near-equatorial regions such as on the floor of Gusev crater [2].

Ejecta extent is quantified using the ejecta mobility (EM) ratio [3]:

$$EM = (\text{maximum extent of ejecta})/(\text{crater radius})$$

Single layer ejecta (SLE) craters poleward of ±40° latitude have average EM values of 1.8 in the north and 1.6 in the south. Double layer ejecta (DLE) craters north of +40° latitude have an average EM of 1.5 for their inner lobe and 3.5 for their outer layer. Corresponding values for the region south of -40° latitude are 1.4 and 2.8, respectively. Pedestal craters have the highest EM values of any ejecta morphology measured, with an average EM of 3.7 for those north of +40° and 3.8 for craters south of -40° latitude.

Ejecta sinuosity is measured through a parameter called lobateness (Γ) [4, 5]:

$$\Gamma = (\text{ejecta perimeter})/[4\pi(\text{ejecta area})]^{1/2}$$

$\Gamma = 1$ indicates a circular ejecta pattern while larger values of Γ indicate an increasing degree of sinuosity. SLE craters have average lobateness values of 1.12 for latitudes > +40° and 1.15 for latitudes < -40°. The inner layer of the DLE craters has an average Γ of 1.09 versus 1.14 for the outer layer. Lobateness values for pedestal craters display a large variation, ranging from 1.0 to 1.8, but the average $\Gamma = 1.12$.

New Observations: The higher resolutions of the Mars Orbiter Camera (MOC) and Thermal Emission Imaging System--Visible (THEMIS VIS) cameras have revealed many more Pd craters than were previously known from Viking analysis. These higher resolutions also permit identification of finer-scale features than previously seen. Although most Pd craters seem to be surrounded by one ejecta layer, we do see a few examples of a double layer structure (Fig. 2). We typically see the DLE-type structure for the larger pedestal craters, suggesting that resolution effects might limit the detection of an inner layer for the smaller craters.

One of the most interesting correlations that we see is between the distribution of Pd craters and the regions of high-H_2O content as revealed by the GRS instrument. This correlation strongly suggests that near-surface volatiles play a role in the formation of the Pd morphology. In addition, the highest concentrations of pedestal craters are found in the same regions where ice-rich mantles have been proposed to occur, based on geomorphic observations and modeling of past obliquity cycles [6, 7].

Discussion: Our analysis of the distribution of pedestal (Pd) craters finds that they often occur in the same regions as DLE craters. Because Pd craters also disply similarities to the EM and Γ values of the outer DLE layer, we propose that these morphologies form in a similar manner. It is entirely possible that Pd craters are the small crater versions of larger DLE craters. We propose that the easily identifiable ejecta layer of Pd craters is the same as the outer ejecta layer of DLE craters.

Formation Hypothesis: Pd craters have been known to be concentrated in fine-grained materials since the first analysis of Viking data. Several models were proposed to explain Pd formation, but the favored model is the eolian deflation model [1]. This model argues that the ejecta blanket somehow becomes armored during its emplacement. Subsequent eolian deflation of the region removes the surrounding fine-grained material, leaving the crater and its ejecta blanket perched above the surroundings.

One of the major problems with this model is the symmetrical shape of the pedestal crater—one must invoke a changing preferential wind direction over the entire 360° to produce such a symmetrical pedestal. With the new information indicating that Pd craters form not just in fine-grained materials but in ice-rich fine-grained materials, we propose a new formation mechanism. We propose that Pd craters result from small impacts which do not excavate entirely through the fine-grained mantle. Some (currently unknown) mechanism armors the ejecta deposit. During periods of lower obliquity, the ice in this mantling material sublimates, lowering the surrounding terrain and leaving the pedestal crater and its ejecta elevated. Other geologic evidence of the sublimation of an ice-rich mantle has been reported in these same regions [6]. Sublimation also would occur more symmetrically around the pedestal, removing the major problem with the eolian deflation model.

References: [1] Arvidson, R. E., et al. (1976) *Icarus, 27*, 503-516. [2] Cabrol N. A. et al. (2003) *JGR, 108*, 10.1029/2002JE002026. [3] Mouginis-Mark, P. (1979) *JGR, 84*, 8011-8022. [4] Kargel, J. S. (1989) 4th *Intern. Conf. Mars*, Tucson, Univ. AZ, 132-133. [5] Barlow, N. G. (1994) *JGR 99*, 10927-10935. [6] Mustard, J. F. et al. (2001) *Nature, 412*, 411-414. [7] Head J. W. et al. (2003) *Nature, 426*, 797-802.

Figure 1: A field of pedestal craters. All craters are less than 2 km in diameter. (THEMIS image I04916007)

Figure 2: 3.9-km-diameter pedestal crater showing a double layer morphology. Crater is located at 35.90°N 147.78°E. (THEMIS image I10293012)

Crater Lakes on Mars: Development of Quantitative Thermal and Geomorphic Models.

C. J. Barnhart[1], S. Tulaczyk[1], E. Asphaug[1], E. R. Kraal[1], J. Moore[2], [1](Department of Earth Sciences, University of California Santa Cruz, 1156 High Street, Santa Cruz, California, 95064, barnhart@es.ucsc.edu, asphaug@es.ucsc.edu), [2](NASA Ames Research Center, MS 245-3, Moffet Field, CA 94035-1000, jeff.moore@nasa.gov).

Introduction: Impact craters on Mars have served as catchments for channel-eroding surface fluids, and hundreds of examples of candidate paleolakes are documented [1,2] (see Figure 1). Because these features show similarity to terrestrial shorelines, wave action has been hypothesized as the geomorphic agent responsible for the generation of these features [3]. Recent efforts have examined the potential for shoreline formation by wind-driven waves, in order to turn an important but controversial idea into a quantitative, falsifiable hypothesis. These studies have concluded that significant wave-action shorelines are unlikely to have formed commonly within craters on Mars, barring Earth-like weather for ~1000 years [4,5,6].

Ice as Protagonist: A different mechanism is required to explain these features. Our efforts are therefore devoted to understanding the geomorphic effects of thick (glacial) ice cover under martian conditions [7]. Terrestrial analogs are not trivially adapted to martian conditions, and thus a number of studies have examined from first principles the thermal evolution and residence time of liquid water and ice cover in martian environments [8,9,10]. However, the linked geomorphic evolution of such a system has yet to be adequately characterized.

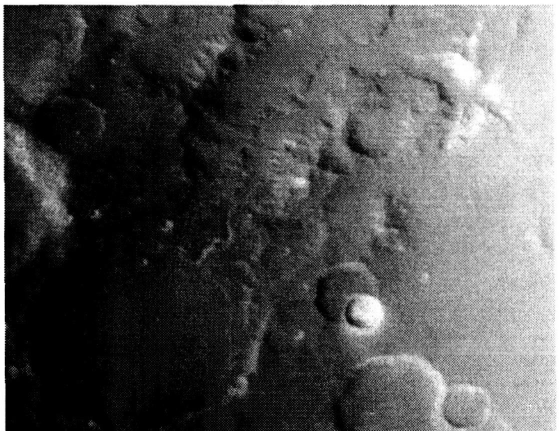

Figure 1: Wide angle image from Mars Global Surveyor, MOC R10-05145 (Malin Space Science Systems). Image is centered on 174.63W 14.51S and width is 120 km.

Possible Scenarios: We have begun to develop detailed models to test specific scenarios for ice-covered lakes (ice battering, thermal expansion, subsidence, burial and exhumation, etc.) exploring their ability to produce shoreline-type features (see Figure 2). In this abstract we describe the preliminary modeling approach for one such scenario, where a lake with thick ice cover experiences volumetric strain from ice/water/brine density variations. This is one of five candidate scenarios to be described during our presentation.

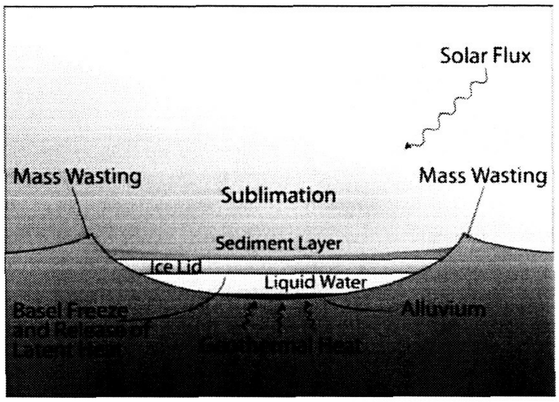

Figure 2: Ice-lake schematic. Mass and energy fluxes involved in our models are indicated. Adapted from McKay et al. (1985).

A lake with thick ice cover is likely to experience volumetric strain in response to extreme temperature changes, for instance the collapse of greenhouse or other severe climate cycling. Thermal expansion and freeze-out leads to strain accommodation and slip, resulting in mass wasting and erosional deformation at the ice margin. The mechanism could repeat with climate cycles if water or brine persist.

Our model, currently under development, begins with a 1D thermodynamical lake model describing energy and sediment inputs and brine-ice interactions. The model is governed by an equation that balances incoming and outgoing energy in the center column of a crater lake. The model provides time scales for the persistence of liquid water/brine and for ice lid longevity. 1D results will be adopted for 2D modified finite element models of ice evolution within evolving crater lake boundary and thermal condiditions, coupled to models for margin deformation and erosion.

Energy Balance: Through energy balance equations it has been shown that ice-covered lakes can exist for up to 700 million years on Mars after the mean global temperature drops below freezing [9,11].

Subsequent research has progressed into the thermodynamics of such systems including: (1) the contribution of crater-formation heating on the persistence of liquid water, and the evolution of ice cover thickness [12], (2) the fate of flood waters emptying into the northern plains [8], (3) the use of detailed thermal and atmospheric models to calculate the lifetime of water and the evolution of ice cover thicknesses [10].

Equation 1 balances the upward conduction of heat at a given depth in the ice cover with the energy input below that level in the ice [9]. A steady state condition is assumed and fluxes are averaged over the year to obtain

$$k\frac{dT}{dz} = S(z) + L + F_g \qquad (1)$$

where k is the thermal conductivity of ice, dT/dz is the gradient of annual mean temperature (T) with depth (z) in the ice, S(z) is the annual mean flux of solar energy absorbed below z and Fg is the geothermal heat flux. As model complexity increases, so will our description of the balance of energy and mass fluxes.

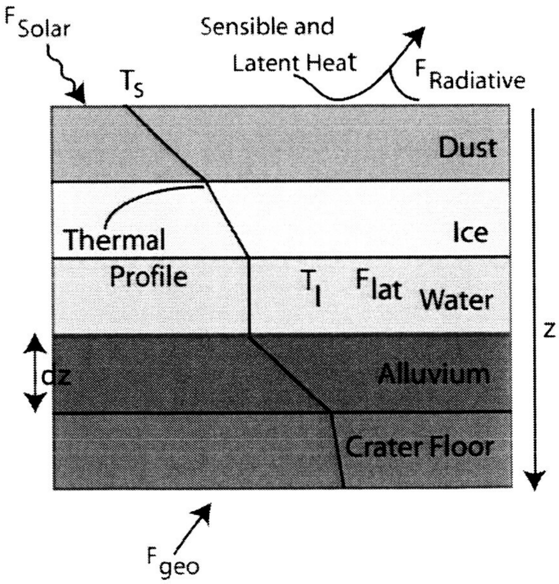

Figure 4: Schematic of a 1D thermodynamic model for an ice-lake. Arrows describe the energy flux, the solid line is a qualitative temperature profile where T_s and T_l are the surface and eutectic temperatures respectively. Model design is motivated by McKay et al. (1985) and Duguay et al. (2003).

Model evolution will include energy balance at discrete layers throughout a one-dimensional column. The speed of this model will facilitate probing consequences of climatic variables and atmospheric forcing on ice-lake longevity and thermodynamic response. Our overall technique will be based on the one-dimensional unsteady heat conduction equation with penetrating solar radiation. The unsteady heat equation is of particular utility, because it describes energy transport and diffusion at depth between different materials; water, ice, dust, alluvium, and bedrock.

Astrobiological Discussion: The exploration of potential sites of astrobiological interest on Mars is one of NASA's main directives. Our model argues that, by comparison to an intracrater ice plug, lacustrine systems on Mars are rather transitory. It is more probable, then, that life would have a greater opportunity to proliferate in an aqueous environment under an ice plug rather than in ephemeral lakes exposed to the myriad hostilities of Mars' surface: UV radiation, sub-arctic temperatures, and the extreme, oxidizing nature of surface chemistries [13].

Conclusion: The glacial geomorphology of crater features is a rich key to the Martian past, yet, despite the wealth of imagery, the interpretation of surface morphology lacks the insight and definition that a quantitative model would provide. Our models explore geomorphic scenarios that posit ice plugs as the formation mechanism for shoreline features. The development of a quantitative model that describes this system will provide new insights—climatic, hydrological, astrobiological—into Mars' history.

References: [1] Cabrol, N. A. and Grin, E. A. (1999) *Icarus, 142*, 160-172. [2] Ori, G. and Baliva, A., (2000), *JGR, 105, E7,* 17629-17641. [3] Cabrol, N. A. and Grin, E. A. (2001) *Icarus, 149*, 291-328. [4] Kraal, E. R. et al. (2003) *LPS XXXIV* Abstract #1725. [5] Lorenz, R. D., et al. (In Press) *Icarus*. [6] Kraal, E. R. et al. in preparation. [7] Barnhart, C. J., et al. (2005) *LPS XXXVI* Abstract #1560 [8] Kreslavsky, M. A., and Head, J. W., (2002) *JGR-Planets*, v. 107, no. E12. [9] McKay, C. P. et al. (1985) *Nature, 313*, 561-562.. [10] Moore, J. M., et al., (1995) *JGR-Planets, v. 100, no. E3*, p. 5433-5447. [11] McKay, C. P. and Davis, W. L., (1991) *Icarus, v. 90*, p. 214-221. [12] Newsom, H. E. et al. (1996) *JGR-Planets, 101*, 14951-14955. [13] Carr, M. H. (1996) *Water on Mars*, Oxford, New York.

THE RUNOUT EFFICIENCY OF FLUIDIZED EJECTA ON MARS.

O.S. Barnouin-Jha[1,2]
[1]Dept. of Complexity Sciences, U. Tokyo, Japan, [2]The Johns Hopkins University Applied Physics Laboratory, Laurel, MD.

Introduction: The distance from rim-crest to distal rampart has typically been used to determine the fluidity of Martian ejecta [e.g., 1]. When craters of a given size possess longer rim-to-rampart distances, these studies typically assume that greater amounts of volatiles are present within the ejecta. Such rim-to-rampart distances have also been shown to increase as $R_c^{1/2}$, where R_c is the crater radius. Such a relationship is expected from impact experiments in an atmosphere [2].

In this study, runout efficiency (i.e., *L/H* analyzes where *L* is the runout distance and *H* is onset height) is used. This efficiency allows to broadly characterize the rheology of landslides on Earth [e.g., 3, 4 and references therein] and the planets [e.g., 5, 6]. It varies mostly with the volume of a landslide, but is also influenced by other factors including the presence of water [e.g., 3, 4 and references therein]. In the case of very large landslides ($V>10^7 m^3$), *L* depends primarily on the flow volume [7], although differences in rheology remain important.

We compare results of *L/H* and *L* as a function of flow volume obtained for several Martian fluidized craters with terrestrial debris flow and rock avalanches to broadly characterize the rheology of these ejecta, once they have begun to flow. However, before such characterization are made, we must first define *L* and *H* of ejecta in a way that is meaningful for comparisons with data from terrestrial mass movements.

Table 1: Symbols

Symbol	Definitions
$dM_e(x)$	Incremental ejecta mass excavated at x
M_e	Total mass of ejecta
x	Distance from crater center to point of ejecta excavation
V_e	Ejecta excavation velocity at x
R_c	Transient crater radius
R_b	Crater radius that defines ejecta mass in continuous ballistically emplaced ejecta
c,μ	Empirically derived crater scaling parameter [3, 4]
e	Empirically derived secondary cratering parameter

Background: The use of *L/H* to characterize mass movements derives naturally from balancing the initial potential energy of a mass movement with the total energy or work lost during its emplacement. Typically, initial potential energy of a landslide is given by *MgH*, where, in this form, *M* is the point mass of the flow, *H* is strictly speaking the height to the center of mass of the source area, and *g* is the acceleration due to gravity. As the flow progresses downslope, the work lost is defined as *MgRL* where *L* is the runout length to the center of mass, and *R* is the resistance coefficient. While it is difficult to directly determine *R*, the energy balance gives

$$1/R=L/H$$

In order to obtain runout efficiency for ejecta, a similar energy balance must be undertaken. In the case of ejecta, the component of its kinetic energy that is injected into along surface flow must be balanced with the work lost by friction during flow. Since most fluidized martian craters are fairly large, the total kinetic energy of the ejecta is computed using gravity controlled crater scaling rules [8, 9, 10] as:

$$\frac{1}{2}\int_0^{R_c} V_e(x)^2\,dM_e(x)$$

$$KE_e=\frac{1}{2}\int_0^{R_c}\left[c\sqrt{R_c g}\left(\frac{x}{R_c}\right)^{-1/\mu}\right]^2\frac{3M_e}{R_c^3}x^2\,dx$$

¿

where the symbols are defined in Table 1. This integral is undefined for certain values of μ. We, therefore, introduce the radius R_b by tracing ballistic paths back into the transient crater from the edge of the continuous ejecta deposits seen on Mercury [11]. We chose continuous ejecta deposits on Mercury as representative of the extent of the continuous ejecta blanket at Mars craters which have not flowed because of the similarity in *g* between these two planets, and the fact that the ejecta on Mercury possesses no evidence for flow. Remember that ejecta velocity, which is partly responsible for defining the edge of the continuous ejecta when no fluidizing agents are present, varies with local *g*. Thus, KE_e of the ejecta becomes

$$KE_e=\frac{3}{2}\frac{c^2 M_e R_c g}{(3-2/\mu)}\left[1-\left(\frac{R_b}{R_c}\right)^{3-2/\mu}\right]$$

The initial kinetic energy injected into the flowing ejecta, KE_f will be somewhat less than KE_e because of some losses that occur prior to flow. These losses result either from sedimentation processes that occur once ballistic first strikes the target surfaces or atmospheric entrainment processes. The variable e parameterizes these losses so that $KE_f = eKe_e$ and can be estimated from laboratory experiments and numerics [8, 9, 10, 12, 13, 14, 17, 18].

Because the energy analysis treats the ejecta as a point mass, the work lost W_l as the ejecta flows is given by $RM_e gL$ in the same form as for landslides regardless of the geometric differences between these flows. In keeping with the *L/H* approach for mass movement, the variable L defines the radial distance that the ejecta flowed after being injected into a continuum flow. A reasonable estimate of L is given by the distance separating the edge of fluidized ejecta with that of continuous ballistic ejecta deposit. As for R_b, the extent of the continuous ejecta when no subsequent flow occurs is provided by Mercurian craters [11].

The resulting ejecta runout efficiency $1/R$ (equivalent to *L/H* for planar debris flows) is thus given by

$$\frac{1}{R} = \frac{2}{3} \frac{(3-2/\mu)L}{c^2 e R_c} \left[1 - \left(\frac{R_b}{R_c} \right)^{3-2/\mu} \right]^{-1}$$

Approach: Several measurements are required to compare the runout efficiency of fluidized ejecta with that of landslides. These include runout distance, rim-to-rim diameter, and volume of the ejecta flows. In the case of landslides, H is also needed. We obtain this data from several fresh craters in Lunae Planum (MOLA), and imagery data from the THEMIS orbiters [15]. In computing the volume of the ejecta, we assume some reasonable rim uplift [e.g., 16].

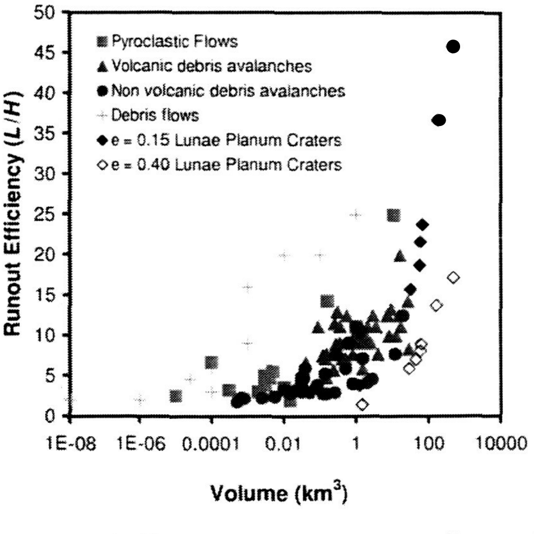

1. Runout efficiency versus flow volume for Martian fluidized ejecta and landslides, and a few terrestrial mass movements. Terrestrial data from [3, 4].

Results and Discussion: Preliminary runout efficiency results for Mars craters are shown in Figure 1. Also shown are terrestrial data for pyroclastic flows, volcanic debris avalanches, non-volcanic debris avalanches and debris flows. The debris flows generally possess a greater volatile content than the other flows shown.

Two sets of results are shown for the fluidized martian ejecta. The first set (closed blue diamonds) is for the case where 15% of the kinetic energy of the excavated ejecta is injected into its forward flow. This corresponds approximately to the amount of energy imparted to ejecta by a secondary crater formed by the impact of a single projectile [9, 10, 12, 13, 14]. This energy probably represents the minimum amount of energy that would be injected into the flowing ejecta since generally ejecta falls as an amalgam of particles rather than as individual particles.

The second set assumes (open blue diamonds) the more realistic situation where primary ejecta strikes the target surface as such an amalgam or cluster of particles. Experiments indicate that while overall impact cratering efficiency (ratio of displaced mass to projectile mass) for such clustered impacts is reduced relative to a single impactor, the total kinetic energy of the ejecta is increased significantly [17, 18]. We assume in this study, therefore, that 40% of the kinetic energy of impacting primary ejecta is injected into the flowing ejecta.

Keeping these two cases in mind, it appears that Mars ejecta in Lunae Planum generally flows less efficiently than volatile-rich terrestrial mass movements. They are more comparable in behavior to the drier volcanic and non-volcanic rock avalanches.

References: [1] Ivanov, B. Solar System Research, V. 30, # 1, 43-58, 1996. [2] Schultz, P.H., *JGR 97*, 11623-11662, 1992a. [3] Iverson, R.M., *Rev. of Geophys. 35*, 245-296, 1997. [4] Hayashi, J.N. and S. Self, *JGR 97*, 9063-9071, 1992. [5] McEwen, A.S., *Geology, 17*, 1111-1114, 1989. [6] Malin et al., *JGR* 97, 16337-16352, 1992. [7] Davies, T., *Rock Mech.* 15, 9-24, 1982. [8] Schultz, P.H. and D.E. Gault, *JGR 84*, 7669-7687, 1979. [9] Housen, K.R., R.M. Schmidt, and K.A. Holsapple, *JGR 88*, 2465-2499, 1983. [10] Barnouin-Jha, O.S. et al., Track 2.204, 1999. [11] Gault et al., *JGR* 80, 2444-2460, 1975. [12] Gault and Heitowit, *Proc. Sixth Hypervelocity Impact Symp.* 2:419-256, 1963. [13] Braslau, D., *JGR 75*, 3987-3999, 1970. [14] Ahrens and O'Keefe, *Geo. Soc. Amer., Special Papers 190*, 103-120, 1982. [15] Barnouin-Jha et al., *JGR* in press, 2005. [16] McGetchin et al., *Earth Planet. Sci. Lett., 20*, 226-236, 1973. [17] Schultz and Gault, *JGR, 90*, 3701-3732, 1985. [18] Barnouin-Jha and Schlutz, *JGR 101*, 21,099-21,115 1996.

ARCUATE RIDGES AND GULLIES IN MARTIAN CRATERS: DEPENDENCE ON ORIENTATION AND LATITUDE.

D. C. Berman[1] W. K. Hartmann[1], D. A. Crown[1], and V. R. Baker[2], [1]Planetary Science Institute, 1700 E. Ft. Lowell Rd., Suite 106, Tucson, AZ 85719; bermandc@psi.edu, [2]Department of Hydrology and Water Resources, University of Arizona, Tucson, AZ.

Introduction: At the bases of many mid-latitude crater walls, arcuate ridges with sharp crests can be seen [1,2]. These features are usually located at the bottom of gullied walls of craters, but gullies are not always present above them. Stratigraphically, the debris aprons of gullies overlie the crater wall-facing slopes of arcuate ridges, where the two features coexist, and the debris aprons may infill the region between the base of the crater wall and the arcuate ridge. Some ridges are only slightly sinuous and form one continuous ridge around a portion of the interior crater wall, but in most cases ridges appear as individual features that abut one another. They are often associated with lineations and pitted textures extending onto crater floors. The arcuate ridges resemble terrestrial protalus ramparts or terminal moraines [3,4,5], which suggests they may have a glacial origin. A general survey [2] has shown these features to be common in certain mid-latitude regions.

Survey: The Phaethontis Quadrangle (MC-24) was selected for a systematic survey because of the large density of craters in that region with gullies, arcuate ridges, and patterned floors. All 1153 MOC images from mission phases AB1 through R02 in quadrangle MC-24 (30° to 65° S, 120° W to 180° W) were surveyed for craters containing the features of interest. Arcuate ridges were identified according to the morphologies described above. Gullies were identified on the basis of having at least two of the primary features described by Malin and Edgett [6]: head alcoves, channels, and debris aprons. Craters with patterned floor deposits, but no arcuate ridges were also identified. This survey resulted in 364 MOC images which contained one or more of these features. All 485 THEMIS VIS images through the 7/1/04 release within the same region were surveyed, resulting in 67 images with the desired features. The images were then grouped by crater and 225 individual craters, which range in diameter from ~1.5 km - ~50 km, were identified, although few craters larger than 30 km in diameter exhibit these features. Of the 225 craters, 188 contained gullies on some portion of their walls. A total of 118 craters with arcuate ridges were identified; 104 of these craters also had gullies. An additional 35 craters had patterned floors, 13 of which also had gullies.

Each crater examined in MOC and THEMIS images was divided into 8 sectors, and the presence or absence of gullies and arcuate ridges on the crater walls was noted for each sector. Gullies on the northwest, north, or northeast wall were identified as pole-facing gullies; gullies on the southwest, south, or southeast walls were identified as equator-facing gullies. Individual craters exhibited gullies and arcuate ridges in multiple sectors. Results are shown in Figs. 1 and 2 for craters with coverage of at least some portion of both the north and the south walls. The existing literature is inconsistent as to whether pole-facing orientations or equator-facing orientations dominate [6,7], but Figs. 1-3 show that at least part of the discrepancy is a striking latitude effect.

For craters with image coverage of the entire crater (34 craters), 20 had only pole-facing gullies, 2 had only equator-facing gullies, 6 had gullies on both walls, 1 had gullies on the east and west walls, and 5 had no gullies at all. Of the 198 craters that had image coverage of at least some portion of both the north and south walls, 165 had gullies. Of those, 98 (59%) had gullies only on pole-facing slopes, 28 (17%) had gullies only on equator-facing slopes, 32 (19%) had gullies on both walls, and 7 had gullies on the E or W walls. As seen in Fig. 3, all of the craters with gullies only on equator-facing slopes were found between 44° S and 56° S. Craters with gullies only on the pole-facing side were found between 30° S and 48° S. Craters with gullies on both N and S sides were found between 37° S and 64° S. Craters with gullies on only the east and/or west walls were found between latitudes 42° S and 50° S.

The arcuate ridges have an even stronger preference for pole-facing orientations than the gullies; a polar plot of their orientations can be seen in Fig. 4. Of the 99 craters with arcuate ridges with image coverage of both crater walls, 75 had ridges only on the pole-facing side, 11 had ridges only on the equator-facing side, and 13 had ridges on both sides. As with the gullies, between 44° S and 65° S, a larger number of arcuate ridges have equator-facing orientations, but the majority are still pole-facing in that latitude band.

Discussion: There are clear associations between gully systems and arcuate ridges, including similarities in geometry of the alcoves and sinuous arcs of arcuate ridges, and the backfilling of arcuate ridges by debris aprons associated with gullies. The latitudinal distribution of gullies and arcuate ridges and the dependence of preserved features on orientation and latitude support a direct association between these features and the emplacement, melting, and removal of an ice-rich mantle [8,9,10]. Mantled crater walls appear to evolve by large-scale mass wasting of ice-rich material to produce patterned floor deposits, followed by cycles of localized wall slope modification. Formation of gullies occurs by either basal melting or breakout of groundwater, and arcuate ridges form by erosion of the margin of the crater floor deposit and/or deposition of material from the crater wall as it encounters the deposits on the crater floor.

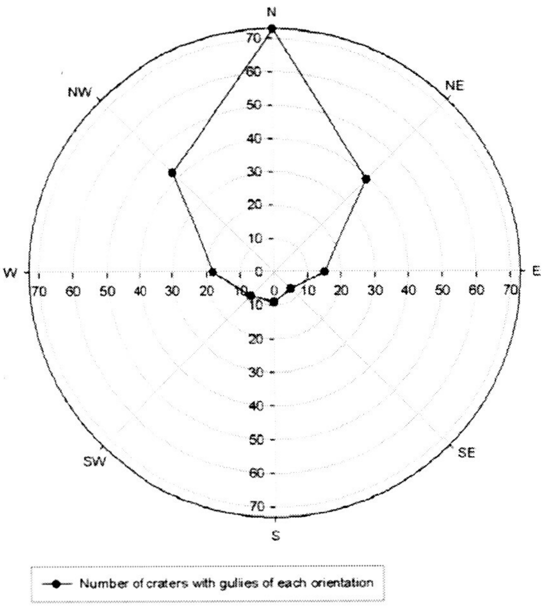

Fig. 1. Orientations of gullies in craters with coverage of N and S walls between 30° and 44° S, in MC-24.

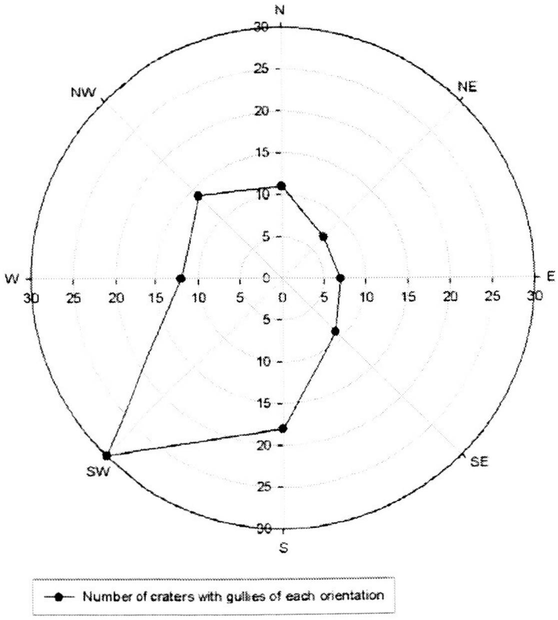

Fig. 2. Orientations of gullies in craters with coverage of N and S walls between 44° and 65° S, in MC-24.

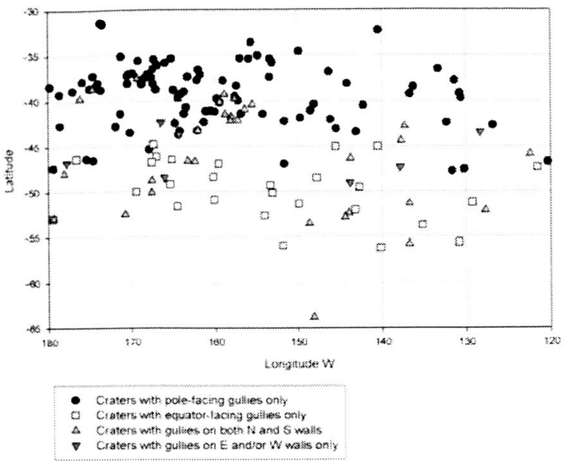

Fig. 3. Orientations of gullies in craters with coverage of both N and S walls in MC-24.

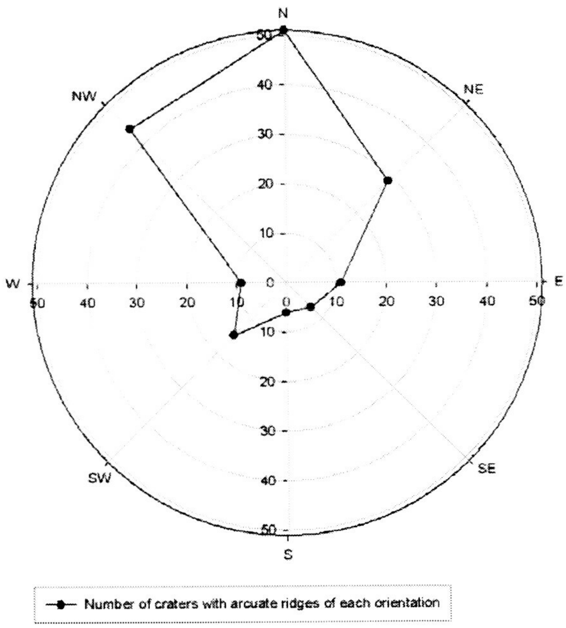

Fig. 4. Orientations of arcuate ridges in craters with coverage of N and S walls, in Quandrangle MC-24.

References: [1] Berman D. C. et al. (2005), *Icarus,* in review. [2] Berman D. C. (2003) M.S. Thesis, U. of Arizona. [3] Howard A. D. (2003) *LPSC XXXIV*, Abstract #1065. [4] Arfstrom J. D. (2003) *LPSC XXXIV*, Abstract #1050. [5] Arfstrom J. and Hartmann W. K. (2005), *Icarus,* in press. [6] Malin M. C. and Edgett K. S. (2000) *Science, 288,* 2330–2335. [7] Edgett K. S. et al. (2003) *LPSC XXXIV,* Abstract #1038. [8] Mustard J. F. et al. (2001) *Nature, 412,* 411-414. [9] Costard F. et al. (2002) *Science, 295,* 110-113. [10] Christensen P. R. (2003) *Nature, 422,* 45-47.

IMPACT CRATER GEOMETRIES PROVIDE EVIDENCE FOR ICE-RICH LAYERS AT LOW LATITUDES ON MARS.

B. A. Black and S. T. Stewart, Harvard University (Department of Earth and Planetary Sciences, 20 Oxford St., Cambridge, MA 02138, bblack@fas.harvard.edu, sstewart@eps.harvard.edu).

Introduction. The impact cratering record documents the history of resurfacing events on Mars. The morphology and distribution of layered (rampart) ejecta blankets provide insights into the presence of volatiles in the upper crust [1-4]. The physical properties of the crust and history of water have been revealed through recent quantitative studies of the geometry of Martian craters [5-9]. Here, we present the results from a study focused on impact craters in Utopia Planitia and the Elysium Mons province to infer the history and properties of resurfacing episodes.

Crater Measurements. Using the HMars program, an interactive toolkit for measuring crater geometries based on the Mars Orbiter Laser Altimeter (MOLA) data [5, 7], we measured 384 craters in Utopia, Isidis, Elysium, the Vastitas Borealis Formation (VBF), Acidalia, Solis Planum, and Lunae Planum. Of these, 208 well-resolved craters (all fresh and intermediately degraded craters greater than 4 km diameter) in the Utopia region were studied in detail.

The MOLA PEDR altimetry profiles are gridded using Delaunay triangulation at a resolution of 0.6 km/pixel. Rim height, cavity depth, and diameter measurements are conducted on the PEDR data and volume measurements are based on the gridded data. The accuracy of measurements with the HMars program are ~10% for rim height and <30% for ejecta volumes based on measurements of simulated craters on realistic background terrains [5, 7].

Results. Our results (Fig. 1) expand previous studies of crater geometries using the HMars program and demonstrate significant differences in crater geometries with region on Mars. For example, VBF craters (□) are distinctly softened compared to Utopia, with in-filled cavities and degraded rims. In the Utopia-Elysium region, we found a set of fresh craters with apparent ejecta volumes in excess of expected excavation volumes (identified by + and ◻ in Fig. 1). Fresh craters are defined by cavity depths, rim heights, and visual inspection of THEMIS imagery. These "excess-ejecta" (EE) craters have volumes above the apparent pre-impact surfaces (V_{above}) several times larger than their cavity volumes (V_{cavity}). We defined two classes of these excess-ejecta craters for illustrative purposes. Class one (EE-I) contains the freshest craters with the highest proportions of excess ejecta: $d_S/D_R>0.08$, $H_R/D_R>0.03$, $V_{above}/V_{cavity}>1.5$. Class two (EE-II) contains craters have slightly lower criteria for freshness and excess ejecta, defined as craters with $d_S/D_R>0.06$, $H_R/D_R>0.023$, $V_{above}/V_{cavity}>1.25$ that do not fall in class EE-I.

We investigated the geologic setting of EE craters and found a spatial correlation with certain flows from Elysium (Fig. 2). Seventy percent of the craters were located on lava and sediment units associated with Amazonian flows extending from the northwest of the Elysium rise [10]. No EE craters were found in Isidis Planitia, Acidalia Planitia, Solis Planum, or Lunae Planum, although surveys of the last three regions were not complete.

In our survey, we identified eight EE-I craters in Utopia-Elysium. The amount of excess ejecta is calculated using two independent methods (Table 1). First, the volume above the apparent pre-impact surface, V_{above}, is compared to the crater cavity volume, V_{cavity}. Second, the observed ejecta, V_{obs_ejecta}, is calculated by subtracting a conservative model for the uplifted surface (defined at a radius r by $H_R(r/R_R)^{-5.5}$), where H_R and R_R are the rim height and radius of the crater), from V_{above}. The observed ejecta volume, V_{obs_ejecta}, is compared to the expected ejecta volume, $V_{expected\_ejecta}$, for the crater diameter [11]. The excess volume ratios from the independent methods are in very good agreement, confirming that the excess volume is robust.

Discussion. Several scenarios were examined to explain the apparent excess ejecta. Based on the geological history of the region, the locations of the EE craters, and the crater geometries, we interpret the excess material in the ejecta blanket as evidence for removal of a volatile-rich layer surrounding the craters. The two volume ratios (Table 1) imply that the apparent excess ejecta is a result of deflation of the pre-impact surface level producing *perched ejecta*. Among the eight EE-I craters, the average apparent ejecta thickness is ~45 m larger than expected.

We rejected scenarios involving removal of material by scouring events (e.g., debris or lahar flows) because of the symmetric preservation of ejecta around most of the craters. Our preferred model is sublimation of one or more water ice-rich surface deposits emplaced before the impact events under a different climate. After the impact events, the ejecta blanket covers and insulates a portion of the layer. As the climate changed, the unprotected icy layer surrounding the ejecta blanket sublimates more quickly, leaving an apparently lower pre-impact surface. The inner ejecta blanket of most EE-I craters appear softened (Fig. 3), suggesting partial sublimation or relaxation.

Such an ice-rich layer may have been emplaced during a glacial period on Mars. Climate simulations suggest that the flank of Elysium Mons may accumulate ice deposits during high obliquity periods [12]. Alternatively, the clustering of EE craters on Elysium flow deposits may indicate that many of these flows were fluidized with liquid water.

We estimate the time scale for sublimation of an icy layer [following methods of 13, 14]. Longevity depends strongly on the thickness of the layer, ice fraction, burial depth, porosity of the insulating ejecta, and temperature. At an average temperature of 210 K, a 45-m thick pure ice layer, buried under 20 m of ejecta (10% porous, 10-μm pores), would sublimate in ~55 Ma. A 45-m thick partial ice layer would sublimate in a few 10's Ma in the present climate.

Conclusions. Craters with perched ejecta in the region of Utopia Planitia provide evidence for an ice-rich layer preserved by overlying ejecta blankets. These observations support climate models and geomorphologic observations that suggest Martian obliquity cycles produced recent glacial periods and deposition of low- and mid-latitude ice [8, 12, 15-17]. The inference of ice-rich layers, residing below the penetration depth of the Neutron Spectrometer [18], is testable with ground-penetrating radar or drilling.

Acknowledgments. This work was supported by NASA NAG5-13474 and the Harvard College Research Program.

References. [1] Cave, J.A. (1993) *JGR* **98**, 11079. [2] Cintala, M.J. and P.J. Mouginis-Mark (1980) *GRL* **7**, 329. [3] Barlow, N.G. and T.L. Bradley (1990) *Icarus* **87**, 156. [4] Stewart, S.T., et al. (2004) *Shock Compression of Condensed Matter -- 2003*, AIP, 1484. [5] Valiant, G.J. and S.T. Stewart (2004) *LPSC* **34**, 1293. [6] Boyce, J.M., et al. (2005) *JGR* **110**, E03008. [7] Stewart, S.T. and G.J. Valiant (2004) *7th Mars Crater Consortium Meeting*. [8] Meresse, S., et al. (2005) *LPSC* **36**, 1748. [9] Black, B.A. (2005), B.A. thesis, Harvard. [10] Russell, P.S. and J.W. Head (2003) *JGR* **108**, 5064. [11] Kring, D.A. (1995) *JGR* **100**, 16979. [12] Mischna, M.A., et al. (2003) *JGR* **108**, 5062. [13] Stewart, S.T. and F. Nimmo (2002) *JGR* **107**, 5069. [14] Moore, J.M., et al. (1996) *Icarus* **122**, 63. [15] Hauber, E., et al. (2005) *Nature* **434**, 356. [16] Head, J.W., et al. (2005) *Nature* **434**, 346. [17] Laskar, J., et al. (2004) *Icarus* **170**, 343. [18] Feldman, W.C., et al. (2002) *Science* **297**, 75.

Table 1. Excess Ejecta Volume. Ratios of observed apparent ejecta volume to expected ejecta volume and ratios of volume above apparent pre-impact surface to cavity volume for EE-I craters.

Crater #	**1**	**2**	**3**	**4**
$\frac{V_{above} - V_{uplift}}{V_{expected\ ejecta}}$	2.79	1.31	1.43	5.45
V_{above}/V_{cavity}	2.07	1.77	1.61	7.36
Crater #	**5**	**6**	**7**	**8**
$\frac{V_{above} - V_{uplift}}{V_{expected\ ejecta}}$	2.76	9.9	1.77	4.47
V_{above}/V_{cavity}	2.03	7.3	1.64	4.17

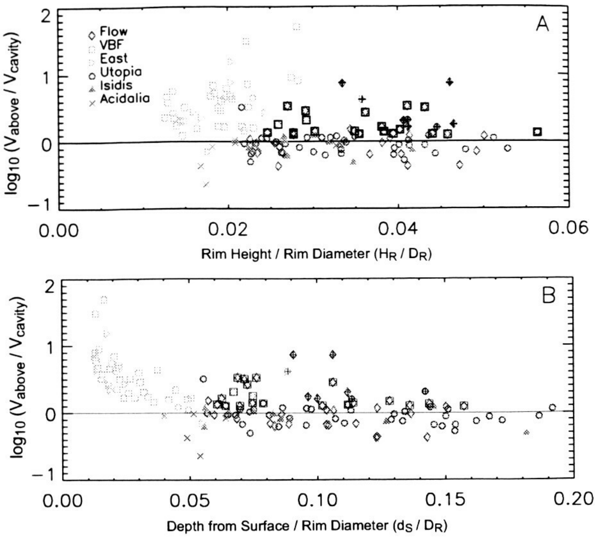

Fig. 1. Log of ratio of volume above apparent pre-impact surface to cavity volume as a function of **A.** rim height / rim diameter and **B.** depth from surface / rim diameter. Craters on the right are considered the freshest. +: class one excess-ejecta craters; □: class two excess-ejecta craters. Log ratio of zero indicates $V_{above} = V_{cavity}$.

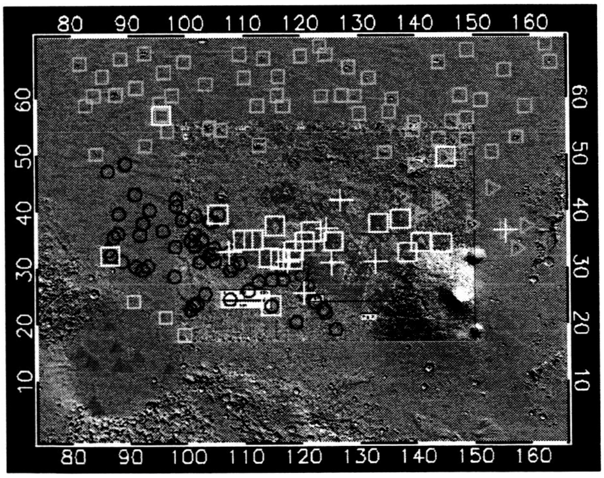

Fig. 2. Locations of excess ejecta craters, overlaid on shaded relief topography and map of Elysium flow units [from 10]. Symbols identify different crater groups (defined in Fig. 1). White +: EE-I craters; white □: EE-II craters.

Fig. 3. Daytime THEMIS IR image of crater no. 4 from Table 1 (6.2-km diameter, 124.3 E, 36.9 N). Note softened appearance of inner ejecta blanket. [THEMIS I10232013, north up].

Martian Craters Viewed by the THEMIS Instrument: Double-Layered Ejecta Craters.

Joseph M. Boyce and Peter J. Mouginis-Mark, both at: Hawaii Institute of Geophysics and Planetology, University of Hawaii, Honolulu, Hawaii, 96822

A global search of THEMIS VIS data (18 m/pixel) allows the identification of 89 fresh appearing double layer ejecta DLE craters in the diameter range 5.5 to 29.6 km. Most of these craters occur in two latitudinal bands, from 28.9° to 51.53°S, and 23.3° to 57.3°N, and at elevations from –6.0 to +2.0 km relative to Mars datum, confirming observations [1] that DLE craters occur at/on a variety of elevations, terrain types and terrain ages on Mars (Fig. 1).

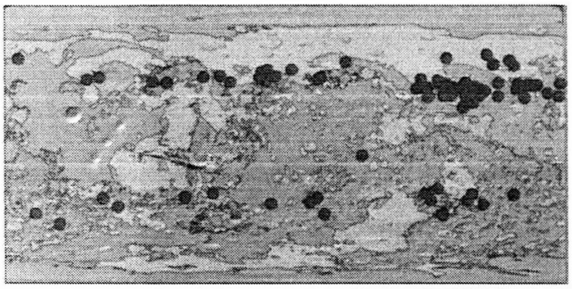

Figure 1: Locations (red dots) of fresh appearing DLE craters identified in this study, plotted on a generalized geologic (age) map of Mars. Blue is Noachian-age terrain, green represents Hesperian-age terrain and gray is Amazonean-age terrain. Geologic base map from USGS Flagstaff.

Morphology: All DLE craters studied here include two ejecta layers; the inner layer is the thickest and extends outward from the rim to ~1-2 crater radii, while the outer layer is thinner (a few tens of meters) and extends outward to ~3-5 crater radii. Both ejecta layers have a pronounced radial texture produced by grooves and ridges that commonly can be traced continuously from near the rim (Fig. 2) to the outer edge of the outer layer. The nature of the texture changes abruptly at the boundary between the two layers: from straight troughs and ridges on the inner layer (Fig. 3) to troughs and ridges on the outer layer that are deflected around obstacles (Fig. 4) and commonly have channel-like shapes in MOC images. The morphologic characteristic of this texture suggests that it was produced by erosion by supersonic surge on the inner layer that changed to deposition by subsonic flow in the outer layer.

Figure 2. The inner ejecta layer of the crater Bacolor (33.0°N, 118.6°E) showing straight grooves and ridges that run radial to its rim. (THEMIS VIS image 12141005).

Morphologic evidence (the ejecta's inability to surmount obstacles ~300 m high) indicates that the outer layer was emplaced at a relatively low speed of <100 m/sec at the boundary between the two layers. The inner layer has a broad distal rampart that may be as much as 175 meters high relative to the surface of the outer ejecta layer. A similar but smaller broad rampart also is common on the outer edge of the outer ejecta layer. A "moat" often exists between the crater's rim crest and the broad rampart on the inner ejecta layer and, in places, may be at an elevation only a few meters higher than the inferred elevation of the preexisting surface. As a result, ejecta deposits close to the rim of DLE craters are generally thinner than those of other types of craters suggesting that either low-velocity near-rim flap material was not deposited near the end of crater formation or that it was transported outward (possibly deposited as part of the broad rampart of the inner layer).

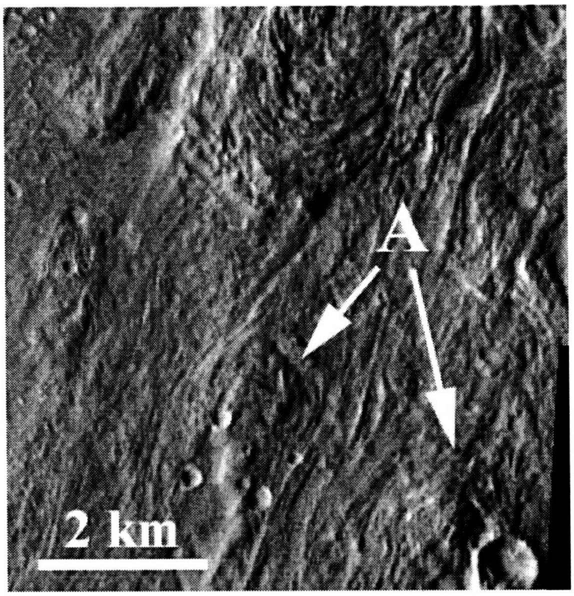

Figure 3. The outer ejecta layer of Bacolor has numerous radial channel-like troughs and ridges. In places these features are deflected around preexisting obstacles (A) (THEMIS VIS image 13988002).

No secondary craters have been identified out to 11 crater radii from these craters. The lack of secondary craters could be the result of fragmentation of ejecta blocks cause by volatile in the target materials, entrainment or crushing of these blocks by the surge that produced the outer ejecta layer, or an observation bias caused by the current spatial coverage by THEMIS images.

Emplacement Model: These observations suggest that emplacement of DLE crater ejecta occurred in two stages, similar to that proposed by [2] where the inner ejecta layer was emplaced before the outer ejecta layer. Furthermore, the high-resolution THEMIS image data suggest that emplacement of the inner ejecta layer was, most likely, by a process similar to that of the ejecta of other fluidized ejecta craters, but the outer ejecta layer was emplaced by base surge. In addition, the comparatively short runout distance of the inner layer is consistent with that predicted by [3] for target materials that contain significant amounts of water ice.

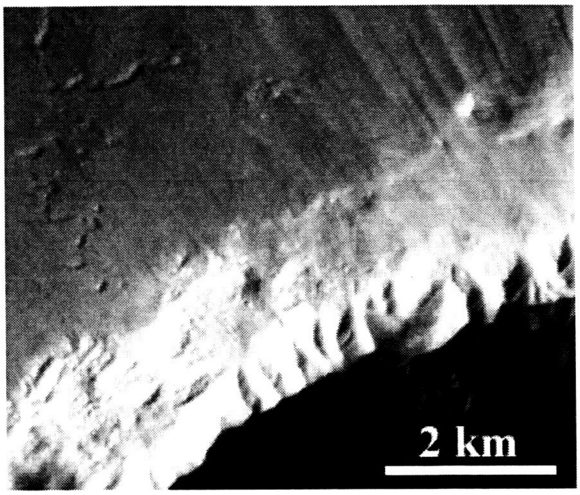

Figure 4. The north rim of Bacolor showing striations that runs from near its crest outward onto the inner ejecta layer (THEMIS VIS image 12453007).

While other mechanisms could produce the observed morphologic features, they require the ejecta to be fluidized throughout its emplacement, and as a result require a broad distribution of localized deposits of easily fluidized materials (e.g., thick, fine-grain deposits) or that base surge dominated the entire ejecta emplacement process with little contribution from ballistic ejection of materials.

References:

[1] Barlow, N. G. and T. L. Bradley (1990) *Icarus* 87: 156 – 179; [2] Mouginis-Mark, P. J., (1981) *Icarus* 45: 60-76; [3] Wohletz, K. H. and M. F. Sheridan (1983) *Icarus* 56: 15 – 37.

ELASTIC GRANULAR FLOWS. C. S. Campbell, USC Aerospace and Mechanical Engineering, Los Angeles CA 90089-1453. campbell@usc.edu

A decade ago, large scale landslide simulations, designed to understand the anomalous behavior on the Earth, Moon and Mars, yielded the surprising result that the effective friction coefficient (the ratio of shear to normal forces at the base of the slide) increased with the shear rate. This might possibly explain the effect of slide volume on the runout of large landslides, but it also indicates that landslides operated in an entirely new and unexplored flow regime.

Previously, granular flows had been divided into (1) the slow, quasistatic regime, in which the effective friction coefficient is taken to be a material property and thus constant, and (2) the fast, rapid-flow regime, where the particles interact collisionally, but which scales in such a way that the effective friction coefficient is independent of the shear rate. Consequently the landslides operated in a separate intermediate regime.

This talk will discuss computer simulation studies into this intermediate regime and into the transitions between regimes. In this way, it is possible to draw the entire flowmap connecting the quasistatic and rapid-flow regimes. The key was to include the elastic properties of the solid material in the set of rheological parameters; in effect this put solid properties into the rheology of granular solids, properties that were unnecessary in previous theories as a result of the plasticity and kinetic theory formalisms on which quasistatic and rapid-flow theories are respectively based. Granular flows are then divided into two broad categories, the Elastic Regimes, in which the particles are locked in force chains and interact elastically over long duration contact with their neighbors and the Inertial regimes, where the particles have broken free of the force chains. The Elastic regimes can be further subdivided into the Elastic-Quasistatic regime (the old quasistatic regime) and the Elastic-Inertial regime. The Elastic-Inertial regime is the "new" regime observed in the landslide simulations, in which the inertially induced stresses are significant compared to the elastically induced stresses. The Inertial regime can also be sub-divided into an Inertial-Non-Collisional where the stresses scale inertially, but the particles interact through long duration contacts, and the Inertial-Collisional or rapid-flow regime.

Finally, it will be shown that Stress-Controlled flows are rheologically different from Controlled-Volume flows. Physically, there is a range of dense concentrations ($0.5<\nu<0.6$) in which it is possible to form force chains and thus to demonstrate elastically. But there are conditions under which force chains may or may not form at a given average concentration. (In other words it is possible for the material to exhibit two different states at the same concentration.) By forcing the material to support an applied loads across force chains, Stress-Controlled flows generally behave elastically through this range of concentrations under the same conditions where Controlled-Volume flows behave inertially.

Keywords: Granular flow, Elastic, Force chains, landslides, flow regimes, flowmaps, Elastic-Quasistatic, Elastic-Inertial, Inertial-non-Collisional, Collisional

DISPERSION AND MIXING OF IMPACT-GENERATED AEROSOLS IN THE MARTIAN MIDDLE ATMOSPHERE.

J. Y-K. Cho[1], S. T. Stewart[2]. [1]Department of Terrestrial Magnetism, Carnegie Institution of Washington (jcho@dtm.ciw.edu), [2]Department of Earth and Planetary Sciences, Harvard University (sstewart@eps.harvard.edu)

Large bolide impacts on the Martian surface load the atmosphere with long-lived, fine-scale particles by direct injection and ballistic fallout [*Pierazzo et al.,* 1998]. When the particles enter the middle atmosphere, the vertically stable region above the troposphere (0 to ~50 km altitude), they remain aloft for very long times of months to years depending on the particle size. There, the emplaced particles are dispersed in a highly complex spatial pattern by the strong, prevailing winds. The detailed evolution of dispersion and mixing of particles in the middle atmosphere has not been addressed. This is due in part to the high resolution and complexity required to accurately track the dispersion for longer than very short times (~minutes to ~hours).

We study the nonlinear dispersion of aerosols over meteorologically significant time of ~10 sols using a high-resolution (~30 km) atmospheric flow model. The model uses the spectral method to solve the atmospheric dynamics equations (the primitive equations) and is capable of resolving the dynamical structures (waves, eddies, and turbulence) critical for accuracy. The model is loaded with the MOLA topography [*Smith et al.*, 1999], winds from a full Mars general circulation model of *Richardson and Wilson* [2002] at different seasons, and starting particle coverage similar to those in *Kring and Durda* [2002] for shallow and steep velocity distributions. Using the model, we study the spreading rates, mixing extent, and potential for global transport in events from ~10 to ~100 km-sized impactors in many different physical conditions (e.g., season, impact location, spatial-temporal distribution of injected particles, strength of topographic waves, etc.).

Because of the mechanics of the vapor plume expansion and factors having to do with different particle sizes, the material entrained into the plume is not initially distributed homogeneously in the middle atmosphere. There, in the presence of high-amplitude jets (of up to 180 m s^{-1}) and thermotidally and topographically excited waves, the long aloft-times allow the starting distribution's unevenness to persist and increase in complexity over time. This is significant for studies of the distribution of volatiles and environmental consequences from impacts.

We find that, in general, while the transport distances can be global and timescales fast, the spreading is not uniform (Fig. 1). Because fine-scale particles couple radiatively to the atmosphere, the unevenness also presents an important and non-uniform feedback, by unevenly heating and thus modifying the winds that chaotically advect them. Even in the very energetic impact case, where the starting area coverage is wider and includes preferential injection at the antipode, the strong jets, waves, and turbulence in the middle atmosphere lead to markedly uneven and patchy distributions (Fig. 2). The particles are diffusively distributed in very low column density over a large fraction of the globe (in low- to mid-latitudes), but most of the material remains concentrated in complex, localized patches over days.

In the more frequent, smaller cratering events, the distribution of long-lived aerosol particles evolves chaotically – often producing concentrated patches persisting over meteorologically significant time scale within the impacted hemisphere. If mixed into the troposphere, the persistent areas may still serve as possible markers for impact-driven volatiles transported by the strong interaction with the atmosphere.

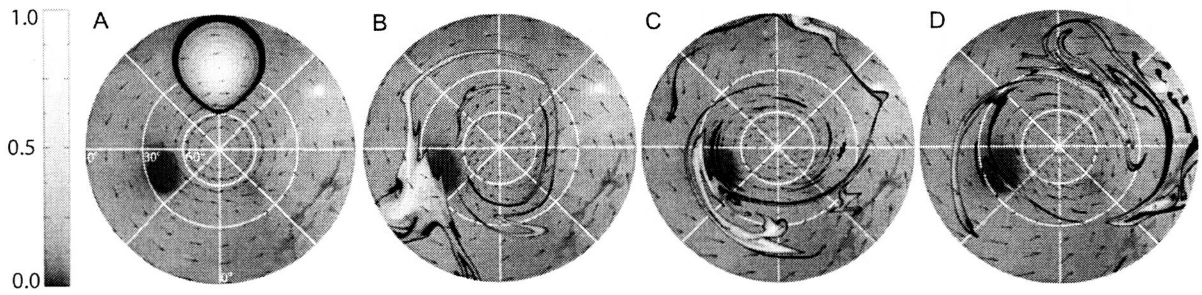

Fig. 1. Evolution of ejecta plume following an impact from a high-resolution (30 km) simulation, initialized with winds at northern hemisphere summer solstice (Ls = 90°). The impact location is at (lon = 180° E, lat = 30° S). The starting distribution (representing few hours after the impact) is a patch near the impact location. The aerosol column density (g cm^{-2}) is shown at four different times (A–D), t = (0, 2.5, 6.0, and 10 sols) in stereographic projection centered on the South Pole.

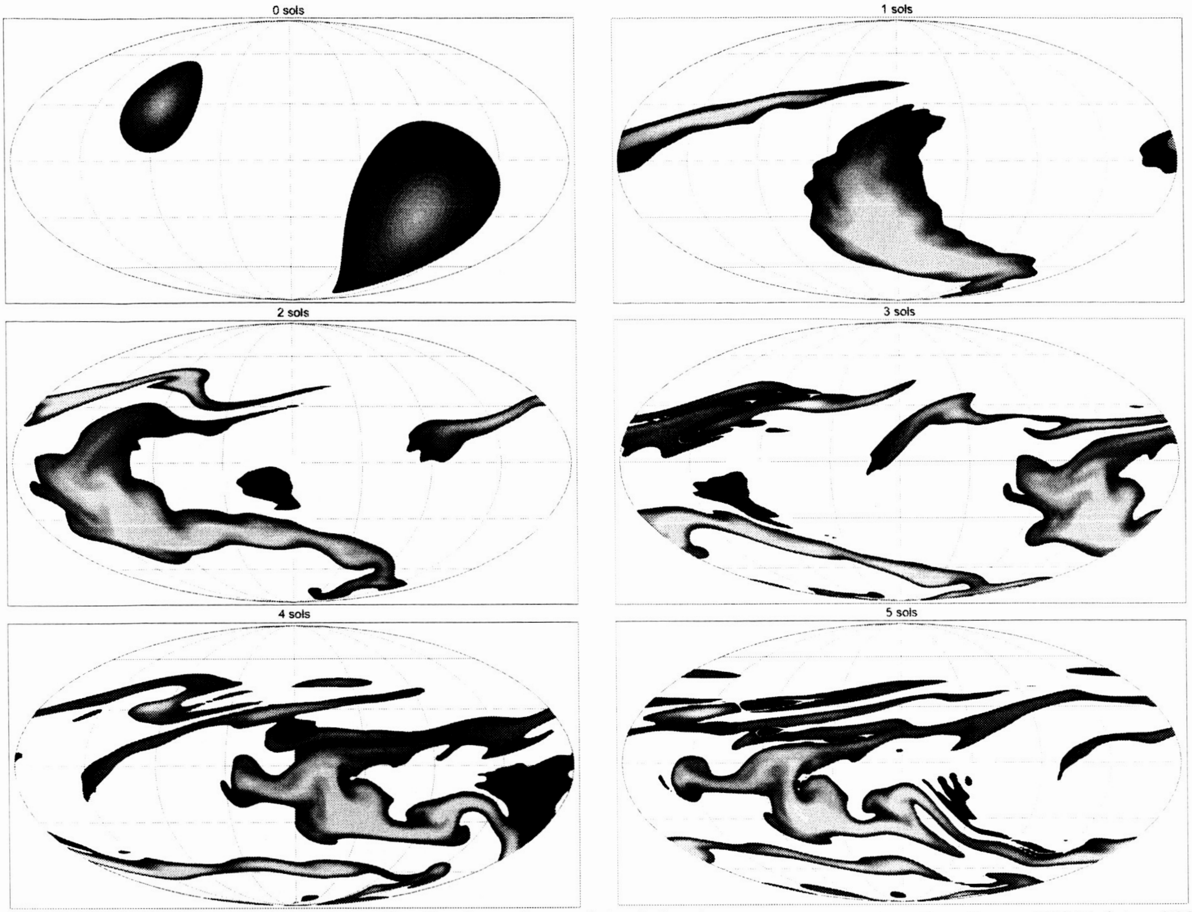

Fig. 2. Evolution of column density distribution of material originating at the impact location (lon = 90° E, lat = 30° N) and the impact antipode. Ejecta are added at the antipode in pulses with time, as found in *Kring and Durda* [2002]. The aerosol column density (scale as shown in Fig. 1) is shown at six different times, t = (0, 1, 2, 3, 4 and 5 sols) after impact. The frames are in Mollweide projection with center longitude of 180° E and the winds are as in Fig. 1. For clarity, contours of lowest column density not shown.

References

Kring, D. A. and D. D. Durda (2002) Trajectories and distribution of material ejected from the Chicxulub impact crater: implications for postimpact wildfires, *J. Geophys. Res.*, *107(E)*, 5062, doi: 10.1029/2001JE001532.

Pierazzo, E. D., D. A. Kring, and H. J. Melosh (1998) Hydrocode simulation of the Chicxulub impact event and the production of climatically active gases, *J. Geophys. Res.*, *103*, 28,607–28,625.

Richardson M. I. and R. J. Wison (2002) A topographically forced asymmetry in the Martian circulation and climate, *Nature, 416*, 298–301.

Smith, D. E. and 19 coauthors (1999) The global topography of Mars and implications for surface evolution, *Science*, *284*, 1495–1503.

The effect of impacts on the Martian climate

A. Colaprete[1], R. M. Haberle[1], T. L. Segura[3], O. B. Toon[3], K. Zahnle[1], NASA Ames Research Center, Moffett Field, MS 245-3, Mountain View,CA 94035, tonyc@freeze.arc.nasa.gov, [2]Program in Atmospheric and Oceanic Sciences, Laboratory for Atmospheric and Space Physics, University of Colorado, Campus Box 392, Boulder, CO, 8030.

Introduction: Evidence for the presence of liquid water early in Mars' history continues to accumulate. The most recent evidence for liquid water being pervasive early in Mars' history is the discoveries of sulfate and gypsum layers by the Mars Exploration Rovers and Mars Express. However, the presence of liquid water at the surface very early in Mars' history presents a conundrum. The early sun was most likely approximately 75% fainter than it is today. About 65-70 degrees of greenhouse warming is needed to bring surface temperatures to the melting point of water. To date climate models have not been able to produce a continuously warm and wet early Mars (Haberle, 1998). This may be a good thing as there is morphological and mineralogical evidence that the "warm and wet" period had to be relatively short and episodic. The rates of erosion appear to correlate with the rate at which Mars was impacted (Carr and Waenke, 1992) thus an alternate possibility is transient warm and wet conditions initiated by large impacts. It is widely accepted that even relatively small impacts (~10 km) have altered the past climate of Earth to such an extent as to cause mass extinctions (Toon et al., 1997). Mars has been impacted with a similar distribution of objects. The impact record at Mars is preserved in the abundance of observable craters on it surface. Impact induced climate change must have occurred on Mars.

Impacts: The impacts of asteroids and comets larger than 100 km in diameter have left more than thirty craters on Mars (Kieffer et al. 1992). Collisions of such large, energetic objects result in the production of meters thick debris layers that are global in extent (Melosh 1989; Sleep and Zahnle, 1997). For example, an object with a diameter of 100 km will result in a global melt/vapor debris layer approximately 10 cm thick (Melosh 1989; Sleep and Zahnle, 1997). This debris layer will be very hot having temperatures in excess of 1000 K.

In addition to the heat introduced by the impact, a substantial amount of vaporized water, both from the impactor itself and from the target material is injected into the atmosphere. Following the impact, the thermal pulse that travels downward into the regolith may release additional water from subsurface reservoirs adding to the total liquid water amount at the surface. Water vapor is an excellent greenhouse gas and works to trap the impact generated heat within the atmosphere. The heat from the debris combined with the additional greenhouse afforded by the injected water vapor could result in periods of warmth. Segura et al. (2002) demonstrated that asteroids with diameters larger than 100 km could warm the surface of Mars for several years to decades. However, numerous valley networks have been dated to periods after the majority of these large (D > 100 km) objects had impacted Mars.

The simulations conducted by Segura et al. (2002) were limited to 1D and thus only considered impacts which would have a thick (> several cm) global debris layers. There are, however, more than 1000 craters with diameters larger than 60 km on Mars. A 60 km crater would result from an impactor with a diameter of approximately 6 km. While these smaller impactors do not have thick global debris layers, they do have dramatic regional effects that are similar to those proposed by Segura et al. (2002).

GCM Simulation: The obvious limitation of the 1D calculations of Segura et al. (2002) is the absence of dynamics and the ability to model smaller impacts that do not have thick global debris layers. An accurate assessment of the effects of impacts on the climate will need to include the transport of both heat and water vapor. Reported here are the results of post impact climate simulations using the Ames Mars General Circulation Model (MGCM). A hydrological cycle has been incorporated into the Ames MGCM that includes the formation of clouds, precipitation, and surface and regolith reservoirs. In these simulations, impacts by objects as small as 4 km in diameter can be simulated.

Each simulation is initialized to represent the conditions just following an impact. After a period of simulation time, an impact debris layer and atmospheric thermal plume is emplaced at any location in the model. The impact debris layer thickness and extent, and the thermal plume temperature and extent, is defined as a function of impact diameter. Regolith water abundance and distribution can be specified for each simulation. If regolith temperatures rise above freezing water is allowed to diffuse to the surface at a fixed rate. Infiltration of the subsurface by surface water is not currently modeled. Both water clouds (wet and cold microphysics) and carbon dioxide clouds are modeled. Water and CO_2 cloud radiative effects are included. In

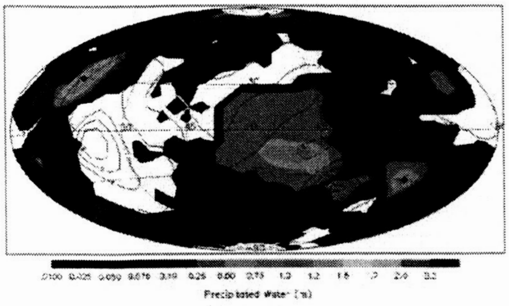

Figure 1 The total integrated rain following the impact of a 20 km diameter impactor into a 300 mbar atmosphere. In this simulation the regolith water abundance as assumed to be 20% (by mass) and to be uniformly distributed.

this presentation results are shown for an early Mars atmosphere containing 300 mbars of CO_2 and a solar flux that is 75% current levels.

Results: Two key simulation results include the total precipitation and the total liquid water at the surface. Total precipitation is defined as either snow or rain. The total liquid water (TLW) at the surface is a measure of any water at the surface that is warmer than 273 K. This water may be in the form of surface melt (e.g. melting snow or ice) or large bodies of water (e.g. seas or lakes). Figure 1 shows and example of the total precipitation resulting from a 20 km diameter impactor (no cloud radiative effects). Following impact surface temperatures can rise well above freezing for several years even for impacts smaller than 10 km in diameter.

A range of impact sizes has been modeled so that the total amount of resulting precipitation as a function of impact diameter can be parameterized. Using this parameterization it is possible to estimate the total integrated precipitation and TLW that has occurred over the history of Mars based on the observed crater record (Figure 2). Based on these results it is likely that impacts have been a significant, and possibly the dominant source of erosion during Mars distant past.

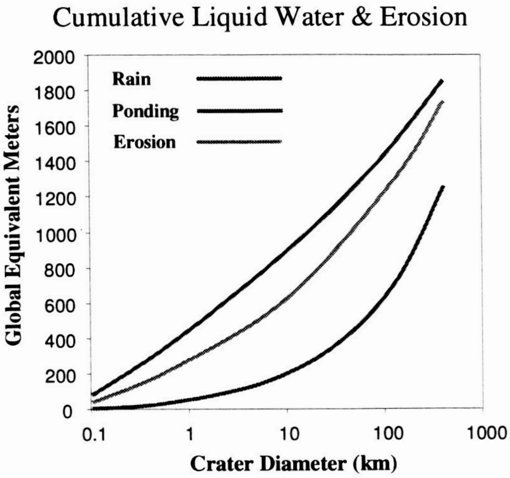

Figure 2 Total precipitation and total liquid water amounts assessed from a series of simulations for a range of impact diameters and the observed Martian crater record. These results do not include the radiative effects of clouds.

MODIFIED IMPACT CRATERS ON MARS: OBSERVATIONS, MEASUREMENTS AND LIKELY PROCESSES.

Robert A. Craddock, Center for Earth and Planetary Studies, National Air and Space Museum, Smithsonian Institution, Washington, DC 20560-0315, craddockb@si.edu.

Introduction: Modified impact craters on Mars were first recognized in early Mariner spacecraft images. From these data, *Leighton et al.* [1] showed that martian craters are in widely different degrees of preservation, which they presumed to be a function of age. Inspired by Mariner 9 spacecraft observations of global dust storm activity *Hartmann* [2] suggested that eolian processes that had removed and redistributed loose crater ejecta over time could explain the morphologies of modified impact craters. Analyses of impact crater populations suggested that Mars had fewer small diameter impact craters than were observed on the moon, leading *Jones* [3] and *Chapman and Jones* [4] to the conclusion that water eroded many of the smaller martian craters during an early obliteration event. Based on Viking data, Arvidson et al. [5] suggested volcanism as yet another possible process responsible for crater modification. Interestingly, despite the improvement in image resolution and clarity eolian processes continued to be the favored process for crater modification by many investigators during the Viking era [6, 7, 8]. However, as topographic data and improved high-resolution images became available from the suite of spacecraft currently orbiting Mars it has become increasingly apparent that only a combination of fluvial processes is capable of explaining the styles of crater morphology, the timing of modification, and the estimated amount of erosion [9, 10, 11, 12, 13].

Erosion Versus Deposition: Many modified impact craters appear to be flat-floored and rimless. They possess no apparent ejecta blanket, nor do they have a central peak, which are characteristic of many "fresh" (i.e., unmodified) impact craters. The flat-floored, rimless morphology typical of most modified impact craters is observed in craters of widely varying diameters that are located next to one another [9, 10]. This observed spatial relationship provides compelling evidence against aggradational processes, such as eolian deposition or volcanism, creating the modified impact craters. A sand sheet or lava flow typically forms a uniformly thick deposit at local scales (10's of km^2). Because crater rim height and depth increase as a function of diameter, a uniformly thick deposit cannot explain the observed size range of modified impact craters. Consider a crater with a rim height less than the thickness of the deposit. The deposit would bury such a crater. In contrast, any crater with a rim height greater than the thickness of the deposit would retain a sharp, raised rim (albeit partially buried). Only a crater with a rim height equivalent to the thickness of the deposit would appear to be rimless. Because fluvial erosion can produce a flat-floored, rimless crater morphology through backwasting and downcutting independent of crater diameter (if given enough time), degradation, as opposed to pure aggradation, must be the dominant mechanism responsible for crater modification.

Measurements and Likely Processes: *Craddock et al.* [11] provided the first estimates of the volume eroded from individual modified craters. Morphometric profiles of fresh and modified craters were extracted from monoscopic Viking orbiter images using photoclinometry [14]. Modified impact crater profiles were compared to profiles of fresh craters, and the diameter of the fresh crater was iteratively changed until the calculated volumes between the fresh and modified craters balanced. Their results indicate that the diameter of most modified impact crater increased by ~10% during erosion, presumably due to backwasting of the steep crater interiors.

Beginning with the morphometric data from fresh impact craters, we ran a variety of computer simulations using *Howard's* [15] model to explore the effects different geologic processes might have on crater morphology from known rate laws. Results of these simulations were compared to measurements of actual degraded craters, thus allowing us to directly evaluate the efficiency of any process or combination of processes at producing the observed crater morphology. The tacit assumption was, of course, that fresh craters preserved on Mars today are morphologically similar to those that formed during the early history of Mars prior to erosion.

In simplest terms, erosional processes can be described as either scale-inefficient ("diffusional" or "dispersive") or scale-efficient ("advective" or "concentrative"). On Earth, these two processes act coevally in drainage basin development. Although there are exceptions (e.g., rock avalanches on steep, bedrock slopes), diffusional processes are commonly equated with mass wasting. Mass wasting is diffusive in that it decreases in efficiency with increasing contributing area, a condition referred to as linear diffusional creep. Solifluction is a terrestrial example of linear diffusional creep. Typically affected slopes follow a convex-to-concave profile [e.g., 16]. The mass wasting model used in our simulations also includes the provision for specifying a critical slope gradient (e.g., the angle of repose) such that mass wasting rates increase without limit as the gradient approaches the critical gradient, a condition referred to as non-linear diffusional creep. A slump block or landslide are terrestrial examples of non-linear diffusional creep. In addition, our model also includes the provision for weathering-limited erosion. The assumption is that weathering processes may be necessary to produce a mobile regolith, thus limiting the rate of vertical erosion.

In contrast, advective processes increase with efficiency as the contributing area increases, so that in steady state conditions the gradient decreases downslope. Such processes are commonly equated with fluvial processes, with exceptions (e.g., in ephemeral systems when discharge decreases downstream due to transmission losses). Fluvial channels can be divided into steeper, detachment-limited ("bedrock") channels and gentler transport-limited ("alluvial") channels. Our model accounts for both types of channels and for spatial and temporal transitions between them. In detachment-limited conditions, the amount of material available for erosion is less than the capacity of the water to carry it (e.g., a flow over bedrock or regolith). Under these conditions, detachment of sediment from the surface is proportional to the shear stress exerted on the bed and banks. In an ideal system, erosion would typically be transport-limited in the lower courses of stream networks where base level control limits relief. In headwater areas, however, the volume of eroded sediment is below the capacity of the water to transport it (detachment-limited conditions).

A classic example of the type of profile produced in environments where advective processes dominate is the concave longitudinal profile (i.e., long profile or thalweg) of a stream. On Mars, advective processes would be very effective at eroding interior crater walls, causing backwasting and an increase in the apparent crater diameter. The eroded materials would then be transported through surface runoff and redistributed, resulting in craters with flat floors. A sharp break in slope at the base of the crater wall also results and is diagnostic of advective processes. Modified craters with these attributes appear to be extremely common, suggesting that the early climate supported rainfall and surface runoff. However, advective processes usually occur together with diffusional processes (e.g., soil creep or rain splash). On Mars, diffusional processes appear to be responsible for producing the rounded rim observed on many modified craters.

We have completed two detailed pilot studies within the Sinus Sabaeus region of Mars [11, 13] as well as a cursory study of the martian highlands where over 100 individual modified craters were analyzed [12]. These analyses indicate that a majority of craters have been modified by a combination of linear diffusional creep and fluvial erosion and deposition. A rounded interior rim, steeply dipping walls, and a sharp break in slope at the crater floor typify such craters. However, approximately 20% of the modified craters observed have well-rounded rims with shallow sloping walls that gradually transition into the crater floor, which is best explained by a linear diffusional creep process working exclusively. The observed morphometric differences in modified craters can be interpreted two ways. Potentially, they are the result of lithologic variations within the martian highlands. For example, it is possible that the infiltration capacity of the regolith in certain areas was higher. In this scenario, rain fell on early Mars to create the diffusional modification of the impact craters, but surface runoff was never (or seldom) initiated so fluvial transport and deposition could not occur. However, because craters modified by diffusional processes exclusively often occur adjacent to those that have also been modified by fluvial erosion and deposition [12] this scenario is unlikely. It is more probable that these craters record a temporal variation in the early martian climate. In this scenario, the amount of rainfall during a given event decreased over time, so the infiltration capacity of the local regolith was no longer exceeded to produce runoff. Alternatively, because linear diffusional creep is also characteristic of solifluction, it may be that these craters record the onset of a wet, but cold periglacial climate that experience regular freeze-thaw cycles.

References: [1] Leighton, R.B. *et al.* (1965) *Science, 149*, 627-630. [2] Hartmann, W.K. (1971) *Icarus, 15*, 410-428. [3] Jones, K.L. (1974) *JGR*, *79*, 3917-3931. [4] Chapman, C.R. and K.L. Jones (1977) *Annu. Rev. Earth Planet. Sci., 5,* 515-540. [5] Arvidson, R.E. *et al.* (1980) *Rev. Geophys. Space Phys.*, *18*, 565-603. [6] Wilhelms, D.E. and R.J. Baldwin (1989) *Proc. LPSC, 19th,* 355-365. [7] Moore, J.M. (1990) *JGR*, *95,* 14,279-14,289. [8] Grant, J.A. and P.H. Schultz (1993) *JGR*, *98*, 11,025-11,042. [9] Craddock, R.A. and T.A. Maxwell (1990) *JGR*, *95*, 14,265-14,278. [10] Craddock, R.A. and T.A. Maxwell (1993) *JGR*, *98*, 3453-3468. [11] Craddock, R.A. *et al.* (1997) *JGR*, *102*, 13,321-13,340. [12] Craddock, R.A. and A. Howard (2002) *JGR*, *98*, 3453-3468. [13] Forsberg-Taylor, N.K. *et al.* (2004) JGR, 109, E05002, doi:10.1029/2004JE002242. [14] Davis, P.A., and L.A. Soderblom (1984) *JGR*, *89*, 9449-9457. [15] Howard, A.D. (1994) *Water Resourc. Res.*, *30*, 2261-2285. [16] French, H.M., *The Periglacial Environment*, 309 pp., Longman Inc., New York, 1976. [17] Craddock, R.A., and A.D. Howard (2000) *JGR*, *105*, 20,387-20,401.

AUTOMATIC RECOGNITION OF CRATER-LIKE STRUCTURES IN TERRESTRIAL AND PLANETARY IMAGES.

Jon Earl[1], Agustin Chicarro[2], Christian Koeberl[3], Pier Giorgio Marchetti[4], and Martin Milnes[1], [1]LogicaCMG UK Ltd (Space & Defense Division), Chaucer House, The Office Park, Leatherhead, Surrey KT22 7LP, United Kingdom (Jon.Earl@logicacmg.com; Martin.Milnes@logicacmg.com); [2]ESA/ESTEC, Scientific Programme, Keplerlaan 1, 2200 AG Noordwijk, the Netherlands (Agustin.Chicarro@esa.int); [3]Department of Geological Sciences, University of Vienna, Althanstrasse 14, A-1090 Vienna, Austria (christian.koeberl@univie.ac.at); [4]ESA/ESRIN, Earth Observation Programme (EOP-GDR), Via Galileo Galilei, I-00044 Frascati, Italy (Pier.Giorgio.Marchetti@esa.int).

Summary: Impact cratering is a fundamental process acting on solid bodies of the solar system. The detection of impact craters on Earth may be aided by recent advances in remote sensing technologies, although visual inspection of large number of satellite images are probably too time consuming. We describe new efforts regarding recognition and detection of impact craters on Earth and Mars by using remote sensing images. In particular, approaches based on the Hough Transform and on the Radial Consistency measure are considered and compared.

Introduction: Impact cratering is recognized to be a dominating (if not the most important) surface-modifying process in our planetary system. Detecting impact craters on Earth is difficult, mostly because terrestrial processes (weathering, plate tectonics, etc.) either cover or erase the surface expression of impact structures on Earth. Many impact structures are covered by younger (i.e., post-impact) sediments and are not visible on the surface. Others are destroyed by erosion. Recent advances in Earth Observation, i.e., the availability of synthetic aperture radar (SAR) and multispectral images covering most of the Earth from scientific missions (e.g., ENVISAT, MODIS), can aid the search for terrestrial impact craters through image processing for the identification of crater features, their detection, and possible recognition. Although it is not possible to unambiguously confirm that a crater-like feature on Earth is of impact origin just from remote sensing, such data can identify potential candidates for further studies. Information that can be derived from remote sensing products refers mainly to crater morphology, which, using relevant criteria, can aid in the identification of potential impact craters.

Geological Background: On Earth, *simple* craters have diameters of up to =2 to 4 km, and *complex* craters, which are larger and have diameters of =2 to 4 km (the exact change-over diameter between the crater types depends on the target rocks). On Mars, this change-over diameter is ca. 10 km. Complex craters are characterized by a peak or peak ring of rocks that are uplifted from greater depth and would not normally be exposed on the surface. Fresh simple craters have an apparent depth (measured from the crater rim to present-day crater floor) that is about one third of the crater diameter, whereas that value for complex craters is closer to one sixth. In reality, most craters are shallower because of erosion and/or infilling (e.g., by crater lakes).

Crater Recognition: On Earth basically all small craters are relatively young, because erosional processes obliterate small (0.5–10 km diameter) craters after a few million years, causing a severe deficit of such small craters. In terms of cratering rates, there are many craters left to be detected (e.g., [1,2]). In this context, we address the issue of recognition and detection of impact craters on the Earth by applying processing techniques to Earth Observation products, complemented by digital elevation data (DEM), to automatically highlight potential targets for future exploration.

Algorithm: Impact craters on the Earth exhibit a much greater degree of variation than impact craters on other planets. Concentrating too heavily on specific crater morphology can be misleading, since similarly sized impact craters on the Earth's surface often exhibit contrasting characteristics. For our purposes we begin by characterizing impact craters in a very simple way by using their circular shape as the main feature. Although this is an oversimplification, it provides a first order approximation which allows a given algorithm to operate on data obtained from different planets and from different sensors (optical, multispectral, SAR, DEM, etc.). On the other hand this approximation reduces the accuracy of the detection process, necessitating the introduction of further steps to reduce the number of false alarms.

A previous study [3] examined the use of a modified Circular Hough Transform to provide this model. This type of algorithm works best on binary edge-detected (or gradient) images. Where the circular features are not clearly discernable in the original image, edge-detection is unlikely to result in identifiable circles that would fit the simple circle model.

The Radial Consistency algorithm developed as part of this work models impact craters as having localised rotational symmetry- this replaces the Circular Hough Transform test (that each pixel (x,y) lies on the circle defined by the triple {a,b,r} with the test that the pixel lies within a region of rotational symmetry centred at (a,b). The peaks in the parameter space {a,b} then correspond to the most likely locations of these regions of rotation symmetry in the input image. This allows partially circular features to be picked up, and provides a natural way of fusing the results from multiple data sources.

Subsequent to the detection of potential crater candidates in multiple data sets further analysis can be performed (using, for example, the morphological rules of thumb specified above) to remove circular non-crater-like features from consideration.

Prototype Tool: A prototype impact crater detection system has been developed and was successfully used to identify a number of known terrestrial craters, and has the potential to search other areas of the Earth for previously undiscovered candidate sites. The prototype system comprises two parts: (i) An interactive standalone tool, for the development and refinement of crater detection and filtering algorithms, which is designed for use with relatively small satellite image scenes; (ii) A more comprehensive batch-processing tool, for the offline processing of large areas of data. The results may be output in various formats for rapid assimilation and assessment of the identified crater candidates. The core stages of processing involved in the detection of crater candidate sites are:

Import data from a range of different sources, in our case multiple satellite sensor data.

Pre-processing of the input data.

Automatic detection of circular features.

Filtering of features based on crater-like characteristics.

This generally results in a small number of likely candidates, which then need to be expertly assessed, in order to determine whether or not further analysis is required.

Results: A number of sites have been processed as part of the prototype development phase. Fig. 1 shows the results of the prototype applied to a typical MOLA image of the Martian surface, Fig. 2. shows the results obtained by combining SAR, Landsat and SRTM datasets along with a morphological post-processing step for the Brent crater in Canada.

Discussion and Conclusions: The early results of this study are very encouraging and have shown how the use of data fusion techniques combining multispectral and DEM datasets can aid the detection process. However, the tests carried out show the limits of exploiting only a shape-based approach in the detection process. Despite some encouraging results on the exploitation of the infrared band in subtropical desert areas and even at very high latitudes, it was not possible to identify a specific band combination more suitable than others for impact crater detection.

This highlights the need to include in the proposed architecture more advanced and specific procedures to use all the information present in the sensor data to increase the detection accuracy.

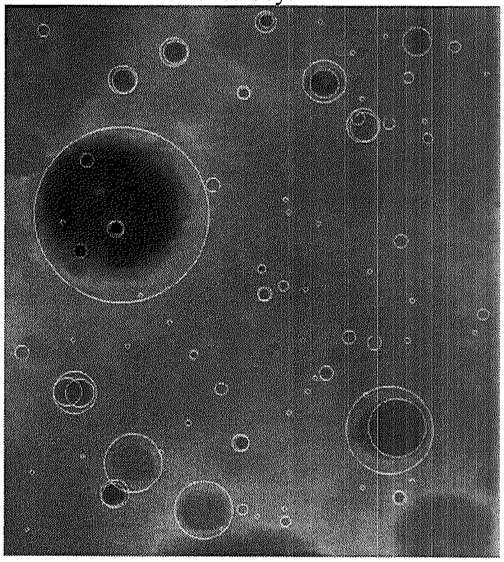

Fig. 1. MOLA data.

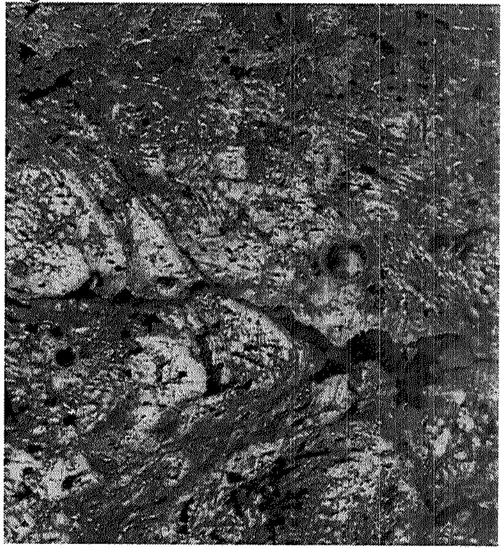

Fig. 2. Landsat (3,2,1) Brent crater on right.

Acknowledgements: This work is supported by the European Space Agency - ESA.

References: [1] Shoemaker E.M. et al. (1990) In: *Geological Implications of Impacts of Large Asteroids and Comets on Earth* (L.T. Silver and P.H. Schultz, eds). GSA-SP 247, pp. 155-170. [2] Trefil J. S., and Raup, D. M. (1990) *J. Geol.*, 98, 385-398. [3] Craters Study – Executive Summary ESA CR July 2002 http://www.esa.int/gsp/completed/ExecSumAll01_A19.pdf

IMPACT CRATERS ON MARS: NATURAL 3D EXPLORATION PROBES OF GEOLOGICAL EVOLUTION.

James B. Garvin[1], [1]*NASA Chief Scientist* at NASA Headquarters, 300 E Street SW, Washington DC, 20546 USA (james.b.garvin@nasa.gov; 202-358-4509).

Introduction: The population of impact craters preserved on the surface of Mars offers fundamental constraints on the three-dimensional mechanical characteristics of the martian crust, its volatile abundance, and on the styles of erosion that have operated during essentially all epochs of martian geological history. On the basis of the present-day wealth of morphologic and geometric observations of impact landforms on Mars [1-3], an emerging understanding of the three-dimensional physical properties of the martian uppermost crust in space and time is at hand. In this summary, the current basis of understanding of the relatively non-degraded population of impact landforms on Mars is reviewed, and new Mars Global Surveyor (MGS)-based (MOLA) measurements of global geometric properties are summarized in the context of upcoming observations by Mars Reconnaissance Orbiter (MRO).

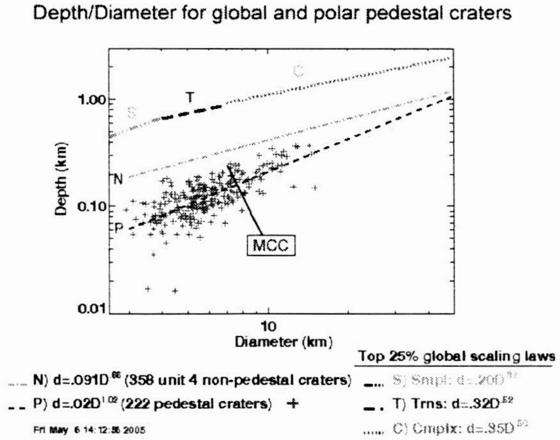

Figure 1. Global d vs D scaling for freshest craters versus population of pedestal craters in northern high latitudes.

MARTIAN CRATER SHAPES: Martian impact craters clearly reflect the interplay of geologic processes associated with erosion by wind, ice, water, volcanism, and tectonics, as reflected in the diversity of their morphologies and states of preservation [1-2]. 3D perspectives from MOLA (MGS) and via stereogrammetry from Mars Express (MEX) have provided a new tool whereby impact craters furnish quantitative boundary conditions in studies of crustal structure, volatile inventories, and sedimentology. And while at a gross scale, the shape or depth and diameter (d vs D) of craters on Mars resemble other planetary environments, at regional scales there exists tremendous variability reflecting a wide range of characteristics associated with the upper most martian crust. Simplified binning of the global geologic units into 8 regionally-connected units allows for more appropriate examination. Near polar units in the northern hemisphere, and to a lesser extent those in the southern near-polar latitudes, display statistically unique scaling properties (i.e, *simple craters* less 7 km : $\mathbf{d = 0.22D^{0.71}}$; *complex craters* 7-70km : $\mathbf{d = 0.68D^{0.17}}$) in comparison with global scaling relationships for all presumably pristine (non-degraded) craters;

Simple: $\mathbf{d = 0.25D^{0.65}}$ $(D < 7\text{ km})$
Complex: $\mathbf{d = 0.33D^{0.53}}$ $(7<D<70\text{km})$
Giant : $\mathbf{d = 3.5D^{0.017}}$ $(D > 70\text{km})$.

Pedestal-style craters within near-polar units are unique as well, apparently reflecting a history of burial and exhumation linked to specific times in the geologic and climatic history of Mars. Such craters display cavity floors that lie above the topographic level of the regional background upon which their preserved ejecta rests. As such, they appear as "pedestals" or "mesa-like" often with monotonically sloping ejecta deposits. We have exhaustively examined over 200 well-preserved pedestals (Fig 1.) in near-polar latitudes (dominantly northern), and across the complex crater diameter range $(5<D<40\text{km})$, such landforms demonstrate a scaling relationship of the form: *Pedestals*: $\mathbf{d = 0.020D^{1.0}}$

The non-degraded complex crater scaling law for the traditional impact features in the same simplified geologic unit as the pedestals is:

Near Polar (N): $\mathbf{d = 0.685D^{0.17}}$

where the difference in exponent (0.17 vs 1.0) between these more shallow than typical (of global complex craters) and the pedestals is reflective of both target properties and erosional history. The essential linear relationship between pedestal depth and diameter D across a size range of 5 to 40km is more akin to simple crater scaling relationships than for any other on Mars. This huge variability reflects the complexities associated with unraveling the full story behind even regional-scale impact crater populations. To first order, the high-latitude pedestal craters appear to reflect a history of post-formational burial and subsequent exhumation that differs strikingly from the freshest impact landforms in the same region. While there remain several tenable "working hypotheses" that explain the formational physics of this population, one particularly attractive possibility may have implications for thick ground-ice within the target at particular times within the geologic record, making craters deepen faster with increasing kinetic energy (D), and allowing more rapid burial due to climate-related forcings, perhaps associated with precipitation or burial by rapidly advancing ground ice. These concepts clearly require further observations, using MRO, the 2008 *Phoenix* near-polar lander mission, and next-decade missions. However, the linkages between aspects of regional cratering history, cratering morphology, crater geometric properties, and the history of volatiles is but one of several scientifically-compelling concepts.

OTHER MORPHOLOGICAL ATTRIBUTES: The advent of global topography from MGS MOLA has augmented an impressive body of analysis of the geomorphic aspects of more than 40,000 martian impact craters, beyond just d and D. In the past five years, analyzes by *Garvin and others* show appreciable evidence of major spatial sub-populations of impact features apparently correlated with target properties and specific erosional histories. The global scaling relationships of these various features is clearly a complicated, non-linear mixture of highlands crater statistics together with drastically different high latitude plains populations.

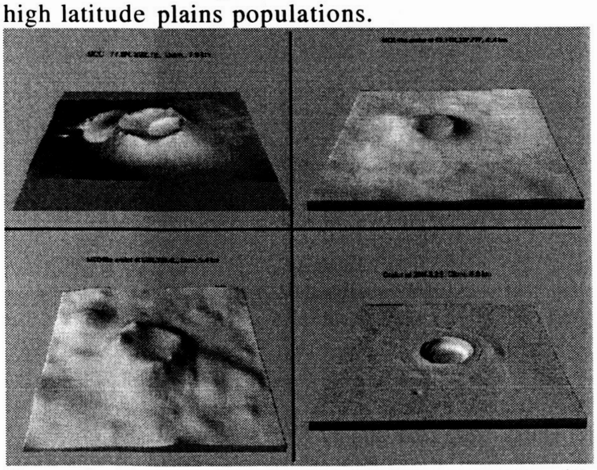

Figure 3: MCC pedestal crater (MOLA+THEMIS) with other high-latitude craterforms.

HIGH LATITUDES: Garvin and colleagues [2] first demonstrated the unique geometric characteristics of non-degraded impact craters in the northern high latitudes (55N to 90N), and interpreted several "pedestal" features as martian lava shields on the basis of early MOLA topography and Viking era imaging. A population of pedestal craterforms has now been examined in detail using sub-km scale MOLA DEM's and MOC and THEMIS imaging, with different conclusions (Figs 1-2). On the basis of geometric properties and their correlation with imaging textures, it is now apparent that the ~ 200 near-polar pedestals represent a unique class of differentially eroded impact craters. One feature in particular, which we original described as a scoria cone [2], is more likely to be a relatively rare form of an exhumed complex crater with ejecta flank slopes that are a factor of 2-3 larger than are most typical, perhaps due to interactions with post-impact formation ice cover. These pedestal craters can be used together with the fresh population to estimate regional erosional volumes as a function of different time intervals.

CONCLUSION: We have explored the geometric properties of the non-degraded global population of well-measured (by MGS MOLA) impact landforms on Mars, ranging from ~2 km to more than 150km. It is evident that global statistical variations are regionally-controlled, given the global complex crater scaling law ($\mathbf{d = 0.33D^{0.53}}$ for d, D in km) varies by geologic unit by large factors. Near-polar region fresh complex impact craters follow a scale law of the form: $\mathbf{d = 0.68D^{0.17}}$, while pedestal craters follow the linear scaling relationship: $\mathbf{d = 0.020D^{1.0}}$ (N=222). Clearly, burial and exhumation processes, perhaps related to climate-induced erosional process variations, have produced a population of landforms from which assessments of regional sediment removal volumes can be estimated. New data from the soon-to-be-launched MRO mission will extend these interpretations and facilitate more quantitative analysis of the impact crater population in the geomorphic history of the planet. Impact craters remain an invaluable, all-natural, probe of the vertical structure of the martian crust, awaiting further scrutiny.

Acknowledgements: This work was made possible via the support of the MGS Science team (MOLA and MOC), and in partnership with James Frawley (Herring Bay Geophysics). We gratefully acknowledge the encouragement of C. Schnetzler, R. A. F. Grieve, M. Malin, J. Boyce, Dave Roddy (*deceased*), and E. J. Weiler in this ongoing work.

References: [1] Barlow N. G. et al. (2000), *JGR 105*, 26733-26738. [2] Garvin J. et al. (2000) *Icarus 144*, 329-352. [3] Mouginis-Mark P. et al. (2005) *JGR*, in press, 26pp.

MARS EXPLORATION ROVER FIELD OBSERVATIONS OF IMPACT CRATERS AT GUSEV CRATER AND MERIDIANI PLANUM AND IMPLICATIONS FOR CLIMATE CHANGE.

M. Golombek[1] J. A. Grant[2], L. S. Crumpler[3], A. F. C. Haldemann[1] and the Athena Science Team. [1]Jet Propulsion Laboratory, Caltech, Pasadena, CA 91109, [2]Smithsonian Institution, Washington, D.C. 20560, [3]New Mexico Museum of Natural History and Science, Albuquerque, NM 87104.

Introduction: The Mars Exploration Rovers have provided a field geologist's perspective of impact craters in various states of degradation along their traverses at Gusev crater and Meridiani Planum. This abstract will describe the craters observed and changes to the craters that constrain the erosion rates and the climate [1]. Changes to craters on the plains of Gusev argue for a dry and desiccating environment since the Late Hesperian in contrast to the wet and likely warm environment in the Late Noachian at Meridiani in which the sulfate evaporites were deposited in salt-water playas or sabkhas.

Gusev Plains: Spirit has traversed a generally low relief somewhat rocky plain dominated by shallow circular depressions called hollows. Hollows are typically 1-20 m in diameter (the smallest observed is 0.4 m), generally have rocky rims characterized by angular and fractured blocks, and smooth soil filled centers. Perched, fractured and split rocks are more numerous around hollows than elsewhere and redder rocks are common near eolian drifts [2]. Hollow morphology and size-frequency distribution strongly argue that they are impact craters rapidly filled in by eolian material. Excavation during impact would deposit ejecta with widely varying grain sizes, which would be in disequilibrium with the eolian regime. This would lead to deflation of ejected fines, exposing fractured rocks, and creating a population of perched coarser fragments. Transported fines would be rapidly trapped within the depressions creating the hollows [2].

Many of the rocks at Gusev show evidence for partial or complete burial, followed by exhumation [2, 5]. These include two-toned rocks with a redder patination along their bases, ventifacts that originate from a common horizon above the soil (suggesting that the lower part of the rock was shielded), rocks that appear to be perched on top of other rocks, and some undercut rocks, in which the soil has been removed from their bases. These observations suggest that surface deflation, perhaps highly localized, of 5 to 60 cm has occurred.

Four craters >90 m in diameter, Bonneville, Missoula, Lahontan, and an un-named crater located to the west of Lahontan, were visited by Spirit. Only Bonneville is relatively fresh. The others have been largely filled in by sediment with diameters of 160 m, 90 m, and 100 m and depths of 3-4 m, 4 m and <1 m, respectively.

Bonneville Crater: Several lines of evidence suggest Bonneville is a relatively fresh crater that was formed into unconsolidated blocky debris [2]. The largest rock increases from 0.5 m to ~1 m to ~2.5 m diameter as the rock abundance increases by a factor of 4-6 from the discontinuous ejecta, through the continuous ejecta to the rim, suggesting a relatively pristine ejecta blanket with a sharp, easily mapped edge. Although the crater is shallow (~10 m deep) the rubble walls show no signs of mass wasting and eolian material deposited inside is limited to 1-2 m thickness by protruding boulders. The low depth to diameter ratio of Bonneville and other small craters in and on its walls suggest that they formed as secondary craters [3, 4].

Meridiani Planum: Far fewer craters have been found by Opportunity at Meridiani Planum due to its relatively young Late Amazonian surface age [6]. A clear progression in the state of modification of the craters by eolian erosion and infilling can be seen in the roughly 10 craters from ~10 m to 150 m in diameter that have been characterized by Opportunity. All of the craters impacted into Late Noachian light toned sulfate rich sedimentary evaporites (exposed in their rims and/or walls).

Three impact craters that were characterized well during the nominal mission are Endurance, Eagle, and Fram, which are 150 m, 20 m and 10 m in diameter and 21 m, 3 m, and 1 m deep, respectively. Fram appears freshest with ejecta blocks on the surface, Endurance retains steep interior walls, and Eagle appears the most degraded with a highly modified shallow sand and granule filled interior.

After Endurance, craters that Opportunity has characterized well prior to arriving in the etched terrain are Naturaliste, Geographe, Vostok, Vega, Viking, and Voyager, which are 11 m, 6.5 m, 50 m, 8 m, 18 m and 18 m in diameter and 2.5 m, 1 m, <1 m, ~0.5 m, 1.5 m, and ~1 m deep, respectively. Two other craters, Jason and Alvin (both ~11 m diameter) were imaged from farther away, but appear similar to Eagle. The smallest craters observed by either rover are 20 cm and 10 cm in diameter (~1 cm and <1cm deep) imaged by Opportunity on sol 433 on the sand, suggesting they are very young.

The freshest craters observed are Vega and Viking, which have ejecta blocks on the surface, blocky raised rims and what appears to be only thin sand in their interiors. Slightly more degraded craters are Fram, Naturaliste, Geographe, and Voyager, which have blocky rims, more sand filled interiors and ejecta blocks on the plain, some of which have been eroded down or planed off even with the sand. Endurance is more degraded with a raised rim, backwasted upper slopes, some sand inside, but no ejecta on the surface (completely eroded away). Eagle, Jason and Alvin are more eroded with more sand filled interiors, eroded rims with some exposed outcrop, but no ejecta. Vostok is the most eroded example as it shows up a ring of light outcrops that have been planed off by the sand sheet with a subdued <1 m central depression (no ejecta or raised rim). Depth diameter ratios and estimates of material filling the craters suggests most are primaries, except for Fram, Vega, Viking, Voyager and the 10 and 20 cm diameter craters, which have low depth/diameter ratios implying they may be secondaries.

Deflation and Erosion Rates: The observed deflation of the cratered plains surface at Gusev is a measure of the cumulative change of the surface since the Hesperian [7]. The gradation and deflation of ejected fines of 5-60 cm and deposition in craters to form hollows thus provides an estimate of the average rate of erosion or redistribution via the vertical removal of material per unit time typically measured on Earth in Bubnoff units (1 B = 1 μm/yr) [8, 9]. The deflation and exhumation of rocks at Gusev suggest of order 10 cm average deflation or redistribution of the site. Deflation and redistribution of a single layer of fines about 10 cm thick would also fill all the hollows and craters. Over the age of the cratered plains (Late Hesperian/Early Amazonian or ~3 Ga [10]) this argues for extremely slow average erosion rates of order 0.1 nm/yr or 10^{-4} B. Such erosion rates fall between those estimated in a similar manner at the Mars Pathfinder landing site (~0.01 nm/yr) [11] and at the Viking Lander 1 site (~1 nm/yr) [12] and argue for very little net change of the surface implying a dry and desiccating environment similar to today's has been active throughout the Hesperian and Amazonian or since ~3.7 Ga [10].

Slightly higher Amazonian erosion rates are implied at Meridiani Planum (and other exhumed Noachian layered rocks on Mars [13]). Geologic mapping relations and the frequency of a population of old degraded craters >1 km diameter, clearly show the Meridiani Planum layered rocks to be Late Noachian in age [6, 14], yet the population of relatively fresh craters on the basaltic sand sheet is much younger, indicating that the entire record of Hesperian craters has been erased. The loss of Hesperian craters suggests at least order 10 m erosion since the Early Hesperian (~3.6 Ga [10]) or >3 nm/yr at Meridiani Planum. These erosion rates are comparable with those derived from the observed erosion and modification of young craters and ejecta by the Meridiani sands. Craters such as Eagle, Endurance and Vostok appear modified with sand filled centers and no ejecta, suggesting erosion of >1 m and <10 m, yielding >3 nm/yr and <30 nm/yr erosion rates during the Late Amazonian or since ~400 Ma [10]. Finally, slightly lower erosion rates (~1 nm/yr) result from the concentration of hematite rich spherules in the upper 1 cm of the sand, which were derived from erosion of ~3 m of the sulfate outcrops [15] in the Amazonian.

Long term average erosion rates this low indicate a dry and desiccating climate similar to today's for the past 3 Ga. An environment in which liquid water is not stable is in accord with the lack of chemical weathering indicated by exposures of basalt and olivine basalt throughout equatorial Mars and in the soils of Gusev and Meridiani (see discussion and references in [16]) and the observed pattern of crater gradation observed at Gusev and Meridiani, which shows no evidence for erosion by liquid water (expected in a wetter environment) [17].

By comparison, erosion rates estimated from changes in Noachian age crater distributions and shapes on Mars are 3-5 orders of magnitude higher [see references in 11] and comparable to slow denudation rates on the Earth (>5 B) that are dominated by liquid water [8, 9]. An estimate of the erosion rates applicable to Meridiani in the Late Noachian just prior to when the evaporites investigated by Opportunity were deposited is estimated at about 8 B from widespread denudation in western Arabia Terra [14]. These rates are 5 orders of magnitude higher than those estimated for the Hesperian and Amazonian cratered plains of Gusev and consistent with the wet and likely warm environment documented in Meridiani Planum during the Late Noachian. A wet environment in the Noachian is also indicated by the strong chemical and mineralogic evidence for aqueous processing of the older rocks of the Columbia Hills at Gusev [18]. The erosion rates from the younger Amazonian Gusev and Meridiani plains as well as those from Viking 1 and Pathfinder strongly limit this warmer and wetter period to the Noachian, pre-3.7 Ga and a dry and desiccating climate since.

References: [1] Golombek M. et al. (2005) *LPS XXXVI*, Abs. 1539; Sub. Nature. [2] Grant J. et al. (2004) *Science 305*, 807-810. [3] Hurst M. et al. (2004) *LPS XXXV*, Abs. #2068. [4] McEwen, A.S., et al. (2005) *Icarus* (in press). [5] Greeley R. et al. (2004) *Science 305*, 810-813. [6] Lane, M. D., et al. (2003) *Geophys. Res. Lett.* 30(14), 1770. [7] Kuzmin R. et al. (2000) *U.S. Geol. Sur. Map I-2666*. [8] Judson S. & Ritter D. (1964) *JGR 69*, 3395-3401. [9] Sanders I. & Young A. (1983) *Earth Surf. Proc. Landforms 8*, 473-501. [10] Hartmann W. & Neukum G. (2001) *Space Sci. Rev. 96*, 165-194. [11] Golombek M. & Bridges N. (2000) *JGR 105*, 1841-1853. [12] Arvidson R. et al. (1979) *Nature 278*, 533-535. [13] Malin, M. C. & Edgett, K. S. (2000) Science 290, 1927-1937. [14] Hynek, B. M. & Phillips, R. J. (2001) *Geology* 29, 407–410. [15] Soderblom, L. A. et al. (2004) *Science* 306(5702), 1723-1726. [16] Christensen P. et al. (2004) *Science* 306(5702), 1733-1739. [17] Grant, J. et al. (2005) *Lunar Planet. Sci XXXVI*, Abs. #1472; Sub. JGR. [18] Ming, D. W. et al. (2005) *Lunar Planet. Sci XXXVI*, Abs. #2125.

FIELD STUDIES OF CRATER GRADATION IN GUSEV CRATER AND MERIDIANI PLANUM USING THE MARS EXPLORATION ROVERS. J. A. Grant[1], M. P. Golombek[2], A. F. C. Haldemann[2], L. Crumpler[3], R. Li[4], W. A. Watters[5], and the Athena Science Team [1]Center for Earth and Planetary Studies, National Air and Space Museum, Smithsonian Institution, Washington, DC 20560, [2]Jet Propulsion Laboratory, California Institute of Technology, Pasadena, CA 91109, [3]New Mexico Museum of Natural History and Science, Albuquerque, NM 87104, [4]Department of Civil Engineering and Remote Sensing, The Ohio State University, Columbus, OH 43210, [5]Department of Earth, Atmospheric, and Planetary Sciences, Massachusetts Institute of Technology, Cambridge, MA 02139.

Introduction: The Mars Exploration Rovers Spirit and Opportunity investigated numerous craters since landing in Gusev crater (14.569°S, 175.473°E) and Meridiani Planum (1.946°S, 354.473°E) over the first 400 sols of their missions [1-4]. Craters at both sites are simple structures and vary in size and preservation state. Comparing observed and expected pristine morphology and using process-specific gradational signatures around terrestrial craters as a template [5-7] allows distinguishing gradation processes whose relative importance fundamentally differs from those responsible for most crater modification on the Earth.

Impact Structures in Gusev Crater: Craters dominate the surficial landscape on the Gusev Plains [2] and most have depth-to-diameter ratios generally <0.10 and possess raised rims and obvious ejecta deposits. Walls bounding the 210 m-in-diameter Bonneville crater (Table 1) are debris-mantled and slope an average 11 degrees, but there is little evidence of down slope movement (e.g. debris chutes or talus). Bonneville is currently only 10-14 m deep, but eolian infilling is generally only a few meters based on observations of protruding rocks. The 163 m-in-diameter Missoula crater and 90 m-in-diameter Lahontan crater located to the south and southeast of Bonneville are even shallower (Table 1) and possess walls sloping only ~6 degrees that are also devoid of talus or debris chutes. Some blocks that partially covering the floor of Missoula are probably ejecta from nearby Bonneville.

Basaltic ejecta around Bonneville, Missoula, and Lahontan craters possess a size and spatial distribution consistent with that expected for pristine deposits [2]. Largest fragments at Bonneville and Missoula, however, are only ~2.5 and ~1.5 meters, respectively, and smaller than the 3.5-10.5 and 2.9-8.6 meter blocks predicted for impact into bedrock [8]. Eolian deposits are local and <50 cm thick, whereas exposed surfaces experienced no more than 10's of cm deflation [9].

Smaller and generally more modified impact structures referred to as hollows (<20 m in diameter) are distributed across the Gusev plains. These craters are mostly sediment-filled and surrounded by abundant fractured and perched rocks [2], though some pristine examples occur.

Impact Structures in Meridiani Planum: Craters explored at Meridiani are fewer and farther between than at Gusev and all are formed into sulfate bedrock [3]. With the exception of the most degraded examples, Meridiani craters have depth-to-diameter ratios >0.10 and preserve walls sloped generally >10 degrees. Endurance crater is 150 m-in-diameter, 22 m deep, and possesses walls sloped between 15-30 degrees, but locally exceeding the repose angle (Table 1). Profiles across Endurance generally display an inflection halfway up the walls corresponding to the occurrence of large rocks. Eagle crater is 22 m-in-diameter, only 3 m deep, and has walls sloping 10-15 degrees and mostly mantled by drift encroaching from the surrounding plains (Table 1). Fram, Geographe, and Naturaliste craters are 10 meter diameter and ~1.1 meter deep, 6.5 meter diameter and ~1.4 meter deep, and 11 m in diameter and ~2.5 meter deep, respectively, and are the only craters retaining visible ejecta. Nevertheless, many ejecta rocks appear planed off at level of the plains and others may be buried.

The most subdued craters are Jason and Alvin, both ~11 m-in-diameter, and the ~45 m-in-diameter Vostok. Drift covers most walls, floor, and the exterior of these craters and minimal rims merge almost imperceptibly with the surrounding plains. Vostok has all but disappeared and is only visible as a low, narrow ring of sulfate outcrop that surrounds a mostly filled and only slightly lower interior.

Gradation Models for Gusev and Meridiani: Many of the craters in Gusev appear to be the result of secondary cratering events. Observed depth-to-diameter ratios are low, there is little evidence that they have been significantly modified by gradation, and forms are most consistent with those expected for secondary craters [10-12]. By contrast, craters in Meridiani are mostly primaries. Current depth-to-diameter ratios are 0.11 to just over 0.2 and most show good evidence for gradation consistent with modification of pristine, primary craters. Fram is the sole candidate for a secondary crater in Meridiani.

Eolian erosion/deposition has dominated at both Gusev and Meridiani since the Hesperian and Amazonian, respectively, and is generally more important in gradation than at terrestrial craters. Nevertheless, significant differences in the amount and range in modification exists between the two sites. At Gusev, crater formation into relatively competent basaltic rubble results in a pristine form that is comprised of more durable basaltic rocks and creates only limited sediments available for transport [2, 13]. By contrast, at Meridiani, crater formation into plains comprised of relatively soft sulfate bedrock and capped by a thin layer of mobile sediments [3] enables eolian stripping of the ejecta, rim, and upper walls that is accompanied by eolian infilling by sediments transported from the surrounding plains. At Endurance, stripping likely accounts for back wasting of at least 5-10 meters of the upper walls and likely creates the inflection noted across blocky talus on the mid wall.

Mass wasting plays a limited role in crater gradation at Gusev and Meridiani relative to Earth, but for different reasons. At Gusev, down slope movement of debris is limited by relatively low wall slopes at even the most pristine craters. At Meridiani, mass wasting is more limited by the higher rate of eolian stripping that removes talus and back wastes to low angles. None of the Martian craters has debris chutes or significant talus associated with mass wasting at terrestrial craters.

At Gusev, impacts occurred in sufficient numbers to account for some modification of pre-existing craters. At Meridiani Planum, the younger Amazonian surface preserves relatively fewer craters, none of which overlap and highlights a gap in the preserved crater record corresponding to the time between the wetter Noachian when the sulfate rocks were deposited and the present dry conditions [13]. Ongoing eolian erosion that continues to modify craters at Meridiani may mostly account for this gap in the crater record.

An absence of evidence for crater modification by water highlights the dry conditions persisting since the Hesperian at Gusev and at least the Amazonian in Meridiani. Analogy with the Earth indicates that signatures associated with appreciable fluvial gradation should persist at these craters if formed [5, 7], but are not present. Small amounts of water at both sites may account for surface coatings and textures, but is not required and did not result in runoff. Instead, craters in these two widely separated locations record a history of dry conditions over much of Martian history that contrasts with the wetter conditions that enabled formation of the sulfates in Meridiani during the Noachian.

Summary: Craters formed on the Hesperian aged floor of Gusev and larger than ~100 m in diameter are generally more pristine than many craters formed on the younger Amazonian aged Meridiani Plains. This conclusion may not be representative of crater gradation across regional landscapes characterized by markedly different landforms and may contradict some interpretations drawn from orbital views. For example, it is difficult to distinguish pristine craters (e.g., Naturaliste) from more degraded craters (e.g., Eagle) in the orbital data and Endurance crater displays a relatively lower albedo deposit of differing radial extent that might be interpreted as ejecta that is not present. Similarly, orbital data may lead to the impression that larger craters (e.g., Bonneville) visited in Gusev are degraded when they are actually fairly pristine secondaries. Results highlight the need for surface and/or higher resolution orbital imaging in order to accurate definition of crater gradation state and processes.

References: [1] Squyres, S. et al. (2004) *Science, 305*, 794-799, 2004. [2] Grant J. et al. (2004) *Science, 305*, 807-810, 2004. [3] Squyres, S. et al. (2004) *Science, 306*, 1698-1703. [4] Haldemann, A.F.C et al. (2004) *7th Mars Crater Consortium*, Flagstaff, AZ. [5] Grant, J.A. (1999), *Int. J. Impact Engin., 23*, 331-340. [6] Grant, J.A. et al. (1997) *J. Geophys. Res., 102*, 16,327-16,388. [7] Grant, J.A. and Schultz, P.H. (1993) *J. Geophys. Res., 98*, 11,025-11,042. [8] Melosh, H.J. (1989), *Impact Cratering*, 245p, Oxford University Press, NY. [9] Greeley, R., et al. (2004) Science, 305, 810-821. [10] Pike, R.J., (1980), USGS Prof. Paper - 1046C, 77p. [11] Hurst M. et al. (2004) *LPS XXXV*, Abs. #2068. [12] McEwen, A.S., et al. (2005) *Icarus* (in press). [13] Golombek, M. et al. (2005) *Nature* (submitted).

Table 1. Selected Observed and Predicted Dimensions for Craters in Gusev and Meridiani Planum

	Observed Crater Dimensions					**Predicted Crater Dimensions[a]**			
Gusev	**Diameter**	**Depth**	**Rim Height**	**Ejecta at Rim**	**Depth/ Diameter**	**Transient Diameter[b]**	**Transient Depth[b]**	**Rim Height[b]**	**Ejecta at Rim[b]**
Bonneville	210 m	10-14 m	4.1-6.4 m	N/A	0.07	176 m	65 m	7.4 m	2.3 m
Missoula	163 m	3-4 m	~3 m	N/A	0.03	137 m	51 m	5.7 m	1.9 m
Lahontan	90 m	4.5 m	~2-3 m	N/A	0.05	77 m	29 m	3.2 m	1.3 m
Meridiani									
Eagle	22 m	2-3 m	0.1-0.7 m	0	0.13	18.5 m	7 m	0.8 m	0.4-0.5 m
Endurance	150 m	21 m	<1-5 m	0-1 m[c]	0.14	126 m	47 m	5.3 m	1.8 m
Naturaliste	11 m	2.5 m	<0.5 m	<0.5 m	0.22	9.2 m	3.4 m	~0.4 m	~0.3 m

[a] Predicted Crater Dimensions Derived Using Equations 1-4

[b] May Be Over-Estimated if Craters are the Result of Secondary Impact Events

[c] Almost all Ejecta is Removed, Only Very Local, Nearest Rim Occurrences Where Preserved Rim is Highest

Volatiles in the Desert: Subtle Remote-Sensing Signatures of the Dakhleh Oasis Catastrophic Event, Western Desert, Egypt.

A.F.C. Haldemann[1], M.R. Kleindienst[2], C.S. Churcher[3], J.R. Smith[4], H.P. Schwarcz, and G. Osinski, [1]Jet Propulsion Laboratory, California Institute of Technology, Mail-Stop 238-420, 4800 Oak Grove Dr., Pasadena, CA 91109, USA, albert.f.haldemann@jpl.nasa.gov; [2]Department of Anthropology, Univ of Toronto, 3359 Mississauga Road North, Mississauga, ON L5L 1C6, Canada, maxine.kleindienst@utoronto.ca; [3] Department of Zoology, Univ of Toronto, Toronto, ON M5S 3G5, Canada, rchurcher@shaw.ca; [4]Earth and Planetary Sciences, Washington Univ in St Louis, Campus Box 1169, One Brookings Drive, St Louis, MO 63130; [5]School of Geography and Geology, McMaster Univ, Hamilton, ON L8S 4L8, Canada; [6]Agence Spatiale Canadienne/Canadian Space Agency, 6767 Route de l'Aeroport, Saint-Hubert, Quebec, J3Y 8Y9, CANADA, gordon.osinski@space.gc.ca.

Introduction: Over the past decade members of the Dakhleh Oasis Project have studied enigmatic signatures in the Pleistocene geologic record of portions of the Dakhleh oasis and palaeo-oasis in Egypt's Western Desert [1,2]. In particular, Si-Ca-Al rich glass melt (Dakhleh Glass, Fig. 1) points to a catastrophic event between c.100,000-200,000 years ago [3] in this well-studied African savannah and freshwater lake Middle Stone Age environment [4,5].

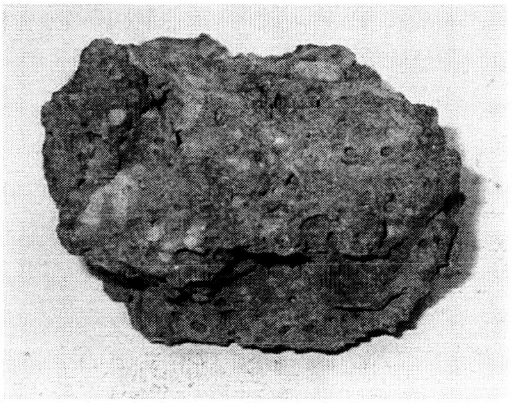

Figure 1. A typical piece of Dakhleh Glass, 4 cm across, from site 397.

The wide extent of glass deposits, over tens of kilometers, may suggest multiple, co-eval impacts or airbursts, or perhaps a record of "high-speed molten ejecta decoupled from the later stages of crater excavation" [6]. Here we report on mapping of remote sensing data (visible, infrared and radar) that is being used to guide wider reconnaissance of the Dakhleh Glass deposits (Fig 2). The remote sensing is anchored on the best-studied element, the Dakhleh Bow Wave Structure (DBWS), where structural elements of a ~400 m cratering event are preserved. These structures are nevertheless highly degraded, and not directly apparent in the remote sensing data. The Dakhleh Glass, while chemically quite unique, is nowhere very extensive, and is thus only a minor constituent in each remote sensing pixel; we attempt to identify its presence by calibrating to the known occurrence locations near the DBWS. Clearly, these subtle remote-sensing signatures of the relatively recent impact(s) into a sedimentary target at Dakhleh, where the erosion rate is estimated at 0.1 mm/yr, underscore the difficulty in accumulating a clear characterization of the range of sedimentary target modifications associated with smaller (100 m - 1 km) terrestrial craters.

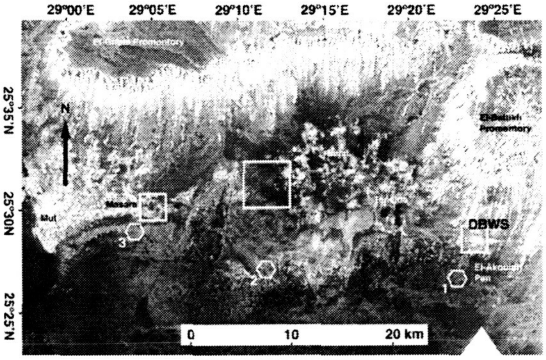

Figure 2. Composite 5-cm wavelength radar image of the Dakhleh Oasis Region, showing the area of Dakhleh Glass at (1) Loc. 211 and the Dakhleh Bow Wave Structure (DBWS) southeast of the oasis. The proposed circular features or 'virtual craters' in the unlabeled boxes located within the oasis proper, and north-east of the Dakhleh Glass occurrences at (2) Loc. 390, and (3) Locs. 397-398, are visible only on the radar imaging. These features may result from meteorite impacts or airbursts, and account for the formation of the glass at these other locations. Images from Shuttle Imaging Radar, SIR-C processing runs 16113 (left) and 16095 (right).

Multiple-impacts or fast glass ejecta: Results from the most recent field season (Smith, 2005, personal communication) tend to discount the idea that the circular feature west of the village of Balat (largest box in Fig. 2, "Balat Bullseye") is a second impact remnant, however new Dakhleh Glass deposits were discovered in the south-west quadrant of the Balat Bullseye. This has led us to consider whether what we are exploring is a remnant of high-speed molten ejecta early in the cratering process when the impactor is obliquely incident (~30°), as reported by [6]. Impact glasses recovered from the Argentine loessoid deposits [7,8] are interpreted to have been generated by this process, and we note the similar mesoscopic aspect of the Dakhleh Glass (Fig. 1) to those samples.

Relevance to Mars: (1) To better understand the role of cratering in the Martian sedimentary record, considering that the study of a new terrestrial crater into a sedimentary target, in particular one with glass ejecta because examples of this are so rare [7], adds a significant increment to the terrestrial analog dataset. This will refine our understanding and expectations for the occurrence of glass among Martian ejecta. (2) the DBWS and associated Dakhleh Glass may be a mappable instance of early molten ejecta, where the relationship of that process to volatiles can be reconstructed from the paleoenvironmental record. (3) The Dakhleh Glass deposits, while apparently widespread are not readily apparent in any remote sensing data down to a resolution of 10 m per pixel, suggesting that studies of the cratering process on Mars will also profit from both higher resolution orbital data as well as future *in situ* studies. (4) Some Dakhleh Glass fragments engulfed extant life at the time of formation, which suggests a tantalizing exobiological possibility for martian glass ejecta.

Discussion: The subtlety of the remnant traces of catastrophe in Dakhleh Oasis need to be explored on the ground; remote sensing can at best serve to guide the exploration. In the Dakhleh Oasis area, which is well-studied by an ongoing multi-disciplinary team we anticipate being able to make a reasonable taphonomic survey of the Dakhleh Glass and thereby reconstruct the ejecta pattern of what may be a unique example of impact process in a sedimentary environment. But to reiterate, the traces on the ground are subtle (Fig. 3), and careful field exploration will be required to tease out the answer to this mystery.

References: [1] M.R. Kleindienst, *et al.* (in press). in: *Oasis Papers IV,* A.J. Mills (Ed.), Oxbow Books, Oxford. [2] Mills, A.J. (2000), Rep. Supreme. Council Antiq., Egypt, 22 pp., www.arts.monash.edu.au/archaeology/dakhleh/. [3] H.P. Schwarcz *et al.* (in press), in The Oasis Papers II, M. Wiseman (Ed.), Oxbow Books, Oxford. [4] C.S. Churcher *et al.* (1999), *Paleo., Paleo., Paleo., 154.* [5] M.R. Kleindienst, *et al.* (2004), *GSA,* Abs. 183. [6] P.H. Schultz and J.F. Mustard (2004), *JGR, 109.* [7] P.H. Schultz *et al.* (1999), *LPSC XXX*, abs. 1898. [8] P.H. Schultz *et al.* (2002) *GSA Spec. Pap.*, *178*, abs. 6.

Acknowledgements: Part of the research described in this paper was carried out by the Jet Propulsion Laboratory, California Institute of Technology, under a contract with the National Aeronautics and Space Administration. We wish to heartily thank the Dakhleh Oasis Project for its encouragement of this work.

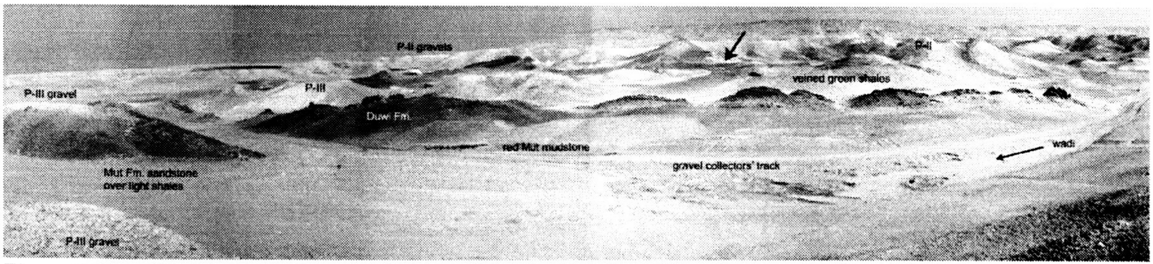

Figure 3. from [1]. West to east composite view of the Dakhleh Bow Wave Structure 'upthrust' feature, as seen from the P-III limestone gravel-capped ridge to the south. Note circular aspect within the veined green shales inside the upthrust (black arrow), which is picked-out by morning light, suggesting that the feature is an eroded impact crater (photo: Kleindienst, Feb., 2004, 11:00 a.m., yellow filter).

IMPACT EROSION OF ATMOSPHERES: SUBSTANTIAL ATMOSPHERIC LOSS BY HORIZONTAL ATMOSPHERIC EXCAVATION.

K. Hamano[1] and Y. Abe[1], [1]Dept. of Earth and Planetary Sci., Univ. of Tokyo (Bunkyo, Tokyo 113-0033, Japan, keiko@eps.s.u-tokyo.ac.jp)

Introduction: Mars exhibits geological evidence of past liquid water on its surface. However, the Martian atmosphere today is too cold and thin for liquid water to exist on its surface. How the atmosphere was lost remains unknown. Several mechanisms have been proposed to account for the decrease of the atmospheric amount, such as formation of carbonate [1] and erosion by atmospheric sputtering [2]. Melosh and Vickery [3] suggested impact erosion of the Martian atmosphere. When impact velocity is sufficiently high, the impactor and a part of the planetary surface around the impact point can vaporize and form "the impact-induced vapor cloud." The vapor cloud has generally high-pressure that it can accelerate the ambient atmosphere with its expansion. When its energy is sufficiently large, some fraction of the atmosphere can be lost, which is called "impact erosion."

Melosh and Vickery [3] estimated the impact conditions for the entire atmospheric loss lying above the tangent plane at the impact point, considering the vapor cloud expansion into vacuum. And they indicated that the significant atmospheric loss was caused by impact erosion on Mars through the heavy bombardment. They used a more sophisticated model to estimate the amount of the atmospheric loss more accurately [4]. The vapor cloud and atmosphere are divided into azimuthal sectors, and the momentum balance within a sector is considered. One can compute the critical zenith angle θ_{esc} that defines the cone-shaped escape region (Fig. 1). Although it is harder to blow off the entire atmospheric mass on the tangent plane, the significant atmospheric loss also occurs with the sector model. However, the effect by the stratified atmosphere is ignored. The validity of their models was examined by Newman et al. [5]. They showed that a strong shock wave was formed in an atmosphere with the vapor cloud expansion and that the shock propagates quite differently from that assumed in the their models. They insisted that the only the atmosphere just above the vapor cloud would escape, and the amount of the atmospheric loss would be a factor ten less than that by the Vickery and Melosh model. However, they don't calculate the amount of the atmospheric loss and the atmospheric escape region, which is defined as initial position of the atmosphere finally lost from the planet.

In this study, we perform numerical simulations using a two-dimensional cylindrical hydrocode and investigate the interactions of the vapor cloud with the planetary atmosphere. The obtained shape of the atmospheric escape region is compared to those by previous works [4, 5]. We also investigate the flow patterns especially around the surface to discuss why the difference in the escape region occurs between the Vickery and Melosh [4] and our study.

Computational Model: We solve fluid equations using the CIP method (Cubic Interpolated Propagation method) [6], which have been applied to various fluid flow problems. It is assumed that all the gases are ideal and their specific heat ratios are constant, respectively. We ignore radiative cooling and assume adiabatic flow. The motion of the gases is described by fluid equations of mass, momentum and energy conservation. The equations about momentum and energy include planetary gravity terms as an external force. The atmosphere is considered to be gravitationally attracted onto the planet. We assume a plane-parallel stratified atmosphere with constant temperature. Thus, the initial atmospheric pressure and density are given exponentially decreasing distributions with altitude. The vapor cloud, which is produced around the impact point, is assumed to be distributed uniformly within a hemisphere centered at the impact point with radius r_v and at rest. We introduce specific length, velocity and pressure scales and normalize the equations and the initial condition. Then we derive four dimensionless parameters as follows,

$$\xi \equiv \frac{R}{r_v},\ \lambda \equiv \frac{R}{H},\ \varepsilon \equiv \frac{e_v}{V_e^2/2} \text{ and } \sigma \equiv \frac{\rho_v(\gamma_v - 1)V_e^2/2}{p_{a0}},$$

where R and V_e are planetary radius and escape velocity. e_v, ρ_v and γ_v are specific energy, density and specific heat ratio of the vapor cloud, respectively. H is the scale height of the planetary atmosphere. The motion of the atmosphere and the vapor cloud is controlled by these parameters.

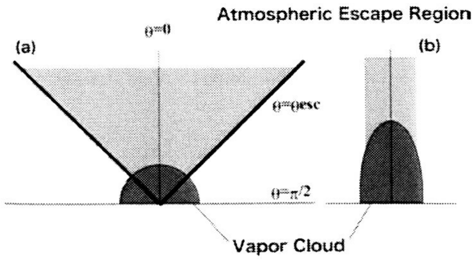

Fig. 1 Schematic illustration of the atmospheric escape region by (a) Vickery and Melosh [4] and (b) Newman et al. [5]. The heavy solid line in (a) shows the critical angle θ_{esc}. For $\theta \leq \theta_{esc}$ the mean velocity exceeds the escape velocity of the planet. The escape region is cone-shaped In contrast, Newman et al. argue the escape region is column-shaped based on the results of their simulations.

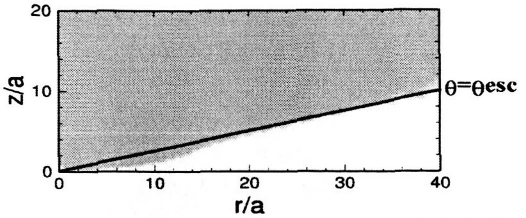

Fig. 2 The atmospheric escape region (shaded zone) obtained by our calculation. The parameters are as follows:ξ=6.4e2, λ_a=5.0e2, ε=1.75 and σ=5.0e5. The solid line shows the zenith angle θ_{esc} obtained by the Vickery and Melosh model.

Comparison of Atmospheric Escape Region: We consider that the gas escapes when its velocity exceeds the planetary escape velocity. The mass of the escaping gas increases with conversion of internal energy to kinetic energy and finally converges to a certain value. We define the final value as "the amount of the escaping gas" which is calculated for the atmosphere and vapor cloud, respectively. It is found by our numerical calculations that the amount of atmospheric loss is larger by a factor than that obtained by the Vickery and Melosh model. We also plot the atmospheric escape region (Fig. 2). The escape region by our code asymptotically approaches that by their model at the small zenith angle θ. On the other hand, the escape region for the lower altitude (large θ) bulges out from the cone determined by the vertex angle θ_{esc}. It increases atmospheric loss significantly because the atmospheric density near the surface is so large.

High-Pressure Region around the Surface: In order to explain the difference in the shape of the escape region, we investigate the flow patterns. Figure 3 shows a representative case of numerical simulations results. Large discontinuity of pressure in this figure represents a strong shock wave formed by a vapor expansion. The ambient atmosphere is accelerated by the passage of the shock wave. During the initial stage, the shock wave propagates preferentially upward – in the direction that the atmospheric density reduces (Fig. 3a). This flow pattern show good agreement with Newman et al. [5] and semi-analytical results (e.g. [7]). A distinctive feature at the later stage is formation of a high-pressure region behind the shock front near the planetary surface (Fig. 3b). Just above the vapor cloud (small θ), the shock wave continues to accelerate and the atmosphere moves away almost radially. In contrast, the shock wave around the surface (large θ) decelerates due to the large inertia of the atmospheric mass. Thus, the most of the shocked mass is concentrated behind the shock and the pressure increases behind the shock front.

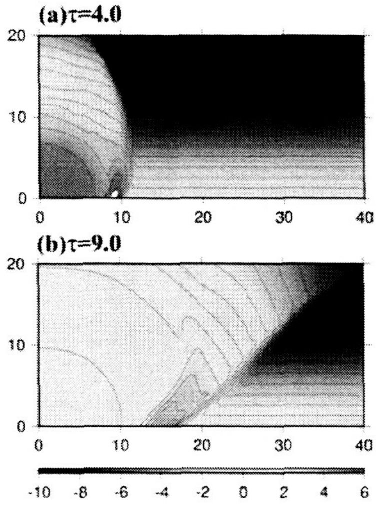

Fig. 3 Snapshots of the motion of the vapor and atmosphere: Contour of logarithm of pressure at dimensionless time (a) τ=4.0 and (b) τ=9.0. The parameters are as follows:ξ=6.4×10^2, λ=5.0×10^2, ε=1.75 and σ=5.0×10^5.

The high-pressure region explains the difference in the shape of the escape region between Vickery and Melosh [4] and our study. The atmosphere around the surface is hard to escape In the Vickery and Melosh model because it has large mass within a sector and large momentum is necessary to move it away radially. Our numerical results show quite different flow patterns from that assumed in Vickery and Melosh [4] around the surface. The formation of the high-pressure region involves the large pressure gradient, which changes the direction of the atmospheric flow upward in and behind the high-pressure region. Consequently, the atmosphere also is excavated horizontally and the amount of the atmospheric loss is larger than obtained from the Vickery and Melosh model.

Summary: The interaction of the impact-induced vapor cloud with the ambient atmosphere has been computed using our hydrodynamic code. The flow at the early stage is consistent with the results in Newman et al. [5]. On the other hand, at the later stage the atmosphere near the surface is accelerated upward due to the formation of the high-pressure region. It results in the atmospheric escape region as shown in figure 2. The horizontal extension of the escape region is not seen the previous studies. Considering the exponential density distribution, it has the significant effects on the impact erosion.

References: [1] Pollack J. B. et al. (1987) *Icarus*, 71, 203-224. [2] Luhmann J. G. et al. (1992) *Geophys. Res. Lett.*, 19, 2151-2154. [3] Melosh H. J. and Vickery A. M. (1989) *Nature*, 338, 487-489. [4] Vickery A. M. and Melosh H. J. (1990) Special Paper Series 247, 289-300, Geol. Soc. Am. [5] Newman W. I. et al. (1999) *Icarus*, 138, 224-240. [6] Yabe T. (1991) *Computer Physics Communications*, 66, 219-232. [7] Laumbach D. D. and Probstein R. F. (1969) *J. Fluid Mech.*, 35, part 1, 53-75.

Martian Megaregolith Properties: Effects on Launch of SNCs and Secondary Ejecta

W. K. Hartmann Planetary Science Institute, Tucson AZ 85719. hartmann@psi.edu

Martian megaregolith in Noachian terrains is likely to be deep granular material impregnated with ice and perhaps also weakly bonded by salts and evaporites. Such material is very inefficient in launching solid rocky debris. This is confirmed by observations of Barlow, who shows that fresh 10+ km craters in older upland have fewer secondary craters than similar sized craters in Amazonian lava plains. This is also supported by the theoretical models of Melosh, Pierazzo, and others, who show that coherent rock in the near-surface spallation layer is needed to facilitate launch of high velocity materials. More work is needed on (1) what depths of granular material atop the coherent rock layer inhibits spallation by dissipating energy, and (2) the role of sub surface ice in causing "steam blast" explosion that my inhibit the launch of rocks. There are many ramifications for Martian meteorite statistics, the production of secondary craters on Mars, the shape of the total production function curve for primaries + secondaries at small diameters, and the use of small craters for surface dating.

INFERENCES FROM OBLIQUE IMPACT CRATERS ABOUT THE ROLE OF THE ATMOSPHERE AND SUBSURFACE VOLATILES IN THE IMPACT CRATERING PROCESS ON MARS

R. R. Herrick, Geophysical Institute, University of Alaska Fairbanks, 903 Koyukuk Dr., Fairbanks, AK 99775-7320 (rherrick@-gi.alaska.edu).

Introduction: Comparison of the ejecta blankets from Martian low-angle impact craters with those on Venus, the moon, and from small-scale experiments suggests that the Martian ejecta are emplaced ballistically and then flow due to the presence of volatiles within the ejecta blanket.

Some relevant observations from experimental, lunar, and venusian craters: On the moon and for experimental impacts in a dry vacuum the ejecta is emplaced ballistically and follows a fairly well-behaved power-law dropoff in thickness away from the rim. In the presence of a dense atmosphere, such as occurs on Venus, the material ejected from the crater gets caught up in a turbulent cloud and is emplaced in something akin to pyroclastic flows [1].

The general variation in ejecta pattern and crater shape with decreasing impact angle on the moon matches well with experimental work conducted in a vacuum [2,3]. For impact angles < ~45 degrees, the ejecta blanket becomes asymmetric. Starting at angles of 20-30 degrees, an area uprange of the crater develops that has no ejecta (a "forbidden zone"). The shape of the forbidden zone is an outward curving "V" with its apex at the crater rim. Coincident with the formation of the forbidden zone is a depression of the uprange rim. As the impact angle becomes more oblique, the amount of ejecta downrange decreases, and the rim topography begins to become saddle-shaped, or depressed in both the uprange and downrange directions. Between 5 and 10 degrees there is an abrupt transition to a complete lack of downrange ejecta (a second forbidden zone), creating a "butterfly" pattern. This downrange forbidden zone is a straight-edged wedge that is always a wider angle than the uprange forbidden zone. There is also a narrow ray extending from the crater wall through the downrange forbidden zone that we interpret as ricocheted impactor material.

In agreement with experimental work, the presence of an atmosphere on Venus significantly increases the onset angle of oblique impact phenomena in the ejecta pattern, and no downrange forbidden zone occurs at low impact angles [1,3].

What happens on Mars: All but the smallest Martian craters have their ejecta emplaced as ramparts, indicative of at least some surface flow of material, and consequently some role for volatiles. Although emplaced as ramparts, the planforms of Martian ejecta blankets more closely resemble those for craters formed in a dry vacuum as opposed to the Venusian craters. As impact angle decreases, the "curving V" forbidden zone appears uprange and the extent of downrange ramparts decreases. At the lowest impact angles there is an abrupt transition to a downrange straight-edged forbidden zone in the ramparts. Unlike the dry-vacuum craters, Martian craters maintain an elevated uprange rim at even the lowest impact angles. The downrange rim appears "blown out" by ricocheted material for the lowest angle impacts, but no Martian craters were observed that preserve a downrange ray, perhaps because this feature is easily eroded on Mars.

The impact angles that the various transitions occur at for Martian craters are similar to those observed under dry vacuum conditions as well.

The similarity in ejecta patterns between the Martian rampart craters and the ballistically emplaced dry-vacuum craters suggests that Martian crater ejecta are first ballistically emplaced. Ramparts then form as a result of modest, post-emplacement flows that preserve the basic ejecta planform.

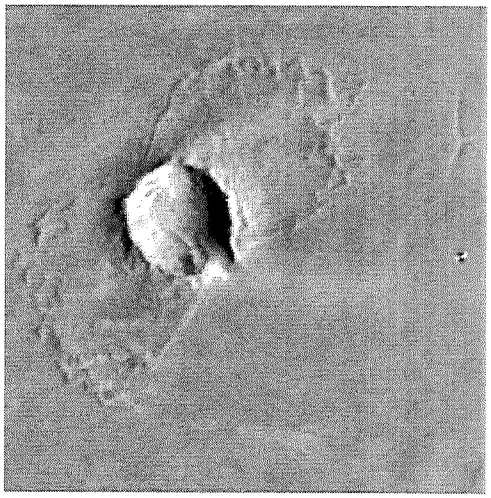

Figure 1. ~13 km crater at 9.2N, 80.4W

The apparent degree of post-emplacement flow does vary, however. For example the crater in Figure 1 preserves a planform that is remarkably similar to highly oblique "butterfly ejecta" impacts in a dry vacuum, but the crater in Figure 2 has a planform where the uprange forbidden zone seems distorted by significant rampart flow.

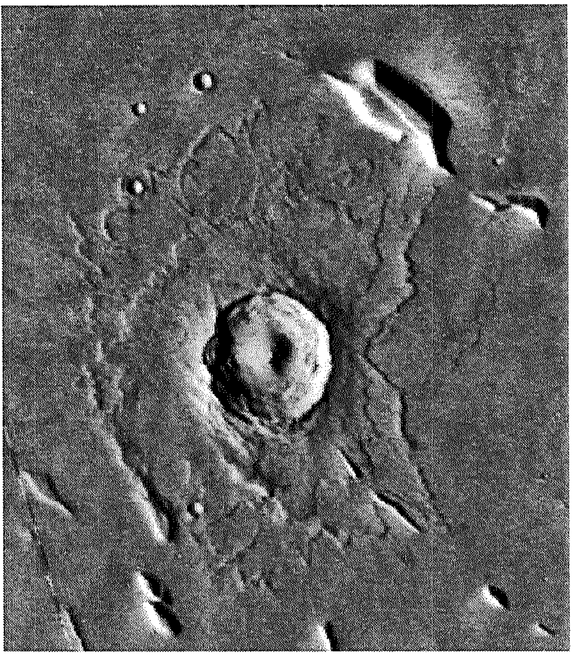

Figure 2. ~16 km crater at 18.2N, 199.2W

References: [1] Schultz P. H. (1992) *JGR, 97,* 16,183-16,248.[2] Gault D. E. and Wedekind J. A. (1978) *Proc. LPSC 9th,* 3843-3875. [3] Herrick R. R. and Forsberg-Taylor N. K. (2003) *Met. and Plan. Sci., 38,* 1551-1578.

CHESAPEAKE BAY IMPACT STRUCTURE: MORPHOLOGY, CRATER FILL, AND RELEVANCE FOR IMPACT PROCESSES ON MARS.

J. Wright Horton, Jr.[1], David S. Powars[1], Gregory S. Gohn[1], and Jens Ormö[2], [1]U.S. Geological Survey, MS 926A, Reston, VA 20192 USA (whorton@usgs.gov), [2]Centro de Astrobiología, INTA/CSIC, Madrid, Spain (ormo@inta.es)

Introduction, structure, and morphology: The late Eocene Chesapeake Bay impact structure (CBIS) on the Atlantic margin of Virginia (Fig. 1) may be Earth's best preserved large impact crater formed in a shallow marine, siliciclastic, continental shelf environment [1]. This complex crater has special features that may be useful analogs for features of layered-target or wet-target craters on Mars [2]. The CBIS formed in a layered target of water (maximum depth 340 m), weak clastic sediments (400 to >750 m thick), and crystalline rock. It is well preserved beneath ~150 to 400 m of postimpact sediments. The buried structure has the form of an inverted sombrero in which a central crater (~38 km wide, ~1.6 km deep) in the crystalline basement and overlying sediments is surrounded by a flat-floored brim known as the annular trough (~85-km wide) [3]. The central crater has a relatively steep outer margin, and it contains an elliptical moat that encircles a broad central uplift (Fig. 2) [4,5].

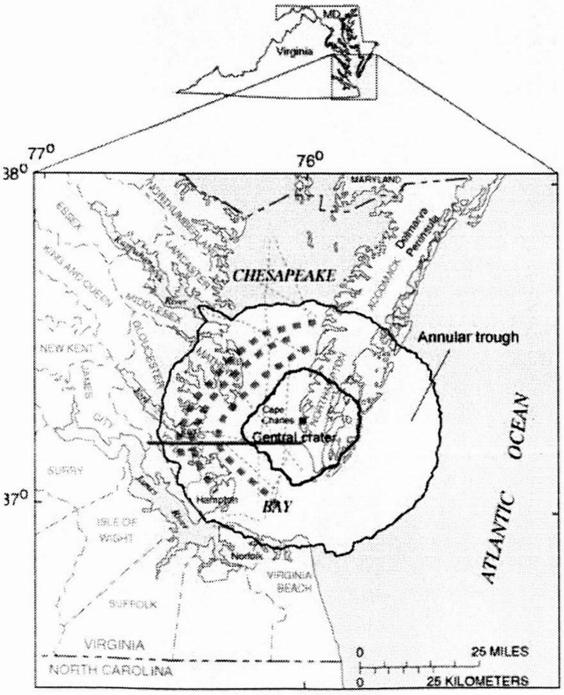

Figure 1. Location of Chesapeake Bay impact structure. Structural rings – heavy dotted lines; seismic tracks – thin dashed lines. Red line shows location of cross section in Figure 2. Adapted from [6,7].

The annular trough is a prominent feature of the CBIS, and it formed by the extensive collapse of thick, poorly consolidated sediments. The collapse expanded the structure to a diameter far exceeding the transient cavity, likely better expressed by the nested central crater (Fig. 2). Large-scale block slumping of sediments along numerous small-displacement faults in the annular trough resembles slumping in the chaotic terrains on Mars. Martian chaotic terrains may have formed by fluidization of stratified material due to catastrophic melting of ground ice and rapid dissociation of clathrates [8].

Seismic profiles across the annular trough suggest that extensional collapse structures (0.5 to 3.9 km wide) are concentrated in structural rings that partly coincide with impact-generated compressional structures in the basement (Fig. 1) [7]. These concentric collapse structures also coincide with the zones of greatest postimpact subsidence in the annular trough.

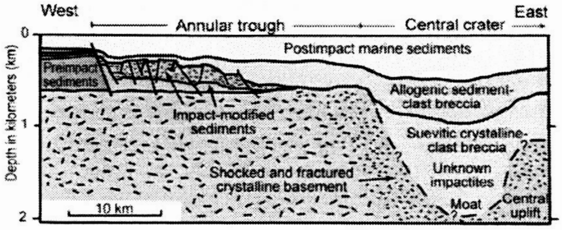

Figure 2. Interpretive cross section of Chesapeake Bay impact structure along line shown in Figure 1, ×10 vertical exaggeration; modified from [9].

Crater-fill materials: Impact-generated crater-fill materials (impactites) in the CBIS include suevitic crystalline-clast breccia and megablocks in the central crater, impact-modified autochthonous to parautochthonous sediments in the annular trough, and allogenic sediment-clast breccias deposited over the entire structure and nearby areas.

Suevitic crystalline-clast breccia. The suevitic crystalline-clast breccia [4,5] consists of metamorphic and igneous rock fragments and less abundant particles of impact-melt rock. It contains megablocks of brecciated crystalline rock and is interpreted as a fallback deposit. Drill core recovered from the central uplift shows pervasive hydrothermal alteration (chloritization and albitization).

Impact-modified sediments. Impact-modified sediments in the annular trough include block-faulted

Lower Cretaceous fluvial target sediments that have been locally fluidized in their upper part; these are overlain by collapsed blocks of parautochthonous Lower and Upper Cretaceous sediment disrupted by faults, fluidized sands, fractured clays, and zones of injected sediments that include exotic, disaggregated Upper Cretaceous and lower Tertiary target sediment particles [1]. Deformation increases upward. This impact-modified section formed in response to acoustic-wave vibrations and subsequent gravitational collapse [1].

Allogenic sediment clast breccias. The allogenic sediment-clast breccias consist of mixed-age clasts in a muddy quartz-glauconite sand matrix [1,3]. These breccias range in thickness from 8 to 400 m and overlie the other impactites and preimpact deposits. They are interpreted to be subaqueous deposits of ocean-resurge debris flows [1] that have been influenced by turbulence, current oscillations, and tsunamis [3]. The sediment-clast breccias fine upward into fine sand and silt interpreted as late-stage resurge deposits. These uppermost resurge deposits grade continuously upward into postimpact marine sediments. There has been no subsequent erosion of crater-fill deposits.

Morphology-material associations: The central and outer parts of the CBIS inverted-sombrero contain different crater-fill materials. Suevitic breccia has been found only in the central crater [4,5], and the fluidized, collapsed sediments have been found only in the brim or annular trough [1]. The allogenic sediment-clast breccia (ocean-resurge deposit) overlies the other impactites and covers the entire structure [1,3]. If found on Mars, resurge sediments would demonstrate a significant surface-water column at the time of impact. However, suevitic breccias or fluidized, collapsed sediments could form in volatile-rich targets on Mars with or without the presence of surface water. An inverted-sombrero-like circular depression, significantly wider than the initial transient crater, may be possible for Martian impacts where near-surface preimpact sediments are thick and contain volatiles or significant pore-fluid pressures. Wide-brimmed impact structures are associated with chaotic terrains in several places on Mars (Fig. 3). Commonly, these structures have an interior chaotic terrain and steep outer margins. Whether the collapse occurred in connection with the impacts or long afterward is undetermined.

Hydrothermal alteration: Hydrothermal alteration is conspicuous in suevitic breccia and megablocks of the CBIS central crater [4,5] but absent or of locally equivocal occurrence in collapsed sediments of the annular trough. If some Martian impact structures have been enlarged by the collapse of weak, near-surface sediments as in the CBIS, the analogy would predict a relatively wide outer brim that is free of hydrothermal alteration.

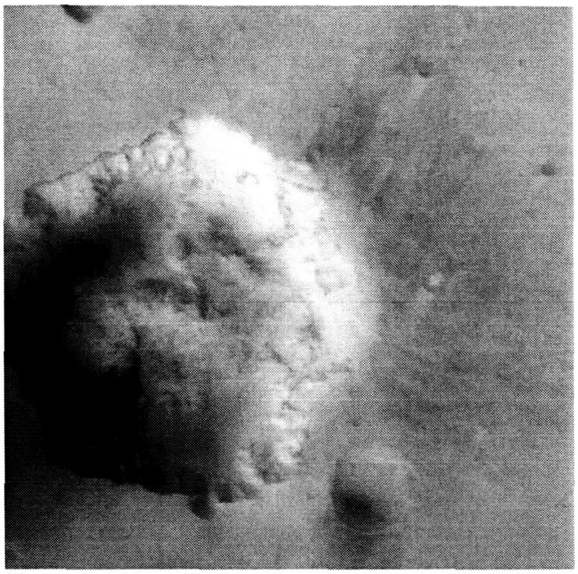

Figure 3. Mars Orbiter Camera (MOC) image showing a crater that expanded due to collapse. The structure (~78 km wide) is located in the Coprates region of Mars. This region is dominated by chaotic terrain, possibly formed by the collapse of a thick, volatile-rich permafrost layer, and associated outflow channels. The collapse may related to block slumping and fluidization of sediments due to rapid dissociation of volatiles (clathrates?) in the upper crust [8]. MOC wide-angle image R10-02030 courtesy of Malin Space Science Systems [image center 52.05W, 2.91S].

References: [1] Horton J. W. Jr. et al. (2005) *GSA Spec. Paper 384*, 147-170. [2] Ormö, J. et al (2004) *M&PS 39(2)*, 333-346. [3] Powars D. S. and Bruce T. S. (1999) *USGS Prof. Paper 1612*, 1-82. [4] Horton J. W. Jr. et al. (2004) *GSA Absts. with Progs. 36(5)*, 266. [5] Horton J. W. Jr. et al. (2005) *LPS XXXVI*, Abstract #2003. [6] Edwards L. E. and Powars D. P. (2003) Palaios 18(3), 275-285. [7] Powars, D. S. et al. (2003) *Third Int. Conf. on Large Meteorite Impacts, LPI Contribution 1167*, Abstract 4053. [8] Komatsu, G. et al. (2000) *LPS XXXI*, Abstract #1434. [9] Powars, D. S. et al. (2004) *USGS Open-File Report 2004-1016*, 76-77.

RIM BREACHING AND PONDING IN MARTIAN IMPACT CRATERS.

R. P. Irwin III[1], [1]Center for Earth and Planetary Studies, National Air and Space Museum, Smithsonian Institution, MRC 315, 6th St. and Independence Ave. SW, Washington DC 20013-7012, irwinr@si.edu.

Introduction: Many degraded impact craters and intercrater basins received drainage from valley networks on early Mars, but the occurrence of paleolakes in most of these basins remains uncertain. Deltas are rare, and the lithology and stratigraphy of most of the low-gradient basin plains are unknown. However, the geomorphic context, topographic setting, and morphology of these breached craters offer insight into an ephemeral fluvial/lacustrine system.

Geomorphic Context: Adjacent Noachian impact craters often exhibit diverse states of degradation. Where superposition relationships are evident, the younger crater is generally better preserved than its predecessor, unless the younger crater is considerably smaller and therefore more rapidly filled. These relationships demonstrate that crater degradation was a prolonged process that occurred over at least the duration of the Middle and Late Noachian Epochs, possibly extending into the Hesperian Period [1] (~250 Ma [2]). Despite this longevity, denudation rates on early Mars [1] were 1–2 orders of magnitude lower than the terrestrial average of ~65 m/Ma [3], suggesting a relatively arid paleoclimate by terrestrial standards even during the warmer, wetter epochs. Martian valley networks have sparsely dissected interfluves, and the drainage basins are poorly graded relative to terrestrial counterparts [4–6]. These conditions are not favorable for long-term paleolake development in most highland basins, although water may have collected in regional lows between episodes of valley activity.

Topographic setting of breached impact craters: Both visible impact crater rims and longer-wavelength, higher-amplitude topography influenced flow paths on early Mars, such that water and sediment were transported toward craters located on drainage basin floors and away from craters on broad ridges. Degraded crater morphology thus depends in part on whether the impact occurred on a ridge, slope, or valley bottom [7]. Upturned rims initially directed external flows away from a crater, producing radial centrifugal drainage patterns [4]. These ridges were lowered over time primarily by retreat of the steep interior wall [1,8], but also by erosion of the ejecta and, in some cases, deposition upslope of the rim. The resulting rimless craters frequently captured drainage from the surrounding uplands, increasing their rate of infilling. Large impacts on broad valley floors could dam a regional flow path, forming an enclosed upslope basin. Some craters in this topographic setting were breached prior to substantial rim degradation, presumably as water filled the shallow upslope basin and overflowed the rim. In other cases, the newly-formed intercrater basin accumulated a low-relief sedimentary or volcanic plain without collecting enough water to overtop the crater rim. The occurrence of both breached and intact crater dams suggests that water supply was limited in upland drainage basins, but that appropriate runoff production relative to terminal basin area was available in some locations to allow breaching of intact rims.

Exit breaches: Some of the craters that received external drainage through an entrance breach also developed an exit breach or outlet, allowing water to flow through the crater. Such craters often retain a shallow, undissected basin on the crater floor between the contributing and outlet valleys, suggesting the possible occurrence of ephemeral paleolakes. Less often, a crater exhibits an outlet valley without an entrance breach. In some cases (Fig. 1), a stable, elevated outlet breach formed and was later entrenched, leaving terraces in the outlet valley. The stability of the outlet at the terrace level may have been maintained by shedding of material from the valley sidewalls at a rate comparable to downslope transport. This would be possible in an environment where throughflow is rare, but less voluminous runoff is available to attack steep slopes.

Deltas in Breached Impact Craters: Our survey of deltas reported in prior literature [8–13] confirms the conclusion of Malin and Edgett [9] that "no discernable expression of deposition" occurs at most sites where deltas have been reported. We have been able to locate or relocate only 23 well-preserved, valley-terminal deposits with an outer scarp, a feature that requires standing water or basal erosion [14]. The crater in Fig. 1 exhibits no delta, despite having a large contributing area and an outlet that occurs well above the elevation of the crater floor. Although deltas have been found in some Martian craters, they are rare and require flows of only centuries to millennia in duration [15]. These deltas do not have dissected surfaces, however, which generally occurs when water levels decline in a terminal basin. These observations suggest that deltas formed during a brief period of intense flows relatively late in Martian history. Earlier conditions may have been characterized by more intermittent or low-intensity flows.

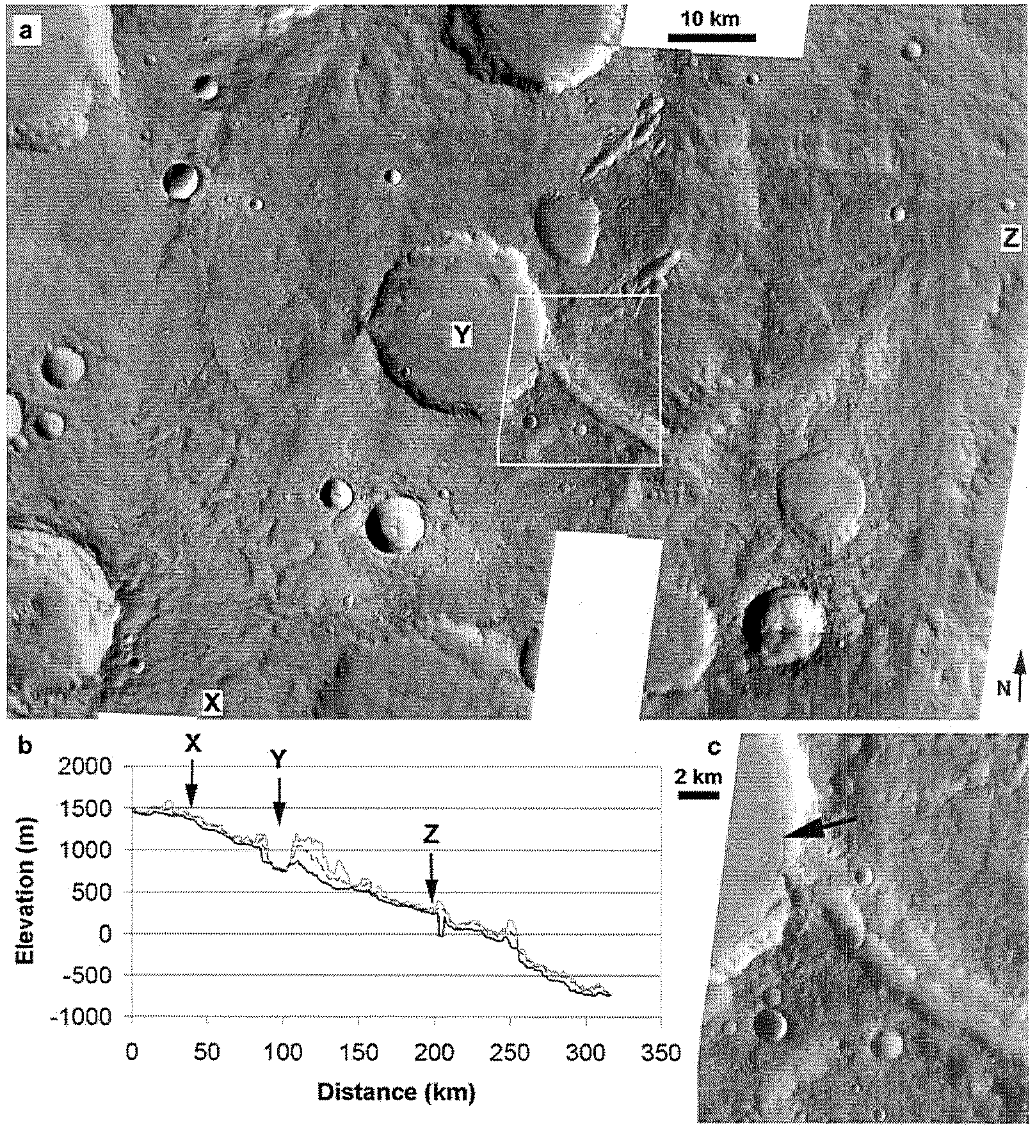

Figure 1. A breached 25 km crater in Terra Sirenum (18.3°S, 169.2°W). (a) Context mosaic of THEMIS visible imaging. The flow direction was from X to Y to Z, and the white box indicates the inset in 1.17c. The valley's longitudinal profile is modified by fresh crater ejecta near X. (b) Longitudinal profile of the valley from MOLA shot data. The black line is the thalweg, the gray line is the exterior surface, and the dashed line shows the elevation below which 75% of the MOLA shots are located (given to approximate the terrace elevation within the outlet valley). Note the grading of the inlet valley to the terrace level and the remnant basin below the level of the entrenched outlet. (c) The terraced outlet valley of this crater, enlarged from 1.17a. The black arrow indicates a ridge at the outer edge of the crater floor.

References: [1] Craddock R. A. and Maxwell T. A. (1993) *JGR, 98*, 3453–3468. [2] Hartmann W. K. and Neukum G. (2001) *Space Sci. Rev. 96*, 165–194. [3] Knighton D. (1998) *Fluvial forms and processes: a new perspective*, Arnold, London. [4] Pieri, D. C. (1980) *NASA TM-81979*, 1–160. [5] Luo W. (2002) *JGR, 107*(E10), 5071, doi:10.1029/2001JE001500. [6] Stepinski T. F. and Coradetti S. (2004) *Geophys. Res. Lett., 31*, L15604, doi:10.1029/2004GL020359. [7] Irwin R. P. and Howard A. D. (2002) *JGR, 107*(E7), 10.1029/2001JE001818. [8] Grant J. A. and Schultz P. H. (1993) *JGR, 98*, 11,025–11,042. [9] Malin M. C. and Edgett K. S. (2003) *Science, 302*, 1931–1934. [10] Cabrol N. A. and Grin E. A. (1999) *Icarus, 142*, 160–172. [11] Ori G. G. et al. (2000) *JGR, 105*, 17,629–17,641. [12] Cabrol N. A. and Grin E. A. (2001) *Icarus, 149*, 291–328. [13] Pondrelli M. et al. (2004) *LPS XXXV*, Abstract #1249. [14] Irwin R. P. et al., *JGR*, submitted. [15] Moore J. M. et al. (2003) *Geophys. Res. Lett.*, 30(24), 2292, doi:10.1029/2003GL019002.

IMPACT CRATERING AND MATERIAL MODELS: SUBSURFACE VOLATILES ON MARS.

B.A. Ivanov[1], N.A. Artemieva[1], and E. Pierazzo[2], [1]Institute for Dynamics of Geospheres, Moscow (nata_art@mtu-net.ru; baivanov@idg.chph.ras.ru); [2]Planetary Science Institute, Tucson (betty@psi.edu).

Introduction: Besides Earth, Mars is the only planet that shows presence of subsurface water/ice/brine. Volatiles change the properties of crustal rocks and affect the impact crater formation process. Spatial and temporal variations of volatiles phase state in the Martian crust make impact crater morphology a valuable tool to obtain insights into crust mechanical properties. However, much work must still be done to translate cratering data into water/ice content and its variation with depth.

Upper crust as a target for impact cratering: Mars' upper crust is believed to have been brecciated during the late heavy bombardment period. Over the next 4 Gyr, the brecciated autochthonous rocks may have been covered by ejecta, volcanic, aeolian, and even marine/lake sediments. In all these rock types porous space may be filled with water (brine) or water ice depending on the local pressure-temperature conditions [1]. Cratering mechanics is affected by target material's density, compressibility, initial strength, and on the dissipative properties (internal friction, effective viscosity) of fragmented material involved in the crater-forming motion. The presence of ice at some depth in the target may influence cratering in two opposite directions: low-temperature ice in permafrost layers increases the strength of porous rocks, while possible shock melting of ground ice overall decreases the rock's strength/friction.

Temperature and pressure gradient: The Martian heat flux is not known. Generally, it is estimated to be ~30 mW m^{-2} [1]. Under many assumptions, the heat conductivity can be estimated to be ~2 W m^{-1} K^{-1} [1], and the resulting near-surface thermal gradient ~15 K km^{-1}. Based on simple estimates of lithostatic equilibrium, pressure in the porous space of the upper 10 km of Martian crust grows from atmospheric pressure at the surface (~600 Pa) to ~100 MPa [1]. The temperature also grows by ~150 K from the surface mean annual value (~150 to 170K at high latitudes and 210 to 220K at low latitudes).

Water/ice content: Based on a model Martian hydrosphere [1] there are various possible saturation states for crustal rocks: (i) upper layer saturated with ice existing only at high latitudes (low T, low ambient pressure); (ii) dry (desiccated) layers at low latitudes; (iii) water-saturated low horizons (T above freezing point of water/brine); (iv) possible intermediate layer of dry porous rocks, when the total water column does not fill all the porous space. Any realistic impact modeling requires reasonable estimates of rock strength for all listed layers (Fig. 1).

Fig. 1. Possible strength profiles for the Martian crust.

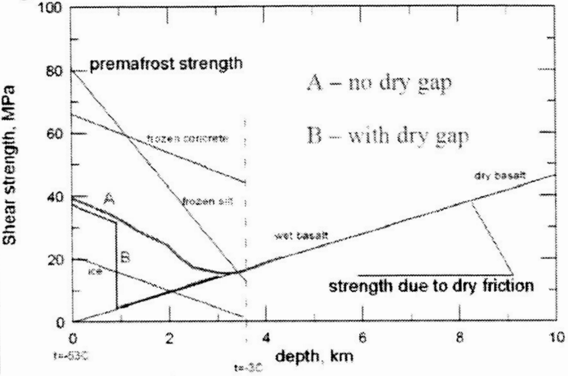

Rock and water EOS. Numerical modeling of impact cratering on Mars and icy satellites to date exploit simple ice equations of state (EOSs; e.g., Tillotoson or ANEOS – [2-4]). These EOSs provide a relatively true pressure/compression description. However, they are unable to *a)* properly describe high pressure ice polimorphs, *b)* model the decrease in ice I melting temperature with increasing pressure, and *c)* describe the higher density of liquid water compared to ice. An additional complication for permafrost is that compression of ice inclusions in rocks is more complex than that in simple planar wave experiments on pure ice normally used to estimate shock melting pressure for ice (e.g. [5]). In the case of ice inclusions in rocks, kinetic effects control the ice compression (c.f. [6]) and multiple shocks increase the characteristic time of compression. The multiphase ANEOS-based tabular water/ice equation of state [7] is a step forward to more accurate estimates of permafrost shock loading and eventually shock melting (Fig. 2).

Impact Shock Melting: Mixed materials in the target may affect shock propagation and consequently the final estimate of melting. When the target is a mixture of materials with very different impedances, as is the case for rocks and water, the shock wave propagation may be affected by the interaction of the original shock wave with shocks reflected at material boundaries (e.g., see [8]). In shock events it is only the first shock that heats the material, while secondary reflected shocks increase the final shock pressure, with a minor contribution to the temperature and entropy. As a result, single- and multiple-shocked materials experiencing the same peak shock pressure will reach substantially different thermodynamic states, with the multiple-shocked material having lower shock temperature and shock entropy. Therefore, for mixtures of materials with very different impedances the maximum shock pressure alone may not be the best criterion for estimating melting and vaporization. In particular, the resulting shock pressure for melting of ice filling voids in rocks may be much higher than for pure ice (Fig. 2). Shock reverberation also controls the shock wave decay in a permafrost target.

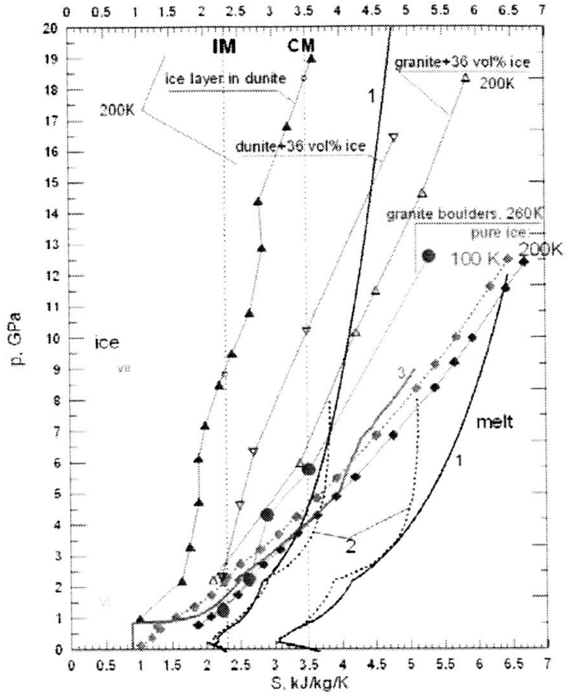

Fig. 2. Pressure-Entropy plot showing maximum shock pressure for incipient and complete melting from multiphase ice EOS [7], *black curves marked with 1*, and a compendium of experimental data from [5] (which used older data for ice VII melt), *black dashed curves marked with 2. Solid diamonds:* shock entropy for pure ice (no strength effects) derived from the multiphase ice EOS at T= 100K (*red*) and 200K (*blue*). *Solid red line marked by 3:* estimates for pure ice at 100K from [5]. Curves with triangles represent numerical modeling results for planar shock compression of multiphase ice using SALEB. *Solid triangles*: ice layer at 200K sandwiched between two dunite plates. Reverberation of the shock wave cause incipient melting of ice in fractures at ~9 GPa. *Upward and downward open blue triangles*: ice/granite and ice/dunite permafrost with 36% of ice by volume at 200K. *Purple circles*: cylindric granite rods with ice filled gaps at 260K. All permafrost model data show increase of incipient and complete shock melting pressure in rock/ice systems compared to pure ice.

Icy crust strength. Due to the dependence of strength on strain rate and the structure of ice, strength data for pure ice are characterized by a relatively large scatter. However, the data show clearly that ice strength grows approximately 5 to 10 times when temperature decreases from the melting point (273K) to ~150K, and then remains approximately constant for lower temperatures. For permafrost, strength depends on temperature (increasing with decreasing temperatures) and size-frequency distribution of rock/soil particles (reflecting the available particle surface that can absorb liquid water). In general, permafrost strength follows the ice strength trend. For many materials strength is 1.5 to 2 times larger than pure ice strength at the same temperature. After failure, broken material behave as a Coulomb material with the friction coefficient depending on ice content (i.e. on rock porosity). For high ice content friction is close to pure ice values, thus about one half the dry friction of rocks. For stress state invariants of shear $T_s=\{[(\sigma_1-\sigma_2)^2+(\sigma_1-\sigma_3)^2+(\sigma_2-\sigma_3)^2]/6\}^{1/2}$ and pressure $p=(\sigma_1+\sigma_2+\sigma_3)/3$ the friction coefficient (T_s/p) for rocks is ~0.7, versus ~0.5 (at low p) to ~0.2 (for $p\geq$ ~20 MPa) for pure ice [9,10]. However for large strains and strain rates the dynamic friction of ice is a complicated dynamic process, which includes possibly shear melting (e.g. [11]).

Perspectives: There is no single incipient and complete shock pressure for shock melting of ice in permafrost. These values depend on dry rock porosity and on the shape of the ice inclusions. Initial numerical modeling with the new multiphase EOS for water/ice looks promising for the study of permafrost shock melting. Depending on latitude, the volatile-rich crust can be represented as layers, where the initial strength is controlled by presence or absence of ice below the freezing point and presence/absence of water saturated fractured rocks in the upper ~10 km of Martian crust. In summary, for realistic models of impact cratering on Mars we must improve on previously published models for the Martian crust that assumed a constant dynamic strength (10 to 20 MPa; e.g., [4]).

References: [1] Clifford, S.M. (1993) *JGR, 98*, 10973. [2] Turtle E.P., Pierazzo E. (2001) Science 294, 1326. [3] Turtle E.P., Ivanov B.A. (2002) 33rd LPSC, Abst. # 1431. [4] Stewart S.T. et al. (2003) in *Shock Compression of Condensed Matter – 2003*, 1. [5] Stewart S.T., Ahrens T.J. (2005) *JGR, 110*, DOI: 10.1029/2004JE002305. [6] Tchijov V. et al. (1997) *J. Phys. Chem. B, 101*, 6215. [7] Ivanov B.A. (2005) *36th LPSC*, Abst. # 1232. [8] Pierazzo E. et al. (2005) *GSA Special Paper 384*, 443. [9] Beeman M. et al. (1988) *JGR 93*, 7625. [10] Sammonds P.R. et al. (1998) *JGR 103*, 21795. [11] Oksanen P., Keinonen J. (1982) *Wear 78*, 315.

IMPACT CRATERS ON MARS AND EARTH: IMPLICATIONS BY ANALOGY. T. Kenkmann[1] and F. Schönian[1], [1]Institut für Mineralogie, Museum für Naturkunde, Humboldt-Universität Berlin, Invalidenstrasse 43, D-10115 Berlin, Germany, thomas.kenkmann@museum.hu-berlin.de.

Introduction: This paper reports on recent investigations on terrestrial impact structures, which may have relevance for understanding Martian impact craters and the role of volatiles during their formation. It focuses on the properties of the ejecta blankets of the Chicxulub and Ries crater. Implications by analogy between Earth and Mars craters support the view that the formation of fluidized ejecta blankets can be linked to the presence of subsurface volatile reservoirs (water or ice) [1, 2]. The role of atmospheric effects [3] for the deposition of ejecta blankets on Earth is currently not clear.

Chicxulub crater, Mexico (180 km Ø): Recently new evidence was found for a widespread preservation of the Chicxulub ejecta blanket at distances ranging from 2.9-3.9 crater radii S of the crater on the Yucatan peninsula [4-6]. Mapping of the ejecta blanket revealed that it filled a pre-existing karstified paleorelief. Ejecta diamictites are largely composed of material derived by erosion of the subsurface (limestone, marl, clay). Crater derived material is of subordinate quantity but it includes shocked quartz grains, crystalline basement and altered melt clasts. The northern part of the ejecta that is nearer to the crater displays a chaotic fabric and complex grain size distribution. At distances >3.5 crater radii from the impact center internal shear planes become a predominant sedimentological feature within the ejecta blanket. Subhorizontal shear surfaces are particularly frequent at the base of the ejecta and around obstacles. Flow directions inferred from striations and grooves on polished shear planes indicate a radial flow pattern with remarkable deviations around obstacles like paleokarst hills. The abundance of locally eroded clays that lubricate shear planes within the ejecta point towards the important role of these lithologies for the development of the flow and its large runout efficiency. Although it is inhibited to infer the primary morphology of the ejecta blanket, the flow can be reconstructed with the help of flow indicators.

The observations indicate that the ejecta flow was non-cohesive and turbulent up to 3.5 crater radii from the impact center (320 km distance). At larger distances it evolved to a cohesive debris flow, may be by detrainment of volatiles. Localization of flow along decameter long discrete shear planes indicates (1) that perturbation by secondary impacts is impeded at this distance, and (2) that the flow strain rate is strongly reduced, because the fault lengths inversely dependent on strain rate magnitude [7].

Implication for Mars: The large runout distance of the Chicxulub ejecta up to 5 crater radii [8] makes it comparable to Martian MLE craters. Since a dense atmosphere and the presence of water are evident for Chicxulub this may also hold for Mars with fluidized ejecta blankets. The transition from a less-cohesive, turbulent flow to a cohesive and localized flow of the ejecta blanket suggests (1) a decreasing amount of water by detrainment (2) and a decreasing flow rate with increasing distance from the crater center. As a consequence, the formation of ramparts could be due to an imbrication and stacking of thin sheets bounded by shear planes within the ejecta blanket. The bulk geometry of the ramparts is then constrained by the resistance to frictional sliding on basal and internal shear planes, and by the bulk rheology of the ejecta and the flow rate.

Ries crater, Germany (26 km Ø): The pre-impact stratigraphy of the Ries crater is composed of ~650 m of partly water-saturated and subhorizontally layered sediments (limestones, sandstones, shales) underlain by crystalline basement rocks (gneisses, granites, amphibolites). The ejecta blanket of the Ries crater is composed of clastic polymict breccias (Bunte breccia) that extents up to 4 crater radii from the impact center as a continuous ejecta blanket of decreasing thickness. Its constituents are mainly sedimentary rocks, with 5-10% of crystalline rocks. The ratio of primary crater ejecta to local substrate components decreases with increasing radial range [9]. Local and crater derived material are thoroughly mixed on all scales and devoid linear structural elements. It is interpreted as a "cold", non-cohesive impact formation [10]. Internal shear planes within the preserved ejecta blanket as observed at Chicxulub are not recorded. In addition to the Bunte Breccia ejecta blanket occurs a suevitic ejecta breccia with a bulk volume of 5-10% of that of the Bunte Breccia. Suevite occurs in 10-25 m thick patchy layers outside the crater and extends up to about 2 crater radii. The contact to the Bunte Breccia is very sharp. Sharp contacts of the Bunte breccia ejecta blanket also occur to the underlying rocks, even if the substrate is formed by unconsolidated sands [11]. Striations on contact surfaces revealed a radial flow. Obstacles of the pre-existing paleorelief caused deflections by up to

30°. None of the contacts observed represents the land surface prior to the impact, because of the lack of a weathering horizon. Recent investigations have shown that the uppermost target layers beneath the ejecta blanket around the crater are mechanically decoupled along incompetent, fluid bearing beds [12]. Decoupling was caused by near-surface spallation. Spallation and subsequent dragging by the ejecta curtain and/or the ejecta blanket flow also induced subsequent outward shearing.

Implications for Mars: Thin-skin delamination of rocks beneath a continuous ejecta blanket is favored in targets with flat lying sediments of large competence contrasts and differences in fluid saturation. The outward directed detachment of thin thrust sheets can lead to buckling of layers or can cause fault-propagation folding above the tip of the thin thrust sheet. The morphological expression in remote sensing studies would be the presence of concentrical ridges that can be traced through the deposits of continuous ejecta blanket. Such features may occur in some of Martian craters ejecta blankets. In opposite, the presence of concentrical furrows within the fluidized ejecta blanket around Mars craters may indicate yielding and subsequent break off of thin layers as a consequence of radial extension and outward flow on weak, fluid-rich layers. If the Ries crater really bears analogies to Martian craters one should find indications for two types of ejecta deposits resting with sharp contact onto each other, namely a volumetrically dominant lower ejecta blanket (corresponding to the Bunte breccia) and an upper, patchy ejecta layer, which is volumetrically of subordinate importance (corresponding to the suevite).

Inverted-sombrero type craters: Target rocks of terrestrial impact craters often display a layered structure with a twofold rheology. A mechanically weak, water saturated and/or unconsolidated sedimentary upper part rests on a much stronger crystalline basement. These craters display geometries of an inverted sombrero with a wider and shallower outer crater that is formed within the sediments and an inner nested crater that is formed within the crystalline basement. Examples for these types of craters are (1) the marine Lockne crater, Sweden, with an inner nested crater of 7 km diameter and an outer crater of 13 km diameter [13, 14], (2) the Ries crater, Germany, with an inner crater of 12 km diameter (inner ring) and an outer crater of 24-26 km diameter [15], and (3) the shallow marine Chesapeake Bay impact crater with a deep inner crater basin of 38 km diameter and an outer crater of 85 km diameter [16, 17].

Implication for Mars: Many craters on Mars show unusually wide outer terrace zones for which the misleading term "peripheral peak ring" was introduced [18]. The ratio crater rim/outer terrace zone is 1.2-1.5 [18] and exceeds common terrace widths [19]. In analogy to inverted-sombrero-type craters on Earth, this flat outer zone may represent a shallower outer crater formed in soft, maybe fluid-saturated sediments of the uppermost part of the crust that were more easily stripped away during the impact.

Acknowledgement: T. K. would like to thank the organizers of the Workshop for their kind invitation and generous travel support.

References: [1] Barlow, N. G. (2005) *Large Meteorite Impacts III.* Kenkmann, T., Hörz, F. and Deutsch, A. (eds.) *GSA Spec. Pap. 384*, 433-442. [2] Mouginis-Mark, P.J. (1978) *Nature 272*, 691-694. [3] Barnouin-Jha, O.S. and Schultz, P.H. (1998) *JGR 103*, 25739-25756. [4] Schönian, F., Stöffler, D., Kenkmann, T. and Wittmann, A. (2004) *LPS XXXV, Abstract #1848.* [5] Schönian, F., Kenkmann, T. and Stöffler, D. (2003) *LPS XXXIV, Abstract #4128.* [6] Schönian, F., Tagle, R., Stöffler, D. and Kenkmann, T. (2005) *LPS XXXVI, Abstract #2389.* [7] Melosh, H. J. (2005). *Impact Tectonics.* Koeberl, C. and Henkel, H. (eds.) 55-80. [8] Pope, K. O. et al. (2005) *Large Meteorite Impacts III.* Kenkmann, T., Hörz, F. and Deutsch, A. (eds.) *GSA Spec. Pap. 384*, 171-190. [9] Hörz, F., Ostertag, R., and Rainey, D.A. (1983) *Rev. Geophys. Space Phys. 21,* 1667-1725. [10] Stöffler, D. (1975) *Fortschr. Miner., 52*, 385-387. [11] Hörz F., Gall H., Hüttner, R. and Oberbeck, V.R. (1977) *Impact and Explosion Cratering.* Roddy, D.J, Pepin R.O., and Merill R.B. (eds.), p. 425-448. [12] Kenkmann T. and Ivanov B. A. (2005) *LPS XXXVI, Abstract #1039.* [13] Ormö, J. and Lindström, M. (2000) *Geol. Mag. 137,* 67-80.[14] Lindström, M. et al. (2005). *Impact Tectonics.* Koeberl, C. and Henkel, H. (eds.) 357-388. [15] Pohl, J., Stöffler, D., Gall, H., and Ernstson, K. (1977). *Impact and explosion cratering* Roddy, D.J, Pepin R.O., and Merill R.B. (eds.), p. 343-404. [16] Powars, D.S. and Bruce, T.S. (1999) *USGS Prof. Paper 1612*, 82 pp. [17] Poag, W., Koeberl, C. and Reimold, W.U. (2004) *The Chesapeake Bay Crater*, 522 pp., Springer. [18] Nycz J.C. and Hildebrand (2005) *LPS XXXVI, Abstract #2167.* [19] Pearce, S.J. and Melosh H.J. (1986) *Geophy. Res. Lett. 13*, 1419-1422.

POST-SHOCK TEMPERATURE MEASUREMENTS OF BASALT: IMPROVING THE BASALT EQUATION OF STATE AND MODELING OF POST-IMPACT CONDITIONS. G. B. Kennedy[1], S. T. Stewart[1], L. E. Senft[1], A. W. Obst[2], M. R. Furlanetto[2], J. R. Payton[2], and A. Seifter[2]. ([1]Harvard University, Department of Earth and Planetary Sciences, 20 Oxford St., Cambridge, MA 02138; [2]University of California, Los Alamos National Laboratory, Physics Division, P-23, Los Alamos, NM 87545.)

Introduction. Direct measurements of post-shock temperatures of rocks and minerals provide strong constraints on their equations of state, the temperature field surrounding fresh impact craters, and the thermal history of meteorites. Multi-wavelength temperature measurements also furnish insights into temperature variations due to porosity and material mixtures.

Here we present preliminary results from simultaneous measurements of particle velocity and free surface emission from shocked Columbia River flood basalt and comparisons to simulations using the shock physics code CTH [1, 2].

Experiments. Planar shock waves with peak pressures up to ~35 GPa are generated in basalt using the 40-mm single stage powder gun in the Shock Compression Laboratory at Harvard. A molybdenum (99.95%) flyer plate impacts an aluminum 2024 driver plate, which forms the impact surface of a vacuum chamber containing the basalt specimen (Fig. 1). Concurrent particle velocity and radiance measurements from the same location on the free surface of the basalt are achieved using a shared optical system. Particle velocity is measured with a VALYN Velocity Interferometer System for Any Reflector (VISAR) [3]. The radiance is recorded by a high-speed, infrared, four-wavelength (1.8, 2.3, 3.5, 4.8 μm) pyrometer with InSb detectors, which was developed at Los Alamos National Laboratory [4-7]. The pyrometer is sensitive to emission temperatures as low as 400 K and has a temporal resolution of ~17 ns.

The pyrometer is calibrated with a black body source that was observed with the same optics and fibers as used in the experiments. The sample vacuum chamber is purged with He gas and evacuated to <0.5 millitorr, eliminating any background emission from gas in the chamber.

The Columbia River Flood Basalt specimens from Pullman, WA ($\langle\rho\rangle$=2.83±0.10 g/cm^3, $\langle V_P\rangle$= 5.73±0.28 km/s, $\langle V_S\rangle$=3.46±0.04 km/s) are cored and cut from hand samples into 3×34 mm discs. The basalt and driver plate are polished to an optical (~100 nm) finish, and the basalt is attached to the driver plate using a thin (~10 μm) layer of epoxy. No macroscopic pores intersect the free surface. The observed area, a ~4-mm diameter spot for the pyrometer and ~1-mm diameter spot for the VISAR, contains microscopic pores that are typically 10s μm across.

Results. The temperature of basalt released from a peak shock pressure of 29.3 GPa is calculated for each pyrometer channel (Fig. 2). By applying a plausible emissivity range, between 0.7 and 1.0 for basalt, we determine mean values and error bars on the true temperature. There is a small temperature excursion at the time of shock breakout, which is seen in previous post-shock temperature measurements on metals and minerals [7-10]. The two longest wavelength channels are in good agreement, with a constant temperature following the breakout. The two shortest wavelength channels record significantly higher temperatures, which increase with time after the shock breakout.

The free surface particle velocity provides information about the pressure-volume release path from the peak shock state. The free surface particle velocities, for basalt subject to peak shock pressures between 2.0 and 32.5 GPa, are shown in Fig. 3.

Discussion. Each experiment is modeled with the CTH shock physics code using the standard equation of state (EOS) tables for the metals and basalt. The results are compared to the observed temperatures and particle velocities (Figs. 2-3, dashed lines). In general, the observed free surface particle velocities are lower than the calculations, indicating that the release path is steeper compared to the model EOS.

In the 29.3 GPa experiment (Fig. 2), the different temperatures in the pyrometry channels cannot be reconciled by varying the emissivity as a function of wavelength. We interpret the discrepancy between the shorter and longer wavelengths to be evidence for hot spots in the field of view related to the microporosity and/or grain boundaries. The long wavelength channels, which are less sensitive to emission from hot spots, record post-shock temperatures slightly higher than calculated. The temperatures observed in the short wavelength channels imply hot spot temperatures >700 K, with the peak temperature sensitive to the total hot spot area. The observations are in good agreement with calculations of free surface emission near a single penny-shaped pore (parallel to the shock front), which reaches post-shock temperatures of ~700-800 K.

Conclusions. New shock experiments on basalt provide fundamental information required to improve EOS models. The new data also provide insight into the distribution of temperatures following impact events. New EOS models will aid in calculations of post-impact conditions on Mars [11], the thermal history of meteorites [12], and conditions for melting subsurface ice [13]. Heterogeneous shock pressures and temperatures are observed around terrestrial craters and in meteorites. Our data quantify the heterogeneity that arises from pre-existing pores and fractures and the effect of mixing materials with different shock impedances. Understanding the effect of heterogeneities on the temperature distribution following impact events will aid in the interpretation of meteorites, terrestrial field studies, and simulating impact events on Mars.

References. [1] McGlaun, J.M., et al. (1990) *Int. J. Impact Eng.* **10**, 351-360. [2] Hertel Jr., E.S., et al. (1993) *Proc. 19th Intl. Symp. on Shock Waves*, 377-382. [3] Barker, L.M. (1999) *Shock Compression of Condensed Matter -- 1999*, 999-1002. [4] Boboridis, K., et al. (2003) *VDI-Bericht* **1784**, 119-126. [5] Seifter, A., et al. (2003) *European Space Agency Special Publication* **540**, 375-380. [6] Seifter, A., et al. (2004) *26th Intl. Congress High-Speed Photography & Photonics* **5580**, 18-23. [7] Seifter, A., et al. (2004) *26th Intl. Congress High-Speed Photography & Photonics* **5580**, 93-105. [8] Raikes, S.A. and T.J. Ahrens (1979) *Geophys. J. R. Astr. Soc.* **58**. [9] Seifter, A., et al. (2004) *Intl. J. Thermophysics* **25**, 547-560. [10] Seifter, A., et al. (2005) *Shock Compression of Condensed Matter -- 2005*, E6.00001. [11] Pierazzo, E., et al. (2004) *LPSC* **XXXV**, 1352. [12] Artemieva, N. and B. Ivanov (2004) *Icarus* **171**, 84-101. [13] Stewart, S.T., et al. (2004) *Shock Compression of Condensed Matter -- 2003*, 1484-1487.

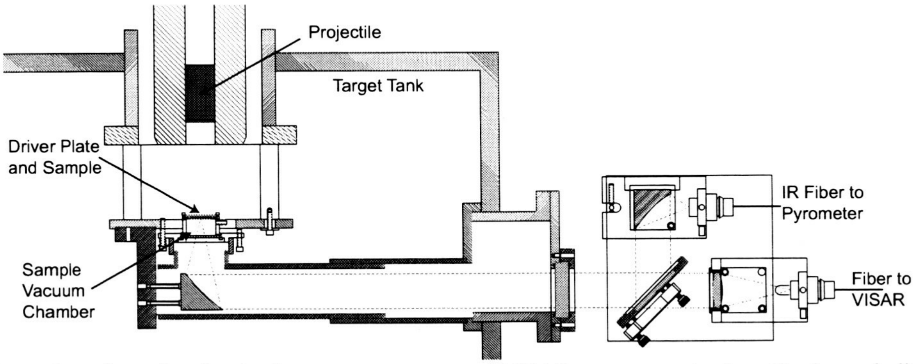

Fig. 1. Experimental configuration for simultaneous pyrometer and VISAR measurements. An off-axis parabolic mirror collects radiance emitted from a ~4-mm diameter spot on the downrange face of the sample. The collimated light is split with a dichroic between the IR pyrometer and the visible (532 nm) VISAR particle velocity measurement. The optical path is enclosed in light-tight tubing to shield from propellant gases for the duration of the experiment.

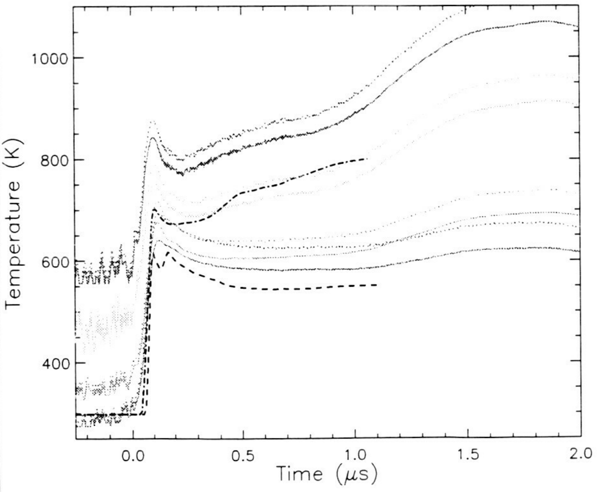

Fig. 2. Multi-wavelength post-shock temperature measurements on basalt subject to peak shock pressure of 29.3 GPa for channels centered at 1.8 (dk. blue), 2.3 (lt. blue), 3.5 (green), and 4.8 (red) μm, assuming emissivity of 1 (solid lines) and 0.7 (dotted lines). Calculated free surface temperatures with (dash-dotted line) and without (dashed line) a single penny-shaped pore near the free surface.

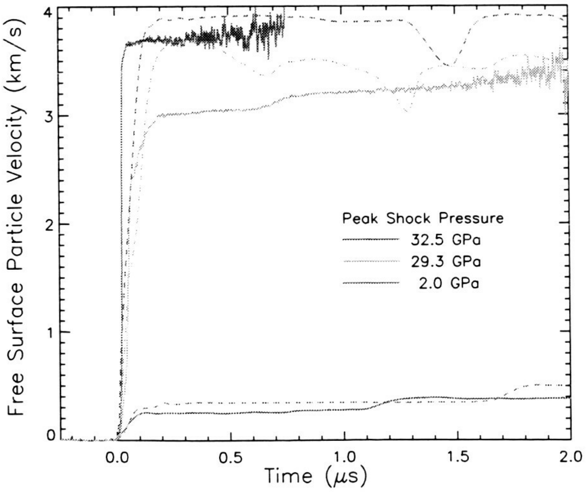

Fig. 3. Measured (solid) and modeled (dashed) free surface velocities of basalt shocked to peak pressures of 2.0, 29.3 and 32.5 GPa.

THE ROLE OF WATER IN THE DEVELOPMENT OF THE LATE CRETACEOUS WETUMPKA IMPACT CRATER, COASTAL PLAIN, ALABAMA

D. T. King, Jr.[1], J. Ormö[2], J. R. Morrow[3], L. W. Petruny[4], R. C. Johnson[1], and T. L Neathery[5]. [1]Dept. Geology, Auburn University, AL 36849 [kingdat@auburn.edu]; [2]Centro de Astrobiología (INTA/CSIC), Madrid, Spain [ormo@inta.es]; [3]Dept. Earth Sciences, Campus Box 100, University of Northern Colorado, Greeley, CO 80639 [jared.morrow@unco.edu]; [4]AstraTerra Research, Auburn, AL 36831-3323; [5]1212-H Veteran's Parkway, Tuscaloosa, AL 35404 [tlneathery@prodigy.net]

Figure 1. DEM of Wetumpka impact crater. The outline of the topographic profile in Fig. 4 (red line) and reconstructed cross sections in Figs. 2-4 is indicated by red line.

Introduction: Wetumpka is a Late Cretaceous marine-target impact structure in the inner Coastal Plain of Alabama. The structure is characterized by a wide, horseshoe-shaped crystalline rim, an interior region of broken and disturbed sedimentary formations, and an extra crater terrain on the south-west composed of structurally disturbed target formations (Fig. 1). The extant crater rim spans 270 degrees of arc and is open on the southwest, the same side as the structurally disturbed terrain just noted. The northwest-southeast diameter of the crystalline rim alone is approximately 5 km. In order to understand the influence of target properties on the cratering and modification of Wetumpka, we needed to find its present state of preservation (i.e., where is the erosional level with regard to an original crater cross section). This was achieved by comparing present geology and topography with standard parameters for impact craters (cf. Melosh), but also incorporating recent results from studies of marine-target craters, especially those strongly affected by the collapse of a thick sequence of poorly consolidated sediments. Studies of marine-target craters such as Chesapeake Bay and Lockne, have brought to light marine-target cratering processes that are also quite evident at Wetumpka. In this paper, we present some new interpretations of this structure in view of this recent information about marine impacts.

Setting: The Wetumpka impact occurred in marine water of the Gulf of Mexico, which was approximately 30 to 100 m deep and likely shallowed toward the north where the coeval shoreline was located. In reverse stratigraphic order, the target (shown in Figs. 2-4) consisted of marine water (blue pattern); poorly consolidated sediment (yellow pattern; comprising 30 m of chalky ooze, 30 m of paralic marine sand, and 60 m of terrestrial clayey sand and gravels, and ultimately,weathered crystalline basement (dark pink pattern). In Fig. 2 we have indicated the original target stratigraphy with slightly paler shades. The parautochthonous breccia lens formed by initial collapse of the transient cavity is colored orange. Later slump deposits of sediments from outside the crater are marked yellow with fragment symbols (Fig. 4). The crystalline basement has a southwest dip of about 10 m per kilometer. This is assumed to play a role in the cratering and modification.

Reconstruction of Wetumpka cratering and modification: We seek an initial, fresh crater that would fit to the present day topography and surface geology. In figure 4, the topography and geology along a SSW-NNE profile (Fig. 1) is connected to a hypothetical subsurface morphology of the crater. Based on standard parameters for impact craters and information from marine-target craters we could reconstruct the dimensions of the fresh crater. The best fit is achieved with a fresh crater having a diameter slightly less than 5000 m. Based on the relations between fresh crater diameter and transient cavity given by Melosh. The diameter of the transient cavity at target surface would have been about 4000 m. The water layer is excavated together with the rocks in craters with water depth significantly shallower than the diameter of the impactor. The rim height of a 5-km wide fresh crater in solid rock, measured from the target surface, should be 203 m, but we assume slightly higher initial rim (250 m) due to the water layer and soft sediments. This fresh crater rim is, of course, transient and will be lowered by removal of the water layer (Fig. 3). Half of the rim height is assumed to be due to structural uplift, and this decreases to zero at approximately 1.3 to 1.7 crater radii from crater center. The structural uplift of the basement would be slightly less on the southern side than the northern due to the structural dip of the basement. Onset of central uplift (Fig. 1) and slight down-faulting of the rim (Fig. 4) are inferred for craters larger than 4 km in crystalline rock. Due to the large influence of water in the rim formation on the southern side, and the lower structural uplift of the basement, this sector of the fresh crater rim will immediately collapse. The collapse is further aided by the onset of a resurge of the seawater. As the seawater was shallower on the northern side, this part of the crater rim could withstand the resurge better. The collapse of this side was possibly further diminished by the more pronounced structural uplift of the basement forming a threshold for the sediments.

When no rim existed to hold back the fluidized sediments of the target, the collapse of the southern sector could reach far outside the initial diameter of the crater (Fig. 4). This is visible today as a wide zone of horst-graben structures to the southwest of the crater (i.e., in the structurally disturbed terrain; Fig. 1). The occurrence of large (d = hundreds of meters) blocks of crystalline rock at the crater center is assumed to be fragments of the southern rim that slumped in to this position.

In these reconstructions we have neglected any influence of the impact angle. Recent numerical simulations of an oblique impact for the Lockne crater have showed a much larger flap-formation and extensive ejecta curtain down-range than up-range. However, the water resurge will be stronger from the up-range direction. If we assume an impact at Wetumpka from the southwest, then the effects on crater collapse that we now infer from the slope of the basement and the deepening of the water, will be significantly enhanced.

Interpretations: The reconstructions show that, most likely, the erosional level of the crater allows only the present northern crystalline rim to be part of the structural uplift. However, recent field observations of disturbed sediments in a position topographically below crystalline rim material in the southeastern rim indicate that some sectors of the rim may have preserved parts of the crystalline flap. If selective failure of rim is due most probably to resurge flow and instability of the rim due to poorly consolidated sediments (Fig. 4), then the presence of this morphologic feature alone in other craters in the Solar System has great importance for interpreting target composition and pre-impact geologic history.

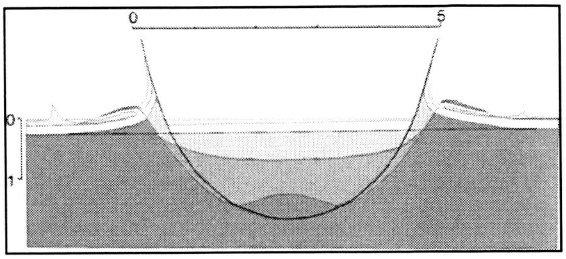

Figure 2. Excavation phase and onset of central uplift (not confirmed). Target stratigraphy is indicated by paler shades (water: blue, sediments: yellow, crystalline: pink). Note dip of basement and deepening of seawater towards the south (left).

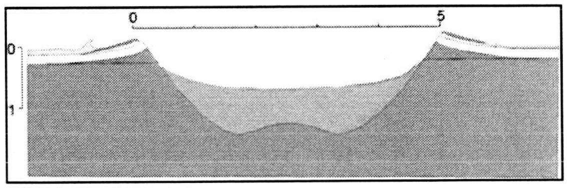

Figure 3. Return of seawater. Due to the situation given in Fig. 2, the southern rim will immediately collapse (thus figure 4).

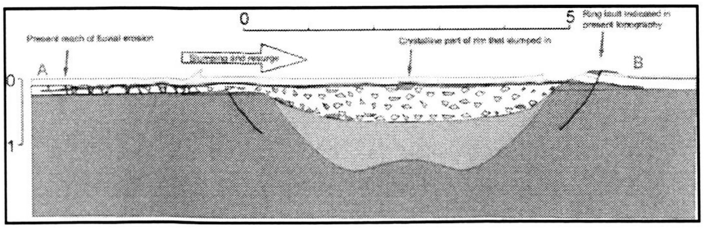

Figure 4. Rim collapse occurs due to resurge of seawater and weakness of the southern rim. The collapse causes large-scale block slumping of poorly consolidated, fluidized sediments outside the crater. This is only occurring in the southern sector resulting in a horseshoe-shaped rim. A, B as in figure 1.

Fluidized Ejecta of Martian Lobate Craters and Composition of the Highland Rocks; G. G. Kochemasov, IGEM Russian Academy of Sciences, 35 Staromonetny, 119017 Moscow, Russia; kochem@igem.ru

A specific martian feature – lobate ejecta blankets around craters extending up to 1.5 times of a crater diameter (much wider than continuous ejecta of lunar – 0.6-0.7 diameter, and mercurian – 0.4-0.5 diameter, craters) is usually attributed for the frozen water in the martian crust. This water could fluidize under impact excavated material and make it flow like liquid. The geomorphological evidences show that the ejected material really behaves like liquid (resembles the heavy clay liquid for drilling), flows and skirts obstacles but usually does not show any significant settling. One would expect this settling for water rich material. Could it have, along with some water, compositional peculiarities? It seems that after Gamma-spectrometry of "Odyssey" and two landers – "Spirit" and "Opportunity" analyses one can say that a "peculiar rock' is marked out.

"Odyssey" show rather low silica over highlands (20-21% [1]) and, that is especially interesting, over high standing Tharsis bulge (18-20%) [1]. Low Fe signifies that this lowering in silica is not due to the basic rocks which were postulated in "entirely basaltic Mars' model (the martian meteorites as a proof). MGS gravity data [2] have clearly shown that the martian southern highlands are composed of "light" (not dense) lithologies, much less dense than the northrrn lowland Fe-basalts, otherwise relatively flat even gravity signals over two hemispheres were not possible [2]. The previous global albedo data also have shown that the southern highlands are much lighter (average albedo 0.25) than the dark northern lowlands (0.15)[3] hinting at different rocks. Very long lobate formations around huge Tharsis volcanoes also require very low viscosity lavas. Density of martian soils on surface and to a depth of about 10 m according to various geophysical methods (radar, polarimetry, IR, "Viking" data) is lower than that of the Moon and is lower for light areas than for dark ones [3].

Now this "whitish" low density material is partly characterized on Meridiani Planum by "Opportunity" [4] – it is salt: sulfates, chlorides, bromides covering and penetrating layered sedimentary (mainly eolian?) rocks. The salts are discovered in craters and, as it shown by an artificial very shallow impact crater (after fall of the "Opportunity"'s heat shield), under thin cover of eolian reddish Fe-rich drifts. The salts cover large areas on Meridiani Planum. Their most probable origin is due to widespread hydrothermal activity, vents being craters and deep cracks (faults) draining depths of the highland crust. So, salts are not just a thin veneer but a significant constituent part of the highland crust. That is why Tharsis is surprisingly low in Si. Silicates are partially replaced by salts (low density substance), this is required by necessity to diminish the mean density of highly standing tectonic blocks of Mars – a rotating planetary body that obeys the physical law of keeping equal angular momenta of hypsometrically different tectonic blocks. The aqueous salts with constituent water not only diminish a mean rock density and explain the presence of hydrogen (H_2O) at the equatorial zones in "Odyssey' data but also bring down the melting temperature of impacted rocks making ejecta easily flowing (like a dough for pan-cakes).

The "Spirit"'s results for the Columbia Hills at Gusev crater go farther [5, 6, 7]. They bluntly shown that an outlier of highlands consists of rocks completely different from lowlands basalts. Keeping the same as in basalts level of Si, these light color rocks are higher in alkalis, Al, P, Cl, S, Ti and lower in Fe, Mn, Mg, Ca, Cr. Al/Ca increases from basalts to this rock. Na up to 4.5%, Al- 8.0%, P – 2.3%, Ti – 1.5% - these are values suitable for syenites. The thinly layered rocks of Columbia Hills resemble very much the layered nepheline syenites of the ring complexes of Kola Peninsula (Khibiny, Lovozero). One layer of the Columbia Hills massif (Wishstone rock) is high in phosphorus (calculated apatite is up to 13%), another – in sulfur (Peace rock). All this resembles layers of apatite and feldspathoids rich rocks of Lovozero massif. Sodalite (Cl and S) and noseane (S) rocks are known there. A very typical process of feldspathoid alteration in the contact with water (ground and atmospheric) is formation of zeolites. These very soft and low density silicates (often shining like water ice) are perfect sinks for water, giving it out and taking back into their crystalline structure depending on P-T conditions and availability of water [8]. These syenites often containing also as a matrix albite – sodic plagioclase (detectd by "Spirit"'s Mini-TES [7]) are melted at temperatures much lower than basalts. Maybe, this is a reason why the lobate craters are widespread on the southern highlands. In addition, zeolitized syenites are soft, this property of Columbia Hills rocks was found by "Spirit"'s grinding instrument –these rocks are much softer than basalts [7]. Very thin layering of rich in alkalis and thus very fluid nepheline syenites is typical at Earth.

Gusev crater lies at the contact between lowlands and highlands. In an earlier work [9] , before "Pathfinder" landing, we insisted on "Possibility of highly contrasting rock types at martian highland/lowland contact", namely on finding albitites, syenites, granites in addition to basalts. "Pathfinder" has found andesites, but more acid and alkaline lithologies were discovered by THEMIS (MGS) and "Spirit". Two localities at Syrtis Major have dacites originated probably from a crustal body long not less than 95 km [10]. "Spirit" has nepheline- normative rocks probably rich in salts penetraiting them in form of own minerals and in feldspathoids structures (sodalite, noseane,and others). So, salts helping to diminish rock density, simultaneously lower its melting temperature what helps to produce such characteristic martian structures as lobate craters.

One more remark. This water, alkali-rich easily fluidized crust is often masked by ubiquitous eolian dunes and drifts rich in Fe-minerals originating from the northern lowlands. Now orbiting Mars "Mars Express" with "Omega" instrument measuring reflected light from drifts discovers signatures of not only salts but also olivines and pyroxenes [11]. Researches often make hasty conclusions about wide presence of basic rocks. Sometimes they are right because the presence of plateau basalts, basic sills and layered basic intrusions at highlands is quite possible (compare with Earth), but often they are wrong taking surface reflectance from widespread Fe-minerals surface contamination for an indication of the deeper geology. In this sense, lobate craters luckily sample deeper horizons and better show the real geology.

References: **[1]** Wänke H., Boynton W.V., Brückner J. et al. (2005) LPSC XXXVI, Abstr.#1389, CD-ROM. **[2]** Smith D.E., Sjogren W.L., Tyler G.L. et al. (1999) Science, v. 286, 94-97. **[3]** Florensky K. P., Basilevsky A.T., Burba G.A. et al. (1981) Essays of comparative planetology. Moscow, "Nauka", 326 pp. (In Russian). **[4]** Rieder R., Gellert R., Anderson R.C. et al (2004) Science, v. 306. #5702, 1746-1749. **[5]** Gellert R., Rieder R., Anderson R.C. et al. (2004) Science, v. 305, # 5685, 829-832. **[6]** Gellert R., Zipfel J., Brückner J. et al (2005) LPSC XXXVI, Abstr. #1997, CD-ROM. **[7]** Squyres S.W. and the Athena Science Team (2005) LPSC XXXVI, Abstr. #1918, CD-ROM. **[8]** Kochemasov G.G. (2002) 36th Vernadsky-Brown microsymposium "Topics in comparative planetology", Abstr., Oct. 14-16 2002, Vernadsky Inst., Moscow, Russia, CD-ROM. **[9]** Kochemasov G.G. (1995) Golombek M.P., Edgett K.S., Rice J.W.Jr. (eds) Mars Pathfinder landing site workshop II: Characteristics of the Ares Vallis region and Field trips to the Channeled Scabland, Washington. LPI Tech. Rpt. 95-01, Pt. 1, LPI, Houston, 63 pp. (p. 18-19). **[10]** Christensen P.R., McSween H.Y.Jr., Bandfield J.L. et al (2005) LPSC XXXVI, Abstr. # 1273, CD-ROM. **[11]** Mustard J.F., Poulet F., Gendrin A. et al. (2005) LPSC XXXVI, Abstr. # 1316, CD-ROM.

DISTRIBUTION AND ORIENTATION OF ALLUVIAL FANS IN MARTIAN CRATERS.

E. R. Kraal[1], J.M. Moore[2], A. D. Howard[3], E. I. Asphaug[1] [1](Department of Earth Sciences, University of California Santa Cruz, 1156 High Street, Santa Cruz, California, 95064, ekraal@es.ucsc.edu, asphaug@es.ucsc.edu), [2](NASA Ames Research Center, MS 245-3, Moffet Field, CA 94035-1000, jeff.moore@nasa.gov), [3](Department of Environmental Sciences, University of Virginia, 291 McCormick Rd., PO Box 400123, Charlottesville, VA 22904-4123, alanh@virginia.edu).

Overview: We present the results of the complete survey of Martian alluvial fans from 0-30 S, initiated by Moore and Howard [1]. Nineteen impact craters contain alluvial fans. They are regionally grouped into three distinct areas. We present our initial results regarding their distribution and orientation in order to understand what controls their formation. Since alluvial fans are formed by water transport of sediment, these features record 'wetter' episodes of Martian climate. In addition, their enigmatic distribution (in regional groups and in some craters, but not similar adjacent ones) needs to be understood, to see how regional geology, topographic characteristics, and/or climate influence their formation and distribution.

Alluvial Fans: Fan deposits are formed by the deposition of sediment from a shifting source (such as a stream migrating over the deposit) and are recognized by their cone-shape morphology. Fans are well studied on Earth and form in many conditions from large underwater deposits at the mouths of rivers to sub-aerial gravity driven flows. This continuum of formation processes produces slight variations in morphology (such as slope, area, and basin size) that can be used to distinguish the formation process as well as information about the sedimentary system (for review see[2]).

Features in some craters on Mars, discovered in THEMIS daytime IR images and MOLA topography, have the same cone shape as terrestrial alluvial fan deposits. Comparison of fan statistics such as fan gradient, fan area, and basin area to statistics of terrestrials fans indicates that Martian fans follow the same approximate trends and compare well to very large terrestrial alluvial fans with possibly finer sediment size and lower sediment concentrations [1].

Fans in Martian Craters: Alluvial fans form because of the abrupt transitions from steep, eroding catchments to low gradient, depositional basins. Over the abrupt transition, the stream power drops significantly and causes deposition of the stream bed load [2]. Impact craters provide the ideal topographic setting for the formation of alluvial fans. There is an abrupt change in slope from the high, steep rims to the shallow, low crater bowls. We have searched for alluvial fan in other areas on Mars, such as Valles Marineris, and have not yet identified any candidate deposits. To date, the only alluvial fans on Mars have been identified in crater rims.

Distribution: Our completed survey results confirm the initial results of Moore and Howard[1]. All alluvial fans are located in craters south of 18 and from -40 to 85 E. Within this large group, there are three distinct regional groups of craters containing alluvial fans, the southern portion of Margaritifer Terra , Southwestern Terra Sabaea, and Tyrrhena Terra.

Orientation: In an effort to understand the factors controlling the formation of these fans, we examine the orientation of the fans from crater rims. Figure 1 shows the orientation of fans in the three regional groups. Though the average fan emerges from the northwest rim of the crater, there is a great deal of spread in the data. Some areas, such as Figure 1A (Margaritifer Terra) have a more distinct orientation pattern. While others, such as Figure 1B (Terra Sabaea) have a wider spread in the orientation. In the case of the craters in Terra Sabaea, the orientations are dominated by a crater system of fans spilling into three a joining craters. The majority rest of the fans in the Terra Sabaea region are below MOLA topographic resolution, and therefore, are not included in the orientation statistics.

Continuing Research: We are in the process of completing a global survey. In addition, we are collecting more data on the crater statistics, regional geologic setting, and orientation patterns to understand the mechanisms controlling alluvial fan formation. The formation of alluvial fans on earth is controlled by tectonic, climatic, and geologic conditions. The same is likely true on Mars. Therefore, by understanding their formation, we will gain insight into the climate history of Mars.

References: [1] Moore, J. M. and A. D. Howard (2005). "Large alluvial fans on Mars." Journal of Geophysical Research (Planets) **110**(E4): E04005 dio: 10.1029/2004JE002352. [2] Harvey, A. M. (1997). The role of alluvial fans in arid zone fluvial systems. Arid Zone Geomorphology: Process, Form, and Change in Drylands.

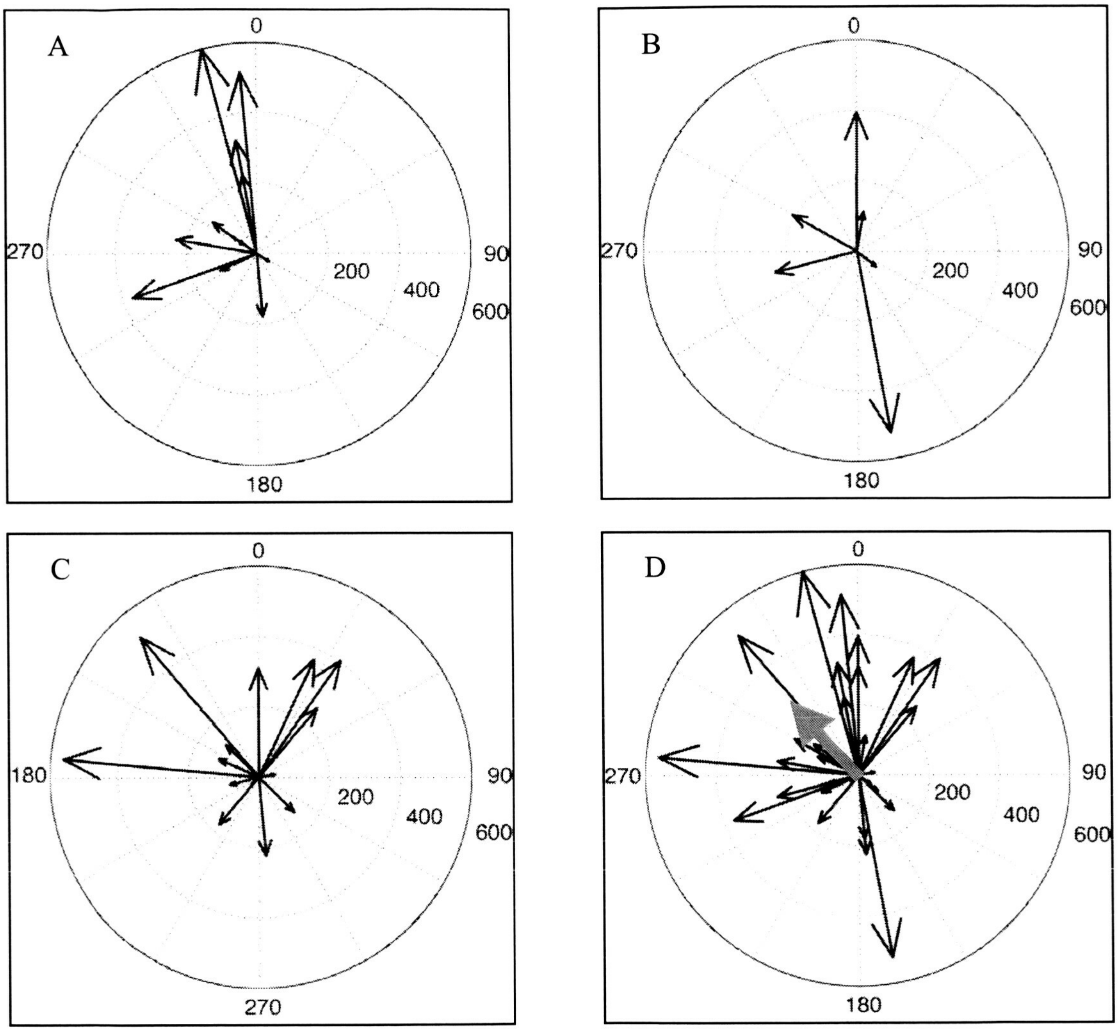

Figure 1: Fan Orientation of Alluvial Fans in Martian Craters.
Arrows point to the direction of emergence of the fan from the crater rim. Their length scales with area of the fan apron. North is up in all cases and area of fan is in km. The only fans included are those above MOLA topographic resolution (see Moore and Howard, 2005). The fans are plotted according to their regional groups. Figure 1A is in located in Southern Margaritifer Terra. Figure 1B is located in Southwestern Terra Sabaea; the extreme variation in this data is because there is only one set of fans above MOLA resolution. It is a system of fans in three ajoining craters. Figure 1C located in Tyrrhena Terra, just north of the Hellas Basin. Figure 1D show the complied data. Average fan is indicated in red. The average fan is 250 km^2 and originates from the northwest rim of the crater (300).

SUBKILOMETER-SCALE ROUGHNESS OF CRATER EJECTA IN THE NORTHERN PLAINS OF MARS: IMPLICATIONS FOR CLIMATE-RELATED ALTERATION.

M. A. Kreslavsky[1,2] and J. W. Hear[1], [1]Dept. Geologcial Sciences, Brown University 1846, Providence, RI, 02912-1846, USA; kreslavsky@brown.edu, [2]Astronomical Institute, Kharkov National University, Kharkov, Ukraine.

Introduction: This study is a follow-up of our work on statistical analysis of surface slopes from MGS MOLA data [1, 2]. We have used profile slopes and curvatures measured along MOLA tracks at different baselines to characterize the roughness of the surface at scales from MOLA shot-to-shot distance (0.3 km) to tens of kilometers. Among other interesting things, we have found strong latitudinal trend of occurrence of steep slopes: even for similar terrain types, steep (>15-20°) slopes are two orders of magnitude less frequent at high latitudes (>40-50°) than at lower latitudes [2]. We have interpreted this [2] as a result of high obliquity periods in the past geological history of Mars: at high obliquity the day-average summer temperature is high and can exceed ice melting point; this favors water-assisted erosion and slope degradation.

Another similar phenomenon is the latitudinal trend of roughness [1]: At high latitudes (>50-60°) the typical subkilometer-baseline slopes are systematically gentler than in geologically similar areas at lower latitudes. This trend does not exist for longer baselines. Typical slopes are on the order of a fraction of a degree, thus the roughness trend is not the same phenomenon as the trend in occurrence of steep slopes. We have interpreted the latitudinal trend of roughness as an effect of a few-meters-thick high-latitude ice-rich mantle, which was observed in high-resolution MOC images [3]. There is no doubt that the mantle does contribute to the smoothing of the high-latitude topography, but it is not the only cause of the roughness trend observed. For example, there is a great difference in roughness signature of ejecta of two impact craters shown in **Fig. 1 A** and **B**. Crater A has rougher ejecta and obviously fresher ejecta morphology, and hence is younger than crater B. However, high-resolution MOC images clearly show the presence of the mantle over ejecta of both craters. This proves that the mantle is not the only cause of the latitudinal trend of roughness and that other climate-related processes, such as like active layer formation, play an important role in topography alteration.

Since craters are emplaced randomly through time, study of craters and their ejecta can provide information about timing or rates of the alteration processes. Here we report our new quantitative results on roughness of crater ejecta.

Observations: We considered craters in the northern plains, more exactly, within the Vastitas Borealis Formation (VBF) [4], which provided us with a similar geological environment, similar "background" roughness characteristics and presumably uniform onset of crater population formation. We excluded areas where dunes and some other topographically pronounced features were present. We considered only craters with diameters D from 10 to 25 km. This narrow range of D assured the maximal possible similarity of a pristine ejecta pattern. For smaller craters, the ejecta are too poorly sampled with MOLA; for larger craters, the multiple layer ejecta dominate [5]; this ejecta morphology is essentially different from the double layer ejecta morphology of 10-25 km craters [5]. We limited ourselves to high latitudes > 52°N, that is within the "smoothed" zone. In total there are 171 craters that match these criteria.

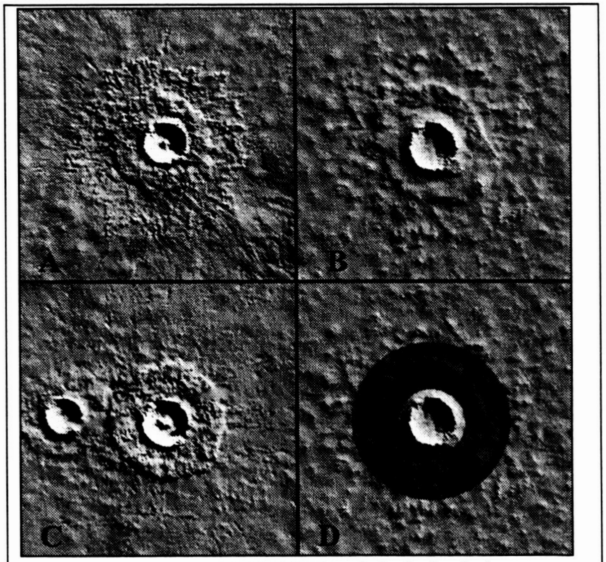

Fig. 1. MOLA-derived simulated shaded topography of craters in the VBF. **A** "Fresh" crater at 73.0°N 38.3°E; D = 12.0 km. **B**. "Smoothed" crater at 73.0°N 22.0°E; D = 12.9 km. **C**. "second roughest" crater at 69.3°N 274.0°E; D = 12.9 km. **D**. Area used for roughness statistics for crater B.

As a measure of ejecta roughness, we used the median total surface curvature, which we calculated in the following way. We used gridded topographic data at 128 pixels per degree resolution. In each pixel we calculated two principle curvatures C_1 and C_2 of the surface at two baselines of 0.9 and 3.7 km and the "total" curvature $C = (C_1^2 + C_1^2)^{1/2}$ at both baselines. For each of the 171 craters, we manually outlined the test ejecta area as a ring loosely inscribing the inner ejecta lobe and excluding the crater rim and floor (**Fig. 1 D**). For clearly asymmetric craters we drew a non-circular outline. We preferred this subjective way to mark the test areas, because it allowed us to exclude small craters that overlap the ejecta, as well as to treat overlapping ejecta carefully. For each of 171 test areas, we calculated the median "total" curvature at both baselines and used it as a measure of roughness. We expressed the difference of roughness between the pair baseline lengths in terms of the Hurst exponent *H*. It varies from 0 to 1. Smaller values of *H* mean steeper decrease of roughness with increase in scale. In other words, small *H* means the prevalence of small-scale topographic features, while large *H* means the prevalence of large-scale features.

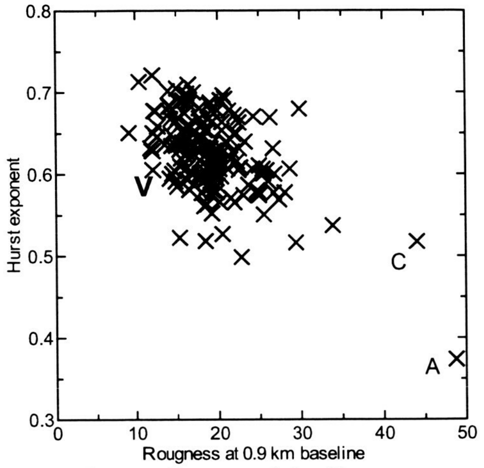

Fig. 2. Scatter diagram of the Hurst exponent and roughness at 0.9 km baseline for 171 craters. Craters A and C are the same as A and C in Fig. 1. **V** marks typical Vastitas Borealis Formation surface. Crater B from Fig 1 is close to the center of the cluster.

Results: The smaller-baseline roughness in arbitrary units and *H* for all 171 craters are shown in **Fig. 2**. It is seen that all craters are clustered in this scatterplot except two obvious outliers A and C shown in Fig. 1. Typical crater ejecta are rougher than the VBF without craters (V in Fig. 2), but show similar *H*, that is the same scale dependence of roughness. Crater A is the only really fresh crater with well preserved small-scale roughness. Crater C has a somewhat atypical morphology: it no second ejecta layer, and it is located in an atypical part of the VBF. It does not represent a transitional morphology between crater A and typical craters like C, and it is not clear if its high roughness is due to a young age or due to some secondary alteration process. At the longer baseline this crater is rougher than A.

Discussion: The Vastitas Borealis Formation lies at the boundary between the Hesperian and Amazonian. If we assume this boundary to be at 3.1 Ga [6], one crater from our crater subset is forming on average each 18 Ma. Our results with one fresh crater give the time scale of topography smoothing on the order of 20 Ma with an obvious high uncertainty.

Repeating deposition and removal of ice-rich mantle following the obliquity cycles can be responsible for smoothing of ejecta at his time scale. Another processes operating at high obliquity can also make some contribution. It is possible that crater A is younger than 4-8 Ma, that is it was emplaced after the latest epoch of high obliquities, when the mean obliquity was 35° and the maximal obliquity exceeded 45° [9]. At these high obliquities the summer day-average surface temperature exceeded the water melting point and an active layer formed [7,8]. The active layer may assist smoothing the topography through solifluction, disintegration of rocks, etc.

Future work: Further study of ejecta morphology and modeling of the smoothing processes is needed to increase the robustness of our conclusions. A correlative study of ejecta roughness and slope steepness is the next step in our analysis. Study of a population of smaller craters with HRSC stereo images can provide better constrained timing estimates and lead to a better understanding of surface alteration in the recent geological past of Mars.

References: [1] Kreslavsky M. A. and Head J. W. (2000) *JGR, 105,* 26695-26712. [2] Kreslavsky M. A. and Head J. W. (2003) *GRL, 30,* DOI 10.1029/2003GL017795. [3] Kreslavsky M. A. and Head J. W. (2002) *GRL, 29,* DOI 10.1029/2002GL015392. [4] Tanaka K. L. et al. (2003) *JGR 108*, 8043. [5] Barlow N. G. (2005) *LPS XXXVI*, 1415. [6] Hartmann W. K. and Neukum G. (2001) Space Sci. Rev. *96*, 165-194. [7] Costard et al. (2002) *Science 295*, 110-113. [8] Kreslavsky M. A. and Head J. W. *LPS XXXV*, 1201. [9] Laskar J. et al. (2004) *Icarus 170*, 343.

GEOLOGY OF LONAR CRATER, INDIA: AN ANALOG FOR MARTIAN IMPACT CRATERS.

A. C. Maloof[1], K. L. Louzada[2], S. T. Stewart[2], and B. P. Weiss[3]. [1]Princeton (Dept. Geosciences, maloofa@mit.edu), [2]Harvard (Dept. Earth & Planetary Sciences), [3]Massachusetts Institute of Technology (Dept. Earth, Atmospheric & Planetary Sciences).

Introduction. Lonar Crater (Fig. 1) formed between 15-67 ka in the ~65 Ma Deccan Traps of western India [1-5]. The bolide, of unknown composition, impacted into ~600-700 m of subhorizontal basalt flows overlying Precambrian basement. Lonar is a unique Martian analog for studies of ejecta flow dynamics [6] and shock magnetization, as it is the only terrestrial crater formed entirely within basalt. Although sketch maps [1, 5, 7, 8] and paleomagnetic work [9] of variable quality have been published, no detailed geologic map or understanding of shock effects on rock- and paleo-magnetics exist for Lonar Crater. Here we present preliminary geologic and topographic maps, from a January 2005 field study, and identify features for comparison to Martian craters.

Geology. With 130-m relief from crater rim to lake level, Lonar Crater is the most significant topographic feature in the area. The raised crater rim is composed of upturned basalt stratigraphy, typically dipping 10-30° out from the crater (Figs. 2, 3, 4). In the crater wall, at least six 10-25 m thick basalt flows (T_{F0-F5}) are exposed, all of which are characterized by broad flow fronts and nearly flat upper surfaces capped by discontinuous flow-top autobreccias. Within individual pahoehoe flows, an internal stratigraphy usually is developed that begins with dense, jointed and sometimes flow-banded basalt, which passes upward into vesicular, fine-grained basalt. Flow tops are variably altered, and paleosols containing root casts are common between flows.

Along the rim crest, Flow 5 is recumbently folded and brecciated, with semi-intact beds preserving a reverse basalt stratigraphy (Figs. 2, 3). Away from the crater edge, the overturned flap toes out into a thin (0-6 m thick) blanket of primary ballistic ejecta.

At localities within the outer continuous ejecta blanket, such as Kalapani Dam Quarry and the Road to Kinhi Quarry, subhorizonal basalts are overlain by a debris flow unit composed of basalt clast ejecta, but also containing rip-up clasts of the pre-impact substrate within a coarse-grained matrix. A black muddy histosol up to 2 meters thick is common in depressions within the pre-impact flow-top autobreccia of T_{F4}. The top of the histosol is penetrated by clasts from the debris flow ejecta to depths of 1.5 m, and cm-size clasts of histosol are incorporated into the ejecta debris flow.

The crater and ejecta blanket are in an excellent state of preservation. Ground cover has stabilized the ejecta blanket and prevented significant (< 10 m vertical) erosion the crater rim [4]. Recent reports of heterogeneous hydrothermal alteration at Lonar Crater [11, 12] were not supported by our observations, which show that previously interpreted altered ejecta are probably highly-comminuted materials originating from autobrecciated flow tops weathered prior to the impact event. At least one comminuted zone contains impact glasses and sub-mm spherules.

Discussion. Study of a simple crater in subhorizontal layers of basalt will provide insight into crater formation in Martian stratigraphy [10]. Lonar may be used to validate simulations of impact events into layered targets.

Lonar is also an excellent analog for investigating the effects of shock on the Martian crustal magnetic field. Based on our preliminary paleomagnetic measurements on oriented Lonar samples from the crater wall, the crater rim, and the continuous ejecta blanket, the impact event was not large enough to impart a hard, shock-induced remanence in the Deccan Trap basalts. However, the shock may have been great enough to change the magnetic properties of the rocks. We see variable post-impact acquisition of low-temperature magnetic overprints that may be directly related to the peak shock pressures experienced by the rock. So far, the most shock-modified magnetic properties appear to be recorded by basalt clasts within the distal edge of the continuous ejecta blanket.

The ballistic ejecta also shows compelling evidence for the development of ground-hugging ejecta debris flows and a rampart edge to the continuous ejecta blanket. These features may be similar to layered ejecta flows on Mars [6].

Conclusions. Lonar Crater is an excellent Martian analog for studies of impact crater formation, shock magnetization, and fluidized ejecta.

Acknowledgements. We appreciate discussions with and field assistance from Horton Newsom and Shawn Wright.

References. [1] Fredriksson, K., et al. (1973) *Science* **180**, 862. [2] Sengupta, D., et al. (1997) *Revista de Fisica Aplicada e Instrumentacao* **12**, 1. [3] Storzer, D. and C. Koeberl (2004) *LPSC* **35**, 1309. [4] Fudali, R.F., et al. (1980) *Moon & Planets* **23**, 493. [5] Ghosh, S. (2003) *Indian Minerals* **57**, 105. [6] Stewart, S.T., et al. (2005) *Volatiles & Atmos. Martian Impact Craters*. [7] Nayak, V.K. (1972) *EPSL* **14**, 1. [8] LaTouche, T.H.D. (1912) *Rec. Geol. Surv. India* **41**, 266. [9] Cisowski, S.M. and M. Fuller (1978) *JGR* **83**, 3441. [10] Edgett, K.S. and M.C. Malin (2002) *GRL* **29**, 2179. [11] Newsom, H.E. and J.J. Hagerty (2003) *3rd Intl. Conf. Large Met. Impacts*, 4116. [12] Hagerty, J.J. and H.E. Newsom (2003) *MAPS* **38**, 365.

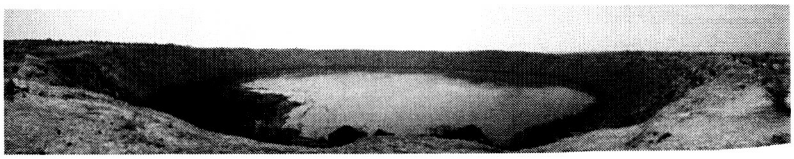

Fig. 1. Lonar Crater, India. View from the N rim showing extent of shallow, saline lake and excellent exposures on crater wall.

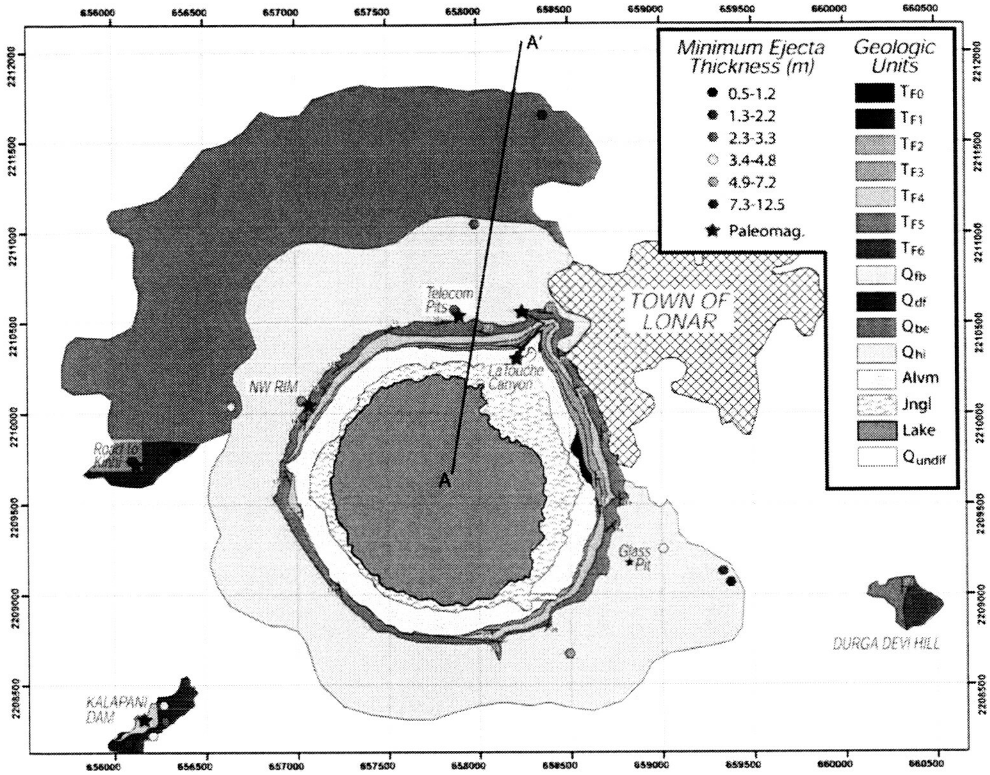

Fig. 2. Preliminary geologic map of Lonar Crater, with: T – Tertiary; T_{F0}-T_{F6} – seven Earliest Tertiary basalt flows of the Deccan Traps; Q – Quaterary; Qfb – overturned flap breccia composed of recumbently folded, variably brecciated basalt flows and forming the most proximal ejecta deposits around the rim of the crater; Qbe – ballistic ejecta, composed of poorly sorted, faintly bedded basalt clast ejecta; Qdf – outcrops of ejecta debris flow at distal edge of continuous ejecta blanket consisting of a mixture of remobilized primary ejecta and secondary material eroded from below, such as regolith, histosol, and alluvium; Qhi – histosol composed of black, organic rich mudstone; Alvm – Post-impact landslides and regoliths developed on the lower canyon wall; Qundif – Undifferentiated post-impact sediments, commonly consisting of bedded conglomerates, sands, soils, and regoliths.

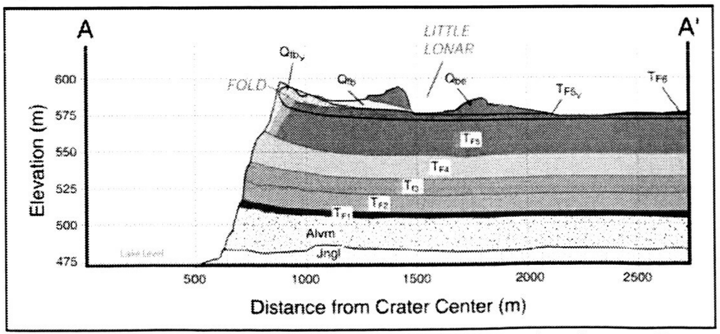

Fig. 3. Cross-section from A to A' (Fig. 3), showing elevation profile (7x vertical exaggeration.) and geology (legend is the same as Fig. 2). Little Lonar is a circular depression within the continuous ejecta blanket (Qbe). T_{F5} transitions smoothly into Qfb, where the crater rim fold hinge is mappable around the N and NW crater rim. T_{F5v} and Qfb_v are in situ and fold-brecciated Flow 5 vesicular flow top, respectively.

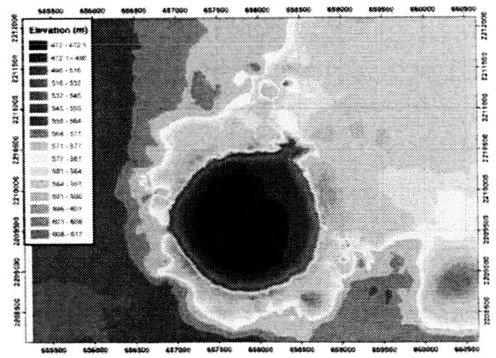

Fig. 4. Preliminary digital elevation map (DEM) computed using a universal Kriging gridding algorithm on 13,000 independent X,Y,Z data acquired with handheld GPS.

INVERTED MARTIAN CRATERS IN LINEATED GLACIAL VALLEYS, ISMENIUS LACUS REGION, MARS.

B. S. McConnell[1], G. L. Wilt[2], A. Gillespie[3], H. E. Newsom[4], [1]Highland High School, Albuquerque, NM 87108 bmcconne@unm.edu [2]Shikellamy Senior High School, Sunbury, PA 17801 grierwilt@gmail.com [3]UT aimeeg@unm.edu [4]Univ. of New Mexico, Institute of Meteoritics, Dept. of Earth & Planetary Sciences, Albuquerque, NM 87131 newsom@unm.edu

Objective We studied small, uniquely-shaped craters found on the surface of lineated terrain in the Ismenius Lacus region of Mars [1]. By utilizing MOC and THEMIS satellite images, we located terrain including lineations (viscous flow features), smoothing of topography, and morphologic features such as polygons and gullies, which appear to be strong evidence of preexisting ice deposits.

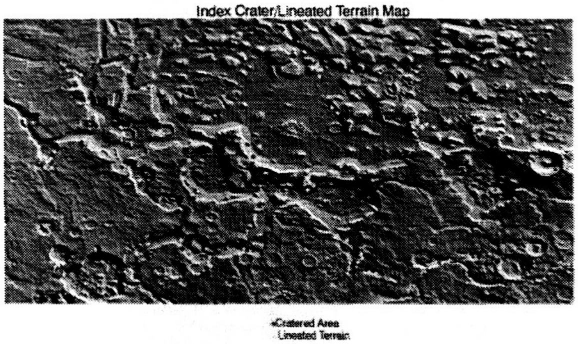

Figure 1. Index map of MOC and THEMIS images examined in this study.

Background Because of Mars's dynamic obliquity, a consistent tilt pattern is evident in which it cycles through every several million years. According to Mustard et al. [1], if the obliquity exceeds 30°, the ice at the north and south poles become very unstable and relocates by sublimation to the mid to high latitudes. This is known as a Martian Ice Age. The most recent Ice Age occurred about 10 Myrs ago when the obliquity was at a steep 35° and the primary water ice was located in the 30-60° latitude bands.

Hypothesis A specific region, Ismenius Lacus with the latitude range of 30-65°, was selected because it has a vast array of heavily cratered canyons and gullies and evidence of unusual features suggesting the presence of preexisting ice in the region [2]. The comparison of craters in both lineated and non-lineated terrain led us to the discovery of very unusually structured craters located in the lineated terrain. The craters located in these areas often consisted of multiple rim rings and plateau-like centers [2].

We developed and tested models for the origin of these unusual circular features. Based on our observations, we suggest that meteors impacted the Martian surface sometime in the last ice age and the meteors penetrated several meters of dust and ice. After their formation, they gradually filled back in with new layers of sediment and debris. As the tilt changed back to a less dramatic and current obliquity of roughly 22-26°, the ice sublimated. As the icy layers sublimated, the surface collapsed and left the uniquely structured inverted morphology [e.g. 3,4].

Methods Images were utilized to observe crater morphology in the Ismenius Lacus region. High resolution Images were examined from the Mars Global Surveyor (MGS) Mars Orbiter Camera (MOC) on the Malin Space Science Systems (MSSS) website, and from ASU's Thermal Emissions Imaging System (THEMIS) website.

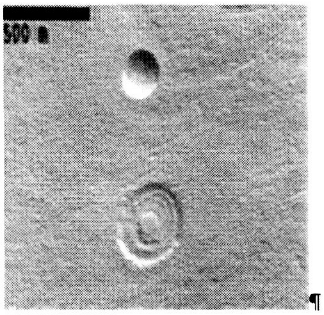

Figure 2 Example comparing a fresh bowl-shaped crater (above) and an older inverted crater (below).

We viewed every MOC image in the southern region of Ismenius Lacus by this process. After the high-resolution MOC images were inspected, the photograph was copied and pasted into Adobe Photoshop. In Photoshop, we searched the pictures for craters and then cropped each crater, with respect to the image size. The image size was vital for scaling the craters. Each high-resolution photo had different meter/pixel resolution, so an MS Excel record had to be kept for each image, and a template of 100x100 pixels was used per image. This process was done for and approximate total of 100 craters. After the craters were cropped and recorded, they were printed out to be thoroughly examined and analyzed.

Based on our sample, the inverted craters range in size from 150-400 meters in diameter. Resolution of the images limited the recognition of the smallest inverted craters.

Observations After careful and complete examination of the high-resolution images, we observed that there were relatively few craters in the lineated terrain and even fewer fresh bowl-shaped craters when compared to the surrounding area. The fact that there are so few craters suggests that the surface is young and reflects a fairly recent chain of events, such as an Ice Age, which caused this phenomenon.

Experiments In testing our hypothesis, we used multiple methods.

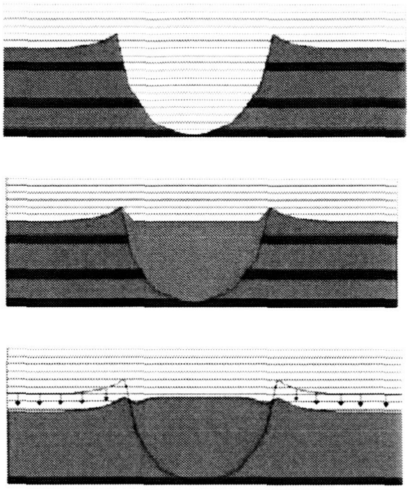

Figure 3. Numerical simulation of the three major sequences involved in inverted crater formation. The first figure shows a fresh bowl-shaped crater. The blue layers represent the sub-surface ice deposits. This simulation represents a relatively low fraction of ice in the sub-surface. The second image simulates the process in which the crater is filled in with debris. The third figure is the concluding phase, after the sub-surface ice sublimates.

Excel Model The Excel Model proved to be very useful in simulating layering and sublimation effects. With Excel, a series of rows and columns were used to simulate the surface and sub surface dust and ice layers of Mars (e.g. figure 3). Once the surface was established, a symmetrical crater was formed by deleting several layers. Each individual column was summed up in a "Totals" row and the totals were then graphed. The graph, when finished, looked very similar to a typical bowl-shaped crater. To simulate dust storms and other weathering factors, new rows of dust and ice were formed inside the crater. To simulate the departing ice age, the ice layers were deleted and the graphs symbolized the shape and structure of the concluding craters.

Physical Model The physical experiments were extremely useful in this project because our simulation was almost identical to the proposed inverted Martian crater process. In this experiment, the beginning phase consisted of three different materials; tin catering trays (to hold the surface that harbored the crater), dry ice (to simulate the sublimation of icy layers), and sand (to represent the Martian surface material). The tin was filled with layers of sand and ice to represent an ice age surface. After the surface was established, a crater was constructed by scooping out several layers in a confined area. Following the fabrication of the crater, several additional layers of sand and ice were applied. After this was complete, the tins were set in the sun so the ice would sublimate. Several hours later, the finished product looked identical the formations observed on the Martian surface in the high-resolution images.

Conclusion We have come to the conclusion that the unique features of the selected craters are due to a recent Martian Ice Age. These craters originally formed on an ice-rich surface and were subsequently covered by sediments and additional ice. Due to the alteration in Mars' obliquity, the ice sublimated back to the poles and consequently, the surface collapsed causing strange features such as multiple rim rings and central plateaus. Through numerical and physical experimentation, we have shown that the proposed inverted Martian crater process is plausible.

References

[1] Mustard J.F. Head J.W. Kreslavsky M.A Milliken R.E. Marchant D.R.(2003) Geological Observations, Climate Modeling, and Ice Stability: Evidence for a recent Martian Ice Age. *Third Mars Polar Science Conference.* [2] Kargel J.S.* Molina B. Tanaka K.L. (2003) Martian Polar Ice Sheets and Mid-Latitude Debris-rich Glaciers, and Terrestrial Analogs, Gullies, and Long-Term Glacial History; Head J.W. Shean D.E (2003) Tropical Mountain Glaciers on Mars: Evidence for Amazonian Climate Change. [3] François Costard Audouin Dollfus (1987)Thermokarstic Evolution of Impact Craters on Mars. *Lunar and Planetary Science XVIII*, 199. [4] Rene A. De Hon (1987)Ring Furrows: Inversion of Topography in Martian Highland Terrains

Acknowledgments

This project was supported by NASA SHARP program (G.L. Wilt, A. Gillespie), and NASA PG&G and broker facilitator programs (B. McConnell, H. Newsom).

Making a grain-bridge connection between two rocky planets, M.J.(Mauri) McSaveney[1] and T.R.H.(Tim) Davies[2], [1]Institute of Geological & Nuclear Sciences, Lower Hutt, New Zealand,[2]Department of Geological Sciences, University of Canterbury, Christchurch, New Zealand

Big, fast grain flows: A characteristic of large landslides of brittle rock when we look inside their deposits is that formerly intact rock is now gravelly sand. We wondered if this might affect their movement. The literature was decidedly unhelpful; there is universal acceptance of grain flow (grains and flow are irrefutable), but little interest in how grains come about. Where fracturing to produce grains is recognised, it usually is assumed to have occurred at the start of movement. An initial momentary fragmentation episode has certain dynamic implications – it is a scenario optimally achieved to dramatic effect in impact cratering. Converting a large block of hard rock to sand takes an enormous amount of energy, at least half of which is released as the rock breaks; the process is accompanied by an enormous explosion when it is instantaneous. We have compelling evidence that there is no momentary fragmentation episode at the start, fracturing occurs throughout landslide motion, and it affects the flow dynamics. We have generalized the process beyond landslides, to present the hypothesis that grain fragmentation causes hypermobility in a variety of grain flows: rock avalanches, blockslides, fault rupture, crater collapse, and ejecta emplacement. Some folks call it low friction, but it's really hypermobility. Large rock avalanches can travel ~10 km (3.2–32 km) in ~100 s (32–320 s); the bigger ones travel faster and further.

Along with grains, come grain-flow characteristics. Flow is fast (10–100 m/s), but laminar. Structural features in the original rock mass, such as bedding, get stretched and distorted, but remain visible in the deposit from grain to grain. New structures are added at the front and base if the flow erodes the land it passes over. The surface debris behaves as if it has some finite strength while moving: it can carry large boulders; and it will fail in discrete zones of shear, rather than shear being distributed uniformly between all grains. The mass appears to slide as a thin flexible sheet as it flows. With millions to billions of tonnes of rock moving at 10–100 m/s, it is no surprise that momentum and kinetic energy are important; these are not falling feathers or tissues to be strongly affected by their environment.

The fragmenting rock bulks up as it turns to gravelly sand; as the grain mass distorts, grains can rotate relative to one another, opening the gaps between grains, but even "unopened" cracks have finite volume. The initial rock mass may be saturated with water, but the rapid increase in pore volume ensures that little if any of the mobile grain flow can be saturated, even when it encounters water along its path. The bulking is generally about 20%, and makes for a very porous deposit, although the permeability often is low.

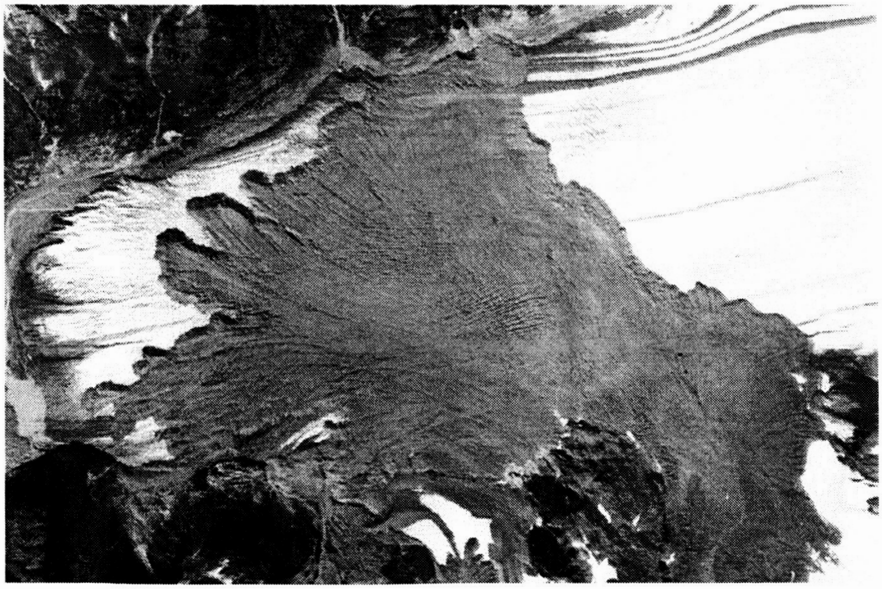

All over in 100 seconds, the 10^7 m^3 Sherman Glacier Rock avalanche of March 1964, was a giant, self-crushing grain flow. Lines on the surface of the debris are grooves parallel to the direction of motion. They indicate that the surface debris had a finite strength and a diverging flow in the last ten seconds or so of motion. Although the landslide contained ice and moved over ice and snow near the melting point, water played no role in the emplacement mechanism. Width of view is about 5·5 km.

The grain-bridge connection: In grain flows, the shearing granular mass develops "bridges" (or arches) – filamentous assemblages of grains aligned in the local direction of maximum compressive strain (at 45° to the local flow direction). Shear strain forces grains together, and stress is transmitted across bridges of grains in contact. The stress arises because the grain bridges are resisting the relative motions of converging grains. Motion stops if the bridges do not fail. In non-fragmenting grain flow, bridges fail by slip between grains, and by rolling of grains.

These control the relative grain motions and give rise to many of the complexities observed in granular flows. Grain-bridge behavior is somewhat unpredictable and bridges are a recognized hazard in industrial grain flows; they stop production, destroy structures and kill people.

A third bridge-failure mechanism has escaped much discussion: if the compressive stress along a bridge is high enough, the weakest grain breaks. This occurs where grains are constrained to limit slip and rotation. This is the mechanism that dominates the behavior of large rapid landslides, and it is the process that converts a large block of rock to powder. A characteristic of breaking brittle rock is a delay between stress application and rupture while microcracks form and propagate. When the stress along a bridge exceeds the compressive strength (elastic limit) of the weakest grain, "super-stressing" is inevitable before the grain explosively disintegrates. An isotropic dispersive stress is transferred to adjacent grains, and while each fragmentation is taking place, the shear resistance within the fragmenting grain volume is vanishingly small or zero. Isotropic dispersion and lowered shear resistance are absent in non-fragmenting grain flows.

The local value of the dispersive stress can be predicted; it is the Hugoniot elastic limit of the rock material at the ambient strain rate and confining stress. It is 1–15 GPa, but no huge explosion is seen, because it is contained within a huge "sand bag". To accomplish the spreading of the 55 x 10^6 m^3 Falling Mountain rock avalanche, we estimate that about one grain in 200 was fragmenting at any instant. In the 1 km^3 Waikaremoana blockslide, about one grain in 35 was fragmenting in the layer of gouge beneath the sliding block to allow it to hit the opposite valley wall at 40 m/s after sliding 1 km on a 7–8° slope. In the moment of impact-crater initiation, almost every grain is fragmenting, but grain fragmentation does not cease with shock-wave dissipation; it continues at a lowering density throughout ejecta-sheet emplacement and crater collapse, until grain flow ceases.

In large grain flows, such as rock avalanches, the fragmenting grains are internal; a carapace of coarser grains reveals the source-rock fracture spacing. The overburden pressure within the carapace is low enough for grain bridges to fail by slip and rotation, without significant grain fracture. A grain-size distribution develops in the fragmenting interior with a fractal dimension of 2.58 indicating that grains have equal probability of failure. Although the grain mass in an ejecta sheet clearly is highly fractured in the moments before ejection, we expect a more finely fragmented interior, beneath a less fragmented carapace from granular flow during emplacement.

A tightly packed grain mass containing all sizes of grains is relatively impermeable, yet a 10^8 m^3 landslide can bulk up by 2 x 10^7 m^3 in ~100 s. Although there is a positive dispersive pressure from the grains, there must be reduced pressure in the void space. At 1–15 GPa in an explosively fragmenting grain, the new void space can be a strong vacuum without limiting the process. Hence, high fluid pressure in the voids is unlikely on any scale useful to the mechanics of emplacement of the deposit. Very large grain flows appear to run as efficiently beneath 10,000 m of seawater as they do on Mars. This possibly is because they can self-regulate the fragmentation density to suit.

How might we use this? The relative motions of grains in large grain flows causes some to break and exert a powerful dispersive pressure within the grain mass. This makes a fragmenting grain flow behave like a heavy vapor. At a high enough fragmenting-grain density, the pressure from fragmenting grains can equal or exceed the weight of overburden. It leads to very high-speed flows of huge masses: the bigger the flow, the greater the fragmentation density, and the faster the flow (and the further it travels). Grain fragmentation is an internal process that is independent of the environment outside the grain flow, and much of the gross morphology of large grain-flow deposits relates to it. One has to look to secondary or tertiary deposit features to infer how a grain flow has interacted with its environment. Here, care is needed because many of the detailed surface features relate only to the last few moments of grain flow, and not to ~99.9% of the duration of motion.

High-energy grain flows can be immensely erosive through grain-bridge connections with their substrate. Anything easily erodible is likely to be eroded, and bringing static mass up to speed takes a lot of energy. In physical models using sand to simulate high-speed, rock-avalanche grain flow, we found that raised distal rims on deposits were formed only in the presence of a thin erodible substrate, and the rim was raised by the eroded material. When models fell on thick erodible substrate, they stopped dead in their tracks. These models were dynamically similar to the last moments of ejecta-sheet emplacement. Hence, we suggest that ejecta sheets with prominent distal rims have run out over a thin erodible substrate. On a thick erodible substrate, we expect the base-surge component to halt quickly, producing a "double-layer" ejecta sheet. The thickness of erodible substrate might vary for a variety of reasons. The presence of a volatile solid, such as water ice, and vapor diffusion along vapor-pressure or thermal gradients, is a ready means of cementing the rubble of past ejecta sheets, to leave a thin, dry, erodible soil in a frigid environment. Cementation is unlikely in the absence of a solute fluid or vapor diffusion.

References: start at - www.gns.cri.nz/who/staff/1723.html

PERCHED CRATERS AND EPISODES OF SUBLIMATION ON NORTHERN PLAINS.

S. Meresse[1], D. Baratoux[2], F. Costard[1] and N. Mangold[1], [1] IDES, UMR 8148, Université Paris-Sud, Bât. 509, 91405 Orsay cedex, France, [2]Observatoire Midi-Pyrénées, UMR 5562, 31400 Toulouse. meresse@geol.u-psud.fr

Introduction: Data from the MOLA instrument have revealed in detail the morphometry and topography of the impact craters and lobate ejecta deposits on Mars. We report in this study the observation of craters in the Northern lowlands where the cavity and the fluidized ejecta blankets are topographically perched above the surrounding terrain. This "perched crater" morphology clearly differs from fresh craters one : the cavity has undergone a filling up over a hundred of meters and the ground at the vicinity of the ejecta seems to be eroded (Fig. 1). Moreover those perched craters can not be considered as pedestal craters. Even if pedestal craters are also topographically perched [1] they never display double layer ejecta morphology (DLE) [1] as we can observe in some perched craters (Fig.1). The diameters of the perched craters are always smaller than 10 km and the cavities are on average 70 meters above the surrounding surface. (Fig. 1-4)

The perched craters have been solely detected between 40° and 70°N and our research was limited to Acidalia and Utopia Planitia. This distribution is consistent with the occurrence of one or several episodes of deflation/erosion in the Northern lowlands. In this study, we focus on morphometric and thermal properties of the discovered morphology with the objective to understand the mechanism of erosion which could preserve the ejecta but erode the intercraters plain. The role of ice-sublimation in this process has also to be determined.

Perched craters. The Utopia/Acidalia surfaces appear to have been modified as indicated by crater's infilling and removal of material in the intercraters plains. The deposits visible in the cavities can result from many origins (volcanic ash, eolian activity [2]). The removal of material is interpreted to be responsible for the observed perched crater morphology. The loss of material happens around the ejecta blankets and decreases the pre-existing surface. This decreasing of surface's altitude is most likely caused by cryokarstic process like the sublimation in the plains, combined with a possible wind deflation of the fines

Thermal properties of perched ejecta. Thermal inertia is the key property controlling diurnal temperature variations at the surface of Mars and represents the subsurface's ability to store heat during the day and to re-radiate it during the night [3-5]. We used the brightness temperature derived from the band 9 (12.56µm) of the THEMIS infrared images to compare the thermal properties of the perched ejecta with the surrounding terrain. At night, the ejecta deposits are colder than the surrounding terrain. They display temperatures close to 182°K while the temperature of the intercraters plains are always above 189°K at the same local time (i.e. 4.7 for these values). During the day, the temperature differences are less striking, but daytime temperature are more affected by albedos and local topography, and are thus more difficult to interpret in terms of relative variations of thermal inertia.

The variations of diurnal temperature are relatively more important inside the ejecta units than elsewhere. Ejecta blankets are characterized by a lower thermal inertia. Thermal inertia variations are often related to grain size variations [3-5]. Indeed, this physical parameter is actually controlled by the porosity and the sizes of the pores of the geological material which are influenced by the grain sizes, but also by processes such as cementation or induration. We interpret the lower thermal inertia of ejecta as a presence of a thin layer (up to a few meters) of porous and isolating material. This porous layer (low thermal conductivity) could result from the ejecta formation and fragmentation process and/or the absence of the superficial ice layer filling the porosity anywhere else in the northern lowlands, as detected by the Mars Odyssey experiment. Contrary to the ejecta, the surrounding terrain conducts the heat more efficiently. We can suppose that it is cemented by the ice which increase the thermal inertia (hotter temperature at night) and conductivity and decrease the porosity. Acidalia is besides among a unit who has thermal inertia values consistent with surfaces of very coarse-grained or highly indurated materials. Its values are likely due to surface exposures of water [5]

Role of ice-sublimation. We propose that the lower conductivity of the ejecta units induce a lower rate of ice sublimation than in the intercraters plains. The ejecta layer is seen as an isolating layer and the ice underneath the ejecta is protected from sublimation during the warmest periods of the year. Then, the higher rate of sublimation in the plains, combined with a possible wind deflation of the fines would result in the observed differential erosion morphology (Fig. 5). This hypothesis is consistent with the observation of disaggregating ice-cemented dust in the 30-70°N latitude range [6].

We also focus on the development of systematic morphometric analyses on perched crater in orders to assess the thickness and volumes of removed material.

According to our measurements from the MOLA data, (Fig. 2 and 3) we report a thickness of 50 meters.

Conclusion. Future work will focus on the description of the different states of degradation of the perched craters with the objective to assess the chronology, duration and importance of the different phases of erosion. We have already noticed the existence of a diversity of states of degradation. Perched craters with highly degraded ejecta or even no ejecta with the rims being the only remnants of the craters have been observed (Fig. 4). We will also develop a model of sublimation based on the values of conductivity and thermal skin depth. The study of these craters is aimed to assess the chronology and importance of the phases of erosion/deflation and removal of the material which have re-shaped the Northern lowlands.

Acknowledgements: This work is supported by PNP-INSU.

References: [1] Barlow et al. (2000) *JGR 105, E11, 26733.* [2] Forsberg-Taylor et al. (2004) *JGR 109,* doi:10.1029/2004JE002242. [3] Mellon M.T. (2001) *Exploring Mars with TES: A data user's workshop.* [4] Mellon et al. (2000) *Icarus 148,* 437-455.[5] Putzig et al. (2005) *Icarus 173,* 325-341..[6] Mustard J.F. and Cooper C.D. (2001) *Nature 412,* 411-414.

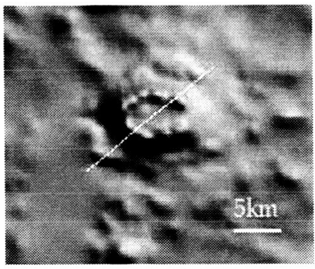

Figure 3. Perched crater in Acidalia Planitia (53,1°N 325°E). the ejecta have totally disappeared. The cavity and the rims are topographically perched as we can see on figure 4.

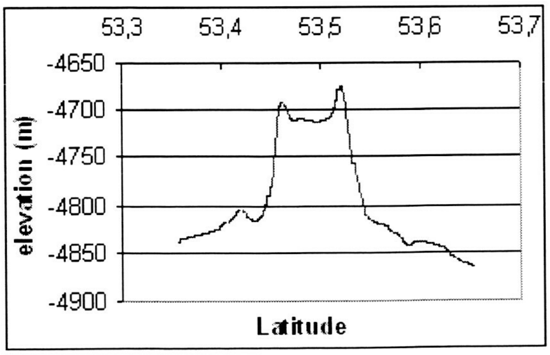

Figure 4. MOLA cross section. White line in figure 3 indicates its location.

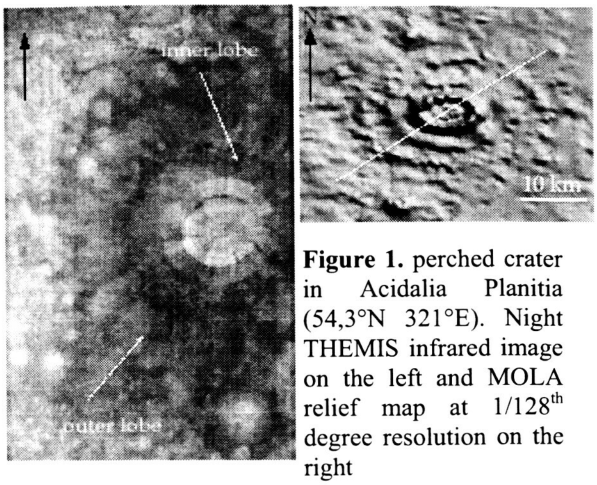

Figure 1. perched crater in Acidalia Planitia (54,3°N 321°E). Night THEMIS infrared image on the left and MOLA relief map at 1/128th degree resolution on the right

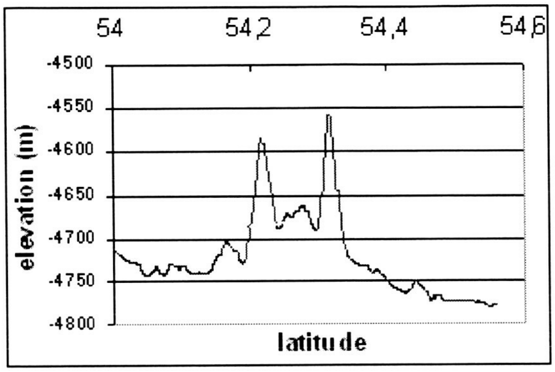

Figure 2. MOLA cross section of the perched crater. White line in figure 1 indicates its location.

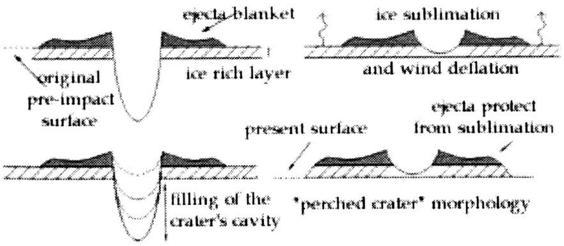

Figure 5. Synthetic sketch showing the resurfacing process in the Northern lowlands.

CHARACTERISTICS OF IMPACT CRATERS AND INTERIOR DEPOSITS: ANALYSIS OF THE SPATIAL AND TEMPORAL DISTRIBUTION OF VOLATILES IN THE HIGHLANDS OF MARS.

S.C. Mest, Planetary Geodynamics Laboratory (Code 698), NASA Goddard Space Flight Center, Bldg. 33, Rm. F320, Greenbelt, MD 21071, mest@kasei.gsfc.nasa.gov.

Introduction: The martian southern highlands contain impact craters that display pristine to degraded morphologies, and preserve a record of degradation that can be attributed to fluvial, eolian, mass wasting, volcanic and impact-related processes. However, the relative degree of modification by these processes and the amounts of material contributed to crater interiors are not well constrained.

Impact craters (D>10 km) within Terra Cimmeria (0°-60°S, 190°-240°W), Terra Tyrrhena (0°-30°S, 260°-310°W) and Noachis Terra (20°-50°S, 310°-340°W) are being examined to better understand the degradational history and evolution of highland terrains. The following scientific objectives will be accomplished. 1) Determine the geologic processes that modified impact craters (and surrounding highland terrains). 2) Determine the sources (e.g. fluvial, lacustrine, eolian, mass wasting, volcanic, impact melt) and relative amounts of material composing crater interior deposits. 3) Document the relationships between impact crater degradation and highland fluvial systems. 4) Determine the spatial and temporal relationships between degradational processes on local and regional scales. And 5) develop models of impact crater (and highland) degradation that can be applied to these and other areas of the martian highlands. The results of this study will be used to constrain the geologic, hydrologic and climatic evolution of Mars and identify environments in which subsurface water might be present or evidence for biologic activity might be preserved.

Methodology: This research utilizes multiple data sets to accomplish the objectives stated above. Images (Viking Orbiter, MOC, and THEMIS vis and IR (day)) are being analyzed to characterize (a) the preservation states (e.g., "fresh", "degraded", "moderately degraded", "highly degraded", and "buried" or "exhumed" [1-3]) and (b) interior deposits of craters. MOLA data and the IDL module GRIDVIEW [4] are being used to estimate morphometric parameters for craters (e.g., diameter, depth, slopes), regional and local slopes, and thicknesses and volumes of crater interior deposits. THEMIS infrared images and TES data are being used to characterize surface properties (e.g., emission, roughness) of crater interior deposits, and the Mars Observer GRS is being used to observe the distribution of surficial hydrogen. These data sets will be used to produce detailed geologic and geomorphic maps of individual impact craters, especially those containing enigmatic deposits, as well as maps at local and regional scales. Individual craters, such as Terby, Rabe, Proctor, Schaeberle, Schroeter, Martz, Gale and several unnamed craters, that are well-covered Mars data, will be mapped in detail. Mapping could determine if similar degradation styles were common, such as by precipitation-driven processes or by a regional mantling unit [5,6] that contributes material to crater floors via mass wasting, or differ from crater to crater, suggesting mostly localized processes were (are) active. Relative age relationships for crater interior deposits will be determined by calculating crater size-frequency distribution statistics.

Observations: Extensive evidence that fluvial, mass wasting, eolian, volcanic and impact-related processes were involved in degradation, infilling and subsequent erosion of impact craters are preserved in the highlands of Noachis Terra, Tyrrhena Terra and Terra Cimmeria.

Fluvial systems dissect large parts of these highland terrains; their tributaries erode crater rim and ejecta materials and breach the rims of some craters. The interior walls of many craters are incised with gullies. Some gullies head at or near crater rims, suggesting erosion by precipitation-derived runoff [1,7-10], whereas other gullies originate at discrete layers along crater walls [11]. Some craters contain small valley networks along their rims, which resulted in emplacement of alluvial fans [12,13] on their floors. The presence of these features suggests fluvial processes were a key factor in crater degradation.

Many highland craters contain lobate debris aprons (Late Hesperian to Amazonian) that extend onto their floors, suggesting volatile-driven mass wasting also actively modified crater interiors and contributed significant amounts of material to crater floors. Mass wasting may have been an equally important process of crater degradation, especially in the highlands northeast and east of Hellas basin [14-18] where volatiles appear to have been abundant, and less important in other areas where volatiles may have been spatially or temporally less abundant [7-9,10].

Dune fields and dark splotches within craters, such as Rabe and Proctor [19], indicate eolian processes may contribute, or at least redistribute, significant quantities of sediments to interior deposits [7-10].

Many craters could also contain materials deposited within lacustrine or playa environments. Morphologic evidence - inflow and outlet valleys, layered deposits, deltas, sedimentary terraces, and shorelines - suggests some martian craters may have contained lakes [9,10,20-25].

Several craters, such as Millochau [9], Terby [26-28], Schaeberle, Schroeter and several large unnamed craters [9,29,30], contain enigmatic interior deposits relative to nearby craters of similar size or age. Some deposits are layered and form plateaus that stand hundreds of meters above surrounding floor materials or in some cases are topographically higher than the crater's rim, such as Gale [31]. Many craters also contain pits, suggesting collapse of volatile-rich material, and (or) they contain deposits that display surfaces that have been modified more significantly than nearby craters of similar size and age.

Several impact craters north and west of Hellas basin contain surface materials that display similar surface textures. One deposit in particular, 'rugged material' mapped in Millochau [9], displays a 'stucco-like' surface texture, is typically found along the outer edges of the crater interior and generally slopes down from the crater wall toward its center. The characteristics of this unit, combined with the fact that it is usually found in craters with gullied interior walls, suggest it may consist of heavily degraded fluvial deposits and (or) mass wasted materials. Similarly, the surfaces of many plateaus and massifs that compose enigmatic crater deposits are generally similar in appearance to the 'pitted material' observed in Millochau [9].

Discussion: Many highland impact craters exhibit evidence that they were modified (eroded and infilled) to various degrees by multiple geologic processes. The morphologies of most craters and the deposits preserved on their floors suggest significant quantities of volatiles were involved, either atmospherically-derived and (or) released from the subsurface. However, the nature of the processes varies spatially and temporally across relatively short distances (100's of kilometers) of the highlands. For example, Promethei Terra (east of Hellas basin) displays large relatively young debris aprons, small Hesperian-aged valley networks, and large outflow systems [14-18], whereas adjacent Tyrrhena Terra (north of Hellas basin) is dissected by extensive Noachian-aged valley networks, contains enigmatic crater interior deposits, and lacks debris aprons [9,10]. In addition, craters that contain similar features (pits, plateaus, etc.) and (or) deposits similar in appearance suggest either emplacement of similar materials (and sequences of materials) and (or) the processes of emplacement and subsequent modification were widespread. It is the ongoing goal of this research to use all available Mars data to identify deposits associated with specific source areas and determine the process(es) of their erosion and emplacement, quantify crater interior deposits (i.e., thickness, volume), and correlate crater degradation processes locally and regionally to spatially and temporally constrain volatile distribution as well as assess climate change on Mars.

References: [1] Craddock R.A and A.D. Howard (2002) *JGR*, **10** , doi:10.1029/2001JE001505. [2] Frey H.V. et al. (2000) *LPS XXXI*, Abs. **#1** . [3] Barlow N.G. (2003) *Sixth Int. Conf. on Mars*, Abs. **9** . [4] Roark J.H. et al., (2000) *LPS XXXI*, Abs. **206** . [5] Milliken R.E. and J.F. Mustard (2003) *Sixth Int. Conf. on Mars*, Abs. **30** . [6] Mustard J.F. et al. (2003) *LPS XXXIII*, Abs. **#28** . [7] Grant J.A. and P.H. Schultz (1993) *JGR*, **9** , 11025-11042. [8] Grant J.A. (1999) *Internatl. J. of Impact Eng.*, **23**, 331-340. [9] Mest S.C. and D.A. Crown (2005) *Icarus*, doi:10.1016/j.icarus.2004.12.008, in press. [10] Mest S.C. and D.A. Crown (2005) *Geol. Map of MTM -20272 and -25272 Quadrangles, Tyrrhena Terra Region of Mars*, U.S.G.S., in review. [11] Malin M.C. and K.S. Edgett (2000) *Science*, **28** , 2330-2335. [12] Howard A.D. and J.M. Moore (2004) *LPS XXXV*, Abs. **#12** . [13] Moore J.M. and A.D. Howard (2004) *LPS XXXV*, Abs. **#4** . [14] Crown D.A. et al. (1992) *Icarus*, **10** , 1-25. [15] Mest S.C. and D.A. Crown (2001) *Icarus*, **15** , 89-110. [16] Mest S.C. and D.A. Crown (2002) *Geol. Map of MTM -40252 and -40257 Quadrangles, Reull Vallis Region of Mars*, U.S.G.S. Geol. Invest. Ser. Map I-2730, scale 1:1M. [17] Mest S.C. and D.A. Crown (2003) *Geol. Map of MTM -45252 and -45257 Quadrangles, Reull Vallis Region of Mars*, U.S.G.S. Geol. Invest. Ser. Map I-2763, scale 1:1M. [18] Pierce T.L. and D.A. Crown (2003) *Icarus*, **16** , 46-65, doi:10.1016/S0019-1035(03)00046-0. [19] Fenton L.K. et al. (2003) *JGR*, **10** , doi:10.1029-2002JE002015. [20] Newsom H.E. et al. (1996) *JGR*, **10** , 14951-14955. [21] Grin E.A. and N.A. Cabrol (1997) *Icarus*, **10** , 461-474. [22] Forsythe R.D. and C.R. Blackwelder (1998) *JGR*, **10** , 31421-31431. [23] Cabrol N.A. and E.A. Grin (1999) *Icarus*, **12** , 160-172. [24] Cabrol N.A. and E.A. Grin (2001) *Icarus*, **19** , 291-328. [25] Grant J.A. and T.J. Parker (2002) *JGR*, **10** , doi: 10.1029/2001-JE001678. [26] Ansan V. and N. Mangold (2004) *2nd Conf on Early Mars*, Abs. **8** . [27] Howard A.D. et al. (2004) *2nd Conf on Early Mars*, Abs. **3** . [28] Wilson, S.A. and A.D. Howard (2005) *LPS XXXVI*, Abs. **20** . [29] Korteniemi, J. et al. (2005) *LPS XXXVI*, Abs. **#0** . [30] Moore J.M. and A.D. Howard (2005) *LPS XXXVI*, Abs. **#52** . [31] Edgett K.S. and M.C. Malin (2001) *LPS XXXII*, Abs. **#6** .

Run-Out Distances of Ejecta Lobes from SLE and MLE Impact Craters on Mars.

Peter J. Mouginis-Mark[1] and Stephen M. Baloga[2], [1]Hawaii Institute of Geophysics and Planetology, University of Hawaii, Honolulu, Hawaii, 96822 ; [2]Proxemy Research, Inc.

Introduction: In an effort to gain better insight into the emplacement mechanism of the ejecta for single layered ejecta (SLE) and multiple layered ejecta (MLE) craters on Mars [1], we are investigating the geometry of the distal ramparts of these craters. Using topographic data from individual orbits of the MOLA instrument, and co-registering these data with 18 m/pixel THEMIS VIS images, we have compiled a data base that includes the run-out distance from the rim crest of the parent crater for many ejecta ramparts. These distances are the extreme values for which rampart heights can be accurately measured. Because many of the ejecta deposits are quite lobate [2,3], some craters have segments of deposits that extend slightly farther than the values we obtained. Nevertheless, our data base is suitable for exploring the influence of elevation and latitude on run-out.

Global Trends in Ejecta Range: We have measured the range from the parent crater rim crest and height of the ejecta ramparts for 32 different impact craters on Mars. Our criteria for making such measurements were that individual MOLA shots had to lie on both the crest of the rampart and close (~1 km) to the foot of the rampart on both the up-slope and down-slope sides of the unit. The range of measured crater diameters was from 11.0 – 35.9 km. Our sample craters lie in the latitude range 35.9°N to 25.1°S, so all examples can be considered low-latitude craters. Target elevations range from –3,867 m to +3,410 m. We find that, although latitude and elevation may be important secondary influences on the ultimate range of the ejecta flow, the dominant behavior is a limitation in the run-out at ~3.0 – 3.5 crater radii from the rim crest of the parent crater (Fig. 1a) for all diameters in the range considered. Also apparent is the decrease in rampart height as the distance traveled from the rim crest increases (Fig. 1b).

Local Variations in Ejecta Range due to Pre-existing Topography: For one 18.8 km dia. SLE crater, located in Sinai Planum (at 21°S, 285°E), we have been able to make 15 measurements to observe the influence of local topography on the flow distance of the ejecta, as well as the height of the rampart. This crater formed on a gentle slope, and it is clear that the ejecta flows traveled further where the elevation difference between the crater rim crest and the distal rampart is greatest (Fig. 2). We find that a clear correlation exists between these two parameters; namely, ejecta flowed further from the crater rim when the local elevation change was greater; when the change was ~200 m, the ejecta traveled only ~16 – 18 km, while for a height drop of ~500 m the ejecta traveled ~26 – 28 km.

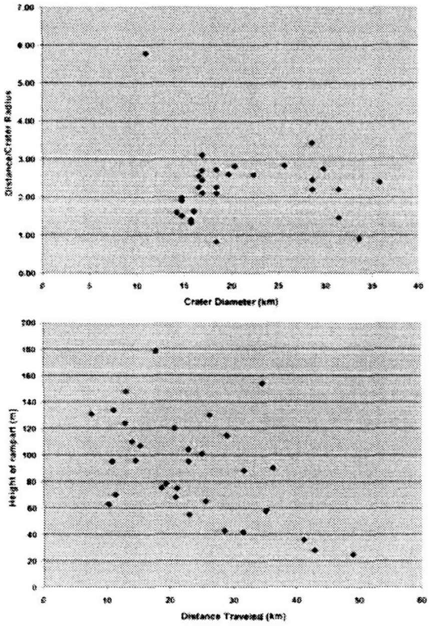

Fig. 1: Top (a): Ejecta range for all 32 craters studied here, expressed as a ratio of the run-out distance compared to the radius of the parent crater. Bottom (b): Rampart heights as a function of distance from rim crest of crater.

We observe that rampart height is also variable, in the range 80 – 160 m. Typically, height decreases with increasing radial range for the ejecta (Fig. 3), as would be expected due to the areal change with distance.

Shape of the Distal Rampart: We have also investigated the cross-sectional shape of the distal rampart. We have developed a photoclinometric technique that can be applied to small segments (<~3 km long profiles) of THEMIS VIS images, using individual MOLA groundtracks to provide the start- and end-elevation points. The photometry can also be checked along the profile using additional MOLA groundtracks that provide "ground truth" for the profile via spot elevation measurements along the length of the profile. In this manner, we have measured the cross-sectional shape of several distal ramparts for the Sinai Crater (Fig. 4).

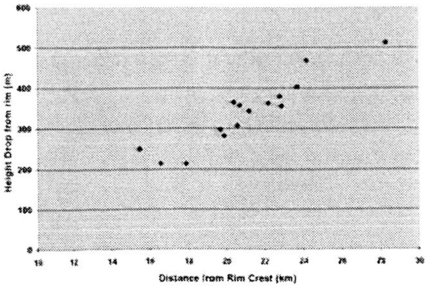

Fig. 2: Comparison of the height drop between the foot of the ejecta rampart and the rim crest of the parent crater compared to the distance that the ejecta have traveled from the rim crest of the parent crater.

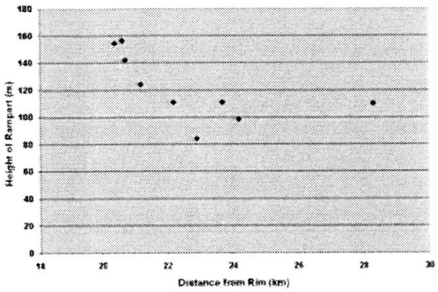

Fig. 3: Rampart height decreases as the ejecta travel a greater distance from the parent crater rim crest.

In all cases, we find that the rampart has a steeper slope on the down-slope direction (Fig. 4b). We also observe that the rampart constitutes virtually the only ejecta within the visible ejecta blanket; specifically, the elevation of the terrain up-slope (i.e., towards the parent crater) is within a few (<4) meters of the elevation of the down-slope terrain (i.e., beyond the ejecta blanket). These observations are thought to have particular significance for the surface flow of the ejecta, in that almost no ejecta were deposited during surface flow until the terminal rampart is formed.

<u>Conclusions and Implications for Future Crater Studies</u>: Our data, while preliminary and sampling only a few SLE and MLE craters, indicate certain attributes for the emplacement of distal ramparts:

1) Run-out distances appear to be affected by local elevation changes of a few tens to hundreds of meters. This implies that gravity influenced the flow as in an unconfined continuum fluid flow, either as a direct gravitational force during overland flow or through a fluid dynamic pressure term acting on spatial gradients during emplacement.

2) The ramparts constitute the only constructional part of the distal ejecta blanket, with almost no up-slope material within the ejecta blanket. We find no evidence of a thick ejecta layer up-slope from the rampart in most of the examples studied so far.

3) The asymmetric cross-sectional shape of the rampart is comparable to deceleration lobes found on terrestrial landslides [4], and implies significant strength for the materials within the rampart such that these materials did not slump following the cessation of the impact cratering process.

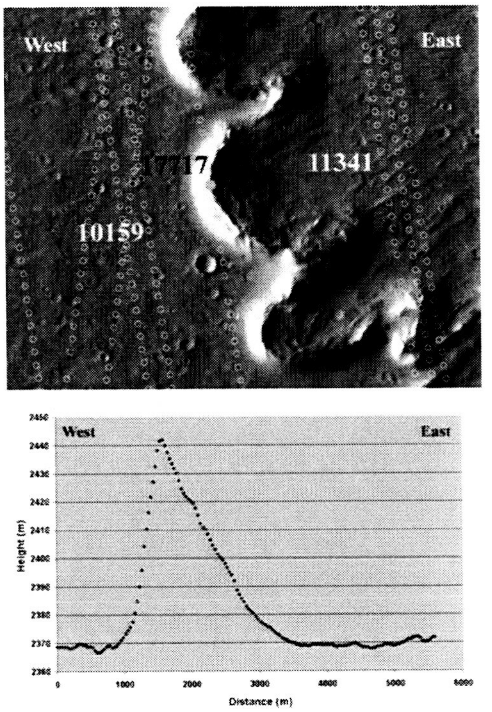

Fig. 4: Top (a) Part of THEMIS image V05808002, showing the location of the MOLA profiles. Red dots mark the start and end of profile shown in 4b. Direction of ejecta flow is from the top right (NE). Bottom (b) Photclinometric profile across the distal rampart of the Sinai Crater. Profile is "anchored" by MOLA orbit 10159 in west, and MOLA orbit 11341 in east. "Validation" of the correct photometric function is provided by the elevation from MOLA orbit 17717, which crosses the crest of the rampart (blue dot).

References: [1] Barlow, N. G. et al. (2000), *JGR* 105: 26,733 – 26,738; [2] Mouginis-Mark, P.J. (1978), *Nature* 272: 691 – 694; [3] Barnouin-Jha, O. S. and P. H. Schultz (1998), *JGR* 103: 25,739 – 25,756; [4] Shreve, R. L. (1968), GSA Sp. Pub. 108, 47 pp.

HYDROTHERMAL PROCESSES AND MOBILE ELEMENT TRANSPORT IN MARTIAN IMPACT CRATERS — EVIDENCE FROM TERRESTRIAL ANALOGUE CRATERS.

H. E. Newsom[1], M. J. Nelson[1], C. K. Shearer[1], and B. O. Dressler[2], [1]Univ. of New Mexico, Institute of Meteoritics, Dept. of Earth & Planetary Sci., Albuquerque, NM 87131, USA newsom@unm.edu, [2]185 Romfield Circuit, Thornhill, Ontario, L3T 3H7, Canada.

Introduction: Hydrothermal alteration and chemical transport involving impact craters probably occurred on Mars throughout its history. [1]. Our studies of alteration products and mobile element transport in ejecta blanket and drill core samples from impact craters show that these processes may have contributed to the surface composition of Mars [2]. Recent work on the Chicxulub Yaxcopoil-1 drill core has provided important information on the relative mobility of many elements that may be relevant to Mars [3].

The Chicxulub impact structure in the Yucatan Peninsula of Mexico and offshore in the Gulf of Mexico is one of the largest impact craters identified on the Earth, has a diameter of 180-200 km, and is associated with the mass extinctions at the K/T boundary. The Yax-1 hole was drilled in 2001 and 2002 on the Yaxcopoil hacienda near Merida on the Yucatan Peninsula. Yax-1 is located just outside of the transient cavity, which explains some of the unusual characteristics of the core stratigraphy. No typical impact melt sheet was encountered in the hole and most of the Yax-1 impactites are breccias. In particular, the impact melt and breccias are only 100 m thick which is surprising taking into account the considerably thicker breccia accumulations towards the center of the structure and farther outside the transient crater encountered by other drill holes.

SIMS studies of mobile element transport: Clays in thin sections from crater drill cores were imaged and analyzed by microprobe for major elements. Trace elements Li, B, Be, and Ba were measured with the Cameca IMS 4f ion probe, using primary O^- ions, a 10 kV potential; a primary beam current of 10 nA and spot diameter of 8 to 10 μm. Numerous standards were analyzed to verify the ability of the SIMS to analyze water-bearing mineral phases, and to show the absence of matrix effects.

Results: The altered groundmass found between clasts of target rocks contain materials with a desiccation texture characteristic of clays. The chemistry of the clays in thin section and preliminary XRD data on separated clays are consistent with smectite at all depths [4, 5]. The chemistry of these alteration materials range from that of an average montmorillonite composition in the uppermost units (from 800.68m to about 836m), to that of a magnesium rich saponite in the lower units (846.7m to 861.72m).

The clay analytical data show interesting trends as a function of depth in the drill core (e.g. **Figs. 1-3**). The elements Li, B, and Be, FeO generally increase upwards in the samples, with Li > B > Be >FeO while the Ba concentration in the clays decreases upwards. The abundance of Al_2O_3 in the clay material is also significantly higher in the suevite than in lower units, even though Al_2O_3 is not usually considered a fluid mobile component. Li in Unit 2 is enriched by factors of 1.1 to 3.5 relative to the lower units. There is a strong correlation between the abundances of Li, Be, and B (e.g. **Fig. 1**). The correlation coefficients among these elements are Li-B = 0.89, B-Be = 0.71, Li-Be = 0.50.

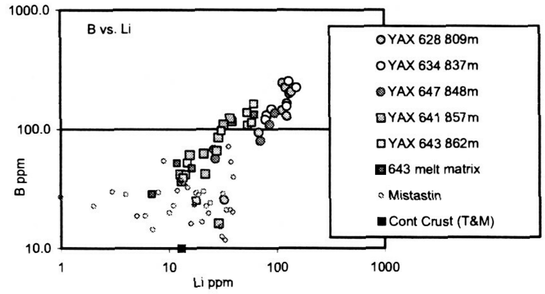

Fig. 1. Boron and lithium abundances in Chicxulub Yaxcopoil-1 matrix clays.

The concentrations of mobile elements determined by SIMS in clays in the Yaxcopoil drill core can be compared with bulk analyses of the impact breccias by Tuchscherer et al., [5]. Although, the types of samples from the core that were analyzed are not identical, a consistent behavior can be seen in the data for a number of mobile elements. For example, in the bulk analyses of the drill core, Tuchscherer et al., [5], documented upward enrichments in the concentration of the trace elements in the relative order Cs > Au > Rb = Zn in stratigraphic units 1 to 4 . The greatest upward increase in this data set is for Cs, which increases a factor of up to 3.7 relative to the lower units, similar to the SIMS data for Li.

Mobile element deposition in sediments above the impactites: Evidence for hydrothermal transport has also been presented by Rowe et al. [6], who studied mobile element concentrations in the sediments overlying the impact breccias. Rowe et al., [6] found that samples of Tertiary biomicrites from depths of 794.01 to 777.02 m have higher concentrations of Mn, Fe, P, Ti, and Al relative samples from higher up in the stratigraphic section. They attribute the observed enrichments to elements mobilized by hydrothermal systems in the impact deposits and deposited in the overlying sediments, analogous to hydrothermal deposits in mid-ocean ridge environments. At the Ries crater, Förstner, [7] found a similar enrichment of mobile elements in the graded sandstones and breccias derived from reworked suevite that was deposited in water in a playa lake environment just above the suevite deposits. The clay-size fraction (< 2 μ) in the lowest sediment sample is enriched in Li, Cd and Na compared to the rest of the sediment higher up in the sediment column.

Discussion: The SIMS data for Li and Be presents a convincing argument for hydrothermal transport. The upper impactite layers are distinctly enriched in these elements compared to the lower units. The data of Rowe et al. [6] for Li and Be show enrichments in the sediments directly above the impact breccias (**Figs. 2, 3**). The explanation for the behavior of these trace elements seems very straightforward, involving partitioning of the trace elements into hydrothermal fluids, with incorporation into clays formed during hydrothermal alteration in the impact breccias, and deposition with the earliest sediments on top of the impact breccias. Our SIMS data for B and the bulk data of Tuchscherer et al., [5] for Cs, Au, Rb, and Zn shows a similar pattern of enrichment to Li and Be in the impact breccias, suggesting that these elements should also be enriched in the sediments above the impact breccias. A mass balance calculation using the bulk data [5, 6] suggests that the extra Li in the sediments above the impact breccias represents less than 7.5% of the remaining Li in the clays in the impact breccias (units 2-5), and the extra Be in the sediments above the impact breccias represents less than 2.2% of the Be in the clays in the impact breccias (units 2-5). Unfortunately, we do not have Li and Be data on bulk samples from the impact breccias.

Implications for Mars: Hydrothermal alteration occurs in ejecta blankets, impact melt sheets and beneath the floor of impact craters of different sizes. The Lonar crater, India, represents nearly the smallest size crater to experience significant hydrothermal processes, but mobile element transport is not seen in our SIMS analyses of the drill cores [8, 9]. Small impact craters in sedimentary targets, like the Bosumtwi and Ries craters, do not seem to have as much impact melt, but hydrothermal processes probably still occur. The drill cores from the Bosumtwi crater Ghana (11 km diameter) that was drilled in September of 2004 will provide new information on hydrothermal processes in an intermediate sized crater emplaced in meta-pelites. Studies of element mobility in drill core samples from the large Chicxulub impact crater shows that if water is available, cratering processes can transport and enrich mobile elements in the surface of planets such as Mars [e.g. 3]. The mobile element transport studies on the Yaxcopoil-1 core suggest that the elements Li and Ce will be the most enriched elements in hydrothermal deposits associated with martian craters, but B, Be, Au, Rb, Zn, Mn, Fe, and P will also be enriched.

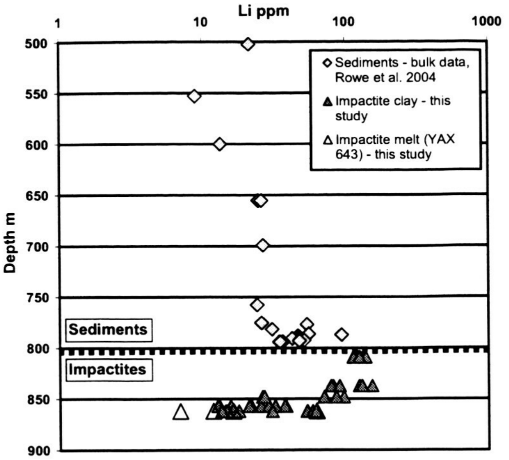

Fig. 2. SIMS results for Li, as a function of depth.

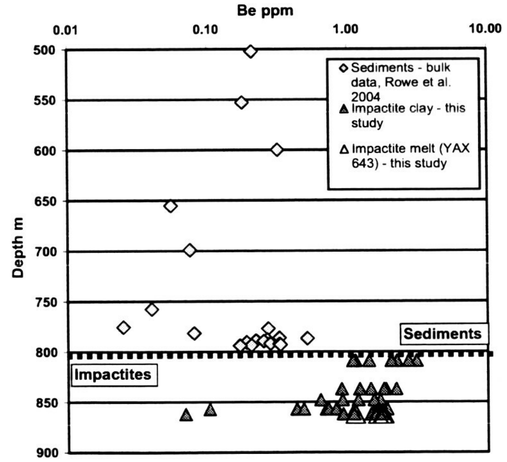

Fig. 3. SIMS results for Be, as a function of depth.

References [1] H.E. Newsom et al., (2001) *Astrobiology, 1*, 71-88. [2] Nelson M. J., Newsom H.E. and Draper D. S. (2005), GCA in press. [3] Newsom et al., (2005) submitted. [4] Nelson et al., (2004) MAPS. 67th Annual Meteoritical Society Meeting, Rio de Janeiro. Brazil,. Aug. 2-6, 2004, #5214. [5] Tuchscherer M. G., et al. (2004). *MAPS 39,* 899-930. [6] Rowe A. J., et al. (2004) *MAPS 39,* 1223-1231. [7] Förstner V. U. (1977) *Geologica Bavarica* 75:37-48. [8] Hagerty and Newsom and (2003) MAPS, *38,* 365-381. [9] Newsom et al., (2005) Lunar Planet Sci. XXXVI, #1143.

Research supported by the NASA Planetary Geology and Geophysics program (NAG 5-10143, H. Newsom P.I.).

Nuclear Cratering Experience in the U.S. and Russia. Milo D. Nordyke, Lawrence Livermore Laboratory (ret.), Livermore, CA, 94551, nordyke@comcast.net

From 1960 to the mid-70s, both the U.S. and Russia carried out a number of nuclear cratering experiments as well as an array of low-yield high explosive cratering tests in a variety of geologic environments which provided useful data on understanding the mechanics of terrestrial explosive cratering. Whereas the majority of U.S. nuclear cratering experiments were in relatively dry unsaturated environments, the Russian tests were in relatively high moisture content or saturated conditions. The results show that larger craters were formed initially, followed by varying degrees of slope failure resulting from the saturated conditions and readjustment of the crater slopes.

However, comparison of the data shows a good correlation when the differences in the geologic conditions are considered. Of special interest to studies of meteoritic craters may be the large yield craters in the saturated coral of Bikini and Enewetak Atolls and the development of numerical tools for predicting the effect of the water-saturated and other more unstable environment.

THE INFLUENCE OF WATER ON THE CRATERING AND MODIFICATION OF MARINE-TARGET CRATERS — SOME THOUGHTS BASED ON RECENT FIELD STUDIES AND LABORATORY EXPERIMENTS.

Jens Ormö. Centro de Astrobiologia (CAB), INTA/CSIC, Ctra de Torrejón a Ajalvir, km 4, 28850 Torrejón de Ardoz, Madrid, Spain. (ormo@inta.es)

Introduction: The most common target for impacts on Earth is volatile-rich, i.e. seawater. Depending on magnitude, the crater may form only in the water column, hence without being preserved, or reach into the seafloor, and form what is sometimes called a marine-target crater [1]. The effect on the crater morphology and geology may be strong if the water depth exceeds the diameter of the impactor [2], but depending on the strength of the substrate also much less water can have great influence [1,3,4].

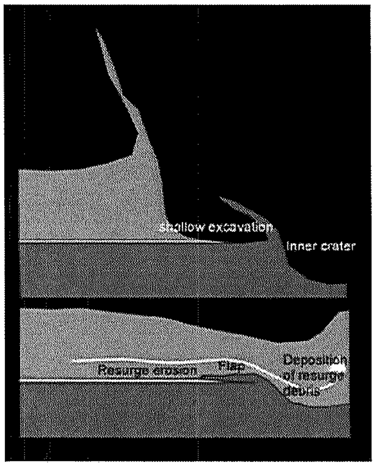

Fig. 1. Higly schematic illustration of excavation and modification at impact into deep water (Water depth exceeding projectile diameter)

Influence on excavation and ejecta dynamics: At great target water depth much of the upper part of the crater may develop in the water column. This reduces the extent of the excavation zone into the seafloor. Water will constitute most of the ejecta, and a relatively large part of the preserved crater is caused by displacement. The Lockne crater, Sweden, illustrates an impact into relatively deep water (i.e., water depth exceeding projectile diameter)[2]. Lockne has a 7.5 km wide basement crater surrounded by a 2.5 km wide brim where water and sediments were removed before the deposition of wide ejecta flaps from the nested basement crater. 3D modeling of the Lockne event shows that the basement crater was generated by a high velocity water stream initiated by the shock wave through the water. Consequently, the crater center lies between the point of initial projectile/water contact and a point near the rim of the transient basement crater where the projectile hits the seafloor [5]. A comparison between the very symmetrical ejecta flaps and the asymmetric ejecta curtain shows that the flaps are formed by overturning of near-surface layers, and not by the ejecta curtain [5]. A simplified illustration of a deep water impact is given in Fig. 1.

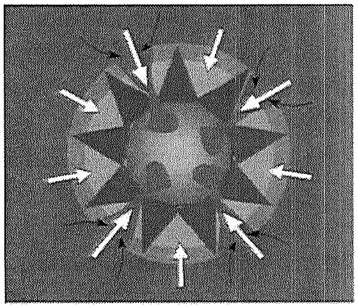

Fig. 2. Schematic illustration of the water resurge at deep water crater. The resurge is channeled by ruptures in the flaps. The darker the shade of blue the deeper water.

Tangential stresses acting on the semi-coherent flaps as they were overturned outwards from the crater generated wedge-shaped rip-a-part openings that later channeled the water resurge [6] (Fig. 2). A detailed study of the variations in elevation of the top of the crystalline basement (i.e., the sub-Cambrian peneplain) around the crater showed that there is no structural rim uplift of the basement below the flaps [7]. It is possible that this is an effect of the cratering driven by the high velocity water stream (i.e., less fracturing and breccia injection). In land-target craters structural uplift is responsible for about half of the rim height [8]. The ejecta around Lockne may have been distributed to great distances by the outgoing water surge and again redistributed by the subsequent resurge into the crater [5]. Possible evidence for ground-hugging flow (fluidized ejecta) and distant influences from the resurge have been reported from locality "Hallen" about 45 km southwest of the Lockne crater center [9]. There, a matrix-supported breccia occurs as a large clast in a reworked ejecta layer. At this distance from the crater the water depth to the seafloor on which the ejecta was deposited, was the same as the target water depth (i.e., about 700 m). Hence, it was assumed that this chunk would have been part of a more coherent ejecta flow passing out over the surface of the sea and then sunk through the water column disintegrating on the way down [9].

At water depths much less than the impactor diameter the growth of the transient cavity follows what is known from the "standard" land-target case and the water is just another layer in the formation of the overturned flap [2]. It is likely that the close interaction between the water and the solid ejecta in the ejecta curtain will cause fluidized ejecta flow outwards from the crater. However, these deposits would be reworked by the water resurge. None of the known marine-target craters has, so far, revealed unequivocal evidence of fluidized ejecta, although this is probably just an effect of a combination of poor preservation, poor exposure, and insufficient studies.

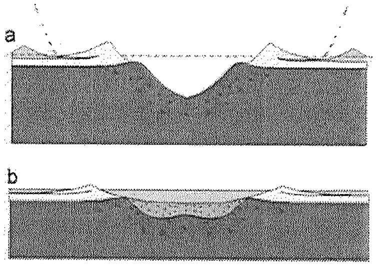

Fig. 3. Schematic cross section of shallow water impact (Modified from [1]

Influence on crater modification: At relatively deep target water the water cavity will be larger than the seafloor crater, and the rim (possibly lacking a structural uplift) will be no obstacle for the resurge flow. This flow will be highly erosive [10,11] and further increase the existing openings in the flaps. It will cause a deposit of reworked ejecta covering large areas outside the crater, but also as a thick unit inside the nested, basement crater, thus adding to the "normal" breccia lens. At relatively shallow water depth, the rim of the crater is better developed (including structural uplift), and, naturally, the surrounding water that wants to reenter the crater is less voluminous. However, large amount of water in the rim may cause it, partially or completely, to collapse [1, 4]. This generates openings where the water can enter the crater. In addition, it has been seen in both small scale [12] and large scale [13] experiments how the propagation of the shock wave cause violent dewatering of saturated sediments far beyond the extent of the transient cavity. This is visible as geyser-like spray due to shock cavitation of the water in the sediments (Fig. 4). Possibly, this causes fluidization and instability of the sedimentary sequence outside the crater. Similarly, poorly consolidated sediments may become fluidized and injected through other beds [14]. At locality "Berget" (Lockne crater), Lower Cambrian unconsolidated sand and gravel was injected as a sill into Middle Cambrian shale [15]. If the crater is surrounded by relatively unconsolidated, saturated sediments, once fluidized, these sediments may continue to flow into the crater through the collapsed rim (cf., Chesapeake Bay, [3]; Wetumpka; [4]) and generate a much larger structure than what is expected from the amount of released kinetic energy from the impact.

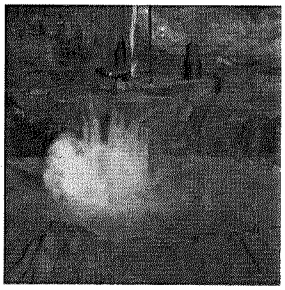

Fig. 4. Impact experiment with a CHUTA IB-060 gun for ordnance disposal (4x7 cm cylindrical projectiles of aluminum or steel)[From experiment presented by 12]. Saturated sand covered with less than 0.5 cm water. During this phase several water escape vents (like miniature geysers) appears to a distance of about 50-60 cm from the point of impact.

Summary and significance: Here is only mentioned a few of the most dominant geological and morphological effects of seawater in the formation of marine-target craters. Nevertheless, it is mainly these features that are of importance for the detection of marine-target craters, or craters formed with any kind of volatiles in the upper part of the target, in remote sensing of other planetary bodies in our Solar System. Although no strong candidates could be presented, Ormö et al. [16] assessed that as many as 1400 detectable (i.e., large enough to have been preserved) marine-target craters may have formed on Mars in the most favorable case (i.e., long-lasting oceanic phases). Continued studies of terrestrial marine-target craters may help in the understanding of past climatic conditions on Mars.

References: [1] Ormö J. and Lindström M. (2000) *Geol. Mag.* 137, 67-80. [2] Ormö J. et al. (2002) *J. Geophys. Res.* 107, E11. [3] Horton J.W. et al., this issue. [4] King D.T et al., this issue. [5] Shuvalov V. et al. (2005) *Impact Studies*, Springer, 405-422. [6] Lindström M. (2005) *Impact Studies*, Springer, 357-388. [7] Sturkell E. and Lindström M., *Met. Planet. Sci.* 39, 1721-31. [8] Melosh J. (1989) Oxford Univ. Press, New York, 1-245. [9] Sturkell et al. (2000) *Met. Planet. Sci.* 35, 929-936. [10] Ormö J. and Miyamoto H. (2002) *Deep Sea Research II* 49, 983-994. [11] Dalwigk I. and Ormö J. (2001) Met. Planet. Sci. 36, 359-370. [12] Ormö et al. (2004) *LPS* XXV, #1276. [13] Jones G.H.S. (1977) *Impact and explosion cratering*, Pergamon, 163-183. [14] Alvarez W. et al. (1998) *Geology* 26, 579-582. [15] Sturkell E. and Ormö J. (1997) *Sedimentology* 44, 793-804. [16] Ormö J. et al. (2004) *Met. Planet. Sci.* 39, 333-346.

VISCOUS RELAXATION OF SECONDARY CRATERS WITHIN THE MARTIAN SOUTH POLAR LAYERED DEPOSITS.

A. V. Pathare[1,2], E. L. Schaller[1], and B. C. Murray[1], [1]California Institute of Technology (MC 150-21, Pasadena CA 91125, avp@gps.caltech.edu), [2]Planetary Science Institute.

Introduction: Schaller *et al.* [1] examined the morphologies of the secondary crater fields of two large impacts on the South Polar Layered Deposits (SPLD): McMurdo crater at 84.5°S, 0°W and an unnamed impact (hence "Crater II") at 80.8°S, 284°W. They found a complete lack of secondary craters smaller than 300 meters in diameter in both crater fields, which implies that at least the upper 30 meters of the SPLD has been resurfaced since the time of these impacts. Moreover, SPLD secondary crater depth-to-diameter ratios are very low, with an average value of $d/D = 0.016$ [1], which is much less than the $d/D = 0.11$ characteristic of fresh lunar and Martian secondaries [2].

Resurfacing Mechanisms: Consequently, significant modification of the SPLD must have occurred since the emplacement of these shallow secondaries. Resurfacing of secondary crater fields—either due to constructional mechanisms such as water ice condensation and dust deposition or destructional mechanisms such as water ice sublimation and eolian erosion—should result in the preferential shallowing of smaller craters. Consider Fig. 1, which plots the depth-to-diameter ratio d/D as a function of diameter D for McMurdo secondaries with measurable depths. If we assume that all secondaries started with an initial $d/D = 0.11$, then a minimum amount of resurfacing equal to 33 m (short-dashed line) is required to explain the lack of observed craters smaller than $D = 300$ m [1]. Yet this amount of resurfacing is clearly not sufficient to explain the shallowness of larger McMurdo secondaries. However, increasing the amount of resurfacing to 148 m—so that a McMurdo secondary with the median diameter of $D = 1600$ m is now at the average scaled depth of $d/D = 0.02$—still does not fit the data (long-dashed line), because this level of resurfacing would produce deeper craters at larger diameters along a trend that is clearly not observed.

Viscous Relaxation: Fig. 1 also illustrates the modification of secondary craters via a simple viscous relaxation model that utilizes the inverse relationship between crater diameter D and *e*-folding relaxation time τ (i.e., the larger the crater, the faster it relaxes) applicable to craters deforming within isoviscous layers [3]. The upper solid line in Fig. 1 represents a "pure" relaxation modification scenario, in which the depth evolution of secondary craters only depends on diameter (the relaxation time was arbitrarily chosen to fit the observed $D = 900$ m crater with $d/D = 0.073$). While this relaxation only model does reproduce the subtle trend of decreasing d/D with increasing D, overall it does not provide a very good match to the observations, as the d/D of most craters fall well below this line. However, combining this simplistic relaxation model with 44 m of vertical resurfacing (such that $D = 500$ m craters are completely eradicated) results in a depth distribution (lower solid line) that fits the data much better than either the relaxation only (upper solid line) or resurfacing only (dashed lines) models, as roughly half of the data points lie above the combined model line and half lie below.

Finite Element Modeling: We will more explicitly simulate the relaxation of secondary SPLD craters via finite element modeling as done by Pathare *et al.* [4] for primary SPLD craters. Pathare *et al.* [4] showed that the observed size, depth, and spatial distributions of primary SPLD craters is most consistent with a modification model predominantly governed by viscous relaxation of water ice over at least the past 100 Myr, combined with a limited amount of vertical resurfacing on the order of tens of meters during this time span. Interestingly, d/D ratios for SPLD secondaries (mean $d/D = 0.016$) are quite similar to those measured by Koutnik *et al.* [5] for primary SPLD craters (mean $d/D = 0.015$), suggestive of a common relaxation history.

We intend to elucidate the modification history of the SPLD through our simulations of both the McMurdo and Crater II secondary fields. Although the specific age of each of these primary impacts is unknown, we can take advantage of the simultaneous emplacement of their respective secondaries to constrain the time at which each primary impact occurred, via relaxation modeling of secondaries at various diameters throughout the entire field. Of course, the relaxation history will not only be dependent on diameter but will also vary with the underlying thickness of the SPLD, which has been estimated by Davies *et al.* [6] through interpolation of circum-SPLD topography (Fig. 2). We will utilize the isopach map of [6] to ascertain whether the spread in observed d/D values at a given diameter (e.g., $0 < d/D < 0.055$ at $D = 2$ km in Fig. 1) can be attributed to differential relaxation due to predicted variations in basal topography (Fig. 2).

References: [1] Schaller E. L. *et al.* (2004) *JGR, 110,* E02004. [2] Hurst M. *et al.* (2004) *LPS XXXV,* Abstract #2068. [3] Scott R. F. (1967) *Icarus, 7,* 139. [4] Pathare A. V. *et al.* (2005) *Icarus, 174,* 396. [5] Koutnik M. *et al.* (2002) *JGR, 107,* E11, 5100. [6] Davies, C. W. *et al.* (2005), AGU Fall, Abstract #P13A-0971.

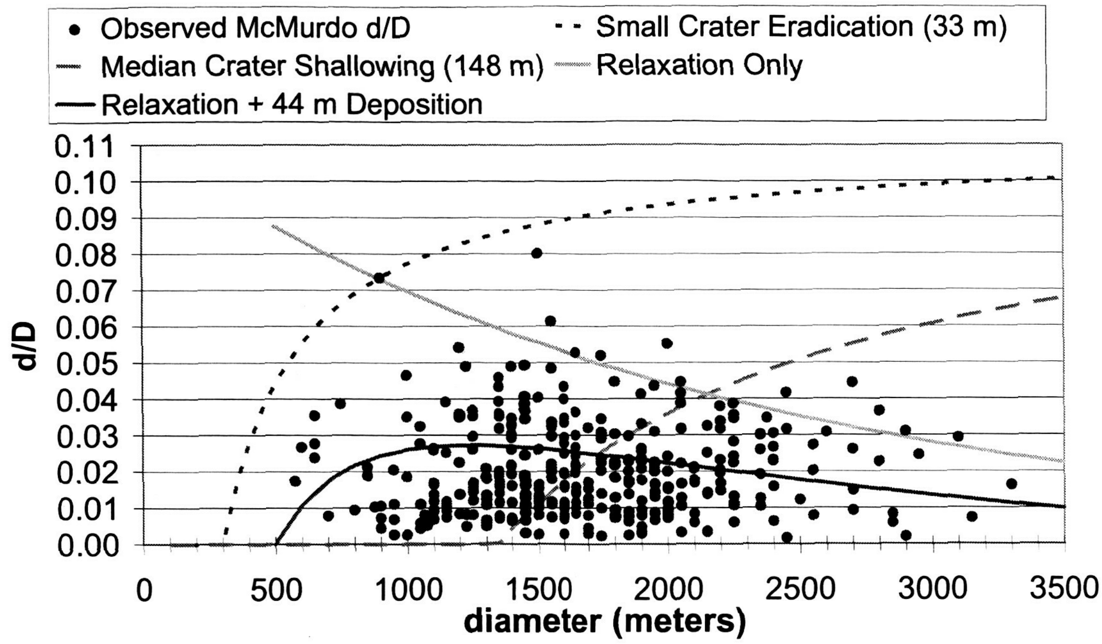

Figure 1 (taken from Schaller *et al.* [1]): Plot of *d/D* ratio vs. diameter for both McMurdo and Crater II secondary fields. Uncertainty in the d/D measurements is approximately 15%. (a) The circles denote actual observations of McMurdo field *d/D*. The upper dashed line models the minimum 33 m of vertical resurfacing required to explain the lack of secondaries with $D < 300$ m (assuming an initial d/D of 0.11 as in [2]). The lower dashed line corresponds to the 148 m of vertical resurfacing needed to degrade the median crater diameter of $D = 1600$ m to the average $d/D = 0.02$ in the field. The upper solid line represents a "pure" relaxation scenario, in which the depth evolution of secondary craters only depends on diameter (the relaxation time was arbitrarily chosen to fit the observed $D = 900$ m crater with $d/D = 0.073$). The lower solid line results from a combination of viscous relaxation with 44 m of vertical resurfacing (the parameters were chosen in order to eradicate $D = 500$ m craters); this is the model that best fits the data.

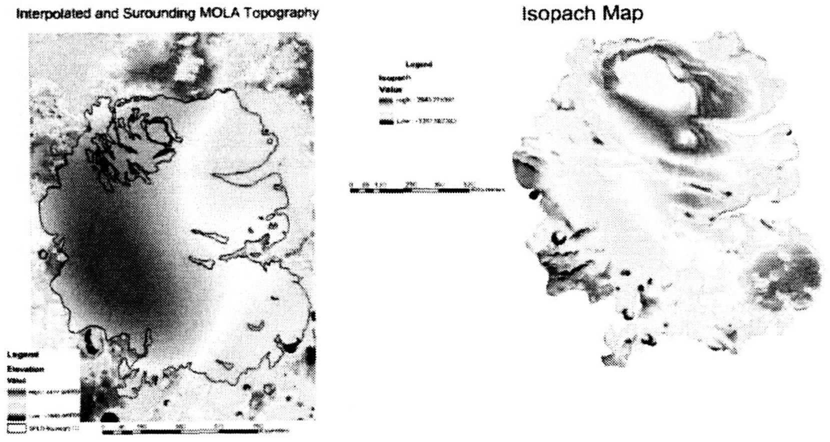

Figure 2: (left) Polynomial interpolation of surrounding topography in the MOLA DEM under the SPLD employed by Davies *et al.* [6] to estimate subglacial topography. (right) SPLD Isopach Map combining interpolated subglacial topography with observed SPLD surface topography to produce estimated ice thicknesses [6].

VERIFICATION AND VALIDATION OF THE RAGE HYDROCODE IN PREPARATION FOR INVESTIGATION OF IMPACTS INTO A VOLATILE-RICH TARGET.

C. S. Plesko[1], E. Asphaug[2], G. R. Gisler[3], M. L. Gittings[4], [1]University of California, Santa Cruz, Earth Sciences Dept. 1156 High St. Santa Cruz, CA 95064 cplesko@pmc.ucsc.edu, [2]UCSC, asphaug@pmc.ucsc.edu, [2]LANL, grg@lanl.gov, [4]SAIC.

Introduction: Before a hydrocode is used to investigate a question of scientific interest, it should be tested against analogous laboratory experiments and problems with analytical solutions. The Radiation Adaptive Grid Eulerian (RAGE) hydrocode[1], developed by Los Alamos National Laboratory (LANL) and Science Applications International Corporation (SAIC)[2,3] has been subjected to many tests during its development.[4,5] We extend and review this work, emphasizing tests relevant to impact cratering into volatile-rich targets.

RAGE: is an Eulerian radiation-hydrodynamics code that runs in a variety of geometries in up to three dimensions, with a variety of equations of state. It was developed for general application, so it does not include *ad hoc* tuning of algorithms or parameters, but relies solely on physical first-principles. RAGE uses a higher order piecewise linear Godunov numerical method to solve the hydrodynamics equations.[6,7] An exceptional advantage to this code is its use of a time- and space-continuous adaptive mesh refinement (AMR), by which it is able to follow shocks and other discontinuities at high resolution while treating smooth regions coarsely, increasing computational efficiency. The radiation component of the code is an optional grey diffusion model with nonequilibrium radiation and material temperatures.[8] Opacities are generated as part of the SESAME equation of state tables, or optionally from an analytic model.

Verification. This process ensures that the model is coded and solved correctly. RAGE is subject to an extensive set of tests in which output of each version of the code, on every computer system on which it is run, is compared to analytical solutions and results of previous versions of the code in order to demonstrate invariance under different running and boundary conditions. Test problems include the Sod shock tube[9] demonstrated in this study, the Noh problem, which checks for errors from shock 'smearing' by finite resolution[10], the Sedov blast wave, which scales self-similarly in time[11], Marshak waves, which tests radiation diffusion [12], and many other problems [4].

Validation. This process ensures that the model is appropriate to the problem at hand, and of sufficient accuracy. To validate the RAGE code, many simulations are used to replicate physical experiments. These include examinations of fluid instability in a shock-accelerated thin gas layer[13], Richtmyer-Meshkov instability growth[14], supersonic fluid flow and shock-induced jetting[15], and shock transmission through boundaries [16]. We extend this effort to shocks in basalt and ice.

SESAME: is a temperature-based tabular equation of state maintained by the Mechanics of Materials and Equations of State group LANL. The table for each material has a unique and thermodynamically consistent fit of semi-empirical theoretical models appropriate to different temperature or pressure regions to experimental data[17,18].

Method: We conduct four simulations of particular relevance to impact modeling. The first is a reproduction of the one-dimensional shock tube verification problem published by Sod[9]. Initially the 1-D planar tube is divided into two sections. In the left section, a gas is in equilibrium at a higher density and pressure (ρ_1=1.0, p_1=1.0, u_1=0.0). In the right section, the gas is in equilibrium at a lower density and pressure (ρ_2=0.125, p_2=0.1, u_2=0.0). At t=0 the high-pressure/density gas expands into the low-pressure/density region, generating a shock wave. The hydrocode results are compared to the analytical solution to demonstrate the accuracy of the finite differencing scheme. The second and third tests reproduce shocks in basalt[19] and water ice[20].

Results: The Sod shock tube performed well. Further tests are ongoing. Detailed results will be presented at the workshop.

Sod Ideal Gas Shock Tube. This model corresponds to the shock tube described above[9], and compared to the analytical solution. Results were graphed for density, velocity, pressure, and specific internal energy at t=0.12 seconds (fig. 1-4), just before the shock wave hit the end of the tube.

Ice Shock Tube. In this experiment[20], aluminum and polycarbonate projectiles were fired into water ice slabs of thicknesses ranging from 3-60 mm. They measured pressure, attenuation, and propagation velocity. In RAGE, we will use a one-dimensional column where an aluminum[21] or polycarbonate[22] projectile strikes an ice (SAIC proprietary water equation of state) target at t=0, at velocities ranging from 300-600 m/s, as in Kato[20]. Pressures and velocities will be recorded for comparison with the original data.

Basalt Shock Tube. In this experiment[19], a copper projectile was fired at a column of basalt plates interleaved with pressure sensors, generating peak shock pressures from 7-9 GPa. They measured the pressure over time through the column. In RAGE, we will use a one-dimensional column where a copper[23] projectile will strike a basalt[24] target at t=0, at velocities between .68-2.7 km/s. Shock pressure and propagation will be recorded for comparison with the original data.

Future Work: When we are confident that verification and validation criteria have been met, we will use the RAGE hydrocode to examine in two dimensions the effects of sub-surface volatiles, such as water ice, on the propagation of impact-generated shock waves through the Martian surface.

References: [1] Gittings, M. L., et al., (2004) computer code RAGE ver. 20041126.002 (LANL, SAIC). [2] Clover, M. and Gittings, M. L. (2002) *APS DCOMP* 2002, G2001. [3] Clover, M. (2002), LA-UR-02-3801. [4] Kamm, J. R. and Rider, W. J. (2000), LA-UR-99-5234. [5] Clover, M. (1998), LA-UR-98-5570. [6] Woodward, P. and Colella, P. A. (1984) *J. Comp. Phys*, **54**, 115-173. [7] Miller, G. H. and Colella, P. A. (2001), *J. Comp. Phys*, **167**, 131-176. [8] Saatdjian, E. (2000), Transport Phenomena: Equations and Numerical Solutions, pp. 181-186, (Wiley, New York). [9] Sod, G. (1978), *J. Comp. Phys*, **27**, 1-31. [10] Noh, W. F. (1978), *J. Comp. Phys*, **72**, 78-120. [11] Castor, J.I. (2004), Radiation Hydrodynamics, pp. 35-37, (Cambridge). [12] Zel'dovich, Ya. B. and Raizer, Yu. P. (1967) Physics of Shock Waves and High-Temperature Hydrodynamic Phenomena, v. 2, pp. 672-676, (AP, New York). [13] Baltrusaitis, R. M. et al. (1996), *Phys. Fluids*, **8**(9), pp. 2471-2483. [14] Holmes, R. L. et al. (1999), *J. Fluid Mech.*, **389**, pp. 55-79. [15] Foster, J. M. et al., (2002), *Phys. Plasmas*, **9**(2), pp. 2251-2263. [16] Goldman, S. R. et al. (1999), *Phys. Plasmas*, **6**(8), pp. 3327-3336. [17] Johnson, J. D. (1994) *12th Symp. Thermophysical Properties*. [18] Lyons, S. P., and Johnson, J. D. (1992), LA-UR-92-3407. [19] Nakazawa, S. et al. (2002), *Icarus*, **156**, pp. 539-550. [20] Kato, M. et al. (2001), *JGR*, **106**(E8), pp. 17,567-17,578. [21] Chisholm, E. D. et al. (2002), LA-UR-6691. [22] Boettger, J. C. (1991), LA-12120-MS. [23] Hayes, D. B. et al. (1999), LA-UR-3276. [24] Barnes, J. F., and Lyon, S. P. (1988), LA-11253-MS. [25]

Acknowledgments: UCSC/LANL Institute of Geophysics and Planetary Physics, NASA PG&G Small Bodies and Planetary Collisions.

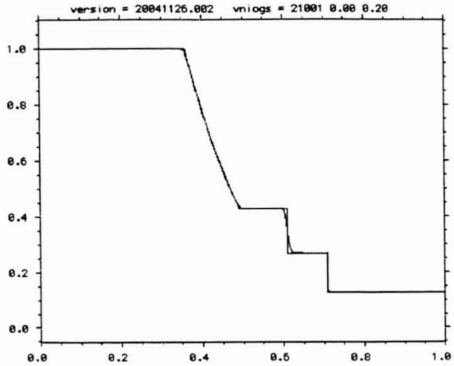

Figure 1. Sod ideal gas shock tube density vs. distance, analytical and RAGE solutions at t=0.12 s.

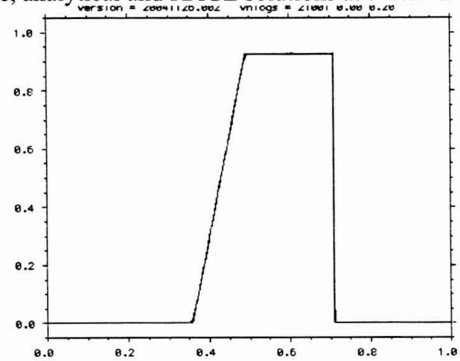

Figure 2. Velocity vs. distance, t=0.12 seconds.

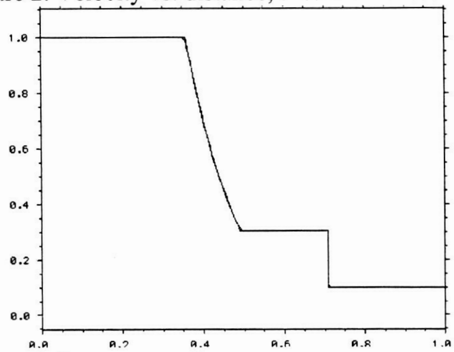

Figure 3. Pressure vs. distance, t=0.12 seconds.

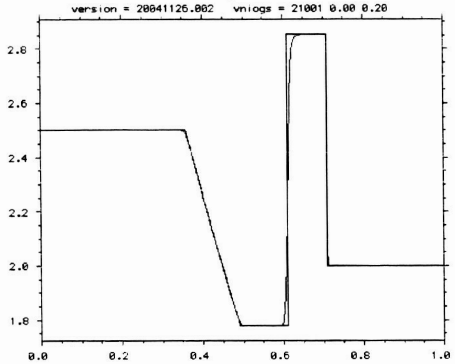

Figure 4. Specific internal energy vs. distance, t=0.15s.

THE ROLE OF THE ATMOSPHERE AND TARGET VOLATILES IN THE EMPLACEMENT OF THE CHICXULUB EJECTA BLANKET AND ANALOGIES WITH MARTIAN IMPACT EJECTA

K. O. Pope[1] [1]Geo Eco Arc Research, 16305 St. Mary's Church Road, Aquasco, MD 20608 kpope@starband.net.

Introduction: The Chicxulub impact into the volatile-rich Yucatan Peninsula produced a 200 km diameter crater and one of the best preserved ejecta blankets on Earth. Emplacement of ejecta south of the impact site occurred largely on an emergent karst land surface, whereas material ejected to the north, east, and west mostly landed in deep water of the Gulf of Mexico or Caribbean Sea. Thus, preserved ejecta deposits in the south provide the opportunity to study emplacement processes that may be analogous to those found on Mars.

The Chicxulub Ejecta Blanket: The Chicxulub ejecta blanket is composed of at least four distinct depositional units. Drill cores outside the rim of the Chicxulub crater document two ejecta units: a basal course breccia unit ~300 m thick containing abundant carbonate, sulfate, and crystalline basement clasts in a fine-grained carbonate matrix, overlain by a thinner (~150 m) suevite unit composed of abundant impact melt fragments and lenses mixed with carbonate and crystalline basement clasts. The suevite unit extends for a 1.5 crater radii, and the basal breccia unit for >2.0 crater radii. There are no drill core samples or ejecta exposures from ~2.0-3.0 crater radii.

The outer portion of the Chicxulub ejecta blanket is exposed in southern Quintana Roo, Mexico and Belize, where it constitutes the Albion Formation. Ejecta of the Albion Formation occur in two units – a basal spheroid bed and an upper diamictite bed. The spheroid bed is composed of a mixture of pebble-sized limestone clasts, impact glass, and carbonate accretionary lapilli in a fine-grained carbonate matrix. Spheroid bed thicknesses range from ~1-5 m over ~3.5 to 4.7 crater radii. The diamictite bed is composed of impact glass and sub-rounded to angular carbonate cobbles and boulders up to 9 m in diameter supported in a in a fine-grained carbonate matrix similar to that of the spheroid bed. The diamictite bed overlies the spheroid bed along the Mexico-Belize border, where it reaches thicknesses >17 m, but it does not extend beyond ~3.6 crater radii.

Evidence for Fluidized Flow: The geomorphic expression once exhibited by these four ejecta units is not known, but they may have at least in part resembled the flow lobes found in martian impact craters. Fluid flow cannot be demonstrated for the proximal suevite and breccia units. The breccia unit is far too thick to be explained by simple ballistic emplacement (Figure 1) and presumably it is composed of a large percentage of debris scoured from the pre-impact surface by secondary impacts (ballistic erosion). Such scouring or "gardening" is observed in lunar ejecta blankets, which lack fluid flow morphologies, even though models of ballistic erosion suggest some lateral flow.

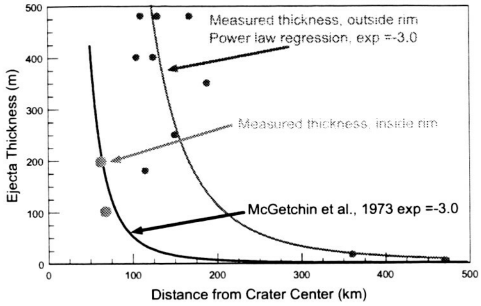

Figure 1. Relationship between ejecta thickness and distance from crater center. Shown are measured thicknesses (in red and blue) and the theoretical relationship from McGetchin et al.

Lateral flow is clearly indicated for the more distal Albion Formation deposits, and these units are good candidates for fluidized ejecta. The spheroid bed shares many features with volcanic pyroclastic flows, including low angle, large amplitude cross-bedding. Evidence for flow in the diamictite bed includes mud coatings on clasts up to 5 m in diameter, the absence of any significant erosion at its base, and possible horizontal shear planes separating individual flows within this unit. Furthermore, the thickness (>17 m) and radial extent (~3.6 crater radii) of the diamictite bed is inconsistent with ballistic emplacement (Figure 1) and is best explained by extensive lateral flow of ejecta beyond the normal ballistic range. The abundance of diamictite bed outcrops along the Mexico-Belize border, and the fact that the most distal exposures are the thickest, may indicate the presence of a terminal thickened rampart, as seen along the outer edge of fluidized ejecta blankets on Mars.

The Role of Target Volatiles at Chicxulub: The impact at Chicxulub produced about 200 Gt of water, 300 Gt of SO_2, and 500 Gt of CO_2 vapor from sediments in the upper 3 km of the target. These vapors comprised about 25-50% of the vapor plume, however, most of the vaporized silicates resided in the globally dispersed high-energy ejecta. Thus, the lower energy ejecta, which formed the ejecta blanket, contained mostly volatiles from the upper sediments, primarily water vapor. An abundance of water vapor is indicated by the large volume of accretionary lapilli deposited in the Albion Formation spheroid bed. Such lapilli form in water-rich ash clouds as water vapor condenses and the fine ash particles adhere to one another and to rock fragments in the plume. Water vapors may have played a similar role in coating of boulders in the Albion Formation diamictite bed. The presence of water vapors in the diamictite bed is also suggested by the presence of degassing pipes with hydrothermal alteration.

The Role of the Atmosphere at Chicxulub: Evidence of atmosphere-ejecta interactions is less definitive in the Chicxulub ejecta deposits. One key possible indication is in the size distribution of clasts in the diamictite bed (Figure 2). Measurements indicate the presence of two populations, with a distinct gap in clasts with diameters from -11 to -10 phi. This gap could represent the critical size, where clasts > -11 phi have escaped atmospheric sorting. Similar processes have benn suggested for the ejecta blankets on Mars.

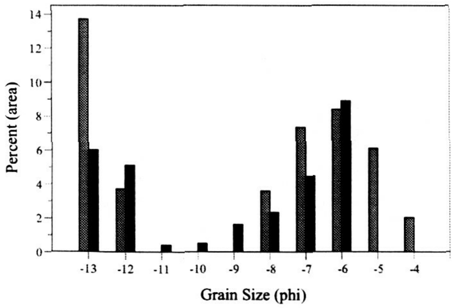

Figure 2. Grain size distribution for clasts >1 cm in the Albion Formation diamictite bed. Data complied from photographs and quadrat samples (red) and linear transects (black).

AGES AND ONSET DIAMETERS OF RAMPART CRATERS IN EQUATORIAL REGIONS ON MARS.

D. Reiss[1], S. van Gasselt[2], E. Hauber[1], G. Michael[1], R. Jaumann[1], G. Neukum[2] and the HRSC Co-Investigator Team. [1]Institute of Planetary Research, DLR, Rutherfordstr. 2, 12489 Berlin, Germany (dennis.reiss@dlr.de) [2]Institute for Geosciences, Freie Universitaet Berlin, Malteserstr. 74-100, 12249 Berlin, Germany.

Introduction: Many large craters on Mars exhibit ejecta blankets which are not observed on other terrestrial planets like the Moon [1]. As found by many researchers [e.g. 2, 3, 4] the morphology is suggested to be caused by volatile rich target material [2] or atmospheric effects [5]. However, in a given area a certain minimum diameter exists for craters which show fluidized ejecta blankets [6, 7], called the onset diameter. Geographic mapping shows a latitude dependence of the onset diameters [8, 9]. In equatorial regions the onset diameters are typically 4 to 7 km versus 1 to 2 km in high latitudes (50° latitude), which might indicate a ice rich layer at depths of about 300 to 400 m near the equator and ~100 m at 50° latitudes [8]. As pointed out by [1] rampart craters may have formed over a significant time interval and therefore reflect the ground ice depths at a given time.

We determined the absolute ages and onset diameters of rampart craters in three equatorial regions on Mars by measuring the ejecta blankets' superposed crater frequencies in Mars Express High Resolution Stereo Camera (HRSC) imagery [10] in three equatorial regions (Figure 1).

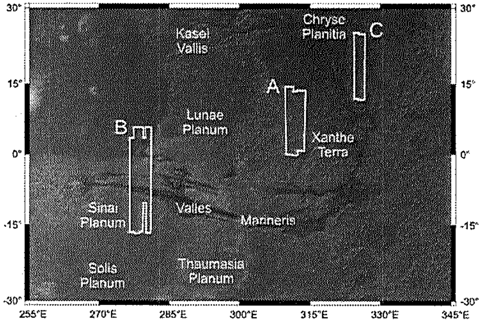

Figure 1. *Regional context of the study areas.* ***(A)*** *HRSC-image mosaic of orbits 894, 905 and 927 in the Xanthe Terra region;* ***(B)*** *HRSC-image mosaic of orbits 71, 97, 887, 920 and 931 in the Valles Marineris region* ***(C)*** *HRSC-image mosaic of orbits 1143 and 1154 in southern Chryse Planitia.*

Methodology: To determine the absolute model ages of the rampart craters we counted the crater frequencies on the ejecta blankets utilizing the the Martian impact cratering model of [11] and the polynomial coefficients of [12].

Results and Discussion: Ages of rampart craters in the Xanthe Terra region (Figure 3A) are in the range of ~4 to ~3 Gyr. Most absolute model ages of individual ejecta blankets are around 3.8 Gyr. The derived ages imply that their formation is connected with the Noachian aged fluvial activity (~3.8 Gyr) in this region [13] (Figure 2A). The formation rate of rampart craters declines in the Hesperian, whereas the onset diameters increase. At the Hesperian-Amazonian boundary the formation comes to an end. This might indicate a lowering of the ground ice table with time which in Xanthe Terra, if present at all, could be several kilometers deep in present days. Either all the ground ice was lost with time due to diffusion to the atmosphere [e.g. 14] or there is still a deep ground ice layer which can only be reached by relatively large (and in recent times rare) impacts.

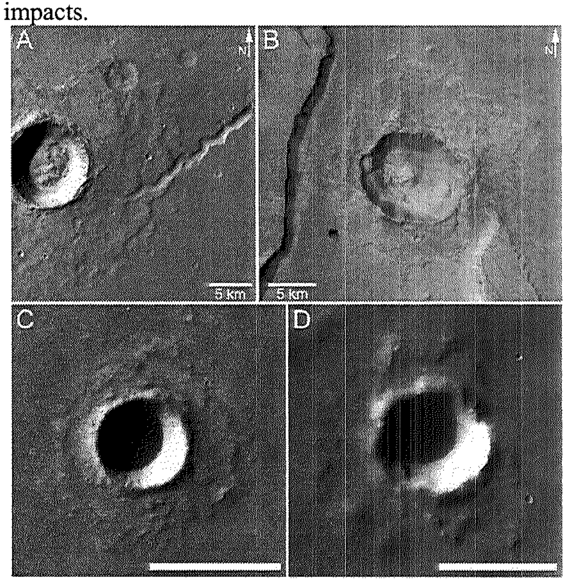

Figure 2. ***(A)*** *Rampart crater in the Xanthe Terra region with an absolute model age of ~3.8 Gyr (HRSC-orbit 927 at 5°N and 310°E). A lateral valley of Nanedi Vallis eroded into the ejecta after the formation of the rampart.* ***(B)*** *Rampart crater in the southern Chryse region on the channel floor of Tiu Vallis with an absolute model age of ~1.5 Gyr (HRSC-orbit 1143 at 15.5°N and 325.3°E).* ***(C and D)*** *Examples of small rampart craters in the Valles Marineris region. Scale bars are 2 km. C: HRSC-orbit 920 at 15.44°S and 278.42°E; D=1.41 km; D: HRSC-orbit 887 at 9.73°S and 280.14°E; D=1.86 km).*

Most rampart craters in the Valles Marineris region show absolute model ages around 3.7 Gyr (Figure 3B), which indicates subsurface ice in the Early Hesperian most probably shortly after the formation of the Hesperian aged plateaus. In addition 20 small rampart craters with onset diameters between 1 - 4 km were observed [16] (Figure 2C and D) and indicate near surface ice at the time of the impacts in this region. Morphologically the ejecta blankets are highly degraded and age determinations by crater counts are not possible. However, the degraded ejecta blankets as well as the lower depth-diameter ratios of the craters in contrast to pristine craters of the same region indicate an old, most likely Hesperian age [16]. These unusual small rampart craters are in agreement with the reported Hesperian-aged fluvial processes in the study region reported by [17] and regional variations of equatorial onset diameters of rampart craters by [18]. However, only one younger relatively large (D = 8.6 km) Amazonian aged (~2.5 Gyr) rampart crater was identified, which could indicate a lowering of the ground ice table after a volatile rich Hesperian phase.

In southern Chryse Planitia the rampart craters where the ejecta have been eroded by fluvial events show absolute model ages around 3.8 Gyr and between ~0.5 to ~1.5 Gyr of channel superposed ramparts (Figure 2B and 3C). These ages are in good agreement with the fluvial activity of Tiu Vallis derived from crater counts between ~3.6 to ~1.5 Gyr BP [19]. The formation of relatively young Amazonian aged rampart craters with onset diameters of 3 km indicates that ground ice could still be present in this region at depths of a few hundred meters. The ground ice might have been recharged by the last fluvial episode of Tiu Vallis and sheltered from diffusion by thick fluvial sediments. The volatile layer in Chryse Planitia in general could possibly be as shallow as ~ 60 m as onset diameters indicate [20, 21].

Conclusions: The ages and onset diameters of rampart craters in three equatorial study regions indicate that the formation is connected to volatile rich phases in the Martian history. The present ground ice table in present times might strongly vary regionally.

1. The correlation of rampart ages with fluvial activity and the lack of young rampart craters in the Xanthe Terra region indicates that the ground ice table is possibly at a depth of several kilometers or nonexistent at present times.

2. Small onset diameters and ages of rampart craters in the Valles Marineris region indicate a volatile rich phase in the Hesperian, most probably in the early Hesperian. The present ground ice table in this region might be several hundred meters deep as indicated by a relatively large Amazonian aged rampart crater.

3. In southern Chryse Planitia young Amazonian aged rampart craters with onset diameters of ≥ 3 km formed after the last fluvial activity in this region. This indicates a ground ice table (possibly a few hundred meters deep) in recent geological times which might be still present today.

Acknowledgements: *This work was supported by a grant from the German Research Foundation (DFG) within the scope of the priority programme "Mars and the Terrestrial Planets", SPP 1115. This work was also supported by the Programme National de Planétologie and by the the European Community's Improving Human Potential Program under contract RTN2-2001-00414, MAGE.*

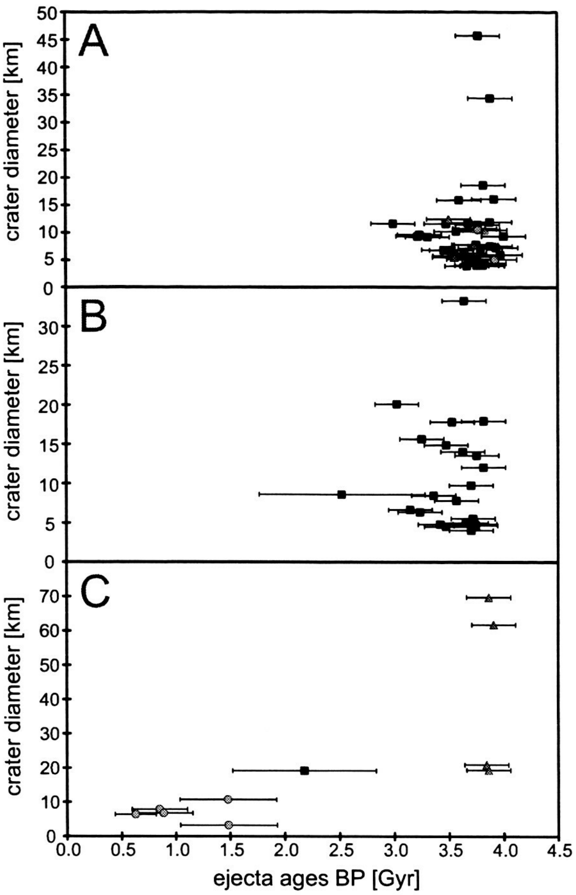

Figure 3. *Absolute model ages of rampart craters versus crater diameter of the Xanthe Terra region **(A)**, the Valles Marineris region **(B)** and southern Chryse Planitia **(C)**. Gray triangles show rampart craters which are superposed on fluvial features. Gray circles show rampart craters which are eroded by fluvial activity. Black squares show no relative age relationships. Error bars are 30% for model ages younger than 3 Gyr and ±200 Myr for model ages higher than 3 Gyr [15].*

References: [1] Squyres S. W. et al. (1992) Mars, Univ. of Arizona Press, 523-554. [2] Carr M. H. et al. (1979), JGR, 82, 4055-4065. [3] Allen C. C. (1978), NASA Tech. Mem, 79729, 160-161. [4] Mouginis-Mark [1979] JGR, 84, 8011-8022. [5] Schulz P. H. and Gault D. E. (1979) JGR, 84, 7669-7687. [6] Boyce J. M. (1980) NASA Tech. Mem., 82385, 140-143. [7] Kuzmin R. O. (1980) Dokl. ANSSSP, 252, 1445-1448. [8] Kuzmin R. O. et al. (1988) Solar Sys. Res., 22, 195-212. [9] Costard F. (1989) Earth, Moon, and Planets, 45, 265-290. [10] Neukum, G., et al. (2004) ESA Special Publications, SP-1240. [11] Hartmann W. K. and Neukum G. (2001) Space Sci. Rev., 96, 165-194. [12] Ivanov B. A. (2001) Space Sci. Rev., 96, 87-104. [13] Masursky H. et al. (1977) JGR, 82, 4016-4037. [14] Carr M. H. (1996) Water on Mars, Oxford Univ. Press, pp. 229. [15] Neukum G. et al. (2004) Nature, 432, 971-979. [16] Reiss D. et al. (2005) GRL, in press. [17] Mangold N. et al. (2004) Science, 305, 78-81. [18] Barlow N. G. et al. (2001) GRL, 28, 3095-3098. [19] Neukum G. and Hiller (1981) JGR, 86, 3097-3121. [20] Costard F. M. (1988) LPS XIX [21] Demura H. and Kurita K. (1998) Earth Planets Space, 50, 423-429.

MARTIAN POLAR CRATERS: POSSIBLE POLAR MATERIALS APPARENT EFFECTS AND POST-IMPACT MODIFICATION BY APPARENT PERRENNIAL PERMAFROST MOUND (PINGO) FORMATION.

S. E. H. Sakimoto[1], [1]Department of Civil Engineering and Geological Sciences, 156 Fitzpatrick Hall, University of Notre Dame, Notre Dame, Indiana, 46556, email: ssakimot@nd.edu.

Introduction: On Mars, as elsewhere, impact craters reveal both target effects as well as post-impact modification processes. The cavity morphology and central peaks or mounds of martian impact craters are key indicators in determining these target properties and processes. The martian polar regions (particularly the northern polar region) display significant departures from the global trends [1,2,] in both crater morphology presumed to be a result of target effects and central deposits presumed to be a result of post-formation processes [e.g. 1,2, 3].

Data and approach for central deposits: The typical central peak topography for martian impact craters has been well-defined (e.g. [1, 2]). Recent work in the equatorial region of Mars has suggested that there is evidence for pingo-like or small perennial permafrost mounds in the Athabascan, Valles region [4,5] that may be tapping sources of water related to the proposed late Amazonian floods in the region (e.g. [6]). Previous results from this study [3] suggest that some of the polar impact crater central mounds are plausible candidates as perennial permafrost deposits (in whole or in part) that may be tapping polar aquifers. In the polar regions, these central mounds cover much of the crater floor (e.g. figure 1), with a north-south slope asymmetry (steeper towards the equator) that suggests a significant volatile component lost through solar-driven sublimation (see figure 2). Several of the northernmost examples retain bright frost cover throughout the north polar summer season, but regardless of such apparent surface frost, the topographic signature for polar region craters frequently includes these gentle central mounds, which are frequently difficult to detect in images due to their subdued topography and probable dust cover [3]. While these mounds could be cold trap-derived accumulated frost deposits, we suggest (e.g. [3]) that hydraulic pingo formation (e.g. [6]) typical of open system aquifers and topographically-driven water flow may well provide the hydraulic head and permafrost disruption to initiate pingo formation. Long periods of climate stability on Mars (relative to Earth) could then explain their relatively larger sizes. The modeling effort: uses MOLA topography to provide cavity and final central mound constraints, assumes decreasing porosity with depth, assumes a basal thermal flux (thermal gradient), rotational symmetry; ambient surface pressure and temperature for the martian polar regions, imposes a phase relationship to govern the depth of the ice/water phase transition, and uses both global average cavity shapes as well as local polar average cavity shapes as starting points. Initial modeling ([3], and this study) suggests that martian hydraulic pingo formation is not difficult to reproduce in model domains for plausible parameter values.

Data and approach for target effects: The polar craters have a noticeably more u-shaped cavity function and simple to complex transition than is observed in equatorial craters as well as the global crater trends (e.g. [2]). This work further supports this observation with specific crater comparisons between polar and equatorial examples with similar diameters, but for selected geologic units after the example of [1]. There are some hints of a latitude dependence for these properties, suggesting not only a unit-based dependence, but also a volatile-based dependent target property of sufficient magnitude that the cavity formation process as a whole is sensitive to it.

Conclusions: We support prior observational results [1,2] showing the following differences for polar impact craters: 1) a simple-to-complex transition at larger diameters, 2) generally higher eject ramparts, and more pronounced near-rim moats, 3) cavity shapes that are more u-shaped than v-shaped, and very common central mound-like deposits. There may be a small latitude dependence for the apparent target effects, suggesting a volatile-based dependent target property of sufficient magnitude that the cavity formation process as a whole is sensitive to it.

We find that topography data is key in morphology analyses for these features, because of generally poor polar viewing conditions (dust and ice and frost-associated albedo variations). We find that these mound-like deposits are well-modeled as hydraulic pingoes [3] particularly in the 65°-80° N and S regions for impact craters > 8 km or so in diameter. These areas are generally higher in mapped water-equivalent hydrogen [7, 8] and thus presumed near-surface ground ice (permafrost) that would be required for a permafrost "cap" necessary for hydraulic pingo formation. The apparent approximately 8 km size minimum for substantial central mound formation tends to support pingo formation rather than simple accumulation of frost deposits, as the associated crater depths (1-2 km) must be sufficient to tap into the local aquifers for pingo formation and growth. If these pingos are still active, tapping into one would produce artesian water flow. Inactive pingoes may well include substantial residual permafrost deposits.

References: [1] Garvin et al., 2003, 6th International Conference on Mars, Abstract # 3277 [2]] Garvin et al., ICARUS, vol 144, pp 329-352, 2001 [3] Sakimoto, 2005, 36th LPSC Abstract # 2099 [4] Burr, D.M. et al., AGU Abstract P13A-0982, 04AGUFM.P13A0982B, 2004, [5] Burr, D.M. et al., ICARUS, In Press, 2005. [6] Gurney, 1998, Progress in Physical Geography, 22, 3, pp 307-324. [7] Boynton et al., 2002, Science 296, 81-85, [8] Feldman et al., 2002, Science 297, 75-78

Acknowledgements: I thank Devon Burr, James Garvin and Herb Frey for helpful discussions on central crater mounds. Early portions of this cratering work were supported by the MOLA Science Team.

Figure 1. Showing a MOLA topography profile for a polar crater compared to a typical cavity model fit for a equatorial impact crater. The central deposits are substantial, and the cavity wall slopes are significantly shallower, as is typical for most polar craters.

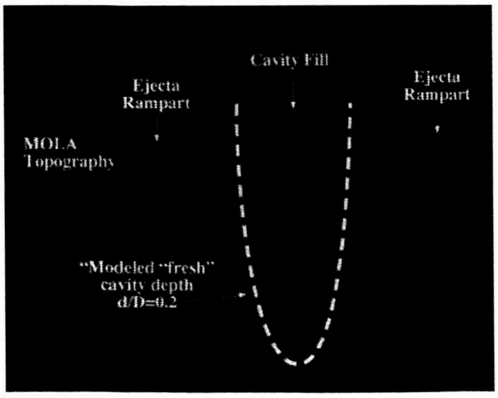

Figure 2. MOLA topography for several polar impact craters showing typical polar ejecta styles and central mounds

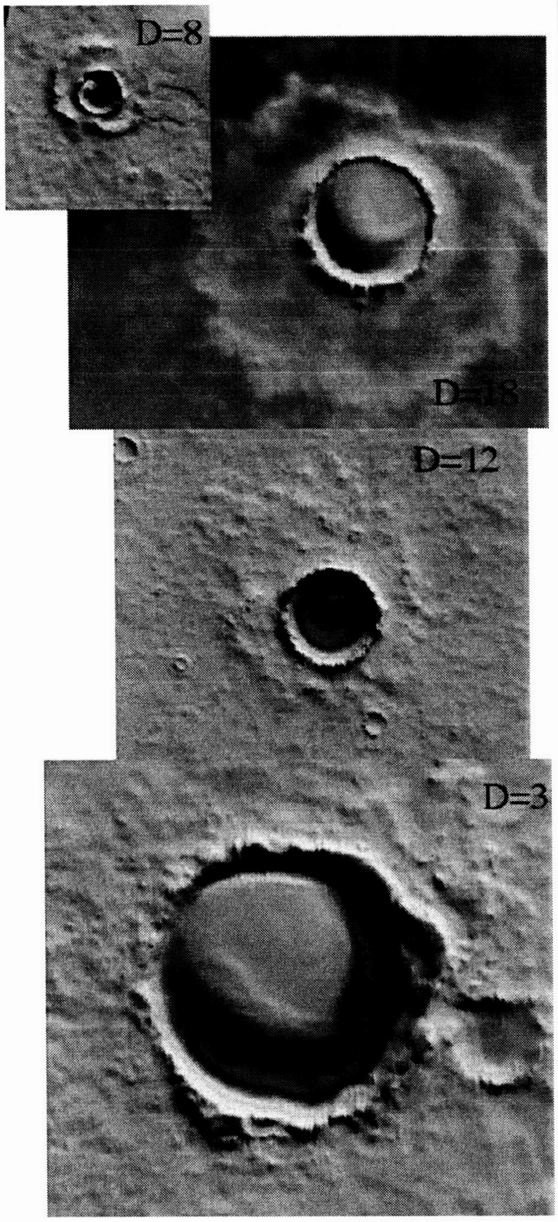

What do Craters on Icy Satellites Tell Us about Martian Craters?: P. Schenk, Lunar and Planetary Institute, Houston, TX 77058 (schenk@lpi.usra.edu)

INTRODUCTION: It seems obvious that if Martian craters are influenced by subsurface ice, then impacts into natural ice-rich targets should offer some valuable insights into how ice might influence crater development in general. With the Voyager and recent Galileo missions to the Jovian system complete, analysis is underway of crater morphology on the 3 ice-rich Galilean satellites Europa, Ganymede and Callisto.

Crater morphology is important on two levels: shape and interior structure, and ejecta. Crater shapes on icy satellites differ radically from those on dry rocky worlds. Complex craters are 60-70% shallower than expected and never exceed 2 km depth [1, 2]. Further, the internal structure of larger craters is dominated by rimmed pits and large domes [2, 3] rather than central peaks or peak rings. Pedestal ejecta facies are the only ejecta morphology on the icy satellites that resembles those found at Martian craters [4, 5]. Pedestals are systematic in dimension and shape, suggesting they are a fundamental part of the ejecta emplacement process on icy bodies. High resolution images show flow lobs (interpreted to be impact melt) draped over parts of the pedestal deposits, but no indications have been found to date that the pedestal itself is emplaced by anything other than "ballistic emplacement"

Although the largest known impact features on Europa (30-45 km across) probably form in a finite ice layer averaging a substantial fraction of the melting point, it must be remembered that craters on the large Galilean satellites formed at colder temperatures than on Mars. Evidence does suggest that craters on ancient Ganymede are different than those formed today, suggesting they formed in a warmer ice layer than at present [6]. This and the fundamental difference in crater morphology on Europa and Ganymede [2] suggests that the temperature of the ice is important in controlling primary crater morphologies. Another important difference is that the outer zones of the Galilean satellites are dominantly water ice. Unanswered questions relate to how much melt and vapor are produced in warm ice (relative to that produced in colder ice), and how high the ice/rock ratio must be for the rheology and melt behavior of ice to begin influencing crater shape and ejecta formation.

REFERENCES: [1] Schenk, P., J. Geophys. Res., 98, 7475-7498, 1993. [Schenk, P., Nature, 417, 419-421, 2002. [3] Moore, J., and M. Malin, Geophys. Res. Lett., 15, 225-228, 1988. [4] Horner, V. and R. Greeley, Icarus, 51, 549-562, 1982. [5] Schenk, P., and F. Ridofli, Geophys. Res. Lett., 29, 31-1, 2003. [6] Schenk, P., C. Chapman, K. Zahnle, and J. Moore, in Jupiter, Cambridge Press, pp. 427-456, 2004.

ON THE BRITTLE FAILURE OF WATER ICE IH: A SHORT REVIEW.

E. M. Schulson, Thayer School of Engineering, Dartmouth College, 8000 Cummings Hall, Hanover, NH 03755-8000, email: erland.schulson@dartmoth.edu.

Introduction: Ice, or more specifically water ice, occurs in a variety of forms, from terrestrial glaciers, floating ice sheets, and airborne particles to micrometerorites, icy satellites, and planetary polar caps. In each form its mechanical behavior is of interest, from the breakup of the Antarctic ice shelf and the Arctic sea ice cover against itself and against off-shore engineered structures, to impact by hailstones and falling ice, to the tectonic history of Europa, Ganymede and other extra-terrestrial bodies. In this presentation I will focus on ordinary or low-pressure ice Ih, which possesses hexagonal crystal symmetry, and will consider the mechanisms underlying the process of brittle failure under quasi-static strain rates, on scales large and small. My thesis is that failure on the larger scale, although complicated by inhomogeneities in stress state and in ice thickness distribution, is in essence governed by the same physics that operate on the smaller scale. I will support this position with evidence of wing cracks, comb cracks and Coulombic shear faults within the icy crust of Europa [1], the Arctic sea ice cover [2] and laboratory specimens [3], and I will present a simple analysis based upon independently-measurable physical parameters that accounts for the measured failure stress under a variety of stress states. I will also consider the ductile-to-brittle transition on scales large and small, and will account for the transition quantitatively in terms of the competition between the building up of internal stress at cracks and the relaxation of stress through creep. If time permits, I will close by showing that the mechanisms that govern the brittle compressive failure and the ductile-to-brittle transition of ice under both moderate and high confinement appear to account for the same phenomena in rocks and minerals, at least on the smaller scale [4].

References:

[1] Schulson E. M. (2002) *JGR, 107*, Article #5107. [2] Schulson E. M. (2004) *JGR, 109,* Article #C07016. [3] Schulson E. M. (2002) *Reviews in Mineralogy & Geochemistry, 51;* see also (2001) *Eng. Fracture Mechanics, 68,* 1839-1887. [4] Renshaw C. E. and Schulson E. M. (2001) *Nature, 412,* 897-900.

ASSESSING LITHOLOGY FROM EJECTA EMPLACEMENT STYLES ON MARS: THE ROLE OF ATMOSPHERIC INTERACTIONS.

P. H. Schultz, Brown University, Department of Geological Sciences, Box 1846, Providence, RI 02912-1846, peter_schultz@brown.edu

INTRODUCTION: There is little question that Mars once had water flowing across the surface and that there are reservoirs currently sustaining the near-surface volatiles at high latitudes. Neither observation, however, establishes water as the controlling ingredient for the distinctive ejecta morphologies surrounding craters on Mars. The purpose of this contribution is to review the alternative hypothesis that the atmosphere is not only a controlling factor but also the controlling process. Such a position is not offered as an extreme end member but as balance to the popular perception that craters can be used as diagnostic indicators of volatile content or groundwater depth. The following is intended to be a review of the basic model and its implications for ejecta emplacement on Mars.

BACKGROUND: The basis for considering the possible role of atmospheric effects on ejecta emplacement can be illustrated by a simple model (1). Basic drag equations can be applied to ballistic ejecta of different sizes even under the presently tenuous atmosphere. Because crater excavation occurs under extension well behind the shock, ejecta leave the crater in a "coasting" phase for gravity-controlled growth. Drag equations applied to late-stage (>50% of growth) ejecta reveal that no ejecta smaller than 1 cm can escape the cavity for a 10 km-diameter crater even under the currently tenuous atmosphere of Mars (excluding other effects). Equivalently, no ejecta smaller than 100 µm should escape a 20 cm-diameter crater in laboratory experiments. Both results are contrary to observations and underscore the underpinnings of the atmospheric conceptual model: the atmosphere not only acts on individual ejecta but also responds to the collective ensemble of ejecta comprising the outward-advancing ejecta curtain. Such a response leads to intense vortices (winds) that entrain sufficiently small ejecta (1, 2, 3, 4). Laboratory experiments with impact velocities ranging from 20m/s (sling-shot speeds) to hypervelocities (6 km/s) illustrate this atmospheric response.

Experiments typically cannot provide 1:1 comparisons. Rather, they allow isolating variables and processes in order to use scaling relations or to pose testable theoretical models. For example, one crater radius from the rim of a 20 cm-diameter crater in the laboratory corresponds to a ballistic speed ~100 cm/s, but one crater radius from the rim of a 20 km-diameter (~ 16 km pre-collapse and ~13 km apparent) crater corresponds to a ballistic speed of ~160 m/s. The ejecta speed for the example for Mars represents about 50% the speed of sound. This illustrates the problem: drop of water (or mud) would atomize in the atmosphere under such conditions and entrained in the atmospheric response (2).

Other "realities" must include the effect of atmospheric coupling inducing the intense blast (overpressures followed by underpressures and heat), range in ejecta sizes, ballistic shadowing, energy and momentum conservation, RT instabilities, secondary cratering, and post-emplacement flow. Such topics (and more) have been treated in various papers (2 through 7). Rather than reviewing such effects in detail, the following outline summarizes basic predictions of the atmospheric model (without the additional effect of water).

Ballistic Ejecta Styles: Such craters indicate the following conditions. First, the post-shock ejecta fragments (or spalls) are large enough to minimize atmospheric deceleration or entrainment. Second, the crater is sufficiently large that most of the ejecta escape the atmosphere (craters-larger than 30 km in diameter). Secondary craters are emplaced prior to the continuous facies. This style should not be confused with "radial" styles.

Contiguous Ejecta Ramparts: Based on experiments and theory, this emplacement style can develop from intense vortices created by the advancing curtain. Ejecta smaller than a critical size become entrained in the ring vortices but larger sizes are carried without suspension, deposited as a terminal rampart. Rampart-bordered facies are most likely to form in lithologies with multi-modal grain sizes. Larger craters (20 km) may also exhibit secondary cratering beyond the terminal rampart with characteristic sizes similar to secondaries on the Moon and Mercury, whereas other lithologies have virtually no secondaries (6).

Multiple Lobate Flows: This style is expected from fine-grained lithologies (e.g., aeolian or fluvial sediments) where most of the ballistic ejecta become entrained (initially) in the vortex. Flow separation results in successive stages of emplacement, over-running each earlier stage. The finest fraction remains entrained in the vortex-driven flow regime the longest and can achieve the greatest run-out distances, contrary to considering the aerodynamic deceleration of a single particle. Emplacement is similar to a matrix-supported debris flow but the final stages of deposition are the most difficult to model (e.g., see ref. 7). Such fine-grained lithologies also respond to thermal buoyancy effects (lofting in heated gas rising in the atmosphere) followed by gravity flows. Radial grooving overprinting the ejecta and extending into the outer facies characterize this style. In the freshest examples, evidence for scouring (removal of fine-scale surface textures) extends to 5-10 crater radii, sometimes with a low relief terminal rampart. This outer facies could be from the separation of the vortex acting on wind-sensitive sediments or a consequence of the initial outward blast (2, 8). An additional signature of a predominately fine-grained target is a moat-like syncline surrounding the rim due to sweep-up by a tornadic-intensity vortex ($v > 200$m/sec) behind the curtain (2). High porosity sediments (> 50%) are found to produce high-angle ejecta trajectories (> 60°) that evolve to lower angles as less porous sediments are encountered at depth (9,10). Consequently, multiple/over-running flows can develop from changes in porosity with depth, flow separation, entrainment of different size fractions, gravity flows from collapse of thermally lofted fines, and the initial outward blast.

Radial Facies: Radial scouring of successive lobate-style ejecta flows provides a possible clue for this emplacement style. In direct contrast with early interpretations (e.g., 11), this style is attributed to the most volatile-rich substrates (2) that result in extreme run-out and dispersal of the finest fractions. Radial facies also develop from differential erosion of the fine-grained outer deposits yet can appear to be a primary emplacement style.

An important prediction of the atmospheric ejecta emplacement model is that run-out distance increase with increasing crater radius (R). Because ejection velocity increases as $R^{1/2}$ dynamic pressures (acting on individual ejecta or in response to the curtain) increases as R. As a result, energy losses created by deceleration of the curtain is balanced by increased entrainment and flow potential. This process is illustrated by the correlation of increased run-out and decreased cratering efficiency (3). Run-out distance, therefore, increases (not decrease) with increasing atmospheric effects (i.e., decreasing ejecta size). A second prediction is that the range in particle sizes within different lithologies (e.g., basalt vs. sediments) is far greater (x 1000) than the range in atmospheric pressures due to obliquity variations (e.g., x 6). A third prediction is that the presence of near-surface volatiles (e.g., high-latitudes) can increase the run-out distances due to auto-suspension, a process in which entrained components can contribute energy in the flow (2) and sustain greater run out. And fourth, the effect of grain size (lithology) is the most important controlling parameter but can be confused with the effect of volatiles (e.g., high-latitude plains) or elevation (volcanic sequences or edifices).

The desire to "follow the water" and attribute ejecta morphologies only to the presence of groundwater (e.g., 12) may miss another indicator of a hydro-geologic past: transport and emplacement of silt-size sediments. Such materials would be the most sensitive to an atmospheric effect.

(1) Schultz P.H. and Gault D.E (1979) *J. Geophys. Res. 84*, pp. 7669-7687. (2) Schultz, P.H. (1992) *J. Geophys. Res., 97*, E7, 11,623-11,662; (3.) Schultz, P.H (1992). *J. Geophys. Res., 97*, E1, 975-1005. (4) Barnouin-Jha, O. and Schultz, P. H. (1996). *J. Geophys. Res., 101*, 21,099-21,115. (5) Barnouin-Jha, O. and Schultz, P.H. (1998), *J. Geophys. Res., 103*, 25,739-25,756. (6.) Schultz P.H. and Singer J. (1980) *Lunar and Planetary Sci. Conf. XI*, pp. 2243-2259. (7) Barnouin-Jha, O. S., Baloga, S. and Glaze, L. (2005), *J. Geophys. Res., 110*, E04010, doi:10.1029/2003JE002214. (8) Wrobel, K. E. and Schultz, P. H. (2005). *Lunar and Planetary Science Conference XXXVI*: Abstract 1221. (9) Schultz, P. H. (2003), *Lunar Planet. Sci. Conf. XXXIV*, CD-ROM, Abstract #2067. (10) Anderson, J. L. B. and Schultz, P. H. (2005), *Lunar and Planetary Science Conference XXXVI*: Abstract 1773. (11) Mouginis-Mark, P.J. (1981). *Icarus* 45, 60 – 76. (12) Head *et al.*, 2001 *Science*, Vol 286, Issue 5447, 2134-2137 ,

POSSIBLE CRATER-FLOOR THERMOKARST IN UTOPIA PLANITIA, MARS

Richard J. Soare[1,2] and J.M. Wan Bun Tseung[1]. [1]Dept. of Geography, Planning and Environment, Concordia University, 1455 De Maisonneuve W., Montreal, Canada, H3G 1M8; [2]Dept. of Geography, Dawson College, 3040 Sherbrooke St. W, Montreal, Canada, H3Z 1A4. e-mail: rsoare@colba.net.

Introduction: Pits, depressions and collapse features that are consistent with the morphology of terrestrial thermokarst have been identified in five mid- to high-latitudinal areas of Mars: 1. the circum-Chryse outflow channels [1][2][3][4]; 2. Chryse Planitia itself [5][6]; 3. the volcanic fields surrounding Olympus Mons and those to the west of Elysium Mons [7]; 4. the southern margin of the Vastitas Borealis formation [8]; and, 5. two of the great northern plains - Acidalia [9] and - Utopia Planitiae [10][11][12]. These are areas where water may have been present in the past and where near-surface ground ice could be extant today.

We focus on a region of Utopia Planitia where pits, depressions and collapse features are highly concentrated (~40^0 - ~50^0 N and ~260^0 - ~281^0 W) in order to evaluate the plausibility of a thermokarst formation hypothesis.

Terrestrial thermokarst: When the thermal equilibrium of terrestrial ice-rich permafrost is disrupted, inducing localised or regional thawing, the formation of thermokarst could occur. Disequilibrium is the result of geomorphic, biological or climatic processes [13]. These processes may be triggered by human activity such as road building and deforestation or by natural activity such as slumping, the ponding of water, or the loss of a vegetative cover [14]. Climate change, induced by anthropogenic and non-anthropogenic factors, also destabilises ice-rich permafrost [15].

Terrestrially, there are a number of landforms associated with thermokarst processes: eroded or slumped shorelines; shallow, steeply-sided, rimless and irregularly-shaped thaw lakes; and pits or depressions that form when thaw lakes drain or fill-in. Thaw-lakes, ponded or drained, could be isolated, clustered or multi-lobed. Lake formation often occurs at polygon junctions, which are natural collection points for meltwater.

Ground ice and impact craters in Utopia Planitia: Lobate-shaped ejecta surround many of the impact craters in Utopia Planitia. They are visible in numerous Viking, Mars Orbiter Camera and Mars 2001 Odyssey wide- and narrow-angle images. The lobate-shaped ejecta are thought to be the products of near-surface volatiles, possibly ground-ice, vaporised during crater formation [16]. The hypothesised presence of near-surface ground ice in this poleward region is consistent with the data delivered by the neutron spectrometer aboard the Mars 2001 Odyssey [17].

Collapse features in Utopia Planitia We have identified two distinct types of collapse features in Utopia Planitia. Each of them could be the result of thermokarst processes. The features are ubiquitous in the landscape and, on occasion, are found within the basins or on the floors of impact craters associated with fluidised ejecta.

The first type comprises dark pits and depressions that often occur at polygon junctions. The pits and depressions are relatively small (~14m - ~44m in diam.), are uniform in size and shape, and are oriented in a northeastern direction. The uniformity of pit size and shape, as well as the occurrence of the pits at polygon junctions, could be indicative of a relatively short period of formation and growth, a common and abrupt end to their development and, possibly, of an origin that is related to polygon genesis.

The second landform type includes pits, depressions and collapse features that are rimless, flat-floored, steeply-sided, shallow and irregular in shape. Some of the features are isolated, others are clustered, some of the features are multi-lobed, others appear to have coalesced (fig. 1). Coalescence could be indicative of multiple episodes of formation. The features are larger than the polygon junction pits and vary substantially in size (~220m - ~1600m in diam.), form and spatial distribution. This could be indicative of a longer period of formation and growth than the polygon junction pits and of an origin unrelated to polygon genesis.

Thermokarst formation hypotheses. We believe that high obliquity (climate change) could be partly responsible for the formation of the collapse features in Utopia Planitia. Were the elevated air and surface temperatures associated with high obliquity sufficient in intensity to reach pockets of near-surface ground ice, the thermal equilibrium of this ground ice could be disturbed. In turn, this might lead to the melting, evaporation or sublimation of the ground ice and to the subsequent collapse of the overlying regolith.

Alternatively, meltwater could collect at polygon junctions, forming small ponds. Upon the meltwater being lost through drainage, evaporation or sublimation, junction pits would develop.

We also hypothesise that thermokarst formation could be induced even in the absence of climate change. For example, if the work of wind is concentrated by the local topography in an area where the albedo is low, the near-surface concentration of ground-ice is high and the regolith is relatively thin, then on-going aeolian deflation or erosion could reduce the thickness of the regolith further, possibly eliminating the regolith completely from the site. As with the climate change hypothesis, the exposure of the near-surface ground ice to new boundary conditions could induce two things: 1. evaporation or sublimation of the ground ice; and, 2. the subsequent collapse of the surrounding regolith.

Alternative hypotheses:

A. Polygon junction pits: Collapse pits have been identified in Alba Patera, Tractus Catena and Tharsis. Some of these pits are similar in size to the polygon junction pits of Utopia Planitia; others are larger. However, the formation of these pits is associated with ground subsidence following lava tube drainage, magma chamber evacuation or graben formation [18].

The small-sized collapse pits of Utopia Planitia, by contrast, occur in an area not usually associated with volcanic or tectonic activity. Furthermore, the occurrence of the pits at polygon junctions is reminiscent of small-sized thaw lakes that form at polygon junctions in periglacial environments on Earth. Pit orientation is consistent with the dominant patterns of wind circulation in the area [19]. Once again, this is suggestive of terrestrial thermokarst lakes such as those in the Tuktoyaktuk peninsula; the orientation of these lakes is thought to be the product of aeolian processes [20].

B. Larger collapse features: Outcrops of layered sedimentary material on the floors or in the basins of impact craters are not unusual on Mars (figs. 2, 3). These outcrops are thought to be the result of erosion by wind or possibly water. We believe that wind erosion or deflation did contribute to the formation of the crater-floor collapse features in Utopia Planitia. However, the impact craters studied by us show no outcrops or layers of sedimentary material. We believe that the absence of these outcrops suggests a formation hypothesis based on thermokarst processes. The morphology and formation hypothesis of the crater-floor collapse features identified in figure 1 is consistent with the morphology and formation hypothesis associated with terrestrial thermokarst landscapes.

Discussion: We suggest that the small-sized polygon junction pits and larger collapse features in Utopia Planitia are the product of thermokarst processes. While these features could have been formed at high obliquity, we hypothesise that other variables could induce surficial collapse even in the absence of climate change.

The presence of two distinct types of collapse features in the landscape is intriguing. A continuum of evolutionary form exists in terrestrial thermokarst landscapes that does not exist in Utopia Planitia. Explaining this divergence is a matter of ongoing inquiry.

References: [1] Carr, M.H. and Schaber, G.S. (1977). *JGR* 82 (28), 4039 - 4054. [2] Chapman, M.G. *et al.* (2003). *JGR* 108 (E10), 2-1 - 2-20. [3] Costard, F.M. and Baker, V.R. (2001). *Geomorph.* 37, 289 - 301. [4] Costard, F.M. and Kargel, J.S. (1995). *Icarus* 114, 93 - 112. [5] ibid. [6] Carr, M.H. and Schaber, G.S. (1977). *JGR* 82 (28), 4039 - 4054. [7] Rossbacher, L.A. and Judson, S. (1981). *Icarus* 45, 39 - 59. [8] Tanaka, K.L. et al. (2003). *JGR* 108 (E4), 24-1 - 32. [9] Costard, F.M. and Kargel, J.S. (1995). *Icarus* 114, 93 - 112. [10]. ibid. [11] Carr, M.H. and Schaber, G.S. (1977). *JGR* 82 (28), 4039 - 4054. [12] Seibert, N.M. and Kargel, J.S. (2001). *JGR* 28 (5), 899 - 902. [13] French, H.M. (1996). *The Periglacial Environment.* [14] ibid. [15] ibid. [16] Barlow, N.G. and Perez, C.B. (2003). *JGR* 108 (E8), 4-1 - 4-10. [17] Feldman, W.C. et al. (2002) *Science* 297, 75 - 78. [18] Wyrick, D. et al. (2004) *JGR* 109 (EO6002), 1 - 20. [19] Wan Bun Tseung, J.M. and R.J. Soare. (2005) *Proceedings*, NESTVAL, in press. [20] Côté, M.M. and Burn, C.R. (2002). *Permafrost Periglac Process.* 13, 61 - 70.

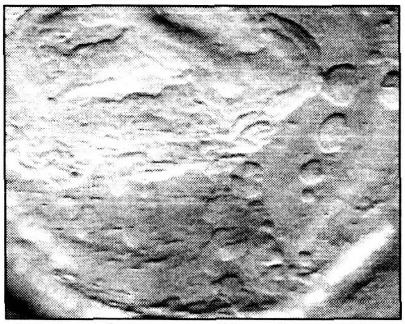

Fig. 1. collapse features, possibly multi-episodic on impact-crater floor, Utopia Planitia (45.1^0 N; 274.5^0 W). Mars 2001 Odyssey VO5265017. Image is ~5km across.

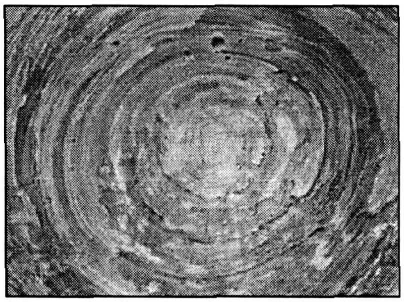

Fig. 2. Layered sedimentary rock in an impact crater northern Terra Meridiana (2.3°N, 356.6°W) (MSSS); mosaic of MOC-M04-01289, E17-01676, and M21-01646. Image is ~2km across.

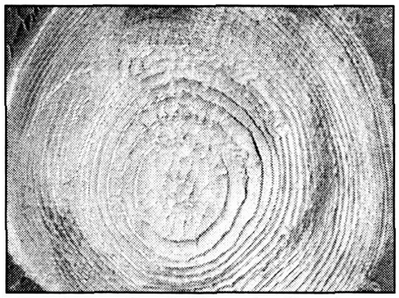

Fig. 3: outcrops of eroded layered sedimentary material in northwest Schiaperelli Basin (0.92^0 S.; 346.41^0 W)(MSSS). MOC-R0600195. Image is ~2km across.

FIELD OBSERVATIONS OF GROUND-HUGGING EJECTA FLOW AT LONAR CRATER, INDIA.

S.T. Stewart[1], K.L. Louzada[1], A.C. Maloof[2], H.E. Newsom[3], B.P. Weiss[4], S.P. Wright[5]. [1]Harvard (Dept. Earth & Planetary Sciences, sstewart@eps.harvard.edu), [2]Princeton (Dept. Geosciences), [3]U. New Mexico (Inst. Meteoritics), [4]Massachusetts Institute of Technology (Dept. Earth, Atmospheric & Planetary Sciences), [5]Arizona State U. (Dept. Geological Sciences).

Introduction. One of the least understood aspects of impact cratering are the processes governing ejecta emplacement. This is due, in part, to the lack of preservation of ejecta at almost all terrestrial impact structures, which are usually subject to extensive post-impact erosive processes. Hence, much of our knowledge of ejection processes is derived from laboratory experiments and explosion craters [e.g., 1] and studies of lunar craters [e.g., 2]. These studies led to the model of ballistic sedimentation [3], where the dominant process is ballistic ejection of primary materials from the crater cavity and incorporation of secondary materials upon impact onto the surrounding surface. However, the best studied ejecta blankets around terrestrial craters (Meteor Crater and the Ries and Chicxulub impact structures) record much more complicated ejecta dynamics and a component of ground-hugging flow [4-6]. The prevalence of layered ejecta morphologies on Mars [7], where the continuous ejecta blanket extends >~1.5 times farther compared to fresh lunar craters [8], suggests that similar processes may affect ejecta emplacement on Earth and Mars that are distinct from the Moon. Suggested mechanisms include the presence of an atmosphere [9], the presence of volatiles (liquid water or ice) [10], and the nature of sedimentary lithologies [11]. In January 2005, we conducted a field study of Lonar Crater, India, and found compelling evidence for ground-hugging ejecta flows following the initial ballistic ejection episode, similar to ejecta flows on Mars.

Lonar Crater. The 1.8-km diameter Lonar Crater (Fig. 1) formed between 15-67 thousand years ago in the ~65 Ma Deccan Traps, India [12-17]. The crater and ejecta are extremely well preserved [15, 17]. See [17] for a description of the geologic setting. In a previous study of Lonar Crater, Fudali et al. [15] note instances of "large, individual blocks of ejecta .... [which] plowed along the original surface for some distance, bulldozing accumulations of soil ahead of them" and concluded that there is "good evidence that ejecta was transported in some sort of ground-hugging debris surge."

Ejecta Observations. The continuous ejecta blanket extends an average of 2265 m from the crater center, >2.6 crater radii (*Rc*) significantly farther than the typical ~2 *Rc* observed on the moon [15]. The ejecta blanket outcrops in small gullies, unlined wells, building foundation pits, trenches, and quarries (Figs. 1, 2 and [17]). The Kalapani Dam Quarry (excavated after the studies of [15] were completed) exposes the entire vertical extent of the edge of the continuous ejecta blanket (Fig. 2) along ~500 horizontal meters, with about half the exposure approximately radial to the crater and half perpendicular to the debris flow.

The ejecta blanket grades from overturned stratigraphy with brecciated units of several m size to unsorted clasts (ranging from mm to m, Fig. 2B) in a coarse matrix in the outer continuous ejecta. Because the mega-blocks are difficult to clear for agriculture, the white-colored area in the ASTER satellite image (Fig. 1) roughly corresponds to the ejecta fold unit [Qfb in 17]. The total volume of preserved ejecta is approximately 3.7×10^7 m^3.

Our measurements of ejecta thickness and field observations indicate that the outer edge of the continuous ejecta blanket is similar to a turbulent debris flow. The edge of the flow may have a possible rampart. Fig. 3 presents our measurements of preserved ejecta thickness as a function of distance from the crater center. Fudali et al. [15] estimate that the pre-erosion thickness of ejecta was $\delta_0 \sim 10$ m on the original crater rim radius of 1.71 km. In Fig. 3, the solid line is the ballistic scaling relation for ejecta thickness, $\delta = \delta_0 \left(R/R_C\right)^{-3\pm0.5}$ [18, 19].

There is a clear accumulation of ejecta at the terminus of the continuous ejecta blanket that is similar to rampart ejecta profiles observed on Mars. At this time, our preliminary digital elevation model is too sparse to make direct comparisons to Martian crater profiles. If our initial measurements sample a continuous rampart around Lonar Crater, the inferred horizontal movement involves $\sim1\times10^7$ m^3 of material, or >25% of the predicted volume of the ejecta blanket.

Beneath the ejecta debris flow, clasts of dense massive basalt penetrate up to 1.5 m into the black, clayey histosol on the pre-impact surface. At KDQ, we mapped 32 clasts (typically several cm) that appear to penetrate the histosol (Fig. 2A, up to 2 m thick) before the arrival of the ejecta debris flow. We interpret a sequence of (i) ballistic ejecta clasts, which are discontinuous at this range, followed by (ii) horizontal movement of the ejecta mass. Assuming the clasts were ejected at 45° from the crater center, the secondary impact velocity was ~140 m/s at about 20 seconds after launch. The crater formation time was

~10 seconds [19], and the ground hugging flow must have reached a radius of 2100 m more than 20 seconds following impact. This sequence is consistent with inferred flow velocities of low 10's m/s around Martian rampart craters [20] and comparable to terrestrial debris flows.

The ejecta debris flow appears to be matrix-supported with a nearly free-slip boundary. At the contact between the ejecta debris flow and the pre-impact histosol, some histosol was incorporated into the flow, but the total contribution of secondary materials to the ejecta is not yet known.

Conclusions. The continuous ejecta blanket around Lonar Crater was partially emplaced by a turbulent matrix-supported ground-hugging flow. The ejecta blanket may terminate in a rampart similar to features observed on Mars. At this time, the possible contribution of liquid water in the flow is not known. Present day water table depths are within the range of excavated materials. Lonar Crater is an excellent terrestrial analog for further field studies to discern the nature of Martian ejecta debris flows.

References. [1] Roddy, D.J., et al., eds. (1977) *Impact and Explosion Cratering*, Pergamon. [2] Pike, R.J. (1976) *Moon* **15**, 463. [3] Oberbeck, V.R. (1975) *Rev. Geophys. Space Phys.* **13**, 337. [4] Hörz, F., et al. (1983) *Rev. Geophys. Space Phys.* **21**, 1667. [5] Osinski, G.R., et al. (2004) *MAPS* **39**, 1655. [6] Grant, J.A. and P.H. Schultz (1993) *JGR* **98**, 15033. [7] Barlow, N.G., et al. (2000) *JGR* **105**, 26733. [8] Mouginis-Mark, P.J. (1978) *Nature* **272**, 691. [9] Schultz, P.H. (1992) *JGR* **97**, 11623. [10] Carr, M.H., et al. (1977) *JGR* **82**, 4055. [11] Kieffer, S.W. and C.H. Simonds (1980) *Rev. Geophys. Space Phys.* **18**, 143. [12] Fredriksson, K., et al. (1973) *Science* **180**, 862. [13] Sengupta, D., et al. (1997) *Revista de Fisica Aplicada e Instrumentacao* **12**, 1. [14] Storzer, D. and C. Koeberl (2004) *LPSC* **35**, 1309. [15] Fudali, R.F., et al. (1980) *Moon & Planets* **23**, 493. [16] Ghosh, S. (2003) *Indian Minerals* **57**, 105. [17] Maloof, A.C., et al. (2005) *Wkshp. Volatiles & Atmos. Martian Impact Craters*. [18] Kring, D.A. (1995) *JGR* **100**, 16979. [19] Melosh, H.J. (1989) *Impact Cratering: A Geologic Process*, Oxford U.P. [20] Mouginis-Mark, P.J. and J.M. Boyce (2005) *Eos Trans. AGU* **85**, P33B-04.

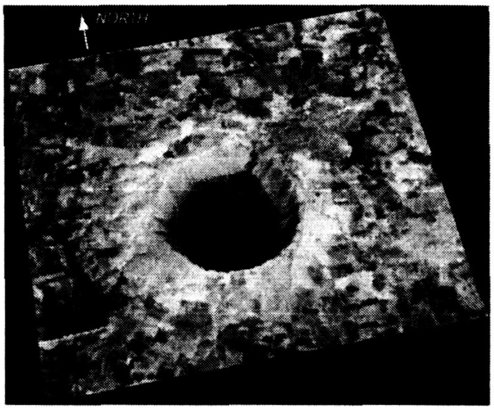

Fig. 1. False-color (Red=Near-infrared(3), Green=Red(2), Blue=Green(1)) ASTER satellite image of Lonar Crater draped over preliminary digital elevation model (DEM) with 3x vertical exaggeration. Bright red indicates areas of dense vegetation. Black region in crater shows extent of shallow lake. Kalapani Reservoir is the dark blue region in the SW. Kalapani Dam Quarry is located at the E end of the dam. Durga Devi Hill is on the SE edge of the image. The town of Lonar is adjacent to the NE rim of the crater.

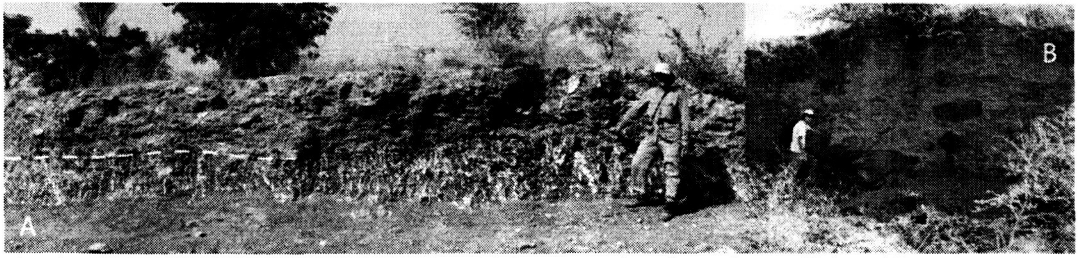

Fig. 2. A. Ejecta contact (dashed line) with histosol containing penetrating ejecta clasts at Kalapani Dam Quarry (KDQ [17]). B. Large boulders (up to 1.5 m) in ejecta flow at KDQ.

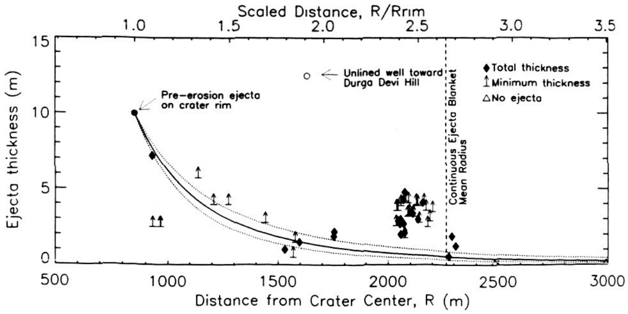

Fig. 3. Ejecta thickness observations at Lonar Crater (symbols) and model ejecta thickness from scaling laws [18, 19] (solid line with error range shown by dotted line) as a function of radial distance from the center of the crater. Selected locations are identified in [17]. Note the significant accumulation of ejecta amounting to ~4 times ballistic predictions at edge of continuous ejecta blanket. The outlier point from a well SE of the crater rim may represent pile up of the ejecta near the base of Durga Devi Hill [see 17].

INTERACTION BETWEEN IMPACT VAPOR CLOUDS AND THE EARLY MARTIAN ATMOSPHERE.

S. Sugita[1] and P.H. Schultz[2], [1]Univ. of Tokyo, Dept. of Complexity Sci. and Eng. (Kashiwanoha, Kashiwa, Chiba 277-8561, JAPAN, sugita@k.u-tokyo.ac.jp), [2]Brown Univ., Dept. of Geol. Sci. (Providence, RI 02912, USA.).

Introduction: Interactions between impact-induced vapor clouds and the ambient planetary atmospheres are considered to have played a very important role in the evolution of planetary atmospheres and surface geology. However, the detailed analysis of such interaction has not been studied extensively before. In this study, we attempt to construct a simple model of vapor-atmosphere interactions taking into account the effects of both fluid dynamics and chemical reactions.

Mars: Whether or not Mars had a warm and wet climate is one of the most controversial issues in Mars science. If a large amount of methane existed in the Mars atmosphere, it may be able to warm Mars to temperatures above freezing [1]. However, it is not known if there was a process that can supply methane at high rate enough to withstand the rapid destruction by UV-induced photochemistry. Because fluvial features on Mars appear to be contemporaneous to the late-stage heavy bombardment [4], the possible warm climate may have been maintained by impact-related processes.

Impact Scenarios: A number of impact-induced mechanisms have been proposed to produce a large amount of CH_4. For example, atmospheric re-entry process of vapor condensates from a large iron-rich impact has been proposed to induce Fischer-Tropsh reaction and produce CH_4 globally [5]. This process, however, requires a relatively high concentration of preexisting H_2 in the atmosphere. Thus, although it is probably very effective for a few hundred million years after the planetary accretion, it may not be very effective near the end of the late-stage heavy bombardment period.

Fischer-Tropsh reaction within vapor plumes due to cometary impacts has also been proposed to produce a large amount of CH_4 [6]. This model, however, assumes that dust condensates from cometary vapor have the same catalytic efficiency as industrial catalysts with metallic iron and nickel on the grain surfaces. Equilibrium calculations indicate that iron and nickel in comet-composition vapor are likely to condense as FeO and Ni_2S_3, whose catalytic efficiencies are much lower than metals. Furthermore, high-temperature impact vapor plumes are likely to be lifted quickly by buoyancy force [7,8]. This uprise will leads to intense entrainment of ambient air, analogously to volcanic eruption plumes [8]. If the ambient atmosphere is dominated by CO_2, oxygen fugacity within the uprising vapor plume will greatly increase. This may reduce methane productivity greatly. Thus, cometary impacts may not be very efficient in delivering methane to a planet with a CO_2-dominated atmosphere.

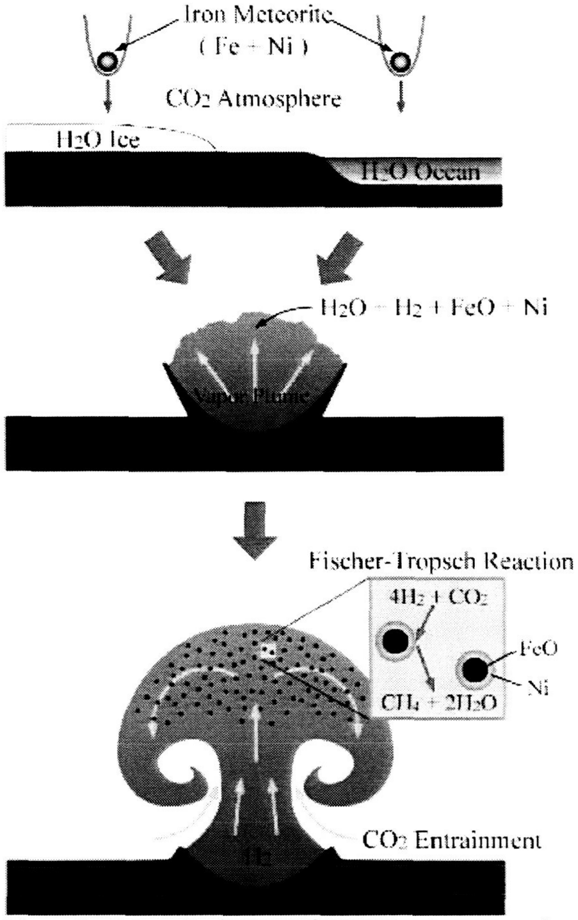

Figure 1. Schematic diagram of interaction between an impact vapor cloud and the ambient atmosphere.

New Process: In this study, we propose a methane-producing mechanism that does not require a reducing atmosphere or efficient catalytic properties of metal oxides or sulfides considering both fluid mechanical and chemical interaction between impact vapor clouds and the ambient atmosphere. More specifically, we consider impacts of iron meteorites into H_2O (e.g., ocean, polar cap, or permafrost) under a CO_2-dominated atmosphere, taking account of oxidation of meteoritic matter, atmospheric entrainment due to buoyancy uprise, and Fischer-Tropsh reaction on the surface of survived meteoritic metals.

Impact Vaporization and Condensation: A simple analytical calculation using the Gamma model [9] indicate that the amount of vaporized water is larger than iron impactor mass if the H_2O layer is thicker than 1/15 – 1/20 the projectile diameter. If this condition is met, the resulting vapor will have an approximately constant yield of H_2 after the adiabatic.

Figure 2 shows the equilibrium chemical composition of Fe-Ni-H_2O mixture as a function of temperature, depicting the condensation sequence within a vapor plume due to an iron meteorite impacting H_2O. Unlike in cometary vapor, nickel condenses as metal in this vapor plume, although iron condenses as oxide. Here, it is noted that metallic nickel condenses after iron oxide condenses, allowing metallic nickel exposed to the gas phase after adiabatic cooling.

Buoyancy Uprise Process: After adiabatic decompression, entrainment of cold ambient air becomes the dominant cooling process of an impact vapor plume. The temperature T of the air-vapor mixture is given by a simple heat balance between hot vapor and entrained cold air. Calculation results indciate that plume temperature goes through the catalytically active range when 1 to 10 times the vapor mass of air is entrained, depending on the post-decompression vapor temperature. This will require > $(2L/g)^{1/2}$ of time (~10^2 seconds for 10 km of vapor plume [8]), where L and g are plume diameter and gravity, respectively. This time scale is comparable to the time needed for industrial catalyst to convert H_2 to CH_4 within a vapor cloud [6]. Because vapor condensates expected in the vapor plumes considered in this study are small iron oxide grains coated with metallic nickel layer, it is very similar to industrially utilized catalysts. Thus the duration of catalytically active temperature condition is likely to be long enough to convert H_2 to CH_4.

Then near-equilibrium concentration of CH_4 can be catalytically produced in an uprising vapor cloud. Figure 3 shows the equilibrium yield of methane from uprising impact vapor plumes. Calculation result shows that methane yield reaches higher than 1/3 the stoichiometric maximum (i.e., 1/4 mole of CH_4 for 1 mole of initial H_2) within the catalytically active temperature range (400 – 600 K) when vapor mixing ratio is >10%. Such high vapor mixing ratios at catalytically active temperatures is achieved when post-decompression vapor temperature is lower than ~2000 K (Figure 3). Because the above Gamma-model calculation indicates that mean pre-decompression vapor temperature for iron meteorites at 10 km/s is 1800 – 2400 K, this condition can be met by a large fraction of iron impactors.

Warm Paleo-Mars? When a 30 km of iron meteorite hit a H_2O ice body, it would produce 0.2% of CH_4 in a 2 bar of CO_2 atmosphere on paleo-Mars. This composition of atmosphere is estimated to warm Mars to temperatures above freezing [1]. Although such a large impact is not expected to occur frequently, it must have occurred at least several times during the heavy bombardment period. Then, a warm climate may have occurred episodically and last for several hundred of years of time (i.e., the photochemical lifetime of methane [10,11]). Such episodic occurrence of warm climate is consistent with geologic record of Mars [12].

References: [1] Kasting, J.F (2002) *AGU Fall Meeting, #P51B-0345*. [4] Carr, M.H. (1981) *The Surface of Mars*, Yale Univ. Press, New Heaven. [5] Sekine, Y. et al. (2003) *JGR, 108*, 10.1029/2002JE002034. [6] Kress M. and C.P. McKay (2004) *Icarus, 168*, 475-483. [7] Jones E. and J.W. Kodis (1982) *GSA Sp. Pap., 190*, 175-186. [8] Suigta, S. and P.H. Schultz (2002) *Icarus, 155*, 265-284 [9] Croft, S.K. (1982) *GSA Sp. Pap., 190*, 143-152. [10] Formisano, V. et al. (2004) *Science, 306*, 1758-1761. [11] Krasnopolsky, V.A. et al. (2004) *Icarus, 172*, 537-547. [12] Schultz, P.H., (1987) *Kagaku, 67*, 486-495; Lee P. and C.P. McKay (2003) *LPSC XXXIV*, CD-ROM #2127.

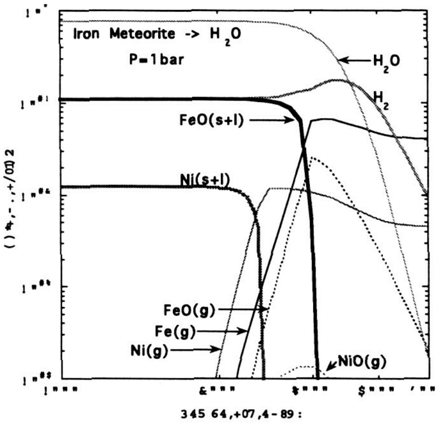

Figure 2. Equilibrium chemical composition of vapor plumes due to iron meteorites impacting H_2O target as a function of temperature at 1bar. The molar mixing ratio in the vapor is assumed to be H_2O:Fe:Ni=1:0.13:0.14.

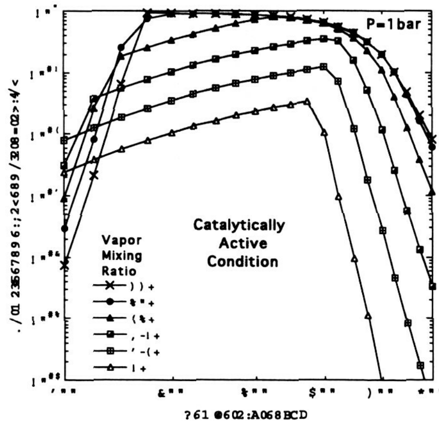

Figure 3. Equilibrium methane yield normalized by the stoichiometric maximum methane yield (i.e., 1/4 of initial H_2) within an impact vapor plumes uprising through a CO_2 atmosphere as a function of temperature and mixing ratio of H_2-rich impact vapor at 1 bar.

INVESTIGATING SURFACE SCOURING PROCESSES AND EJECTA DEPOSITION BY IMPACT GENERATED WINDS.

A. Suzuki[1] (ayako@eri.u-tokyo.ac.jp), O. S. Barnouin-Jha[2, 3], I. Kumagai[4], Y. Nagata[5] and K. Kurita[1], [1]Earthquake Research Institute, [2]Dept. of Engineering and Complexity Science, U. Tokyo, Japan, [3]JHUAPL, Laurel, MD, [4]Institut de Physique du Globe de Paris, [5]Fac. of Engineering, Tokyo University of Agriculture and Technology.

Introduction: The Martian atmosphere and subsurface volatiles could both contribute to the formation of fluidized ejecta on Mars. In this study, we investigate the late stages of ejecta deposition and surface scour by atmospheric winds generated during an impact. We focus on both the mechanics of surface scour as well as transport of material generated by strong winds generated from an impact. We will emphasize both the formation of surface lineations in order to address their existence on pedestal craters [1, 2, 3, 4] (recently also called double layered ejecta (DLE) craters [5, 6]), and the mechanics of how such winds generate ground-hugging surface gravity currents.

We consider only the very late stages of ejecta emplacement, when a ring vortex produced by an ejecta curtain advancing into an atmosphere [7] becomes decoupled from the curtain to strike and erode the target surface. We decouple this vortex from the ballistic ejecta curtain by conducting experiments in a water tank, examining the interaction between a vortex ring and a layer of surface particles. Our results indicate that even present Martian conditions are sufficient to form surface lineations seen on fluidized ejecta of pedestal craters. These experiments also show that gravity flows resulting from plumes of particulates uplifted by the vortex ring help generate the fluidized appearance of ejecta when deposited by an atmosphere.

Experimental Approach: Many laboratory experiments examine the role of the atmosphere during impact cratering [7, 8, 9, 10]. These experiments consider primarily ejecta entrainment and transport processes, and to a lesser extent emplacement. Our experiments differ because they detail the late stage interactions between the impact-derived vortex ring and particles sitting on a surface. They are somewhat idealized in that they do not include prior entrainment and transport of ejecta before the arrival of a curtain-derived vortex ring on the surface.

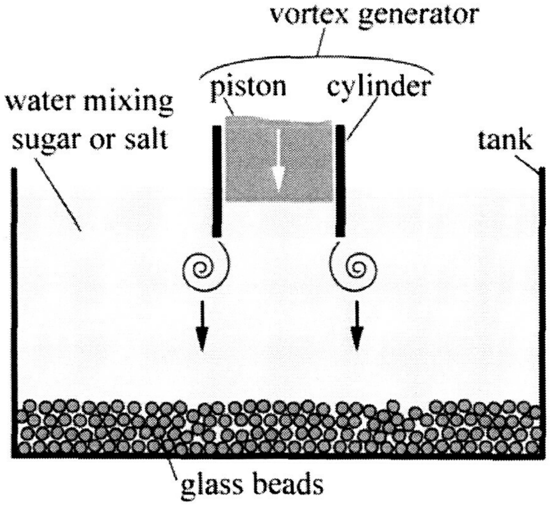

Figure 1: A cross-sectional schematic view of the experimental setup. The downward displacement of the piston forces water through the cylinder, causing flow separation and the generation of a vortex ring.

Our experiments were carried out in a transparent rectangular tank filled with a mixture of water and sugar or salt, at the bottom of which we placed a layer of glass beads uniform in size (Figure 1). A vortex ring generator, which is composed of a piston and a cylinder, was placed at the top of the tank. The water is pushed through the cylinder by dropping the piston leading to flow separation at the edge of walls of the cylinder and subsequent generation of a vortex ring [e.g., 11]. The displacement length and velocity of the piston controls the flow velocity in the vortex ring. We vary this velocity and the ambient fluid conditions by mixing in sugar or salt into the water. We also change the size of the glass beads.

Each experiment is filmed with a high speed camera, and fluid motion is measured using Particle Image Velocimetry (PIV). After each experiment, we analyzed the deposits created in the particle layer.

Results: We find that three surface morphologies are generated in the particle layer following interactions with a vortex ring (Figure 2): (Mode 1) petal-like features and radial lineations formed as the vortex ring sweeps, lifts, transports and deposits the glass beads; (Mode 2) a circular erosion zone with few radial lineaments formed as the vortex ring only sweeps beads aside without lifting them; and (Mode 3) nothing happens as the vortex ring is too weak.

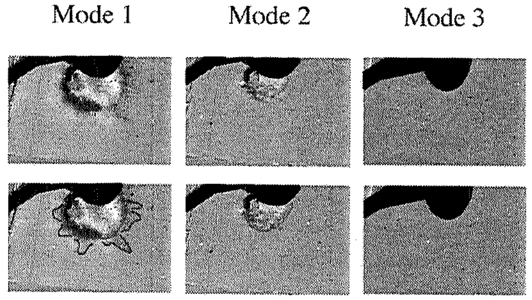

Figure 2: Three modes of vortex ring-surface interactions. Each column represents an oblique view of one mode (illuminated from upper right; black area is the shadow of vortex generator). Bright and dark area indicates regions of particle displacement. (Second row) Outlines of a circular erosion (red) and petal-like deposition zone (blue).

Our results indicate that these three styles of interaction between the vortex ring and the surface depend on the parameters we varied. All these variables can be expressed by two dimensionless numbers, θ and *Re* (Figure 3). The variable θ is the ratio of inertial resistance of the surrounding fluid to buoyancy acting on the particles in the surface layer [e.g., 12]. The Reynolds number *Re* is the ratio of inertial to viscous forces acting on these same particles. The greater θ and *Re* the more likely Mode 1 occurs; the smaller these values the more likely nothing or Mode 3 occurs.

Our experiments also show how little gravity currents are generated by the particles uplifted in the vortex when Mode 1 occurs. These little plumes collapse under gravity to form flows akin to debris flows or powdery snow avalanches leading to a fluidized features.

Discussion: Figure 3 illustrates that the range of θ and *Re* obtained in the laboratory is equivalent to those that can be achieved on Mars for winds ranging from 10-100m/s under current atmospheric conditions. Thus all three modes of vortex ring-surface interactions are possible on Mars. Consequently, some craters that possess finer ejecta may have lineations form, while others will not. Winds strengths could be another contributing factor.

While scour is expected only under some conditions, transport of material is expected under many impact conditions on Mars because, contrary to these experiments, the ring vortex already possesses entrained ejecta before it reaches a target surface. This material will be deposited as a gravity flow, as illustrated in these experiments in Mode 1.

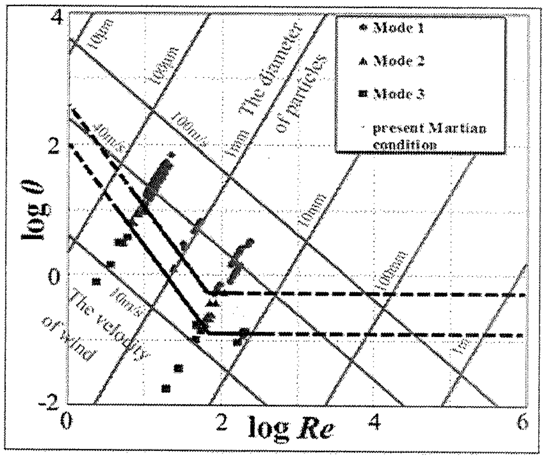

Figure 3. Regime diagram of the experimental results between θ and *Re* differentiating the various modes of vortex ring-surface interactions (see text). The red lines indicate Martian condition; positive slopes indicate the variation of wind velocity; negative slopes indicate the variation of particle diameter.

References: [1] Mouginis-Mark, P. (1979) *JGR, 84,* 8011-8022.[2] Mutch, P. and A. Woronov, (1980) *Icarus, 41,* 259-268. [3] Mouginis-Mark, P. (1981) *Icarus, 45,* 60-76. [4] Ogawa, Y. and K. Kurita, (2003) *Proc. 36th ISAS Lunar and Planet. Symposium,* 85-88. [5] Barlow, N. G. et al., (2000) *JGR, 105,* 26733-26738. [6] Mouginis-Mark, P. (2004) *7th Mars Crater Consortium,* Abstract #0711. [7] Barnouin-Jha, O. S. and P. H. Schultz, (1996) *JGR, 101,* 21099-21115. [8] Schultz, P. H. (1992) *JGR, 97,* 11623-11662 [9] Schultz, P. H. and D. E. Gault (1979) *JGR, 84,* 7669-7687. [10] Barnouin-Jha, O. S. and P. H. Schultz, (1998) *JGR, 103,* 25739-25756. [11] Saffman, P. G. (1978) *J. Fluid Mech., 84,* 625-639. [12] Eames, I. and S. B. Dalziel, (2000) *J. Fluid Mech., 403,*305-328.

Evidence for the role of sub-surface volatiles in the formation of large rayed crater systems on Mars: Implications for the ejection of the Martian meteorites. L. L. Tornabene, Department of Earth and Planetary Sciences, University of Tennessee, Knoxville, Tennessee 37996-1410.

Introduction: Five definitive and three probable large rayed crater systems have been discovered on Mars using thermal infrared (TIR) images from the Thermal Emission Imaging System (THEMIS – 100m/pixel) and visible images from THEMIS (~18m/pixel) and narrow-angle Mars Orbiter Camera (MOC) images (several meters per pixel)[1, 2]. Morphological characteristics (e.g. apparent youth, crater diameter, oblique impact origin, fluidized ejecta, etc.) and a geographic bias to predominately young volcanic plains for rayed craters are all strong links to the proposed characteristics of the Martian Meteorite (MMs) source region [1], which is based on geochemical ages (i.e. crystallization and ejection) and characteristics of the MMs [3]. Here we present evidence in the form of visible image observations and from the most recent MM delivery a model that implicates subsurface volatiles may have played a positive role in the formation of rays and increased spallation volumes for the delivery of the MMs.

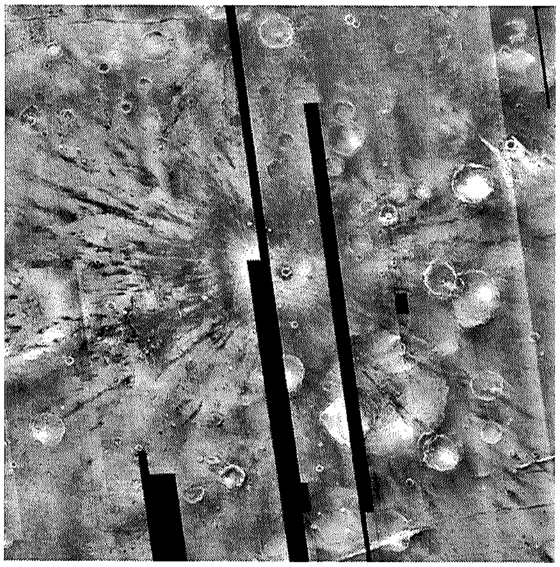

Figure 1. THEMIS nTIR mosaic (one strip is ~ 30 km wide) of Gratteri crater, an excellent example of a Martian rayed crater with very distinctive thermophysical contrasts. Crater diameter: 6.9 km; Max ray length measurable in THEMIS nTIR mosaic: ~595 km.

Martian Rayed Crater Characteristics: Martian rayed craters range from the smallest apparent diameter (rim to rim) of 1.5 to the largest 10.1 km [1]. The five definitive rayed craters carry the IAU provisional names of Zunil (D_a = 10.1 km), Tomini (7.4), Gratteri (6.9), Zumba (3.3) and Dilly (2.0). The three probable rayed craters (unnamed) have apparent diameters of 1.5, 4.2 and 5.7 kms. Ray lengths can be distinguished up to ~900 km from the primary in THEMIS nTIR mosaics[1, 2] (Fig. 1) and distinctive secondaries bearing intact 1-2 ejecta/ray facies can be discerned up to 1600 km away in MOC images[2, 4].

There is reasonable evidence to suggest that these craters are the result of oblique impact events. Ray asymmetries, forbidden zones in ejecta and non-circular primary cavities (Fig. 2c) all suggest moderately oblique trajectories (>15-60°) for most of these craters [1, 2].

Martian rayed craters have a geographic bias to the young lava plains (relatively regolith-free?) of Elysium with outliers within or in close proximity to the lava plains that issue from the Tharsis region. This bias may be a possible link to restrictions with respect to their formation.

Subsurface volatiles, ray formation and MM delivery:

Morphological evidence for subsurface volatiles within rayed crater target surfaces: Fluidized ejecta blankets (FEBs) are typically associated with subsurface volatiles, which was first proposed by [5; see review by 6]. Martian rayed craters Gratteri, Zunil and Tomini all exhibit classic FEBs (Fig. 2a, b and c). Several rayed crater primaries, typically towards the smaller apparent diameters, do not themselves exhibit FEBs. However, volatiles may have still played a significant role in their formation. For example, craters with larger diameters that are observed in the same geological unit and are not to distant from the Dilly and Zumba primaries possess both single and multi-layered FEBs. Two craters >5 km lying ~60 km to the north of Dilly (Fig. 2d) exhibit a single-lobate FEBs, and another crater with multilobate fluidized ejecta (D_a=21.5 km) lies 120 km to the NW (Fig. 2e). The closest crater (D_a=4.0 km) with a fluidized ejecta blanket to Zumba crater is 175 km to the NNW (Fig. 2f), but is still within the same geologic unit in which Zumba impacted.

From these observations, subsurface volatiles appear to exist at depth, or at least existed during rayed crater formation. Because rayed craters appear to be amongst the youngest craters in their size-class [1, 2], these subsurface volatiles may exist during recent times. Recent results from the gamma-ray and neutron spectrometers aboard the Mars Odyssey 2001 orbiter suggest that the target terrains for rayed craters currently have low abundances of subsurface-H (4-6%) [7], but this is only from the upper most meter of the surface and ice-stability is likely to vary with depth. It is apparent that constraining the timing of the formation of FEBs is difficult to determine since subsurface volatile stability varies with latitude over past obliquity cycles (~5 Ma) [8, 9] and crater/terrain ages are not well constrained, however at first order, we can conclude that volatiles likely played a role in the formation of these craters.

Increased spallation from subsurface volatiles: In addition to oblique impact formation, models by [10] indicate that subsurface volatiles increase spallation volumes up to 10% than impacts into dry targets. The "wet" Mars simulation involves an asteroid (Granite EOS at 10 km/s) impact into a surface that is 80% Granite EOS and 20% Ice EOS. The 20% volatile content is lower than previous estimates and is considered a good approximation for average Mars. By increasing the volume of spalled component ray formation and MM ejection probabilities increase.

The fact that rayed crater primary ejecta are fluidized, or the terrains that rayed craters formed in have abundant FEBs, strongly suggests that volatiles played a significant role in the ray formation process. Ray formation is intimately linked to the spallation process because rays are likely to be a physical manifestation of the spallation process [1]. Spallation is purported to be the mechanism for MM ejection [11, 12].

References: [1] Tornabene et al. (submitted), *JGR-E.* [2] McEwen et al. (2005), *In Press, Icarus.* [3] Nyquist et al. (2001), *Space Sci.Rev.*, 105-164. [4] Preblich et al. (2005), LPSC XXXVI, Abstract #2112. [5] Carr et al. (1977), *JGR*, 82, 4055-4065. [6] Barlow and Perez (2003), *JGR-E*, 108, E8, 5085. [7] Feldman et al. (submitted), *JGR-E.* [8] Laskar et al. (2002), cycles. [9] Levrard et al. (2004), *Nature*, 431, 1072-1075. [10] Artemieva and Ivanov (2004), *Icarus*, 71,84-101. [11] Melosh H. J. (1984) *ICARUS*, 59, 234-260. [12] Melosh H. J. (1985) *Geology*, 13, 2, 144-148.

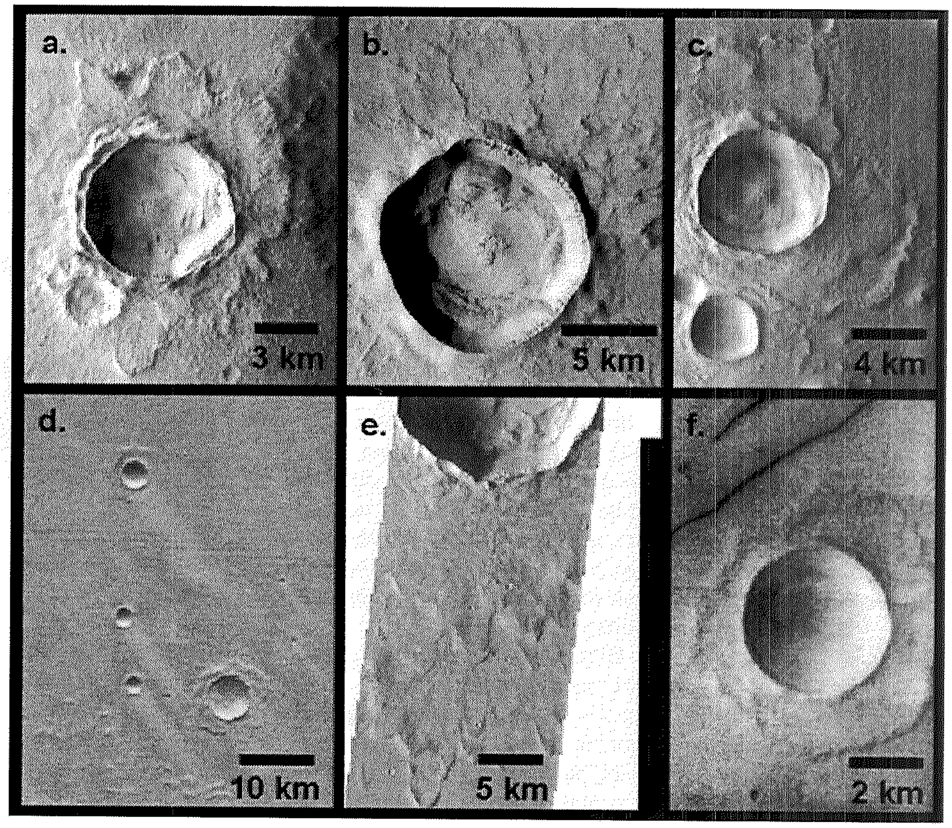

Figure 2. Fluidized ejecta blankets associated with Martian rayed craters. All THEMIS visible image are band 3 (654 nm) grayscale images at ~18 m/pixel resolution. **a.** THEMIS image V14248001 of the Gratteri primary exhibiting a single-lobate fluidized ejecta blanket. **b.** Double- to multi- lobate ejecta blanket emanating from the Zunil primary (V09818024). **c.** Tomini primary exhibiting a double-lobate ejecta blanket (V14387010). **d.** Fluidized ejecta blankets of two craters within the same unit and 60 km from the Dilly primary (Viking MDIM 2.0). **e.** Multi-lobate ejecta for a 21km diameter impact crater 120 km from the Dilly primary (THEMIS V). **f.** A 4 km diameter crater bearing a fluidized ejecta blanket within the same geologic unit as the Zumba primary and only 175 km away.

"SOFTENING" OF MARTIAN IMPACT CRATERS BY CREEP OF ICE-RICH PERMAFROST.

E.P. Turtle[1,2] and A.V. Pathare[1,3], [1]Planetary Science Institute, 1700 E. Fort Lowell, Tucson, AZ, 85719, [2]Lunar and Planetary Lab., Univ. of Arizona, Tucson, AZ, 85721 (turtle@lpl.arizona.edu), [3]California Institute of Technology, Pasadena, CA.

Introduction: Since the initial *Mariner* 9 mapping of Mars, researchers have noted the curious "softened" characteristics of high-latitude terrain, which are widely theorized to result from the viscous creep of a near-surface layer of ice-rich permafrost within the Martian megaregolith [*e.g.*, 1-5]. Squyres and Carr [4] classified creep-related landforms, including: (1) debris aprons, produced by mass wasting along escarpments, examples of which include lobate debris aprons, lineated valley fill, and concentric crater fill; and (2) terrain softening, resulting from *in situ* viscous deformation, which is most clearly expressed by craters with degraded rims and flattened topographic profiles (Fig. 1). Squyres [5] also conducted finite-element simulations that qualitatively established the ability of viscous creep deformation to reproduce the morphologies of craters in martian softened terrain.

Jankowski and Squyres [6] subsequently performed a more quantitative analysis of Martian crater relaxation, concluding that the morphology of mid-latitude craters is consistent with relaxation in a deforming layer no more than 1 km deep. In order to explain the extent of terrain softening observed by [5] with a two-layer model, Jankowski and Squyres [6] required subsurface ice equivalent to a global layer of water 17 m thick, a figure which rises to 55 m if likely locations of terrain softening are included and 125 m if softening conditions are met everywhere poleward of 30° latitude.

We are using finite-element models of viscous creep relaxation to simulate terrain softening, incorporating more recent laboratory measurements of ice/rock mixtures [7-11]. By comparing the resulting landforms to structural and topographic characteristics documented in *MGS* MOC and MOLA data we can constrain the conditions necessary to allow such deformation on Mars [*e.g.*, 12,13]. The original intent of this project was to determine how much different past conditions would have to have been, *e.g.*, warmer, higher ice content, etc., in order to allow the observed deformation. However, to our surprise we found that significant deformation of ground ice can occur quite rapidly under current martian conditions.

Rheology of Ice-Rich Permafrost: Jankowsksi and Squyres [6] had been forced to make some assumptions regarding the rheology of martian ground ice that may no longer be viable. For example, they devised a soil structure parameter S that relates the viscosity of pure ice to that of ice-rich permafrost. In order to allow 3-km diameter craters to relax gradually over time scales of 4 Gyr, they needed to assume a value for S of approximately 10^{-6}. I.e., by constraining the relaxation times to be slow enough to be consistent with the continued existence of $D \sim 3$ km craters in Noachian terrain they needed the viscosity of the ground ice to be one million times greater than that of pure ice.

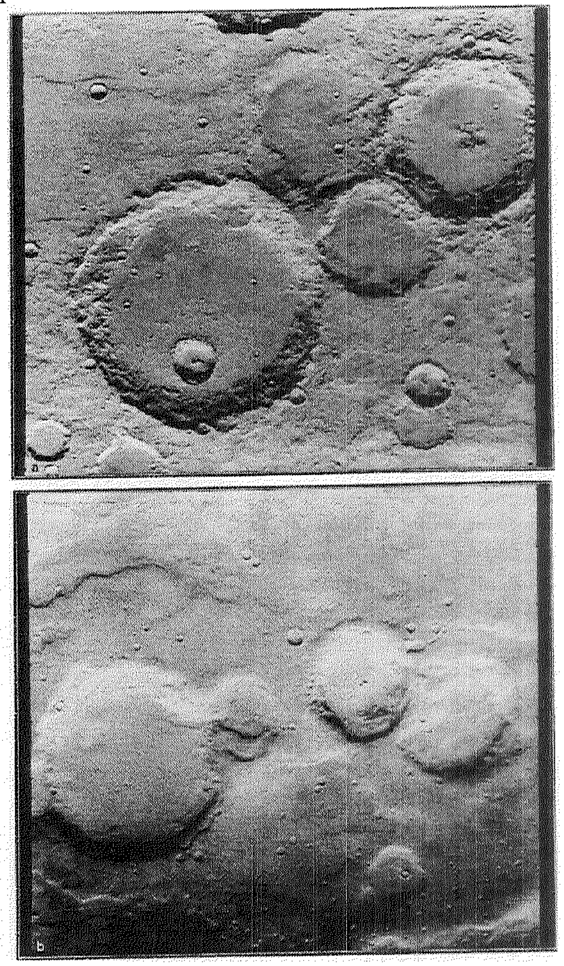

Figure 1: Comparison of unsoftened and softened terrain. **(A)** *Viking Orbiter* image 423S10 of craters in unsoftened terrain (32°S, 227°W) which have sharp rims and walls with steep, concave profiles (from Squyres, 1989). **(B)** *Viking Orbiter* image 195S20 of craters in softened terrain (33°N, 313°W), which exhibit broad and rounded rims, and walls with gentle, convex profiles (from Squyres, 1989).

However, more recent laboratory measurements of dust - water ice mixtures conducted by both Durham *et al.* [7] and Mangold *et al.* [11] have yielded maximum relative viscosities of no more than 100 times that of pure ice. The reason for this is that when the volumetric dust fraction gets too high (typically above 75%), the dust grains come in contact with each other and the mixture crosses the brittle-ductile transition and can no longer undergo viscous creep [7,11]. Hence, it is unlikely that the relative viscosity of Martian permafrost is much greater than 1000 times that of pure ice. Consequently, $D = 3$ km craters in a 1-km-thick deforming layer should relax on time scales of Myr (at most), not Gyr. This conclusion is consistent with the finite element modeling of Pathare *et al.* [13], who showed that 2-km-diameter craters in the South Polar Layered Deposits undergo relaxation on time scales less than 10 Myr.

Simulations Under Present-Day Conditions: We have performed finite-element simulations to investigate the deformation of martian impact craters by creep of an ice-rich surface layer. These models incorporate laboratory measurements of the rheological parameters for dust/water-ice mixtures undergoing dislocation creep and grain size dependent creep [7-9], both of which are relevant under present Martian conditions: Tsurf = 200 K [14]; dT/dz = 15 K/km [15,16].

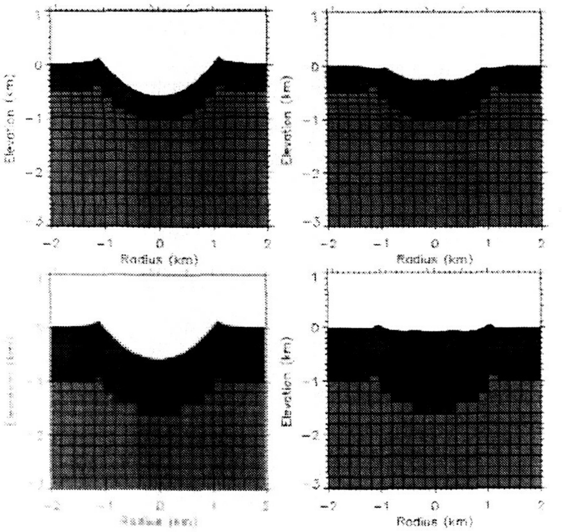

Figure 2: Finite-element models of a 2-km-diameter simple crater before (left) and after (right) relaxation by creep of 0.5-km-thick (top) and 1.0-km-thick (bottom) ice-rich (30% by volume) layers indicated by darker shading; lighter shading is bedrock.

Simulations with only 30% ice (by volume) demonstrate that even under present Martian conditions, viscous creep can occur quite rapidly: the timescales for the simulations illustrated in Figures 2 and 3 are 10^3-10^4 years. This result implies that there cannot currently be a high volume fraction or deep (~1 km) extent of martian ground ice. Another possibility is that the mobility of ground ice is restricted by a surface layer that resists deformation; if, for example, the high volume fractions of ice inferred to be present within a ~1 m surface layer [17] do not continue to significant depths, or a higher viscosity material, *e.g.*, clathrate [18], were present near the surface, the deformation timescales could be significantly longer.

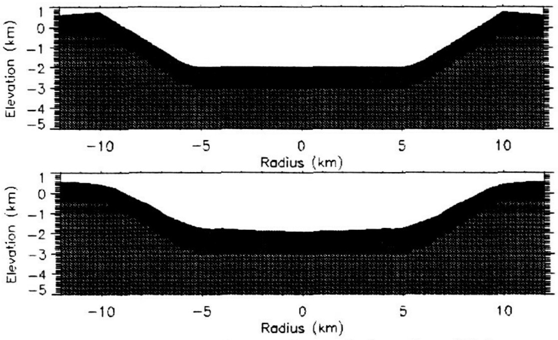

Figure 3: Finite-element models of a 20-km-diameter simple crater before (top) and after (bottom) deformation by creep of a 1.0-km-thick, ice-rich (30% by volume) layer indicated by darker shading; lighter shading is bedrock.

References:

[1] Sharp R.P. (1973) *Icarus* **7**, 139-148. [2] Carr M.H. and Schaber G.G. (1977) *JGR* **82**, 4055-4065. [3] Lucchitta B.K. (1981) *Icarus* **45**, 264-303. [4] Squyres S.W. and Carr M.H. (1986) *Science* **231**, 249-252. Squyres S. (1989) *Icarus* **79**, 229-288. [5] Squyres S. *et al.* (1992) in Mars, Ed. H. Kieffer, Univ. Arizona Press, Tucson, 523-554. [6] Jankowski D.G. and Squyres S.W. (1993) *Icarus* **106**, 365-379. [7] Durham, W.B. *et al.* (1992) *JGR* **97**, 20883–20897. [8] Durham W.B. *et al.* (1997) *JGR* **102**, 16293-16302. [9] Durham W.B. *et al.* (2000) Second Intl. Conf. on Mars Polar Sci. and Exploration, LPI Contribution #1057, 28-29. [10] Durham, W.B., and Stern, L.A. (2001) *Ann. Rev. Earth Planet. Sci.* **29**, 295–330. [11] Mangold N. *et al.* (2002) *Planet. Space Sci.* **50**, 385-401. [12] Turtle E.P. *et al.*, (2003) Third Intl. Conf. on Mars Polar Sci. and Exploration, LPI Contribution #1184, Abstract #8091. [13] Pathare A.V. *et al.* (2005), *Icarus* **174**, 396-418. [14] Martin T.Z. (1981) Icarus 45, 427-445. [15] Schubert G. et al. (1992) in Mars, Ed. H. Kieffer, Univ. of Arizona Press, Tucson, 147-183. [16] Clifford S.M. (1993) JGR 98, 10973-11016. [17] Boynton W.V. *et al.* (2002) *Science* **297**, 81-85. [18] Durham,W.B. *et al.* (2003), *JGR* **108**, 2-1–2-11.

EJECTA FLOW FROM 3-D GRANULAR FLOW MODELS.

K. Wada[1] and O.S. Barnouin-Jha[2,3], [1]Institute of Low Temperature Science, Hokkaido Univ., Sapporo, Japan; [2]Dept. of Complexity Sci. and Engineering, U.Tokyo, Japan; [3]JHUAPL, Laurel, MD.

Abstract

Currently two main models are considered viable for the emplacement of fluidized ejecta: (1) initial ballistic emplacement of ejecta and subsequent flow primarily as a consequence of volatile presence [1, 2, 3, 4], and (2) impact derived winds, which entrain, saltate and eventually emplace ejecta as a gravity current [5]. Some authors have proposed that a mixture of both models could also explain the morphological features seen. However, no study exists where a simple granular flow is used to explain fluidized ejecta. Yet there are many instances where granular flows can explain a wide range of flow features seen at terrestrial rock avalanches and falls [6, 7, 8, 9]. These include the formation of multiple ramparts and circumferential lineaments , as well as the incredible long runout of so called long-runout landslides.

In this effort, we explore the circumstances under which granular ejecta may generate a flow during emplacement using a 3-D granular flow model. In this model, each grain of ejecta is treated as a distinct element [10]. Using this distinct element model (DEM), we investigate the process of ballistic sedimentation and subsequent flow without invoking either water or atmosphere. Thus, even though ejecta flows are seen lacking on the Moon and Mercury (suggesting that granular flows may not be viable on Mars), such an investigation provides at a minimum insights into the mechanics of interaction between ejecta in the thickest portions of the curtain and a target surface. Such information did not exist before, and is particularly important for determining how much kinetic energy of the ejecta goes into creating an advancing flow. Eventually coupled fluid flow and 3-D DEM models will also be available to determine the transport and emplacement of ejecta by winds created during an impact in the presence of an atmosphere.

3-D Distinct Element Model

In our DEM, particle motions are calculated directly in three dimensions by solving the equations of momentum for each particle. Mechanical interactions between the colliding particles are expressed by the Voigt-model, which consists of a spring and dash-pot pair (Figure 1) [11]. The spring simulates elastic restitution, describing the storage and release of elastic energy that occurs during a collision. The dash-pot acts like a shock absorber dissipating energy during contact. A friction-slider model takes into account friction losses between sliding particles via Coulomb friction. Two parameters- the coefficient of restitution, *e* and friction, *mu* - parameterize energy losses due to collision and friction respectively.

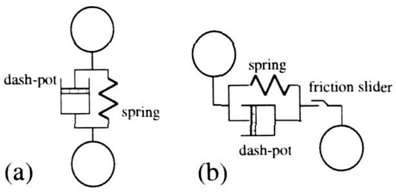

Figure 1. Schematic of the Voight model.

Preliminary results are obtained by computing the motion of ejecta provided by a large numerical investigation of a 6mm-diameter projectile launched vertically into a target of randomly distributed 2 mm-diameter spheres at 300m/s. More details on the cratering conditions and results are provided in [12. 13] . In summary, the calculated ejecta excavation follows behavior expected from scaling rules and experimental data. The computed ejecta curtain thus provides good starting conditions for the volume and velocity of ejecta during the ballistic phase of transport prior to any flow. We also begun modeling the ejecta curtains using the Z-model [14] so that larger planetary scale craters can be investigated [15]. However, at the time of writing this abstract no results using the Z-model were obtained.

The computational domain used is shown in Figure 2. We consider a 15^{o}wedge of the ballistic ejecta prior to deposition. The use of such a small domain is justified as no circumferential collisions or hoop forces have been seen in the 3-D computed ejecta curtain. For each computation each sphere possesses a density of 2.7g/cm^{3}and gravity is set to 1G. The vertical walls of the domain are all smooth and our baseline case assumes reasonable values of *e*=0.4 and *mu*=0.5.

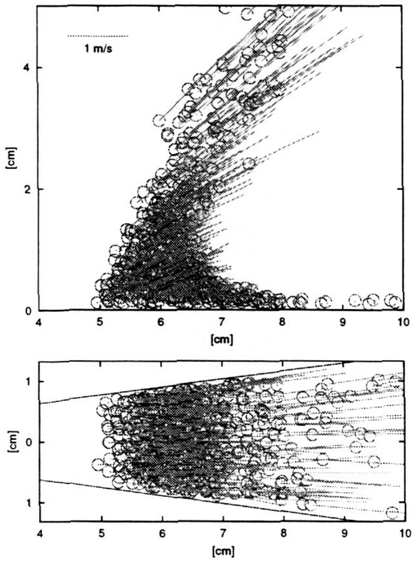

Figure 2. Initial conditions: Side (top) and top (bottom) view. Green lines show the velocity vectors.

We explore the influence of various parameters on the flow dynamics and emplacement of our model landslides relative to our baseline case. In particular, we change the properties of the surface on which the ejecta falls from smooth to very rough. We also consider an erodible surface and changes in *mu.*

Preliminary results and implications

Our results (Figure 3) show that flow can occur simply because of differences in the properties of the surface on which the ejecta lands. If a surface is relatively hard and smooth, flow is easily achieved, while if it is rough, flow is much less likely. In addition, models [16] and experiments [17] of landslides flowing onto an erodible plain indicate that such a terrain is very dissipative and causes flow to stop quickly. Such behavior is also expected for ejecta sedimentation and flow.

These results suggest that the difference in morphological appearance of the continuous ejecta on Mars and the Moon and Mercury are due to the condition of the target surface: on the Moon and Mercury it is fairly soft and highly dissipative because these surfaces are primarily composed of a battered and broken up megaregolith. On Mars, however, the surface have become indurated and smooth mainly due to the presence of volatiles, permitting the flow of ejecta upon deposition.

References: [1] Carr, M., et al., *J. Geophys. Res. 82*, 4055-4065, 1977. [2] Mouginis-Mark, P., *J. Geophys. Res.*, 84, 8011-8022, 1979. [3] Gault, D.E. and R. Greeley, *Icarus 34*, 486-495, 1978. [4] Greeley, R. J. et al, *Proc. Lunar Planet. Sci. Conf. 11*, 2075-2097, 1980. [5] Schultz, P.H., *J. Geophys. Res.*, *97*, 11623-11662, 1992. [6] Campbell, C.S., P.W. Cleary and M. Hopkins, *J. Geophys. Res. 100*, 8267-8283, 1995. [7] Daerr, A., *Physics of Fluids*, v. 13, 2115-2124, 2001. [8] Davies et al., *Can. J. Geotech. 36*, 1096-1110, 1999. [9] Friedmann, S.J., et al., *J. Geophys. Res. 108 (B8)*, 2380, doi:10.1029/2002JB002174, 2003. [10] Cundall, P. A. and Strack, O.D.L. (1979) *Geotechnique 29-1*, 47-65.[11] Duran, J. Sands, Powders anf Grains, Springer, 212pp., 2000.[12] Wada et al., *Lunar Planet Science Conf. XXXIV*, 1529, 2003.[13] Wada et al, submitted to *Icarus*, 2005.[14] Maxwell, D.E., In Impact and Explosion Cratering, 1003-1008, 1977. [15] Ivanov, B. *Solar System Research, V. 30*, # 1, 43-58, 1996. [16] Barnouin-Jha et al., *Lunar Planet. Sci. Conf. XXXVI*, 1588, 2005. [17] McSaveney, M.J., T.R. Davies and K.A. Hodgson, *Proceedings of 8th ISL, Vol 2*, 1053-1058, 2000.

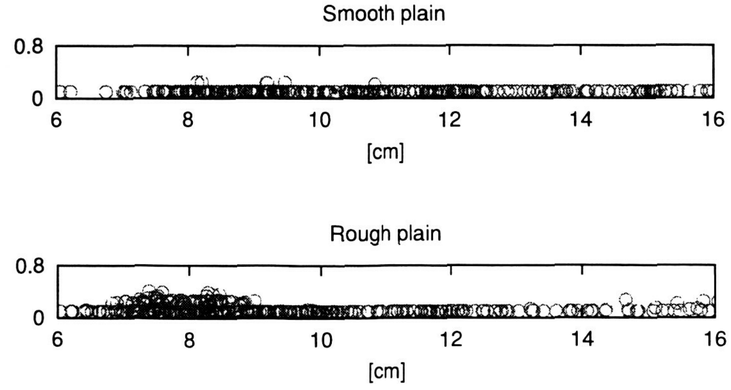

Figure 3. Cross-sectional view of ejecta that has fallen on a smooth (top) and rough plain (bottom). The bottom scale is distance from the crater center. Ejecta flows very efficiently in the case of the smooth plain, leaving behind a very thin and dispersed deposit. In the case of the rough plain, a thick deposit is left behind near the crater rim at aproximately 7cm and the density of particles is greater.

EFFECTS OF AN EARLY-TIME IMPACT GENERATED VAPOR BLAST IN THE MARTIAN ATMOSPHERE: FORMATION OF HIGH-LATITUDE PEDESTAL CRATERS.

K. E. Wrobell[1] P. H. Schultz[1], and D. A. Crawford[2], [1]Department of Geological Sciences, Brown University, Box 1846, Providence, RI 02912 (Kelly_Wrobel@brown.edu), [2]Sandia National Laboratories, P. O. Box 5800, MS 0836, Albuquerque, NM 87185.

Introduction: Following impact, vapor expansion creates an intense airblast that interacts with the ambient atmosphere [1-3]. The resulting hemi-spherical shock wave leaves a signature on the surface that is dependent on initial atmospheric and surface conditions. Here we propose that the formation of pedestal craters (craters surrounded by an erosion-resistant pedestal) may be a direct consequence of extreme winds and elevated temperatures generated by such an impact-induced atmospheric blast.

Pedestal craters, first recognized in Mariner 9 data [4], are a unique feature on Mars and likely a signature of near-surface volatiles [e.g., 5-10]. They are found at high latitudes (small pedestals, Amazonian to Late Hesperian in age) and in thick equatorial mantling deposits (larger pedestals, early Hesperian to Noachian in age). Previously suggested mechanisms for pedestal crater formation (e.g., wind: ejecta curtain vortices [11] or vapor blast [5,11]; and ejecta dust: armoring [12]) do not provide a complete picture. The clear evidence for near-surface volatiles at high latitudes requires a re-evaluation of these alternative models. The results presented here suggest that a combined atmospheric blast/thermal model provides a plausible formation hypothesis.

Background: Impact-induced vaporization is a key component of early time cratering mechanics. Many previous studies, both experimental [13-15] and computational [e.g., 16], focused on the generation and expansion of vapor clouds in an attempt to better understand vaporization in hypervelocity impacts. Here we investigate the response from energy directly imparted from the early time vapor to the surrounding atmosphere on Mars. Such a response, and its possible expression on the surface, has been examined for impacts on Earth [e.g., 17].

The CTH shock physics analysis package [18] with adaptive mesh refinement [19] was used to construct a model of a point-source instantaneous release of a large amount of energy into a small volume of gas during a short time interval. Energies corresponding to 0.1% and 1.0% of the total impact energy (and momentum) required to create a 10 km diameter crater (6 km "apparent" pre-collapse crater) on Mars were coupled to a CO2 atmosphere (specific heat ratio of 1.3) with an ambient density of 1.55e-5 g/cc and an ambient temperature of ~240 K at the surface (y=0).

The model results show a very good correlation to analytical calculations of the physics behind an airblast created by an intense explosion (see [20]).

Results: A fast blast wave (followed by recovery winds) and a large temperature pulse will engulf the surface surrounding a 10 km crater on Mars. Prior to ejecta emplacement, powerful winds (> 100 m/s) sweep over the region surrounding the impact, thereby stripping the surface of loose soil and dust (Figure 1). The surface is then immersed in an atmosphere with temperatures exceeding 273 K over times approaching 1 minute (even for the case of 0.1% coupling) (Figure 2).

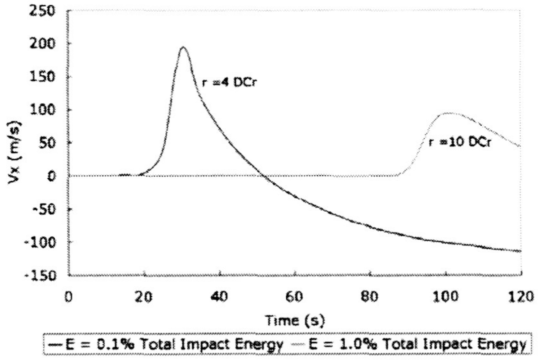

Figure 1: Horizontal velocity as a function of time for y=0 (surface) from computational models releasing 0.1% and 1.0% of the total energy required to create a 10 km diameter impact crater. DCr stands for apparent crater diameter. Results are displayed for positions of 4 apparent crater diameters (~25 km) for the case of 0.1% coupling and 10 apparent crater diameters (~60 km) for the 1.0% coupling case. These locations mark the distances from the crater center at which the front of the atmospheric shock blast equilibrates to ambient atmospheric pressure [11].

Residual temperatures behind the blast wave are much higher than ambient conditions, particularly close to the crater (1000 K at 2 apparent crater diameters). Even at greater distances (e.g., 4 apparent crater diameters), atmospheric temperatures radiating into the upper surface will produce a thermal wave that can extend down to ~15 cm in only 30 seconds for an ice-rich substrate (see Figure 3).

Implications: The combined effects of an intense atmospheric wind blast and thermal pulse should have particular significance for regions covered by an ice-rich mantle, e.g., high latitudes. Some possible residual signatures include; scoured zones (characterized by radial striations and muting of surface detail – see Figure 4a), armored surfaces created by thermally indurated soil (melting and migration of subsurface water), and pedestal craters.

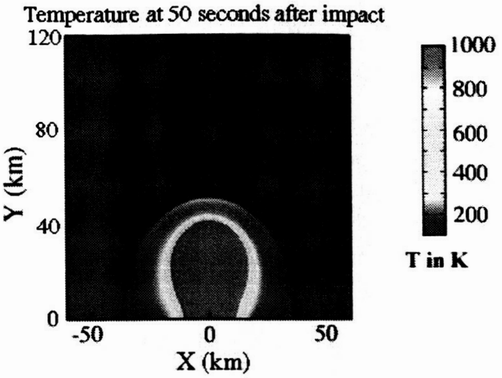

Figure 2: Temperature image from a computational model of a point source explosion releasing ~10^{23} ergs of energy into a Martian atmosphere. This energy correlates to a 0.1% coupling of the total energy involved in the creation of a 10 km diameter crater on Mars. Red denotes temperatures of 1000 K or greater. Blue indicates temperatures of 100 K or less.

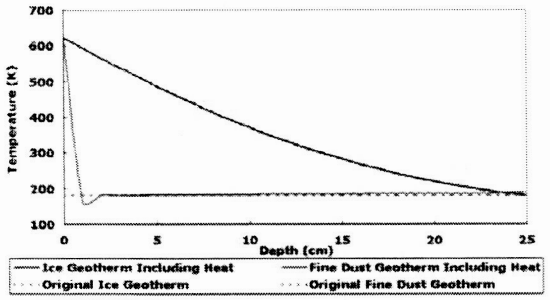

Figure 3: Temperature as a function of depth below the surface at 30 seconds after impact. The large temperature pulse and lingering atmospheric temperatures created from the direct coupling of impact energy (0.1% coupling plotted here) to the atmosphere results in a thermal wave that travels down into the upper surface layers. Comparisons between normal geotherms (for both ice and fine dust) and geotherms including this extra heat source are shown for the location of 4 apparent crater diameters (r = 25 km). Geotherm equations can be found in [21].

Pedestal Craters: Volatile-rich surface layers at high latitudes are highly susceptible to erosion over short times as a response to orbital forcing [6]. The calculated atmospheric winds and subsurface thermal wave discussed here would form a crater-centered erosion-resistant indurated surface layer around craters at high latitudes (Figure 4b).

Martian pedestals can extend up to ~10 crater diameters depending on crater size, age, and location [5-6]. Based on our study, energy coupling of at least 1.0% (into an atmospheric blast) would be necessary to create an erosion-resistant surface lag as a result of the combination of blast winds and thermal effects out to a distance of 10 crater diameters.

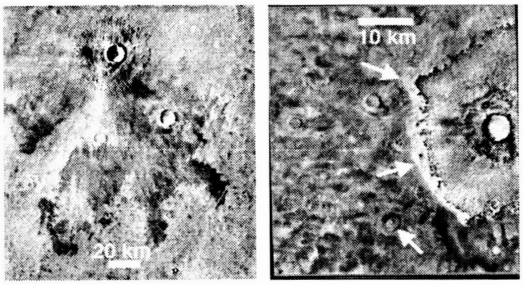

4a 4b Figure 4: (4a): Image of a ~12 km diameter Martian pre-pedestal crater. Scouring of the surface extends to ~8 crater diameters. (4b): Image of a ~6 km diameter Martian pedestal crater. Pedestal extends out to ~4 crater diameters. The bottom arrow points out an example of a much smaller pedestal crater.

Present / Future Work: Recent laboratory experiments [15] have captured the interplay between the expanding vapor generated on impact and the developing ejecta curtain, permitting investigation of the mechanics of the early stages (~150 ms after impact) of the cratering process. Comparisons of this experimental data with computational data from applications of the present model at such early times will lead to a better understanding of the interactions between an impact-induced vapor blast and the surrounding atmosphere, perhaps narrowing down the possible values for the extent of energy transfer.

More detailed modeling, benchmarked by laboratory experiments, is needed to test the relative roles of the atmospheric wind blast and temperature pulse for different volatile-rich lithologies. This, in turn, will help assess locations of past volatiles across Mars.

References: [1] O'Keefe, J. D. and Ahrens, T. (1982) *Geological Implications of Impacts of Large Asteroids and Comets on the Earth, Special Paper 190*, 103-120. [2] Ahrens, T. and O'Keefe, J. D. (1987) *Int. J. Impact Eng., 5*, 13-32. [3] Roddy, D. J. et al. (1987) *Int. J. Impact Eng., 5*, 123-135. [4] McCauley, J. F. (1973) *JGR, 78*, 41234137. [5] Schultz, P. H. (1988) *LPS XIX*, 1039-1040. [6] Schultz, P. H. and Lutz, A. B. (1988) *Icarus, 73*, 91-141. [7] Thomson, B. J. and Schultz, P. H. (2004) *LPS XXXV*, Abstract #1885. [8] Schultz, P. H. (2003) *6th Mars Conf.*, Abstract # 3263. [9] Mouginis-Mark, P. J. (1987) *Icarus, 45*, 268-286. [10] Barlow, N. G. (2005) *LPS XXXVI*, Abstract #1415. [11] Schultz, P. H. (1992) *JGR, 97*, 16183-16248. [12] Arvidson, R. E. et al. (1976) *Icarus, 27*, 503-516. [13] Sugita, S. *et al.* (1998) *JGR, 103, E8,* 19,427-19,441. [14] Schultz, P. H. (1996) *JGR, 101*, 21117-21136. [15] Wrobel, K. E. and Schultz, P. H. (2004) *LPS XXXV*, Abstract #1800. [16] Pierazzo E. and Melosh, H.J.(1999) *Earth Planet. Sci. Lett., 165, 2,* 163-176. [17] Adushkin, V. V. and Nemchinov, I. V. (1994) *Hazards due to Comets and Asteroids*, 721778. [18] McGlaun, J. M. et al. (1990) *Int. J. impact Eng., 10*, 351-360. [19] Crawford, D. A. et al. (2002) *New Models and Hydrocodes for Shock Wave Processes in Cond. Matter*, Edinburgh, U.K. [20] Wrobel, K. E. and Schultz, P. H. (2005) *LPS XXXVI*, Abstract #1221. [21] Arfstrom, J. D. (2004) *LPS XXXV*, Abstract #1105.

Acknowledgements: This material is based on work supported by NASA Grant No. NAG5-11538 and a 2004-2005 Rhode Island Space Grant Fellowship.